Quantum Dot-Dye Hybrid Systems for Energy Transfer Applications

Dissertation
zur Erlangung des Grades
„Doktor der Naturwissenschaften“
In Promotionsfach Chemie

am Fachbereich Chemie, Pharamazie und Geowissenschaften
der Johannes Gutenberg-Universität Mainz

Ting Ren
geb. in Shanghai, P.R. China

Mainz, 2010

Table of Contents

1 Introduction

Semiconductor quantum dots (QDs) have been extensively studied for over 20 years for their size dependent optical properties. Strong quantum confinement of the charge carriers in QDs increases their effective band gap energy significantly with decreasing particle size, resulting in size dependence of QD electronic absorption and luminescence spectra [1, 2, 3]. Due to their unique optical and spectroscopic properties, luminescent semiconductor QDs have proven to be very effective donor fluorophores in numbers of processes and bioassays based on fluorescence (or Förster) resonance energy transfer (FRET). Use of semiconductor QDs as components of nanoarchitectures where FRET takes place has generated a tremendous amount of interest in recent years.

FRET is a process whereby the electronic excitation energy of a donor fluorophore is nonradiatively transferred to a nearby acceptor fluorophore [4, 5]. FRET processes are driven by through-space dipole-dipole interactions between the donor-acceptor pair and depend on the degree of spectral overlap between donor photoluminescence (PL) and acceptor absorption, as well as on the spatial distance and orientation between donor and acceptor pair. FRET-based studies involving pairs of organic dye molecules as the donor-acceptor couple are often limited by cross-talk caused by spectral overlap of the donor and acceptor emission. In addition, the broad emission spectrum of the donor, with its long red tail, can often overlap significantly with the acceptor emission spectrum. QDs can be considered as efficient ‘‘inorganic dyes’’ that offer a compelling alternative to conventional organic dye molecules. Unique advantages of QDs as a FRET donor include: 1) broad tunable absorption spectra with large absorption cross sections, which allows them to be excited at wavelengths remote from acceptor direct excitation, minimizing cross-excitation; 2) narrow and tunable symmetric PL spectra with high quantum yields, which alleviates the common problem of donor red tailing into acceptor emission wavelengths and allows for optimal spectral overlap with acceptor absorption; 3) exceptional resistance to photo- and chemical degradation; 4) high photobleaching thresholds; 5) the capacity to bind multiple acceptor molecules, which enhances the effective FRET cross section; and 6) the ability to excite mixed QD populations at a single wavelength far away from their respective emissions or assemble several receptors with different properties/functionalities on QD donors, which could

allow extensive multiplexing [1, 6, 7, 8, 9, 10]. However, use of QDs does have limitations. Some disadvantages of QDs [11, 12] include the toxicity, the size which is larger than conventional organic dyes and might hamper some applications (e.g., does not allow very close approach of acceptors or may cause steric interference with protein function), and blinking processes which can cause complications especially when single molecule spectroscopy needs to be carried out. Moreover, the accurate determination of the QD concentration is still a problem so far.

Energy transfer processes involving semiconductor QDs have been widely studied. Apart from the fundamental photo physical aspects, FRET-related QD systems hold promise to develop more efficient nanoscale FRET-based sensors [13, 14, 15, 16, 17]. Until now the energy transfer-based QD hybrid systems include QD-QD, QD-dye and QD-metal hybrid systems. Energy transfer between QDs of different sizes is not only of scientific interest, it may also be applied for light harvesting purposes. Differently sized semiconductor QDs have been assembled to be contained in thin solid films or form small aggregates in solution. Energy transfer between two chemically coupled QDs has not been reported yet. Controlling energy transfer on a nanometer scale where especially coupling with dye molecules or metal nanoparticles offers new avenues for detection schemes that can be used in bio-imaging and possibly other areas, such as in novel scanning probes for FRET-based near field microscopy [18, 19, 20, 21]. In many of these hybrid systems, the acceptor is either covalently bound to the organic coating ligand using standard cross-linking chemistry [22], or bound using a biotin-streptavidin interaction [23]. An additional component such as polymers [18, 24], proteins [25, 26], or peptides [27, 28], is needed to mediate the attachment of the acceptor to the QD donor.

In this thesis, silica is chosen as a possible mediating material for coupling QD donors and dye acceptors. Silica is chemically inert and optically transparent. The silica shell may provide both chemical and physical shielding from the direct environment, thereby improving the stability of the nanoparticles. Furthermore, since the surface chemistry of colloidal silica is well understood, the main advantage of silica over polymer is the ease of introduction of functional groups such as amines, thiols, carboxyls, and methacrylate on the surface by modification of surface hydroxyl groups for further use [29, 30, 31, 32]. Therefore, silica chemistry can offer various ways for attaching dye molecules to a silica surface. In addition, the silica layer allows for controlled placement of various

dyes [33]. Based on silica chemistry, a QD-silica-dye hybrid system was designed where QD donors are covered by a silica shell and dye acceptors are then attached to the silica shell. To achieve this structure, QD-silica hybrid systems were prepared first. There are two methods to incorporate QDs into silica: the "Stöber" method and the water-in-oil (W/O) reverse microemulsion method. Using these two methods, two kinds of QD-silica hybrid structures were obtained: the silica-QD-silica structure where CdSe/CdS/ZnS QDs are adsorbed on a "pure" silica core followed by further growth of a silica shell, and the QD-silica structure where one single CdSe/CdS/ZnS QD is encapsulated in a silica nanosphere. After optimization of reaction conditions, it was found that both structures had their own limitations for further investigations of energy transfer between QDs and dye molecules after attaching dye molecules to the silica surface. For the QD-silica structure, the obtained minimum thickness of the silica shell was still beyond the range where FRET between QD and dye could take place. For the silica-QD-silica structure, the uneven surface after growing a thin silica shell did not facilitate the definition of the QD-to-dye distance. Nevertheless, the study of the QD-silica structure shows the potential to prepare QD-dimers encapsulated in a silica particle and this makes it possible to study the energy transfer between two single QDs. More importantly, a new QD-silica-dye hybrid system has been assembled inspired by the silica-QD-silica structure. This structure comprises a silica core coated with an outer silica layer containing organic dyes, followed by QD surface adsorption. Using this QD-silica-dye hybrid system, the energy transfer between multiple QD donors and multiple dye acceptors can be studied. By varying the thickness of the dye-containing silica shell, the energy transfer process has been investigated and described in the framework of Förster theory.

Because the FRET efficiency is inversely proportional to the donor-to-acceptor distance to the sixth power [5], an increased separation due to the use of mediating materials can significantly reduce the energy transfer efficiency. To shorten the distance between QD and dye, a versatile route was developed to prepare QD-dye hybrid systems in organic solvents, in which dye molecules with dicarboxylate functional groups were directly attached to the QD surface without any spacer in between. It was proven that dye molecules with dicarboxylate functionality revealed a strong and robust attachment to QDs and the prepared QD-dye complexes were stable against repeated precipitation-

dissolution cycles and long-term storage. By proper choice of dye and QD components, a broad spectral range from the visible up to the NIR can be covered and additionally the efficiency of energy transfer can be easily tuned. Since the QD-dye distance can be precisely controlled by simply varying the QD size while preserving the binding geometry, this particular QD-dye hybrid system also gives unprecedented insights into the energy transfer mechanism. Although in most cases the QD-based energy transfer is discussed as a FRET process [34], for QD-dye hybrid systems there are only a few reports where FRET has been quantitatively identified to be the energy transfer mechanism [25, 35, 36, 37], and in those experiments dye molecules have been attached to QD via mediating materials. Recently, many studies on QD-dye mixtures, where dye molecules are directly attached to QDs, demonstrate that in short-range energy transfer from QDs to dye molecules, other non-Förster type processes appear to play a role in addition to the Förster mechanism. Such non-Förster type processes involve contributions of surface states [38], spatial extension of the exciton wave function outside of the QD [39, 40], and degree of interdigitization of alkylamino chains on dye molecules into alkyl-capping layers on QDs [41]. In order to experimentally clarify the energy transfer mechanism in the QD-dye hybrid system, the systematic quenching of QD emission with changing dye/QD molar ratios and the dependence of energy transfer efficiencies on the QD-dye distance were studied, confirming that FRET was the dominant mechanism. In addition, the high stability of the QD-dye hybrid systems allows directly transferring the QD-dye complexes from organic solvents into water using conventional transfer methods. The developed versatile route also provides a way to prepare QD dimers. Preliminary experiments were done to link QDs by bifunctional dye molecules. Using this versatile route, other organic molecules, e.g., calixarene molecules were able to complex with QDs and the QD-calixarene complexes also showed potential for QD-based energy transfer studies.

The organization of this thesis is as follows: a short summary on the basic properties of semiconductor QDs and on the FRET formalism and an overview of the major classes of hybrid FRET systems with semiconductor QDs as at least one component are given in chapter 2. The materials and methods used to prepare and characterize QDs and QD hybrid systems are described in chapter 3. The following chapters present the experimental results: Synthesis and optimization of the two QD-silica hybrid systems —

the silica-QD-silica structure and the QD-silica structure — are described in chapter 4. Assembly of the QD-silica-dye and QD-dye hybrid systems and investigations of energy transfer in these two systems are presented in chapter 5 and 6, respectively. At last, chapter 7 gives a short summary of all the results.

2 Theoretical background

2.1 Quantum dot properties

Colloidal quantum dots (QDs), also termed zero-dimensional semiconductor nanocrystals (NCs), are composed of an inorganic core, made up of between a few hundred and a few thousand atoms, surrounded by an outer organic layer of surfactant molecules (ligands).

Typically, for the 1 - 20 nm size range semiconductor nanocrystals show optical, electronic and mechanical properties distinct from those of the corresponding bulk material.

2.1.1 Bulk semiconductors

In a bulk semiconductor, the properties of the material are independent of the size and shape and are only chemical composition-dependent. The large number of atoms in a bulk crystal leads to the generation of sets of molecular orbitals with very similar energies which effectively form a continuum. At 0 K, the valence band is filled with electrons, while the conduction band is unoccupied. These two bands are separated by an energy gap (E_{gap}), the magnitude of which is a characteristic property of the bulk material (at a specific temperature). Figure 2.1 gives an overview of the band alignment of III–V and II–VI bulk semiconductor materials, and Table 2.1 lists the properties of the semiconductors included in this thesis.

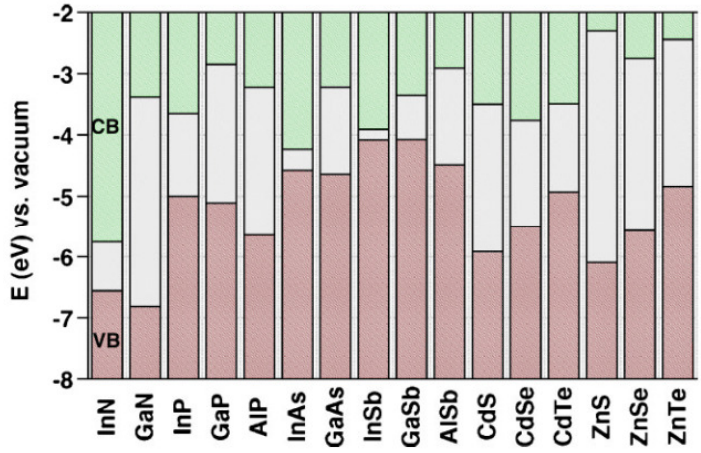

Figure 2.1: Electronic energy levels of selected III–V and II–VI semiconductors. VB: valence band, CB: conduction band. (Adapted from Ref 42)

Table 2.1: Properties of bulk II-VI compound semiconductors (Adapted from Ref 43)

compd	band gap[a]/eV	type[b]	structure	Lattice spacing/Å
CdSe	1.74	d	wurtzite	a: 4.299 c: 7.010
CdS	2.53	d	wurtzite	a: 4.136 c: 6.713
ZnS	3.8	d	wurtzite	a: 3.814 c: 6.257
ZnS	3.6	d	zinc blend	5.406

[a] at 300 K. [b] d, direct.

At temperatures above 0 K, electrons in the valence band may get enough thermal energy to be excited across the band gap into the conduction band. An excited electron in the conduction band together with the resulting hole in the valence band forms an "electron-hole pair".

In conventional bulk semiconductors electrons and holes are the charge carriers. They can form a bound state when they approach each other in space. This bound electron-hole pair, known as a Wannier exciton, is delocalized within the crystal lattice and experiences a screened Coulombic interaction.

2.1.2 Quantum dots

Two fundamental factors distinguish the behavior of quantum dots from that of the corresponding bulk material. The first is the large surface/volume ratio, and the second factor is the actual size of the particles [44]. As the size of a crystal decreases to the nanometer regime, the electronic structure is altered from the continuous electronic bands to discrete or quantized electronic levels. As a result, the continuous optical transitions between the electronic bands become discrete and the properties of the QDs become size dependent [45, 46, 47, 48]. Such size dependent optical properties occur [49] when the size of the nanoparticle is smaller than the bulk-exciton Bohr radius, a_B, of the semiconductor.

$$a_B = \frac{\hbar^2 \varepsilon}{e^2}\left(\frac{1}{m_e^*} + \frac{1}{m_h^*}\right) \tag{2.1}$$

where ε represents the bulk optical dielectric coefficient, $\hbar$ is Planck's constant, e is the elementary charge, and m_e^* and m_h^* are the effective mass of the electron and hole, respectively.

Based on the effective mass approximation, for CdE (E = S or Se) nanocrystallites, the first electronic transition energy can be expressed as [50, 51, 52]

$$E(1S_h - 1S_e) = E_{gap} + E_{10}^h + E_{10}^e + E_{coul} = E_{gap} + \frac{\hbar^2 \pi^2}{2R^2}\left(\frac{1}{m_e^*} + \frac{1}{m_h^*}\right) - \frac{1.8e^2}{\varepsilon R} \qquad (2.2)$$

where E_{gap} is the bulk semiconductor energy gap, E_{10}^h and E_{10}^e are the confinement energy of hole and electron respectively, E_{coul} represents the Coulomb interaction between electron and hole, and R is the radius of the nanocrystal. Equation 2.2 is illustrated by Figure 2.2.

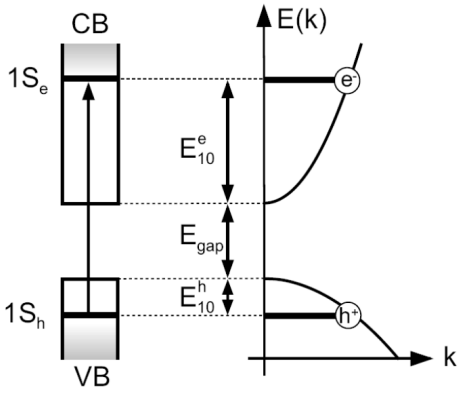

Figure 2.2: Left: electronic state diagram of a nanocrystalline semiconductor (VB: valence band, CB: conduction band). Right: the dispersion of the energy of the conduction and valence bands, respectively, of the semiconductor with direct energy gap in k-space (k is the wave vector of the reciprocal space). (Modified from Ref 60)

According to equation 2.2, with decreasing QD size, the quantization energy increases by $1/R^2$, whereas the Coulomb energy shifts the first excited electronic state to lower energy by 1/R. The Coulomb energy varies in a less pronounced manner than the quantization energy as the size of the QD changes. Consequently, as the QD size decreases, the electronic excitations shift to higher energy. Such quantum size effects have been observed experimentally in optical absorption measurements for nanocrystalline semiconductors. By using absorption spectroscopy technique, one can observe the development of discrete features in the spectra and the enlargement of the

energy gap in semiconductor nanocrystals [1, 46, 53, 54, 55]. CdSe QDs are a model semiconductor system which has been extensively studied [1, 46, 53, 54, 55, 56, 57]. For CdSe QDs, $1S_{3/2} - 1S_e$, $2S_{3/2} - 1S_e$, $1S_{1/2} - 1S_e$ and $1P_{3/2} - 1P_e$ are the commonly observed lower energy transitions [57, 58]. Figure 2.3 shows the absorption spectrum of 6.4 nm CdSe QDs and the corresponding transitions. Figure 2.4 shows the size dependence of the band gap for CdSe: the band gap decreases as the CdSe size increases from the molecular scale to the bulk.

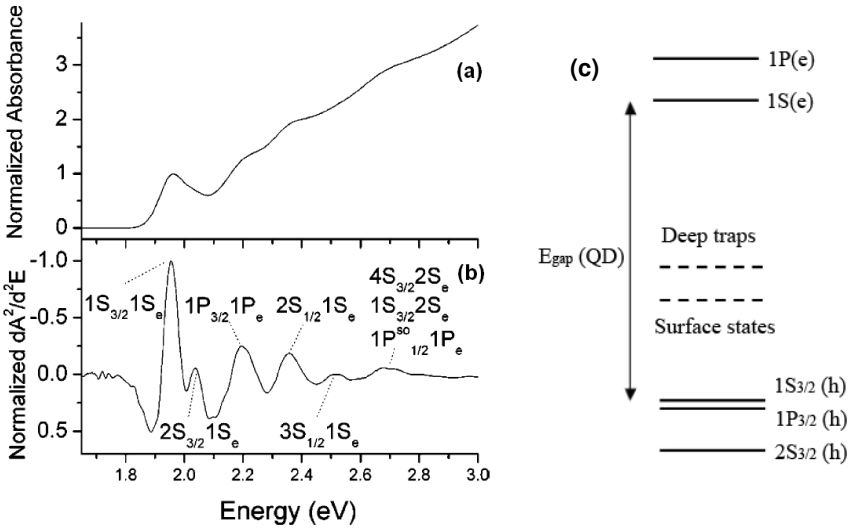

Figure 2.3: (a) Absorption spectrum of 6.4 nm CdSe quantum dots and (b) normalized second derivative of (a) (Adapted form Ref 59). The transitions are assigned according to Norris and Bawendi [58]. In this absorption spectrum, the $1S_{1/2} - 1S_e$ transition can not be resolved. (c) The electron and hole states of CdSe QDs in the strong confinement regime. The dashed lines represent surface states and deep traps of the QDs (Adapted from Ref 60).

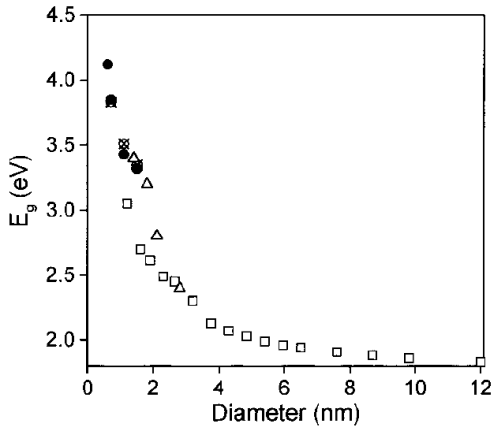

Figure 2.4: Size dependence of the band gap for CdSe from the molecular regime to the bulk. Filled (crossed) circles represent the band gap of cluster-molecules from Ref 61. Squares and triangles represent the band gap values for CdSe nanocrystals from Refs 1 and 62, respectively. (Modified from Ref 61)

Experimentally, quantum size effects are observed as a shift towards higher energy values in the absorption edge (a blue shift) and a corresponding larger separation between electronic transitions with decreasing QD diameter. Figure 2.5 shows the absorption spectra for a series of CdSe QDs with different sizes. The absorption spectra show a consistent red shift as the QD size increases and up to 10 discrete optical transitions can be resolved. A high-quality absorption spectrum for monodisperse QDs can be used to calculate and calibrate the size and size distribution of the synthesized QDs directly. Empirical relationships between the size and the first absorption wavelength can be derived for various types of semiconductor QDs, and the size can be read out after determination of the first absorption wavelength from the absorption spectra. Figure 2.5 also shows how the first absorption peak changes as the QD size changes for CdSe, CdS and CdTe QDs.

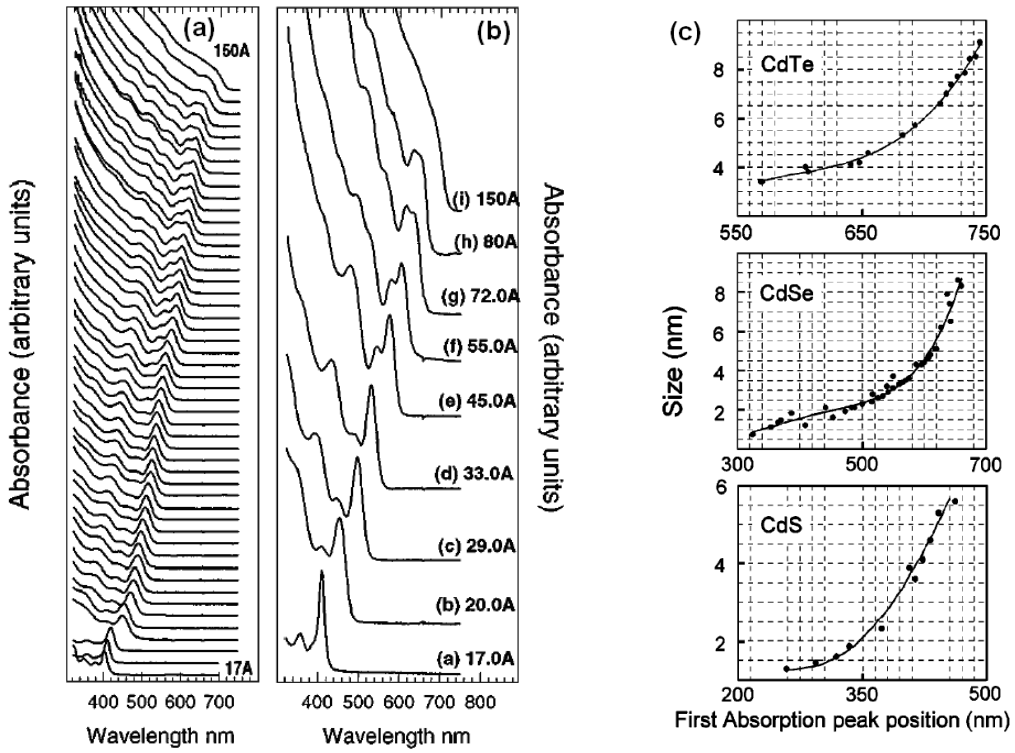

Figure 2.5: (a) Blue shift in the absorption edge and a larger separation between electronic transitions for a homologous size series of CdSe QDs and (b) Observation of discrete electronic transitions in optical absorption of QD dispersions, collected at room temperature (Adapted from Ref 53). (c) First absorption peak position versus the size of the QDs (Adapted from Ref 63).

2.1.3 Core-shell quantum dots

The key parameters that determine the applicability of luminescent QDs are (i) high photoluminescence (PL) quantum yield (QY), (ii) stability of luminescence properties under real operation conditions and (iii) solubility of QDs in a desired solvent. In certain cases, organically passivated QDs can provide high PL QY. However, the organic ligands are labile and in dynamic equilibrium with the surrounding medium. As a result, the PL QY is strongly dependent on the QDs' surroundings. Furthermore, these QDs typically exhibit surface related trap states acting as fast nonradiative de-excitation channels for photogenerated charge carriers, thereby reducing the quantum yield. They also exhibit some red-shifted luminescence and complex decay of the excited state [64, 65]. Therefore, the organically passivated nanocrystals do not yet have a perfectly passivated surface.

An important strategy to improve QDs' surface passivation and thereby their stability is to grow a shell of a wide band gap semiconductor on the outside of the QD, resulting in core-shell systems. Such core-shell QDs have been shown to improve the PL quantum yields by passivating surface nonradiative sites. Particles passivated with inorganic semiconductor shell structure are also more robust than organically passivated QDs and are of practical interest for biological imaging and light-emitting devices. Some reported examples of core-shell QD structures include CdS/$Cd(OH)_2$ [66], CdSe/ZnSe [67, 68], CdSe/ZnS [69, 79], CdS/HgS/CdS [70, 71], CdSe/CdS [72], InP/ZnS [73, 74], PbSe/PbS [75, 76], and Si/SiO_2 [77].

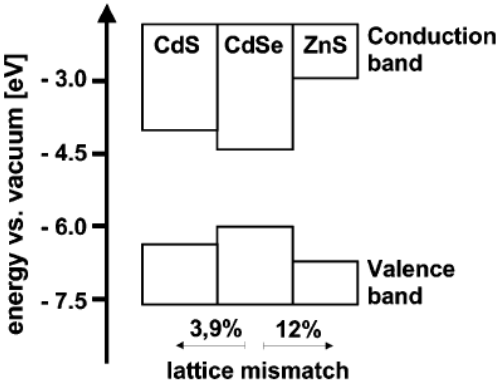

Figure 2.6: Energetic band positions and lattice mismatch of bulk semiconductor material combinations. Lattice mismatch was calculated using: $(c_{core}-c_{shell})/c_{core}$, lattice spacing c is shown in Table 2.1. (Adapted from Ref 78)

In particular, for CdSe core-shell QDs, several wide band gap semiconductors, such as ZnS [7, 79], CdS [80, 81, 82, 83] and ZnSe [84, 86], were employed as the shell material to establish a core-shell system. In Figure 2.6, the band gap and lattice mismatch of bulk semiconductor materials included in this thesis are compared.

ZnS is a nontoxic, chemically stable wide band gap semiconductor. Potentially, the ZnS shell should provide the best passivation of the CdSe core. However, as the thickness of the ZnS shell increases by more than ~ 2 monolayers, the strain due to the large lattice mismatch between CdSe and ZnS leads to the formation of dislocations, relaxes the structure and causing the growth to proceed incoherently [7, 85]. The defects in the ZnS shell produced due to the generation of misfit dislocations could be the source of nonradiative recombination sites and thus lead to a decline in the quantum yield and negatively affect the stability of the CdSe/ZnS core-shell QDs. It is worth mentioning that the particle size distribution often broadens substantially upon growing the ZnS shell around CdSe cores [7].

In the case of CdSe/CdS core-shell QDs, the lattice mismatch between the core and the shell materials is small enough to allow epitaxial growth of the CdS shell [81, 82, 83]. As a result of the low concentration of defects in the shell, CdSe/CdS QDs exhibit very high quantum yield [80, 81, 86]. However, the band gap of CdS is not large enough to provide the potential barrier necessary to block both electrons and holes inside the CdSe core [7, 83]. Moreover, the CdS shell can be excited by UV light broadly used in biological tagging application. The direct excitation of the QD shell causes its fast photooxidation that makes CdSe/CdS QDs unsuitable for many biolabeling applications [87].

To combine the advantages of both shell materials, between the CdSe core and the wide band gap ZnS shell a CdS shell is introduced with lattice spacing intermediate to CdSe and ZnS, resulting in multishell CdSe/CdS/ZnS QDs [78]. CdS has both the band gap and the lattice spacing intermediate to those of CdSe and ZnS (see Figure 2.6). Such double shell structure allows a stepwise change of lattice spacing from the emitting CdSe core to the protecting ZnS shell and thus allows reducing the strain inside the QDs considerably, leading to a high quantum yield.

Figure 2.7 a shows the absorption and photoluminescence spectra of multishell CdSe/CdS/$Cd_{0.5}Zn_{0.5}S$/ZnS QDs during shell growth. The $Cd_{0.5}Zn_{0.5}S$ shell is used as a

buffer layer to gradually change the shell composition from CdS to ZnS in the radial direction. It can be seen that the absorption and PL spectra shift to the red when the shell with the composition of CdS is grown, and this red shift can be explained using both molecular orbital and particle-in-a-box models [81], as shown in Figure 2.8.

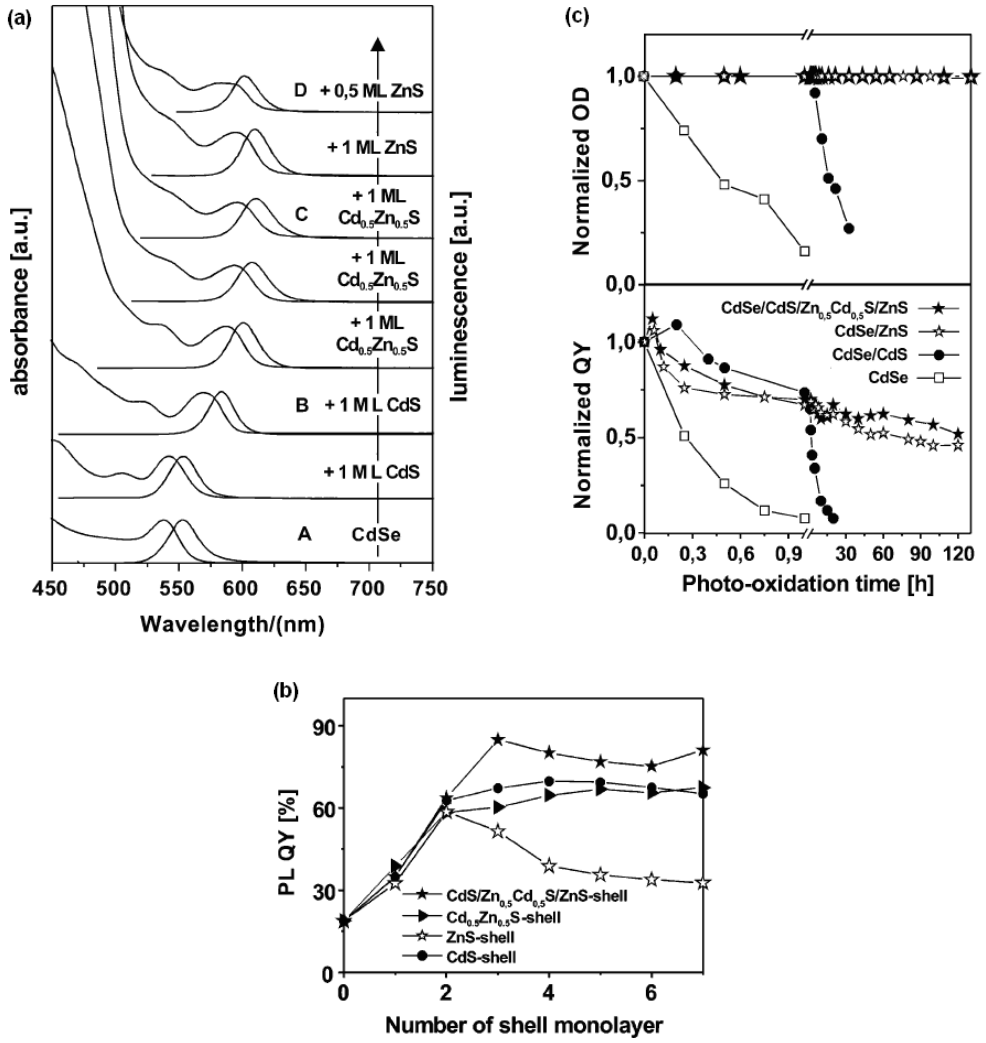

Figure 2.7: (a) Evolution of the absorption and photoluminescence (PL) spectra upon consecutive growth of the concentric shells. (b) Evolution of the PL quantum yield for several core-shell particles. (c) Photochemical stability of QDs in oxygen saturated chloroform solutions under UV-irradiation. (top) change in optical density and (bottom) change in PL quantum yield for the CdSe core and different core-shell particles. (Adapted from Ref 78)

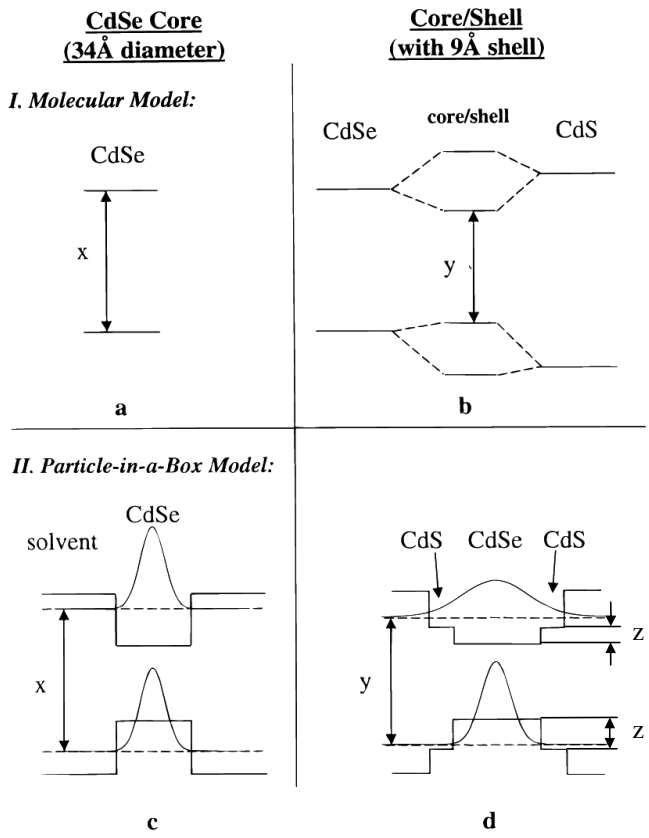

Figure 2.8: Schematic core and core-shell potentials (solid lines) and electronic energy levels (dashed lines) as described by a molecular model (a,b) and a particle-in-a-box model (c,d). (a,c) represent a core, while (b,d) represent a core-shell QD. "x" represents the absorption onset for a CdSe core, "y" for a core-shell grown from this core, and "z" represents the potential step. The Gaussians shown are the results of effective mass calculations for electron and hole wavefunctions. (Adapted from Ref 81)

In the molecular orbital model, the core and shell are viewed as molecular fragments. Since in CdSe/CdS core-shell QDs the core and shell bind together epitaxially and with minimal defects, their energy levels mix and a new set of core-shell levels emerges. The individual core and shell LUMOs will mix strongly since they are relatively close in energy. Consequently, the core-shell LUMO will be largely delocalized throughout the structure. However, the energy difference between the core and shell HOMOs is relatively large, and the core-shell HOMO will be predominantly corelike and localized. Thus, the electron-hole overlap in the core-shell first excited state is confined mostly to the core.

The particle-in-a-box model can be used to obtain a first qualitative approximation of the election and hole wavefunctions. As shown in Figure 2.8 d, in the core-shell structure, the electron potential step (see "z") is about half as large as that of the hole

(0.27 vs 0.51 eV). Figure 2.8 c and d also show the electron and hole wave functions calculated with the particle-in-a-box model [88]. These results suggest that the electron is delocalized throughout the core-shell structure, while the hole is mostly confined to the core.

These two models present a picture of core-shell energy levels. The red shift is predominantly a result of the high degree of mixing of the core and shell LUMOs in the molecular orbital model, the loss of quantum confinement in the particle-in-a-box model (a bigger box). Confinement of the hole to the core would also be consistent with the very high observed quantum yields when growing CdS shells (Figure 2.7 b), as the highest probability of electron-hole overlap would then be in the core, away from the nonradiative traps and defects associated with the QD surface.

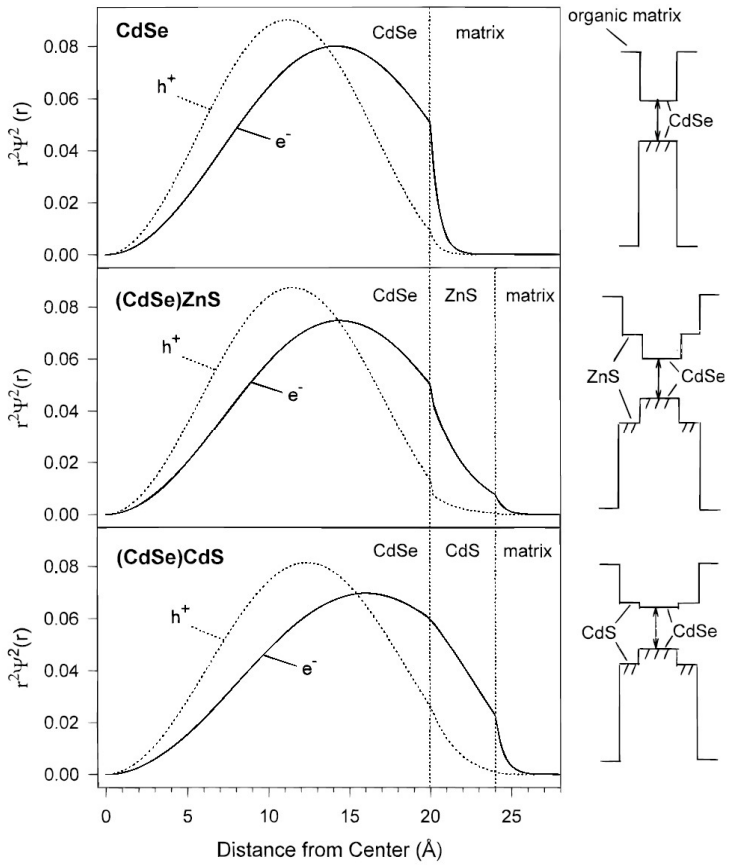

Figure 2.9: Radial probability functions for the lowest energy ($1S_{3/2}$-1S(e)) electron and hole wave functions in bare 20 Å diameter CdSe dots, CdSe/ZnS dots with a 20 Å diameter core and a 4 Å ZnS shell, and CdSe/CdS dots with an identical core and a 4 Å CdS shell. The sketches to the right show the approximate band offsets between the various components. (Adapted from Ref 7)

From the models, the spreading of the electron wavefunction into the shell is also predicted. Figure 2.9 shows the radial probability functions of the electron and hole for bare CdSe dots, and for the same dots with a ZnS or CdS shell.

In the bare dots, the wave function of the lighter electron spreads over the entire particle and tunnels only slightly into the surrounding organic matrix whereas the heavier hole has a higher probability to be found at the center of the dot and does not extend into the surrounding matrix. When a shell of ZnS surrounds the CdSe particle, the electron wavefunction tunnels into the ZnS shell while the hole wavefunction has a negligible probability of spreading into the ZnS layer. Beyond a certain thickness of the ZnS shell the electron and hole wavefunctions cannot spread out further. In CdS the barrier height for the electron is smaller than the total energy of the electron (also see Figure 2.8), and thus its wavefunction extends well into the CdS shell. The hole, however, has lower probability of penetrating into the surrounding CdS matrix than the electron but extends into the CdS more than it does for a ZnS shell. Therefore, the ZnS shell can provide more efficient confinement of not only hole but also electron wavefunctions inside the QDs. As a result, the QDs with an outer layer of ZnS have a higher photochemical stability and also higher long-term fluorescence intensity, as can be seen in Figure 2.7 c.

Summarizing, the combination of low strain, provided by the intermediate CdS layer serving as a ‘‘lattice adapter’’ and efficient passivation and charge-carrier confinement assured by the outer ZnS shell offers core-shell QDs with high stability against photo-oxidation and high quantum yields.

2.2 Fluorescence resonance energy transfer

Fluorescence (or Förster) resonance energy transfer (FRET) between optically active species is a well documented process [5, 89, 90] and has become widely used. FRET occurs between a donor (D) molecule in the excited state and an acceptor (A) molecule in the ground state without the appearance of a photon, and is the result of long range dipole-dipole interactions between the donor and acceptor. The rate of energy transfer depends upon the extent of spectral overlap of the emission spectrum of the donor with the absorption spectrum of the acceptor, the quantum yield of the donor, the relative orientation of the donor and acceptor transition dipoles and the distance between the donor and acceptor molecules.

FRET therefore is a powerful photophysical reporting technique. The power of this technique derives from its high intrinsic sensitivity to small changes (0.5 -10 nm) in the separation distance and orientation between the donor and acceptor dipoles, which has led to the characterization of FRET in several reports as a "spectroscopic ruler" [5].

2.2.1 Characteristics of FRET

The mechanism of FRET was theoretically described for the first time by Theodor Förster in 1948 [91]. He considered the so-called "homo" transfer between the donor and the acceptor being of the same type of fluorophore. In 1949, Förster extended his theory to the situation where the electronic transition of the donor involves a larger energetic step $\Delta E_D = E_D^1 - E_D^0$ compared to the electronic transition of the acceptor $\Delta E_A = E_A^1 - E_A^0$ [92], as illustrated in Figure 2.10. The initial step of energy transfer from the donor to the acceptor is resonant or isoenergetic. A transfer from the excited donor level E_D^1 can only take place into a vibronically excited acceptor level $E_A^{1,*}$. However, the excess vibronic energy is readily dissipated, leaving the acceptor in state E_A^1 (Figure 2.10). This second step of energy dissipation is usually much faster (typically within less than a picosecond) than the time scale of the original resonant energy transfer and therefore FRET becomes a "one way" process. This means that the probability of the back transfer is substantially reduced because it is unlikely that the relaxed acceptor gains thermal energy $\Delta E_{th} = E_A^{1,*} - E_A^1$ [34].

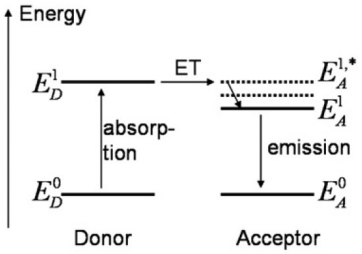

Figure 2.10: Schematic representation of the FRET process. After absorption of a photon by the donor, the energy is transferred resonantly to an excited state $E_A^{1,*}$ of the acceptor. The excess energy is quickly dissipated. Finally, the fluorescence emerges from the acceptor.

It is important that FRET is a process that does not involve emission and re-absorption of photons. The theory of energy transfer is based on the concept of a fluorophore as an oscillating dipole, which can exchange energy with another dipole with a similar resonance frequency [93]. In contrast, radiative energy transfer is due to emission and re-absorption of photons and depends upon non-molecular optical properties of the sample, such as the size of the sample container, the path length, and so on. Thereby, non-radiative energy transfer contains a wealth of structural information concerning the donor-acceptor pair.

2.2.2 Principles of FRET

The rate of energy transfer from a donor to an acceptor $k_T(r)$ is given by [5]

$$k_T(r) = \frac{1}{\tau_D}\left(\frac{R_0}{r}\right)^6 \tag{2.3}$$

where τ_D is the decay time of the donor in the absence of acceptor, r is the donor-acceptor distance and R_0 is the Förster radius, where the FRET efficiency is 50%. In other words, R_0 is the distance between the donor and the acceptor at which 50% of the excitation energy of the donor is transferred to the acceptor and 50% deactivates in other radiative and nonradiative processes. The rate of FRET depends strongly on distance, and is proportional to r^{-6} (equation 2.3).

The FRET efficiency (E) is the fraction of photons absorbed by the donor which are transferred to the acceptor. This fraction is given by [5]

$$E = \frac{k_T(r)}{k_T(r) + \tau_D^{-1}} \tag{2.4}$$

which is the ratio of the transfer rate to the total decay rate of the donor in the presence of acceptor.

Taking equation 2.3 and 2.4 together, the FRET efficiency can be described as

$$E = \frac{R_0^{\,6}}{R_0^{\,6} + r^6} = \frac{1}{1 + \left(\frac{r}{R_0}\right)^6} \tag{2.5}$$

As can be seen from equation 2.5, the FRET efficiency is strongly dependent on D-A distance (r) and Förster radius (R_0).

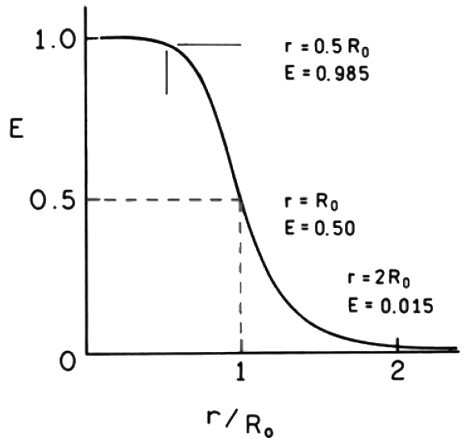

Figure 2.11: Dependence of the energy transfer efficiency (E) on distance. (Adapted from Ref 5, **94**)

Figure 2.11 shows the dependence of FRET efficiency on the distance. The efficiency quickly increased to 1 as the D-A distance decreases below R_0. Conversely, the transfer efficiency quickly decreases to 0 if the D-A distance is greater than R_0. Because E depends so strongly on distance, measurements of the D-A distance (r) are only reliable when r is within a factor of 2 of R_0.

$$R_0 = 0.211(\kappa^2 n^{-4} Q_D J(\lambda))^{1/6} \tag{2.6}$$

The Förster radius (R_0) depends on the orientation factor (κ^2) describing the relative orientation in space of the transition dipoles of the donor and acceptor, the refractive index of the medium (n), the QY of the donor in the absence of acceptor (Q_D), and the

spectral overlap integral ($J(\lambda)$). When the wavelength is expressed in nm, the Förster distance in Å is expressed by equation 2.6 [5].

The overlap integral ($J(\lambda)$) describes the degree of spectral overlap between the donor emission and the acceptor absorption [5]:

$$J(\lambda) = \int_0^\infty F_D(\lambda)\varepsilon_A(\lambda)\lambda^4 d\lambda = \frac{\int_0^\infty F_D(\lambda)\varepsilon_A(\lambda)\lambda^4 d\lambda}{\int_0^\infty F_D(\lambda)d\lambda} \qquad (2.7)$$

$F_D(\lambda)$ is the fluorescence intensity of the donor and $\varepsilon_A(\lambda)$ is the extinction coefficient of the acceptor at λ, which is typically in units of M^{-1} cm^{-1}. In calculating $J(\lambda)$ one should use the corrected emission spectrum with its area normalized to unity (equation 2.7, middle), or normalize the calculated value of $J(\lambda)$ by the area (equation 2.7, right).

FRET can be reliably assumed to occur whenever the donors and acceptors are within the Förster radius, i.e. suitable spectral overlap occurs. The R_0 value can be reliably predicted from the spectral properties of the donors and the acceptors. Energy transfer is a through-space interaction that is often independent of the intervening solvent and/or molecule. Therefore, one can assume that FRET will occur if the spectral properties are suitable and the D-A distance is comparable to R_0.

When a single donor interacts with multiple acceptors brought in close proximity and all acceptors are equally separated from a central donor, the FRET efficiency is given by

$$E = \frac{nR_0^{\,6}}{nR_0^{\,6} + r^6} = \frac{n}{n + \left(\frac{r}{R_0}\right)^6} \qquad (2.8)$$

where n is the number of acceptors surrounding a single donor [10, 25].

2.2.3 Measurement of FRET

FRET efficiency can be experimentally determined by quenched donor emission or sensitized acceptor emission using steady-state measurements, or by a decrease of donor fluorescence lifetime in the presence of the acceptor using time-resolved measurements.

Reduced donor emission Upon excitation of the donor fluorophore, the occurrence of FRET leads to a decrease in donor emission intensity, also called quenching of the

donor fluorescence or quenched donor emission. Intensity-based FRET measurement determines FRET efficiency by analyzing steady-state spectra of the donor emission. The FRET efficiency can be measured using the relative fluorescence intensity of the donor, in the absence (F_D) and presence (F_{DA}) of acceptor [5]:

$$E = 1 - \frac{F_{DA}}{F_D} \tag{2.9}$$

To calculate E by analyzing fluorescence intensities from steady-state spectra, the concentrations of the donor and acceptor should be taken into account.

Sensitized acceptor emission In a FRET experiment, the acceptor does not need to be fluorescent, although its absorption must overlap with the donor emission. If the acceptor is a fluorophore, the quenched donor emission is simultaneously accompanied by an enhanced acceptor emission. Assuming that the donor does not emit at the acceptor wavelength, the FRET efficiency is given by [5]

$$E = \frac{\varepsilon_A(\lambda_D^{ex})}{\varepsilon_D(\lambda_D^{ex})}\left[\frac{F_{AD}(\lambda_A^{em})}{F_A(\lambda_A^{em})} - 1\right]\left(\frac{1}{f_D}\right) \tag{2.10}$$

where $\varepsilon_A(\lambda_D^{ex})$ and $\varepsilon_D(\lambda_D^{ex})$ are the extinction coefficients (single D-A pairs) or absorbance (multiple acceptors) of the acceptor and donor at the donor excitation wavelength (λ_D^{ex}). $F_{AD}(\lambda_A^{em})$ and $F_A(\lambda_A^{em})$ are the acceptor intensities measured at an acceptor emission wavelength (λ_A^{em}) in the presence and absence of donor, and f_D is the fractional labeling with the donor. The acceptor is almost always excited directly at the donor excitation wavelength [95]. Therefore, the enhanced acceptor emission requires considering all these interrelated intensities. It is also important to correct further for the donor emission at λ_A^{em}, which is not considered in equation 2.10.

Reduced donor lifetime The occurrence of FRET shortens the average lifetime of the donor. The FRET efficiency therefore can also be calculated from the decay of the donor emission in the presence (τ_{DA}) and absence (τ_D) of the acceptor [5]:

$$E = 1 - \frac{\tau_{DA}}{\tau_D} \tag{2.11}$$

If the intensity decays are multi-exponential, an average decay time that is proportional to the steady-state intensity should be used. These averages are given by the sum of the $\alpha_i\tau_i$ products, where τ_i are the decay times and α_i are the amplitudes of the components.

It's important to remember that equations 2.9 and 2.11 are only applicable to donor-acceptor pairs that are separated by a fixed distance. A single fixed donor-acceptor distance is not found for a mixture of donors and acceptors in solution, nor for donors and acceptors dispersed randomly in space.

2.3 Energy transfer with quantum dots

Energy transfer processes involving semiconductor QDs have been widely studied and most of the energy transfer processes can be explained using the Förster theory [10, 25, 94, 96, 97, 98]. In applying the Förster formalism to analyze the non-radiative transfer of excitation energy in systems involving QD fluorophores (e.g. from an excited QD to a proximal ground-state dye acceptor), the QD excited state (or exciton) is approximated as an oscillating (point) dipole. This approximation is derived from the combination of two factors: 1) strong overlap of the electron and hole carrier wavefunctions in the QD, and 2) the spatial extent of the carrier wavefunctions as well as the separation between electron and holes carriers inside the QDs are much smaller than the wavelength of light [14].

2.3.1 Energy transfer between quantum dots

2.3.1.1 Energy transfer in thin solid film containing quantum dots

The first demonstration that CdSe QDs (core only) can engage in efficient non-radiative energy transfer was reported by the Bawendi group [96]. Energy transfer between randomly distributed QDs in close-packed solid films was studied. Solutions containing two CdSe QDs of different diameters were prepared, using small 3.9 nm CdSe QDs functioning as exciton donors and large 6.2 nm CdSe QDs serving as energy acceptors. These solutions were then spin cast to form films of close-packed interpenetrating networks of donor-acceptor QDs. Steady-state fluorescence data collected at room temperature and at 10 K showed that there was a clear decrease in the PL from the smaller QDs along with an increase in larger QD PL when exciting at the blue edge of the first absorption maximum of the smaller QDs (Figure 2.12). Time-resolved fluorescence experiments also showed a decrease in the PL lifetime of the donor and an increase in the acceptor PL lifetime, which corroborated the steady-state results. Data were successfully analyzed within the Förster formalism, showing that dipole-dipole interaction is the dominant mechanism for energy transfer between nearest neighbor QDs.

In subsequent studies, the authors showed that in a population (with a finite size distribution) of close-packed CdSe QDs, there is shift of the PL maximum wavelength

compared to the wavelength of their dilute solution counterparts, which was attributed to FRET from small- to larger-size nanocrystals. They further confirmed that the shift is more pronounced when the size distribution becomes broader [97].

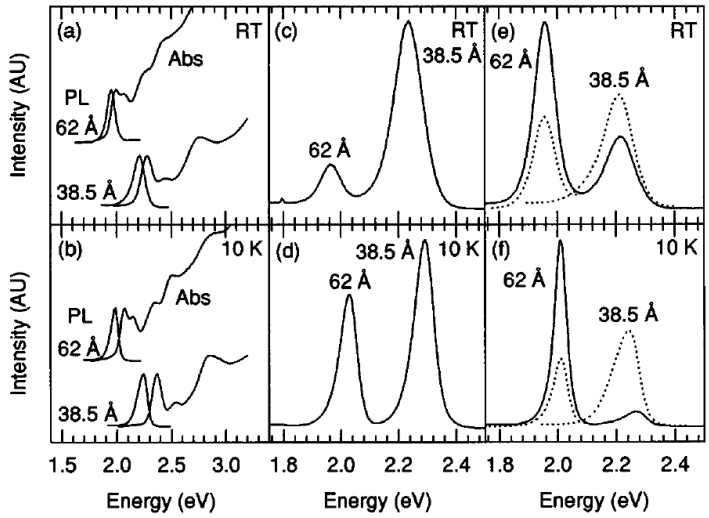

Figure 2.12: Absorption and emission spectra for 3.9 and 6.2 nm CdSe QD solids at (a) room temperature (RT) and (b) 10 K. PL spectra for the mixed system (solid lines) dispersed in solution at (c) RT and (d) 10 K and close-packed in the solid films at (e) RT and (f) 10 K. Dotted lines plot the relative quantum yields for 3.9 nm dots in a pure film and for 6.2 nm dots in the mixed film when excited to the red (578 nm) of the 3.9 nm dots absorption edge at (e) RT and (f) 10 K. (Adapted from Ref 96)

2.3.1.2 Energy transfer in layered assemblies of quantum dots

In layer-by-layer assembled structures of QDs, all the excitation energy that is absorbed by QD layers containing smaller particles (donors) can be concentrated in the larger QD layers (acceptors). The first reported structure consisted of two monolayers of differently sized QDs capped by long-chain organic ligands covalently bound by dithiol linker molecules [2598]. Because of the relatively large length of the linker molecule, which caused a large interdot separation (~ 6.2 nm center-to-center), the energy transfer was relatively slow and had a FRET rate of $(750\ ps)^{-1}$. This study was followed by an investigation of bilayers of similar QDs (1.5 nm and 1.9 nm in radius, respectively) fabricated using the Langmuir–Blodgett technique (Figure 2.13 a), thus avoiding the linker molecules in between to minimize the distance between donor and acceptor QDs and achieve a faster energy transfer [99]. Figure 2.13 b shows the spectra of this structure recorded at different times after excitation. With increasing time, the high-energy PL (smaller QD monolayer) rapidly decays, while the low-energy PL (larger QD monolayer)

grows. The energy transfer related dynamics in the two layers recorded at 2.30 and 2.17 eV, which approximately correspond to PL peaks in monolayers of the smaller and larger QDs, was compared in Figure 2.13 c. The exponential fit to the initial PL decay at 2.30 eV and its growth at 2.17 eV yielded an improved inter-layer energy transfer rate of $(120\ ps)^{-1}$.

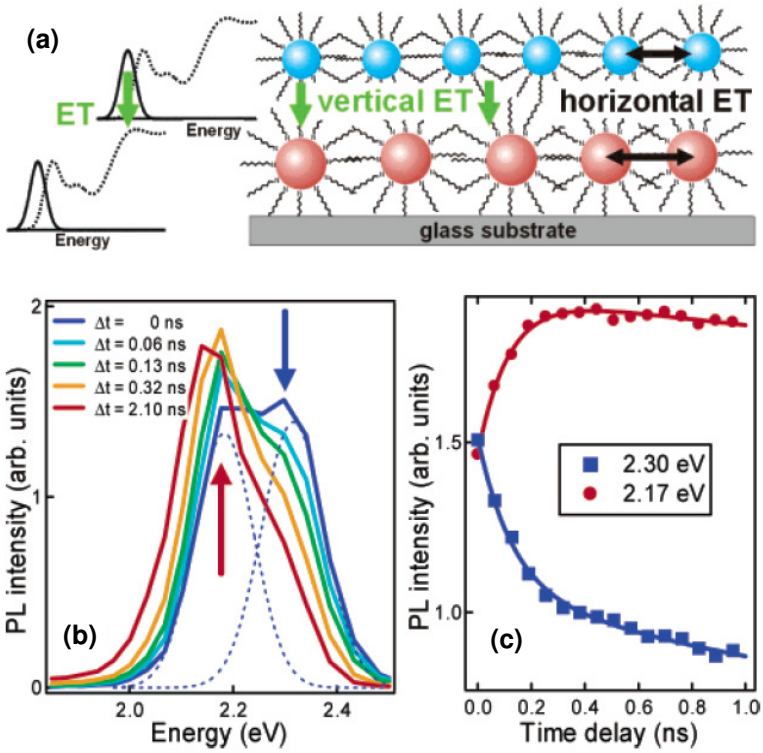

Figure 2.13: (a) The bilayer structure fabricated from QDs with different sizes. (b) Normalized PL spectra of the QD bilayer measured at different times after excitation. The zero-delay-time spectrum is decomposed into two Gaussian bands (blue dashed lines) that correspond to emission spectra from individual monolayers. (c) The bilayer PL dynamics measured at 2.30 eV (blue squares) and 2.14 eV (red circles). (Adapted from Ref 99)

The energy transfer mechanism between QDs was further experimentally verified by measuring PL dynamics in a bilayer structure where the distance between QD monolayers was precisely controlled by a spacer layer (Figure 2.14 a) [100]. As shown in Figure 2.14 b, the energy transfer rate from the donor(D)-QDs to the acceptor(A)-QDs becomes smaller with increasing spacer-layer thickness. The dependence of energy transfer rate on the distance between two QD monolayers can be quantitatively explained by the Föster model. Accordingly, the energy transfer between the donor and acceptor QDs is dominated by the dipole-dipole interaction.

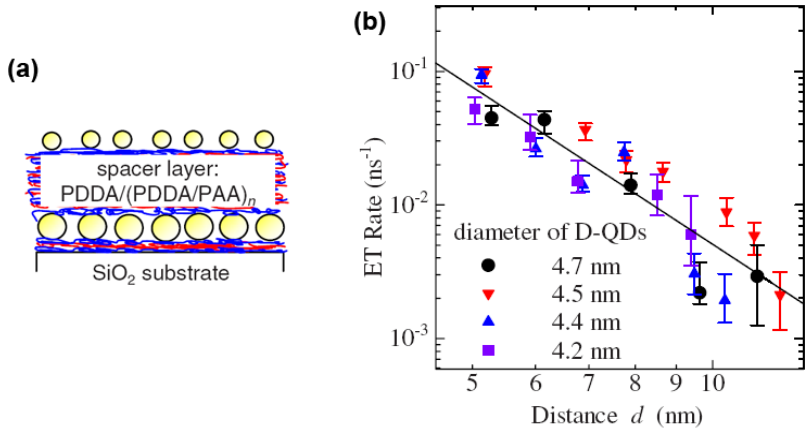

Figure 2.14: (a) Schematic diagram of the deposition process of the bilayer structure. (b) The dependence of energy transfer rate on the distance between donor(D)-QDs and acceptor(A)-QDs. (Adapted from Ref 100)

2.3.1.3 Energy transfer in solution-based complexes containing quantum dots

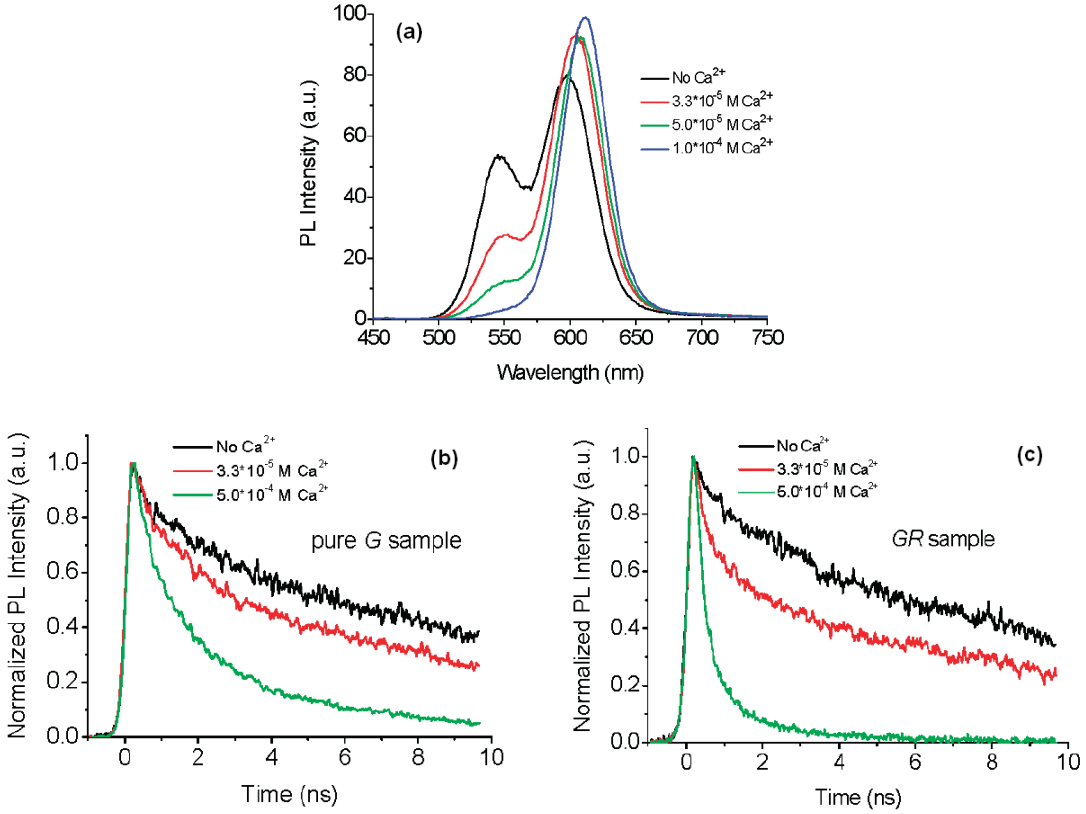

Figure 2.15: (a) PL spectra of CdTe QDs as a function of the concentration of Ca^{2+} ions in GR mixture solution, and PL decay curves of (b) pure G and (c) mixed GR samples at 550 nm at different Ca^{2+} concentrations. (Adapted from Ref 105)

The energy flow in coupled QD pairs [101] or small aggregates of QDs in solution [102, 103, 104] has been reported. Recently, an efficient energy transfer has been demonstrated in stable clusters of CdTe QDs. Ca^{2+} ions acting as electrostatic chelating linkers were used to induce clustering of water-soluble CdTe QDs through coordination to the negatively charged carboxylic acid groups of their ligands [105]. As shown in Figure 2.15 a, the effect of Ca^{2+} on the cluster containing green- (G) and red- (R) QDs (denoted as GR sample) resulted in a strong decrease of green emission of the G donor QDs, accompanied by a slight increase and a red shift of the red emission of R acceptor QDs. This is consistent with FRET from the high-energy donor QDs to the low-energy acceptor QDs. A comparison of the decay curves for green-emitting CdTe QDs in a pure G sample and in a GR mixture (Figure 2.15 b, c) shows that the PL from green QDs decays much faster in the GR samples than in the G samples. This is because there are more suitable acceptors in the GR sample than in the pure G sample. Time-resolved fluorescence measurements reveal that at least part of the energy transfer involves long-lived intermediate trap states and the recycling of this trapped excitation energy by transfer to red-emitting QDs.

2.3.2 Energy transfer from quantum dots to organic dye molecules

2.3.2.1 Energy transfer in quantum dot-dye mixtures

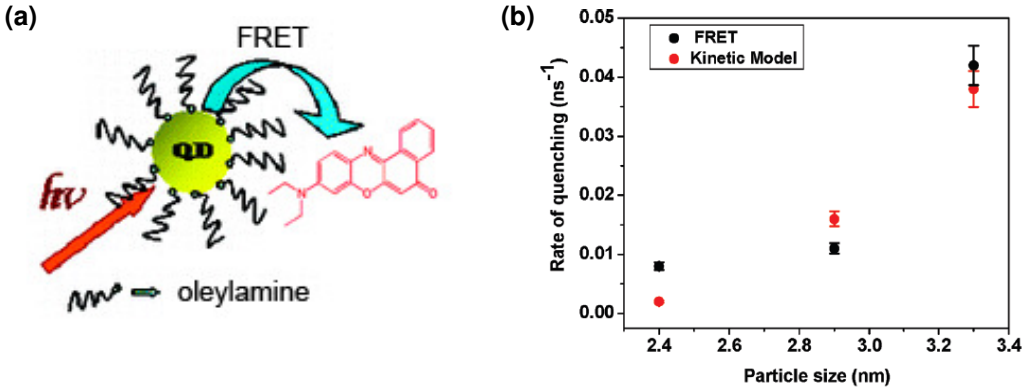

Figure 2.16: (a) Schematic representation of a QD-Nile Red dye complex. The arrow indicates the direction of resonant energy transfer (FRET). (b) Plot of the rate of quenching vs. the particle size of CdSe QDs. (Adapted from Ref 108)

Sadhu et al. [106] has reported the energy transfer in a mixture of CdS QDs and the organic dye Nile Red in n-hexane (Figure 2.16 a). Van der Waals type interactions

between CdS QDs and dye molecules contribute to the binding of the energy acceptor to the QD surface. A quenching in photoluminescence (PL) intensity of QD emission was observed in the presence of Nile Red. A stochastic model for the kinetics of energy transfer from CdSe QDs to Nile Red dye molecules was proposed [107]. The energy transfer form CdSe QDs with different sizes to Nile Red dye was investigated using FRET and kinetic model [108]. The estimated energy transfer rates from the kinetic model were nicely matched with FRET data (Figure 2.16 a).

There are also many studies on QD-dye mixtures where PL quenching of QDs was not assigned to FRET. Schmelz et al. [109] observed a complete quenching of CdSe/ZnS QD fluorescence upon attachment of diazaperylene dye molecules, which was assigned to charge transfer. A complete quenching of CdSe QD fluorescence by single dye molecules (Texas Red C5 and Lissamine Rhodamine B ethylenediamine) was also reported [110]. The competition between electron and energy transfer from CdSe QDs to adsorbed rhodamine B (RhB) molecules was examined by Boulesbaa et al [111]. The major pathway (~ 84%) for exciton quenching in this system was through electron transfer to RhB, whereas energy transfer accounted only ~ 16%. Blaudeck et al. [112] investigated the photoluminescence (PL) quenching of CdSe/ZnS QDs induced by functionalized porphyrin molecules (Figure 2.17 a). The majority of the observed strong quenching of the QD PL was assigned to neither FRET nor charge transfer, but to the extension of the wave function of the exciton outside of the QD (Figure 2.17 b). It was suggested that the attachment of dyes resulted most likely in a modification of the excitonic wave function close to the QD surface causing new and/or enhancing non-radiative deactivation channels. Their further investigations extended the non-FRET quenching mechanism to ligand dynamics that forms effective quenching sites close to or on QD surfaces [40]. In addition, other reported non-Förster type parameters for QD-dye mixture systems included QD surface effects [38] and degree of interdigitization of alkylamino chains on dye molecules into alkyl-capping layers on QDs [41].

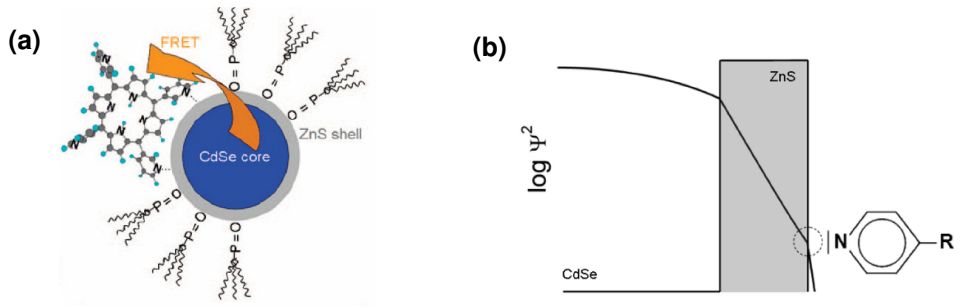

Figure 2.17: (a) Schematic representation of nanoassemblies formed by self-aggregation of pyridyl-functionalized porphyrin molecules on the CdSe/ZnS surface. The arrow indicates the direction of resonant energy transfer (FRET). (b) Scheme of the PL quenching model: Upon excitation, an electron-hole pair (exciton) is created in the CdSe core of the QD. The electron is delocalized over the core and the ZnS shell. As a result of the finite ZnS energy barrier, the electron can tunnel to the ZnS surface (and the environment). Because of the presence of a pyridyl-coordinated porphyrin molecule, the electron becomes partly localized in a volume element in the vicinity of the attachment site, described by $\Psi^2(r)$. (Adapted from Ref 112)

2.3.2.2 Energy transfer in polymer-mediated quantum dot-dye complexes

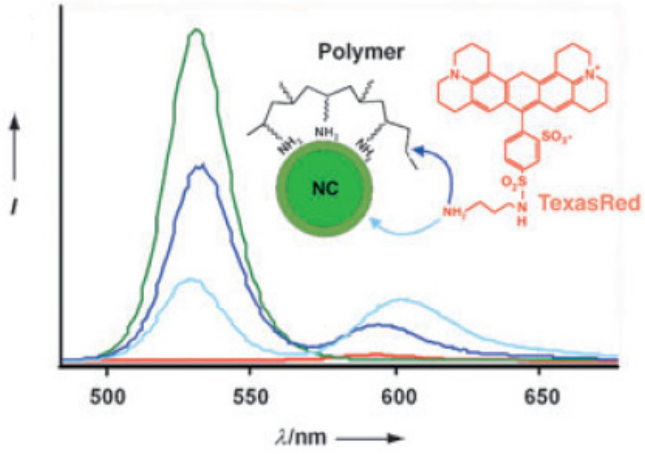

Figure 2.18: Fluorescence spectra of the QDs (green), dye (red), QD-polymer-dye (dark blue), and QD-dye (light blue), respectively, upon excitation at 488 nm. Dye fluorescence can only be observed upon energy transfer within the QD-dye and QD-polymer-dye complexes. (Adapted from Ref 18)

QD-polymer-dye complexes were found to be of higher photostability than QD-dye complexes formed in pure mixtures [18]. When mixing CdSe/ZnS QDs and Texas Red dye molecules in chloroform to form complexes through the amino group on the dye or by nonspecific binding, the measured energy transfer efficiency increased within the first minutes and then decreased over the next few hours. This decrease is most likely a

result of a time-dependent degradation of the dye, which is thought to be induced by hole-transfer process from the QDs to the dye molecules [109]. The polymer ligands were designed to have amine groups as anchors for the QD surface and functionalized groups to enable the polymer to be decorated with dye molecules. The polymer backbone in the QD-polymer-dye complexes leads to a spatial and energetic barrier to the charge transfer, and thereby the QD-polymer-dye complexes are much more stable than the QD-dye complexes against dye degradation. In the same way the polymer spacer also leads to a reduced FRET efficiency which can be seen in Figure 2.18.

Although direct linking of dye to QD surface makes the acceptor as close as possible to the donor, water-soluble QDs have only limited long-term stability in aqueous solution and tend to aggregate, as eventually the ligands and hence also the acceptor will unbind from the donor [113]. In order to provide colloidal stability to the QD donor, the dye acceptor was directly embedded in the amphiphilic polymer used to make the QD donor water soluble [24]. In this way, the linkage of the acceptor to the QD donor is very stable, the whole assembly has excellent colloidal stability, and the D-A distance is potentially reduced.

2.3.2.3 Energy transfer in biomolecule-mediated quantum dot-dye complexes

Semiconductor QDs are potentially useful fluorophores for developing biological assays [114, 115, 116]. The application of the QDs in the FRET process has been studied in several types of QD-based bioconjugates [25, 26, 36, 37, 117, 118, 119, 120, 121, 122, 123]. Willard et al. reported the first biologically relevant FRET investigation using QDs as donors [26]. Water soluble CdSe/ZnS QDs were conjugated to biotinylated bovine serum albumin (bBSA) via a thiol linkage. StreptAvidin (SAv) was covalently labeled with tetramethylrhodamine (TMR) and used as acceptor. The two subunits were allowed to react to form QD-bBSA-SAv-TMR complexes via avidin-biotin interactions. A decrease in the QD PL and an increase in the TMR PL was observed as the molar ratio of SAv-TMR to QD increased, indicating FRET between QDs and TMR on the SAv. Low FRET efficiencies were obtained in this QD-protein-dye configuration.

A classic study to understand FRET between QDs and dye molecules in bioconjugates, showing the potential of QDs in a quantitative analysis of protein binding, is based on applying maltose binding proteins (MBP-zb) onto surfaces of CdSe/ZnS QDs capped

with dihydrolipoic acid ligands [25]. By attaching a cyanine dye (Cy3) to MBP, dye labeled protein could be bound at a well-defined distance to QDs through electrostatic self-assembly. The QD-MBP-dye complex is shown schematically in Figure 2.19 a. Steady-state fluorescence measurements showed that, as the fraction of dye-labeled proteins per QD increased, the QD PL systematically decreased and a concomitant enhancement of Cy3 PL was measured (Figure 2.19 b). Similarly, time-resolved fluorescence experiments on these self-assembly QD-protein-dye bioconjugates showed a progressive decrease of the QD excited state lifetime with increasing dye to QD ratio (Figure 2.19 c). These two sets of observations confirmed that efficient nonradiative energy transfer between QD donors and dye acceptors was realized by using dye-labeled proteins self-assembled on a QD surface. Analysis of the results using Förster theory allowed the determination of the D-A separation distance, which was in agreement with the distance determined using structural characterization techniques.

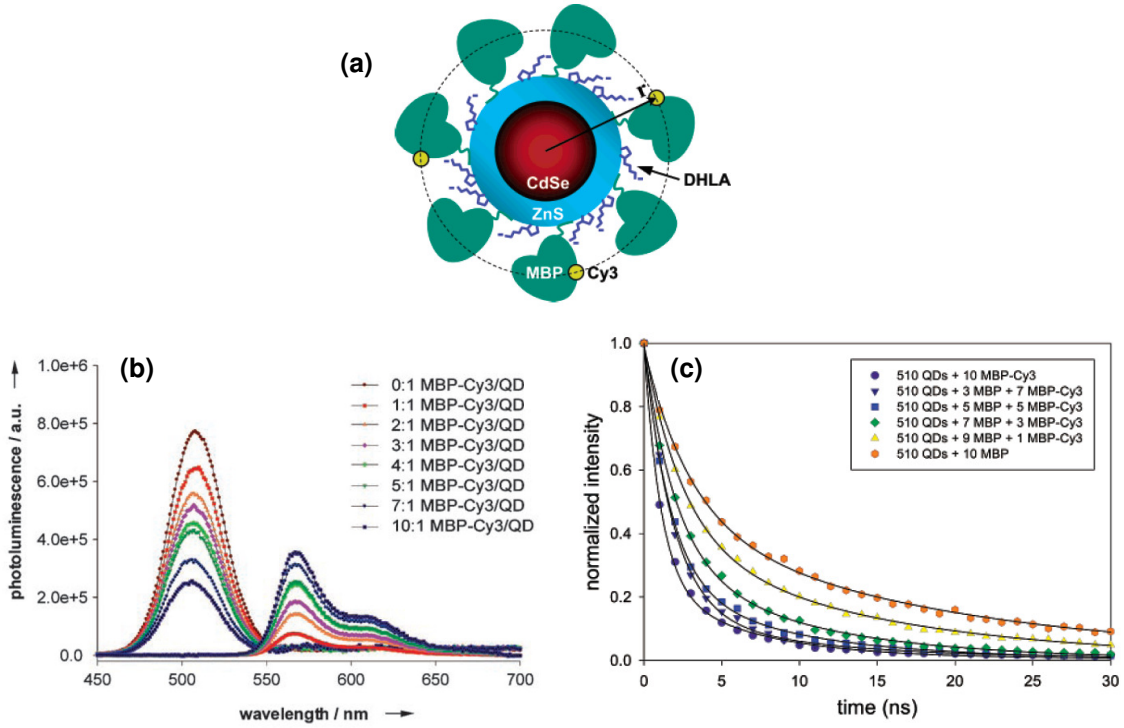

Figure 2.19: (a) Schematic representation of a QD-protein-dye complex. (b) Evolution of the PL spectra derived from titrating 510-nm emitting QDs with an increasing ratio in QD-MBP-Cy3 assemblies. Spectra have been deconvoluted and corrected for direct excitation contribution to acceptor emission. (c) Plot of the QD emission intensity at 510 nm vs. time immediately after a short pulse excitation signal. Data are shown for various QD-MBP-Cy3 conjugates where the number of Cy3-labeled proteins was increased from 0 to 10, while maintaining the total number of proteins fixed at 10 MBP/QD. (Adapted from Ref 25)

2.3.3 Energy transfer from quantum dots to metal nanoparticles

Energy transfer between semiconductor QDs and metal nanoparticles is currently attracting increased attention. Gold nanoparticles (Au-NP) have been shown to be efficient quenchers of QD emission in solution-based assemblies [102, 124, 125] and solid samples [126]. The assemblies of QDs (CdSe/ZnS QDs [102] or CdTe QDs [124]) and Au-NPs have been prepared in aqueous solution through electrostatic interactions. The QDs were significantly quenched upon binding with Au-NPs. The quenching efficiency was affected by both the concentration of Au-NPs in the complex and the length of spacer between the QD and Au-NPs which was tuned by varying the length of the ligand chains on the Au surface. In such QD-nanogold assemblies, long-range FRET is sufficiently effective to account for the observed quenching of donors, but the presence of additional mechanisms cannot be excluded.

Using a rigid variable-length polypeptide as a bifunctional biological linker, Pons et al. monitored the photoluminescence quenching of CdSe/ZnS QDs by Au-NP acceptors arrayed around the QD surface, where the center-to-center separation distance was varied over a broad range of values (~ 50 - 200 Å) [125], as schematically represented in Figure 2.20 a. The steady-state PL spectra of QD-YEHK$_7$-Au-NP conjugates showed that the QD PL was progressively quenched as the Au-NP to QD ratio increased (Figure 2.20 b). Time-resolved data also showed a significant decrease in QD excited-state lifetime upon conjugation to Au-NP-labeled YEHK$_7$. Figure 2.20 c shows a plot of the QD quenching efficiency for each of the Au-NP- YEHK$_m$ as a function of the separation distance, together with data collected for QD-dsDNA-Au-NP (from Ref 127) and QD-YEHK-Cy3 (from Ref 28). The experimental data were fit to the FRET, NSET (nanosurface energy transfer) and DMPET (dipole-to-metal-particle energy transfer) analytical treatments. The NSET treatment appears to provide a better description of the experimental quenching of QDs by proximal Au-NPs. FRET and DMPET underestimate the rate of quenching and are also unable to describe the trend observed at longer separation distances. The nonradiative quenching of the QD emission by proximal Au-NPs was found to be due to long-range dipole-metal interactions that extend significantly beyond the classical Förster range.

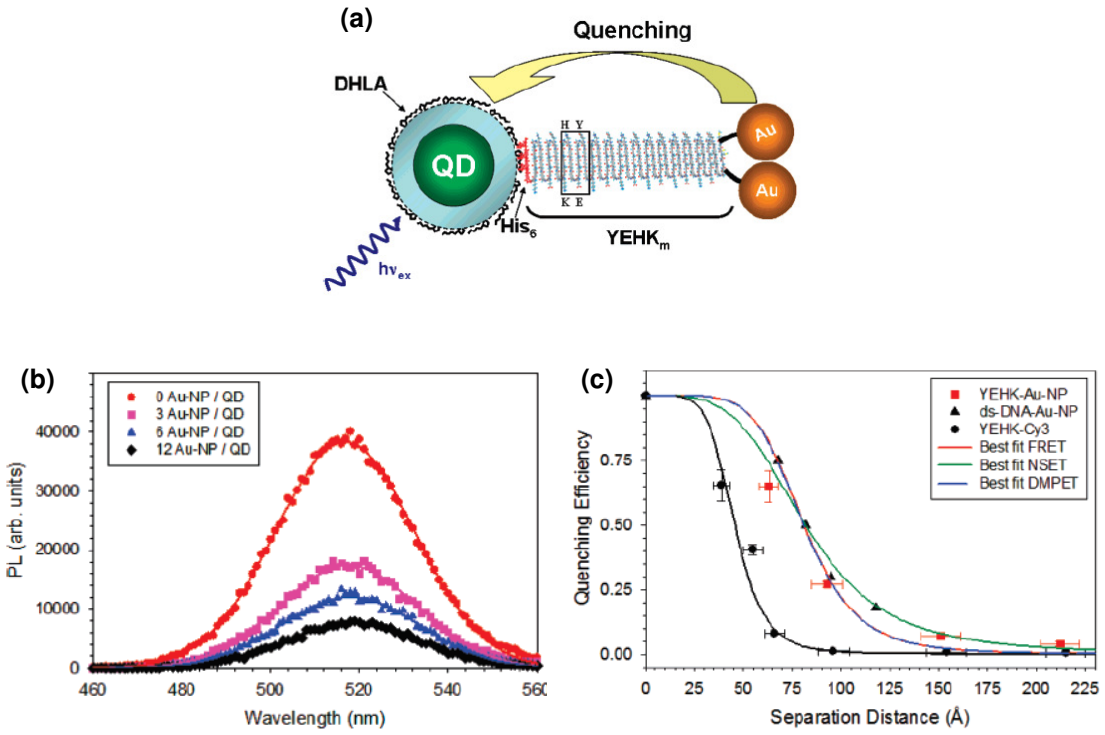

Figure 2.20: (a) Schematic representation of the QD-peptide-Au-NP bioconjugates. (b) PL spectra collected from QD-YEHK$_7$-Au-NP conjugates using 300nm excitation. (c) PL quenching efficiency vs R for QD-YEHK$_{5,7,14,21}$-Au-NP conjugates (red squares) and QD-dsDNA-Au-NP from Ref 127 (black triangles) together with best fits using FRET (red line), DMPET (blue line), and NSET (green line). The quenching efficiencies for QD-YEHK$_{1,3,5,7,14,21}$-Cy3 conjugates from Ref 28 along with a fit using Förster FRET formalism are also shown (black dots and back line). Comparison between fits and data using R_0 as a fitting parameter. Horizontal error bars are the standard deviation of the distance and vertical error bars are the standard deviation of the measurement. (Adapted from Ref 125)

In conclusion, luminescent QDs, offer several unique advantages as energy donors compared to conventional dye molecules due to their enhanced photostability and tunable surface chemistry. FRET-related studies of QDs in solution hold promise to develop efficient FRET-based sensors, while the investigations of solid state structures may allow the creation of novel light-harvesting devices. Exciting developments in this area involve controlling energy transfer on a nanometer scale where especially coupling with metal nanoparticles or dye molecules offers new avenues for detection schemes that can be used in bio-imaging and possibly other areas, such as in novel scanning probes for FRET-based near field microscopy. Light-harvesting and directional energy transfer utilizing semiconductor QDs is one particularly promising approach for the development of new concepts in hybrid photovoltaics [34].

3 Materials and methods

3.1 Materials

Chemicals (Table. 3.1) were purchased from Merck, Sigma-Aldrich, Alfa, Acros or prepared. Carboxylate-modified calix[4]arene was supplied by the workgroup of Prof. Dr. Böhmer (Abteilung für Lehramtskandidaten der Chemie der Johannes-Gutenberg-Universität Mainz). Organic dyes (Table. 3.2) were supplied by the workgroup of Prof. Dr. Klaus Müllen (Max Planck Institute for Polymer Research, Mainz, Germany) or purchased from Invitrogen (Carlsbad, CA, USA). All chemicals were used without further purification.

Table 3.1: Chemicals used in the study

Chemical	Structure	Molecular Weight	Supplier
Trioctylphosphine oxide (TOPO, 98%)	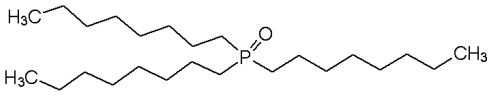	387	Merck
Trioctylphosphine (TOP, 90%)	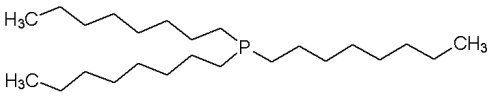	371	Sigma-Aldrich
Octadecene (ODE, 90%)	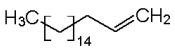	252	Sigma-Aldrich
Oleic acid (OA, 90%)	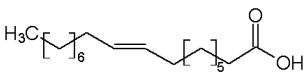	282	Sigma-Aldrich
Oleylamine (70%)	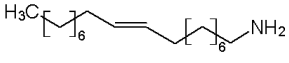	267	Sigma-Aldrich
Tetradecylphosphonic acid (TDPA)	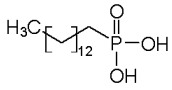	278	Lab [128]
Mercaptopropionic acid (MPA, 99%)	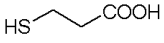	106	Sigma-Aldrich
11-mercaptoundecanoic acid (MUA, 99%)	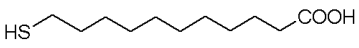	218	Sigma-Aldrich
Dihydrolipoic acid (DHLA)	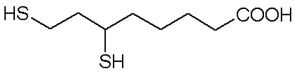	208	Lab [128]

Chemical	Structure	Molecular Weight	Supplier
Carboxylate-modified calix[4]arene	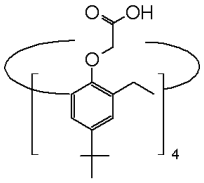	885	Prof. Dr. Böhmer
Tetraethyl orthosilicate (TEOS)	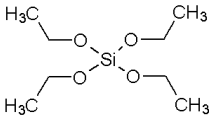	208	Acros
(3-Aminopropyl)triethoxysilane (APS, 98%)	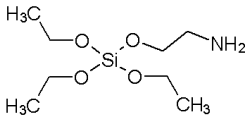	221	Sigma-Aldrich
Polyvinylpyrrolidone (PVP-10)	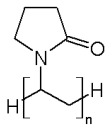	~ 10,000	Sigma-Aldrich
Triton X-100	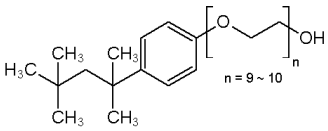	~ 625	Sigma-Aldrich
Igepal CO-520 (NP-5)	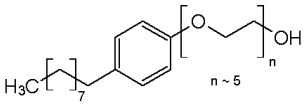	~ 441	Sigma-Aldrich
Synperonic NP-10	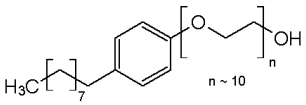	~ 660	Sigma-Aldrich
tetramethylammonium hydroxide (25 wt. % in methanol)	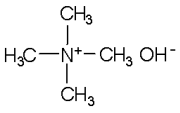	91	Sigma-Aldrich
Cadmium oxide (CdO, 99.5%)		128	Sigma-Aldrich
Zinc oxide (ZnO, 99%)		81	Sigma-Aldrich
Sulfur (S, 99.98%)		32	Sigma-Aldrich
Selenium (Se, 99.5%)		79	Alfa

Table 3.2: Organic dyes used in the study

Fluorophore	Structure	Molecular Weight	Supplier
PDI	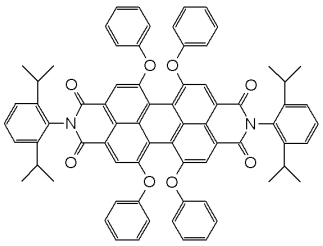	1079	AK Müllen
PMIMA	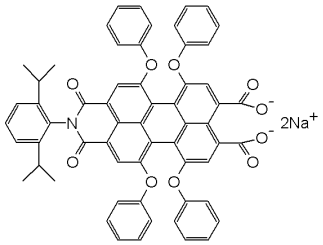	982	AK Müllen
PDIDC	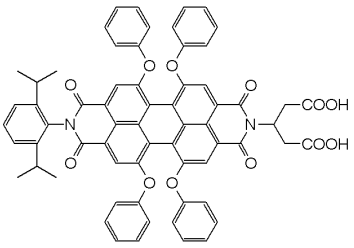	1049	AK Müllen
TDIDC	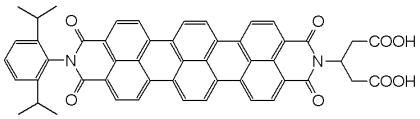	805	AK Müllen
TA-PDI	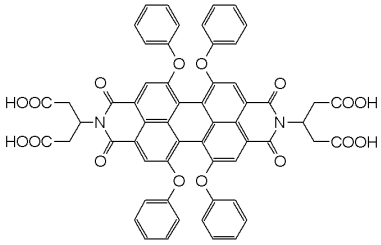	1019	AK Müllen

Fluorophore	Structure	Molecular Weight	Supplier
TDA	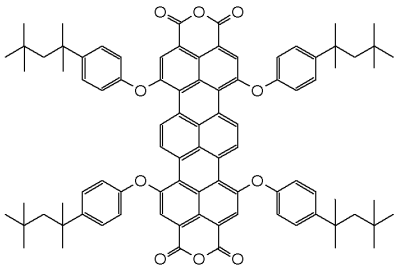	1334	AK Müllen
PMI	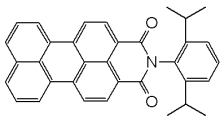	482	AK Müllen
Texas Red-X, STP ester, sodium salt	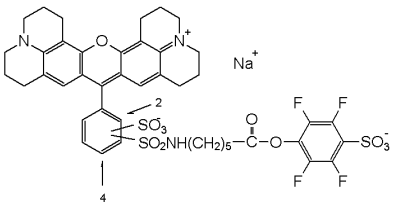	970	Invitrogen

3.2 Synthesis methods

3.2.1 CdSe/CdS/ZnS core-shell quantum dots

Luminescent CdSe/CdS/ZnS core-shell QDs were synthesized based on the methods developed by Peng et al. [82, 129] and our previous work [78]. All reaction steps of the synthesis were performed under an argon inert gas atmosphere Schlenk line (Figure 3.1). Experiments under vacuum were done at about 1-4 mbar. The temperature was adjusted at a heating rate of 10 - 15 °C / min in the temperature interval 20 ~ 800 °C under a continuous argon flow of 20 - 30 ml / min.

Figure 3.1: Experimental set up for QD synthesis: 1. schlenk glass ware; 2. to vacuum pump; 3. pressure indicator; 4. heating mantle; 5. magnetic stirrer; 6. thermocouple; 7. condenser; 8. to argon gas cylinder.

CdSe core To synthesize CdSe QDs, the standard hot injection approach was used. For a typical reaction, a mixture of 0.0514 g of CdO powder, 0.2232 g of tetradecylphosphonic acid (TDPA) and 3.7768 g of trioctylphosphine oxide (TOPO) in a 50 mL three-neck flask was evacuated at 100 ºC for 10 min and heated to 320 ºC under Ar flow. At about 300 ºC, reddish CdO powder was dissolved and generated an approximately colorless homogeneous solution. The temperature was then lowered to 290 ºC, and a 2.5 ml Se solution (0.158 g Se powder dissolved in 10 ml TOP) was injected into the reaction flask. QDs grew at 250 ºC for 1 - 5 min to reach the desired size. Then, the reaction solution was cooled to room temperature. Methanol was added

to precipitate the QDs. After centrifugation and decantation, the particles were dispersed in, typically, 4 ml of chloroform or toluene for further processing.

Concentration determination of CdSe core Typically, 50 μl of the prepared CdSe solution was added to 3 ml of toluene. Absorption and fluorescence spectra of this solution were then recorded. According to the procedures described by Yu et al. [63], the diameter of the CdSe particles and the extinction coefficient per mole of particles (ε, l/mol·cm) can be obtained from the wavelength of the first exciton absorption peak (according to Figure 2 and Figure 4 in Ref 63). The CdSe molar concentration (C, mol/L) was then calculated using Lanbert-Beer's law:

$$A = \varepsilon \cdot C \cdot L \tag{3.1}$$

where L is the path length of the radiation beam used for recording the absorption spectrum (L = 1 cm) and A is the absorbance at the peak position of the first exciton absorption peak. It should be noted that other methods for determining the CdSe concentration has also been reported [109, 130, 131, 132]. However, the CdSe concentrations determined using different methods show a large discrepancy [132]. There is still no common method to accurately determine the CdSe concentration. So far, Yu's method is widely adapted.

Precursor solutions for shell growth The zinc precursor solution (0.1 M) was prepared by dissolving 0.2034 g ZnO in 10 ml oleic acid (OA) and 15 ml octadecene (ODE) at 310 ºC. The cadmium precursor solution (0.1 M) was prepared by dissolving 0.3204 g CdO in 10 ml oleic acid and 15 ml ODE at 240 ºC. The sulfur precursor solution (0.1 M) was prepared by dissolving 0.08 g sulfur in 25 ml ODE. All these solutions were prepared under Ar atmosphere.

Calculation of the amount of precursor solutions The amount of the injection solution for each monolayer (ML) can be deduced from a calculation of the number of surface atoms. The average thicknesses of one CdS-ML (0.35 nm) and one ZnS-ML (0.31 nm) are estimated on the basis of the wurzite structure of the respective compounds [82, 78]. To calculate the amount of Cd-precursor for the growth of the first monolayer, it is assumed that the surface of the CdSe cores consists equally of Se- and Cd-atoms and therefore used only 50% of the amount of calculated Cd-precursor for a complete ML [78]. The amounts of the following Zn or Cd and S precursors are

calculated from the respective volumes of concentric spherical shells with a thickness of one hypothetical monolayer.

Shell growth on CdSe core Core-shell QDs were synthesized using the successive ion layer adsorption and reaction method (SILAR) [82, 78]. This technique allows for growing very complex shells around a given CdSe core with precise thickness control. A typical SILAR synthesis was performed as follows: 3 mL of ODE, 0.5 ml of oleylamine and 1 ml CdSe QDs in toluene (8.5×10^{-5} mol/L) were loaded into a 50 mL three-neck flask, pumped to remove the toluene and heated to 100 ºC under vacuum for 10 min. Subsequently, the solution was heated to 240 ºC under Ar flow. Then the calculated amount of the Cd or Zn precursor solution and the S precursor solution were injected into the reaction flask, respectively, with a reaction period of 10 min between each addition. After the reaction was completed, the solution was cooled to room temperature. Acetone was added to precipitate the products. After centrifugation and decantation, the particles were dispersed in chloroform or toluene. The emission wavelength and size of the core-shell QDs can be adjusted by CdSe core size, the composition and the number of shell monolayers. Core-shell QD concentration was determined based on the concentration of the CdSe cores. Assuming no loss during shell growth and further purification, the particle number concentration will not change.

3.2.2 Quantum dot hybrid systems

In this thesis, the prepared quantum dot hybrid systems include quantum dot - silica hybrids, quantum dot - silica - dye hybrids and quantum dot - dye hybrids. The structures and preparation of these QD hybrids are briefly described in this section. The detailed experimental procedures and results will be discussed in the following chapters.

3.2.2.1 Quantum dot - silica hybrids

Two kinds of QD-silica hybrids were designed: a QD-silica architecture and a silica-QD-silica architecture. The typical synthesis procedures will be described in chapter 4.

Silica-QD-silica architecture To assemble the silica-QD-silica architecture, “pure” silica cores were prepared first. For synthesizing large “pure” silica cores, the Stöber method [136] was used: hydrolysis of TEOS in ethanol containing water and an appropriate amount of ammonia. Small “pure” silica cores were prepared using the

reverse microemulsion method. Hydrophobic CdSe/CdS/ZnS QDs were coated with the amphiphilic polymer polyvinylpyrrolidone (PVP), which makes QDs soluble in ethanol and facilitates the growth of further silica layers in the next reaction step. The silica cores were functionalized with (3-aminopropyl)triethoxysilane (APS), which permits the attachment of the PVP-coated QDs onto silica. By simply mixing, the PVP-coated QDs were then adsorbed on the APS-functionalized silica "core" particles. Finally, these QD-decorated silica particles are directly coated with a silica layer of variable thickness by the addition of TEOS to an ammonia/ethanol solution. An outline of the synthesis is shown in Figure 3.2.

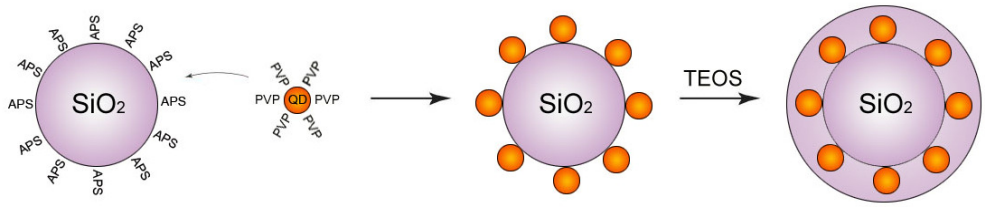

Figure 3.2: General procedure for embedding nanoparticles in silica colloids.

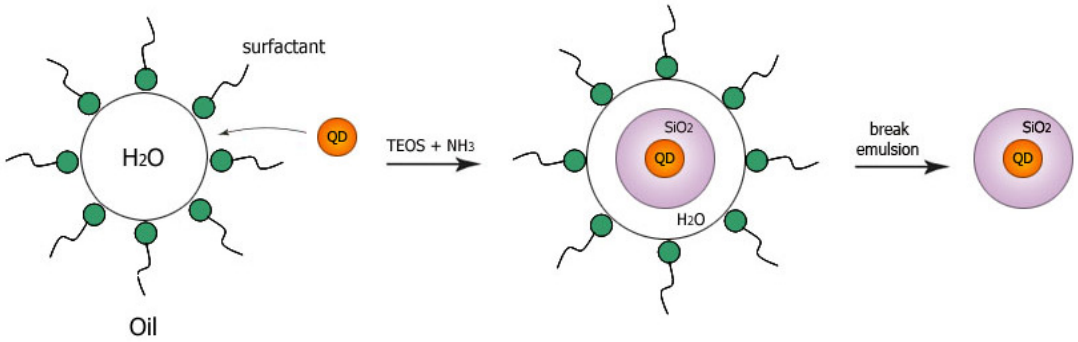

Figure 3.3: Incorporation of a single QD in a silica sphere by the reverse microemulsion method.

QD-silica architecture Homogeneous silica coated CdSe/CdS/ZnS QDs were prepared by the hydrolysis of tetraethyl orthosilicate (TEOS) in water-in-oil (W/O) reverse microemulsion. The microemulsion solution was prepared by mixing adequate amount of surfactant, cosurfactant, organic solvent, water and aqueous ammonia. Aqueous ammonia acts as both a reactant (H_2O) and a catalyst (NH_3) for the hydrolysis of TEOS. Igepal CO-520 or Synperonic NP-10 was used as the surfactant in the ternary microemulsion system, and Triton X-100 was the surfactant in the quaternary microemulsion. QDs and TEOS were added to the microemulsion solution. Hydrolyzed TEOS molecules (and initially also surfactant molecules) replace the hydrophobic

ligands of QDs, resulting in the transfer of QDs into water droplets of the micelles where silica growth takes place. Figure 3.3 illustrates the synthesis process.

3.2.2.2 Quantum dot - silica - dye hybrids

The assembly of QD-silica-dye hybrids was performed using the modified silica-QD-silica hybrid synthesis procedure. The detailed synthesis procedure will be described in chapter 5. Figure 3.4 illustrates the synthesis route from "pure" silica core to QD-silica-dye hybrids.

Figure 3.4: Synthesis route of QD-silica-dye hybrid.

"Pure" silica cores were first prepared using the Stöber method. Texas Red-X STP ester (structure see Table 3.2) was used as the dye in this system. The Texas Red dye was covalently linked to APS and then the APS-dye conjugates were incorporated into a silica shell while further shell growth on silica cores, resulting in the formation of a homogeneous dye layer on the silica core. These silica-dye particles were functionalized with APS and subsequently mixed with PVP-coated CdSe/CdS/ZnS QDs to obtain QD-silica-dye hybrids.

3.2.2.3 Quantum dot - dye hybrids

Extraordinarily stable QD-dye hybrids were prepared by using dicarboxylate anchors to bind ryleneimide dyes to QD. The typical synthesis procedures will be described in chapter 6.

QD-dye hybrids in non-aqueous solution Complexes between QDs and dyes (PMIMA, PDIDC or TDIDC) were formed by sonicating a mixture of dye (in methanol) and QD (in chloroform) after addition of a weak base K_2CO_3. Next, the QD-dye complexes were precipitated, washed and redispersed in chloroform yielding clear solutions. Figure 3.5 shows the dye structures and the binding of the PDIDC-dye onto hydrophobic QDs in organic solution as an example.

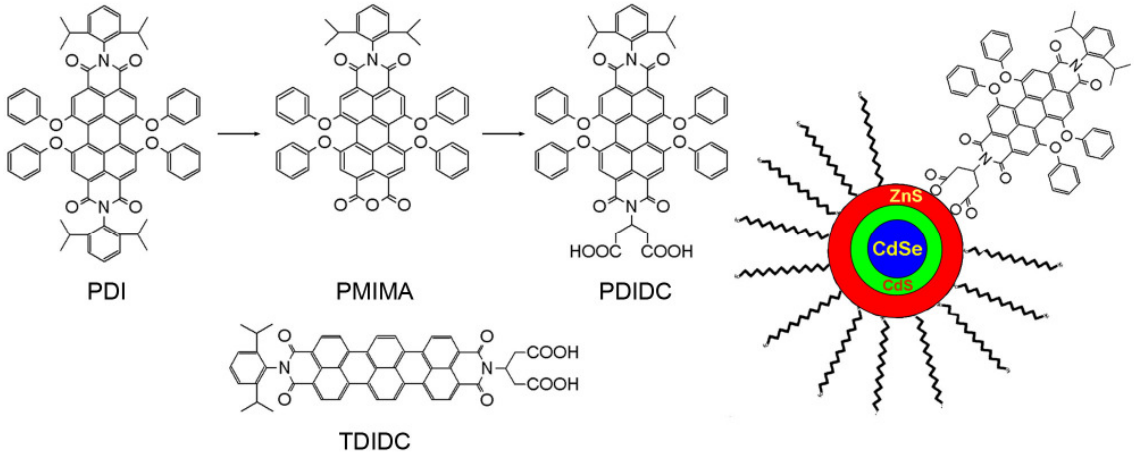

Figure 3.5: Ryleneimide dyes and QD-dye binding model.

QD-dye hybrids in aqueous solution The QD-dye complexes were transferred from the organic phase into the aqueous phase by exchange of the original ligands (oleic acid, oleylamine) by mercapto-propionic acid (MPA) or dihydrolipoic acid (DHLA) under basic condition (Figure 3.6). Two methods were used: phase transfer method and refluxing method. In the phase transfer method, a mixture of QD-dye complexes dispersed in chloroform and distilled water containing MPA or DHLA was vigorously stirred under basic condition. After six hour stirring, the QD-dye complexes were transferred from the organic phase to the aqueous phase. The aqueous solution was then centrifuged and the precipitate was redispersed in water. In the refluxing method, QD-dye complexes and MPA, 11-mercaptoundecanoic acid (MUA) or DHLA in organic solvent were refluxed under stirring in an Ar atmosphere. The products were then precipitated and, after centrifugation, redispersed in water.

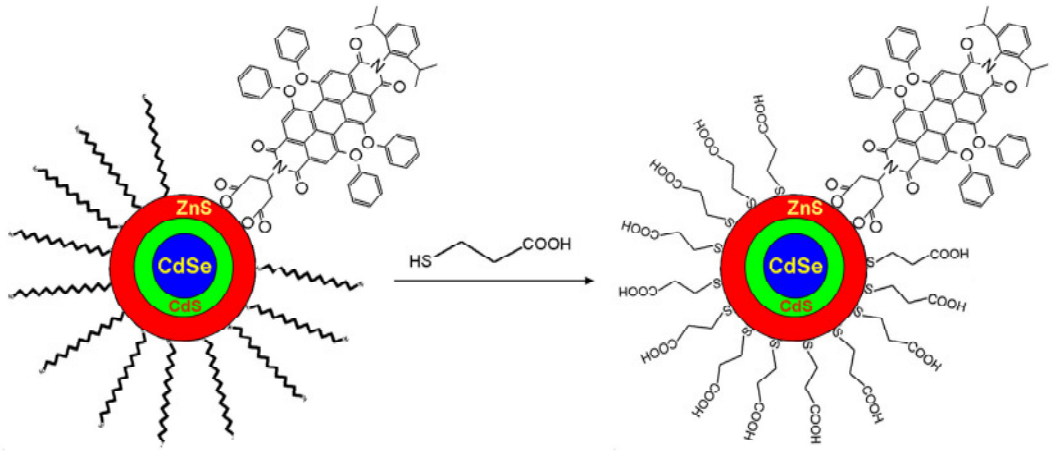

Figure 3.6: Transfer process of QD-dye hybrid. Exchange ligand is MPA.

3.3 Characterization techniques

3.3.1 Absorption spectroscopy

UV visible absorption spectra were taken with the spectrometer OMEGA 20 from Bruins Instruments. Cuvettes with two or four quartz windows and a thickness of 1 cm were used. Spectra of the solutions were taken against the respective pure solvent reference. The OMEGA software package allowed the calculation of absorption coefficients of the dissolved compounds. The absorption spectra were recorded in a wavelength range from 360 nm to 1100 nm with an increment of 0.5 nm and a slit width of 0.5 mm. The recorded spectra were usually shown as optical density versus wavelength and were transferred into ASCII files and further processed with the ORIGIN software package.

3.3.2 Steady-state fluorescence spectroscopy

Steady-state photoluminescence spectra were measured with a FluoroMax-2 spectrofluorometer from ISA JOBIN YVON-SPEX Instruments S. A., Inc. 1 cm thick cuvettes with four quartz windows were used as sample cells. To ensure a linear relationship between fluorescence intensities and fluorophore concentrations, the samples were always kept dilute to record spectra within the linear range of the detector. Fluorescence spectra were corrected for the wavelength dependence of the fluorometer (Sc/R). The spectra were usually displayed as fluorescence intensity vs. wavelength and were transferred into ASCII files and further processed with the ORIGIN software.

The fluorescence quantum yield was determined as follows: The absorption spectra of the sample and the reference dye were recorded. An intersection of the two absorption spectra, where the optical density of the sample is equivalent to that of the reference, was chosen as the excitation wavelength for fluorescence measurement. The optical density at the intersection was kept below 0.05 to avoid inner filter effects. The fluorescence spectra of the sample and the reference dye were recorded, and quantum yield of the sample was calculated according to [5]

$$\Phi = \Phi_R \frac{I}{I_R} \frac{OD_R}{OD} \frac{n^2}{n_R^2} \tag{3.2}$$

where Φ is the quantum yield, *I* is the integrated fluorescence intensity, *OD* is the optical density, and *n* is the refractive index of the solvent. The subscript *R* refers to the reference dye of known quantum yield. The reference dye used to calculate the quantum yield of QDs was N-(2,6-diisopropylphenyl)perylene-3,4-dicarboximide (PMI). The PMI structure is shown in Table 3.2. Figure 3.7 shows the absorption and fluorescence spectra of the reference PMI. The quantum yield of the PMI in toluene is 70%. Since the sample and standard dye was excited at the same wavelength, it was not necessary to correct for the different excitation intensities of different wavelengths.

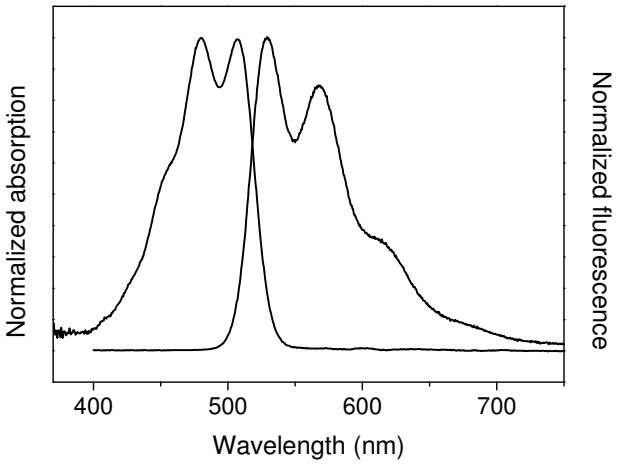

Figure 3.7: Normalized absorption and fluorescence spectra of PMI in toluene.

3.3.3 Transmission electron microscopy

Low-resolution images were taken on a Philips EM-420 transmission electron microscope (TEM) with an acceleration voltage of 120 kV. Samples for TEM were prepared by depositing a drop of the sample solution onto a copper grid supporting a 5 nm thin film of amorphous carbon. The excess liquid was removed with filter paper, and the grid was dried in air. Randomly oriented QDs on the TEM substrate were obtained by using diluted sample solutions with an absorbance at the first absorption peak of the QDs below about 0.05. If the absorbance was above 0.2, densely packed QDs were observed.

The size of the QDs was determined by measuring more than 1,000 particles in each QD sample from their TEM images using the software ImageJ, from which the area of

each particle can be obtained. Assuming that all the particles were spherical, the diameter of the QDs was calculated.

3.3.4 Fluorescence lifetime spectroscopy

Time-resolved fluorescence measurements were performed on a FluoroLog-3 spectrofluorometer connected to PicoHarp 300 (PicoQuant, Berlin) Time Correlated Single Photon Counting (TCSPC) unit. The photon arrival times with respect to the excitation by a pulsed light source to construct the fluorescence decay histograms were measured with 4 ps time resolution within a range of 0 ~ 1000 ns. In order to measure fast decays due to energy transfer a pulsed laser diode LDH-P-C-470 (PicoQuant, Berlin) with pulse duration of $\tau_p \approx 70$ ps was used for excitation ($\lambda_{ex} = 470$ nm, $\nu_{rep} = 10$ MHz or 1 MHz), and a fast single photon avalanche diode (SPAD, Micro-Photon-Devices) was coupled to the exit slit of the emission monochromator. The overall time resolution of the setup was quantified by the FWHM (Full Width at Half Maximum) of the Instrument Response Function (IRF) to ≈ 180 ps at $\lambda_{em} = 470$ nm. The experiments were done by Mathias Haase.

The measured time-resolved fluorescence decay $I(t)$ of the sample is the convolution of the decay model function $M(t)$ and the instrument response function $IRF(t)$. The instrument response function $IRF(t)$ is a convolution of the impulse function $L(t)$ and the instrumental function of the detection system $D(t)$. This is expressed symbolically as [133]

$$I(t) = M(t) \otimes IRF(t) = M(t) \otimes L(t) \otimes D(t) \tag{3.3}$$

where the symbol ⊗ represents numerical convolution. Analysis was performed by convoluting the IRF with the model function and then comparing the result with the measured decay. This was done by a iterative least squares procedure until the best agreement with the measured decay curve was achieved.

3.3.5 Dynamic light scattering

Hydrodynamic radii (R_h) of the nanoparticles was determined by dynamic light scattering (DLS) using an experimental setup consisting of a He-Ne laser (JDS

Uniphase 1145p-3083, 632.8 nm, 25 mW output power), a goniometer SP-86(ALV), and an ALV-3000 digital correlator/structurator. The particle size polydispersity was estimated from exponential decay fits of the time-intensity-correlation functions (in case of water-soluble particles), and from the 2nd cumulant in case of the much smaller (on average) hydrophobic precursor nanoparticles. All light scattering measurements were carried out with filtered samples (Millipore LG filters of pore size 0.2 μm). The experiments were done by PD Dr. Wolfgang Schärtl.

Information about the light scattering spectrum can be obtained from the autocorrelation function $G(\tau)$ of the light scattering intensity. The exponentially decaying autocorrelation function $G(\tau)$ is related to the diffusion coefficient D_s [134]:

$$G(\tau) = A \cdot exp\,(-2D_s q^2 \tau) + B \tag{3.4}$$

where

$$q = \frac{4\pi n}{\lambda}\sin(\frac{\theta}{2})$$

n is the refractive index of the medium, λ is the laser wavelength, and θ is the scattering angle. By fitting the autocorrelation function $G(\tau)$ according to equation 3.4, the diffusion coefficient D_s can be determined and related to the hydrodynamic radius R_H using the Stokes-Einstein equation:

$$D_s = \frac{k_B T}{6\pi\eta R_H} \tag{3.5}$$

where k_B is the Boltzmann constant, T is the absolute temperature, η is the shear viscosity of the solvent, and R_H is the hydrodynamic radius.

4 Quantum dot - silica hybrid system

4.1 Introduction

Silica (SiO_2) is an attractive material for embedding nanoparticles. A silica surface coating allows surface modification for the interaction potential and makes it possible to disperse colloids in a wide range of solvents from very polar to apolar. The chemical and physical protection provided by the silica shell improves the stability and prevents photooxidation in the case of QDs [135]. Furthermore, the silica chemistry permits an accurate control of the thickness of silica shells grown around a semiconductor core.

The incorporation of QDs in silica spheres has been accomplished using two different methods. The first method is the "Stöber" method [136], a base-catalyzed hydrolysis of tetraethyl orthosilicate (TEOS, $Si(OC_2H_5)_4$) with subsequent condensation of the hydrolyzed silica species, i.e.,

hydrolysis $\quad Si(OC_2H_5)_4 + 4H_2O \rightleftharpoons Si(OH)_4 + 4C_2H_5OH$

condensation $\quad Si(OH)_4 \rightleftharpoons SiO_2 + 2H_2O$

overall reaction $\quad Si(OC_2H_5)_4 + 2H_2O \rightleftharpoons SiO_2 + 4C_2H_5OH$

In the adapted Stöber growth, QDs act as seeds for silica growth in an ethanol/ammonia mixture, yielding smooth surfaces since the growth takes place on a molecular scale [137, 138, 139]. There are many surfaces that can be directly coated with silica because of the high chemical affinity of these materials, like hematite [140], zirconia, and titania [141]. However, many other surfaces can only be coated or modified with stabilizers, surfactants and silane coupling agents. Liz-Marzán and co-workers have extensively studied metal-silica core-shell particles prepared by a liquid-phase procedure in which the use of a surface primer (a silane coupling agent) was necessary to provide the surface with silanol anchor groups [142, 143]. To incorporate semiconductor QDs into silica, 3-mercaptopropyl-trimethoxysilane (MPS) was frequently used as the coupling agent [144, 145, 146]. Graf et al. developed a novel method for the embedding of semiconductor, noble metal and metal oxide nanoparticles in silica colloids, using the amphiphilic polymer poly(vinylpyrrolidone) (PVP) as the coupling agent [30, 147]. The major disadvantages of this method are the high requirements on purity of the reactants,

the difficulty and multiplicity of the preparation steps, and the fact that nanoparticles with nonpolar ligands cannot be coated easily.

The second method to incorporate QDs into silica is the water-in-oil (W/O) reverse microemulsion method, where small water droplets are stabilized by a nonionic surfactant in a hydrophobic continuous phase [148]. Hydrolysis and condensation of the silica precursor (e.g., TEOS) take place at the W/O interface or in the water phase. The confined ‘‘nanoreactor’’ environment within the reverse micelle has been shown to yield highly monodisperse particles even at small sizes (> 25 nm), and to increase the incorporation of non-polar molecules, which are often difficult to incorporate into the hydrophilic silica matrix. Metallic [149,150], magnetic [151, 152] and semiconductor [153, 154] nanocrystals have been successfully coated with silica using the reverse microemulsion method. In comparison with the “Stöber” approach, this method is very robust against slight changes in the reaction parameters and the purity of reactants, and it does not need any surface modification and pretreatment. Furthermore, the control over particle size and size dispersion is better [154], and no purification steps are required before the growth of the silica shell.

In this work, both “Stöber” and reverse microemulsion methods were used to incorporate the CdSe/CdS/ZnS QDs into silica. The purpose of preparing such QD-silica hybrid system was to assemble QD-silica-dye hybrids by attaching dyes on the silica shell, and then study the energy transfer between QDs and dye molecules mediated by the silica shell. The Stöber-based method usually yields multiple QDs per silica sphere due to the relatively large silica particle size (usually more than 100 nm with good monodispersity) compared to the small QD size. In this case, QDs will be randomly located in the silica sphere which does not favor the subsequent energy transfer study because the QD-dye distance will not be defined. Therefore, the QDs were attached around a silica “core” particle and then a silica shell was further grown on this QD-decorated silica particle. Alternatively, using the water-in-oil microemulsion, it is easy to achieve a relatively small silica particle size (below 100 nm) and obtain silica particles with only one QD inside. The focus was how to improve the particle monodispersity and control the thickness of the silica shell in the range where FRET between QD and dye can take place after attaching dye molecules on the silica shell.

4.2 Silica - quantum dot - silica architecture

4.2.1 Experimental procedure

A. Silica core: Large "pure" silica core particles with diameter more than 100 nm were prepared by hydrolysis of tetraethyl orthosilicate (TEOS) using the well-known Stöber method: 4.5 mL TEOS, 28.5 mL H_2O and an appropriate amount of 25 wt% aqueous ammonia solution were added to 65.5 mL ethanol. The size of the silica core was controlled simply by changing the amount of the ammonia solution. Silica cores with a diameter of ~ 250 nm were obtained when 2 mL of ammonia solution was added, and the addition of 1.5 mL ammonia solution resulted in silica cores of ~ 140 nm diameter. The reaction was allowed to continue for 6 h at room temperature at moderate stirring. For purification, the particles were centrifuged, washed and redispersed in ethanol. Small silica cores with diameters of 25 - 30 nm were prepared by the microemulsion method: 0.44 g Igepal CO-520, 10 mL cyclohexane, 90 μL H_2O and 60 μL aqueous ammonia solution were mixed to form a microemulsion solution. 100 μL TEOS was then added. After the mixture was stirred for 24 h, ethanol was added to break the emulsion. The particles were centrifuged, washed and redispersed in ethanol.

B. APS-functionalized silica: The surface of these silica cores was then functionalized with (3-aminopropyl)triethoxysilane (APS) following the procedure by Graf et al. [147]: Typically, 10 μL APS were added to 1 mL silica core solution (c = 13.4 g/L), dispersed in 47 mL ethanol plus 3 mL ammonia solution (25 wt %), and this mixture was stirred for 12 h. The resulting APS-functionalized silica nanoparticles after centrifugation were washed twice with ethanol to remove the unreacted reactants and then redispersed in ethanol.

C. PVP-coated QDs: CdSe/CdS/ZnS QDs were prepared as described in Chapter 3.2.1. The core-shell QDs were coated with polyvinylpyrrolidone (PVP) polymer chains prior to mixing with the APS-functionalized silica nanoparticles. For this purpose, a PVP (M = 10,000 g/mol) stock solution was prepared by dissolving 27.1 g PVP in 1 L butanol and sonicated for 30 min before use. 7 mL of this PVP solution was then mixed with 1 mL of a QD chloroform dispersion (concentration: ~ 1×10^{-5} mol/L), and this mixture

was stirred for 24 h at room temperature. The dispersion of the PVP-coated QD was not further purified.

D. Silica-QD-silica spheres: 7.5 mL of this freshly prepared PVP-coated QD dispersion were added under stirring to 10 mL of the dispersion of APS-functionalized silica particles in ethanol. The mixture was then stirred for 24 h at room temperature. The resulting particles were centrifuged, and the supernatant was removed. To grow an additional silica shell, the resulting QD-decorated silica particles were redispersed in 47 mL of ethanol containing 3 mL of ammonia solution (25 wt %). Immediately after this, a mixture of TEOS and 3-(trihydroxysilyl)-propylmethylphosphonate (THPMP) was added under stirring in two steps over 4 h. The thickness of the shell was controlled by the added amount of TEOS. The reaction mixture was then stirred for another 12 h. The final products were centrifuged, washed and redispersed in ethanol.

4.2.2 Results and discussion

4.2.2.1 TEM characterization

A. CdSe/CdS/ZnS QDs

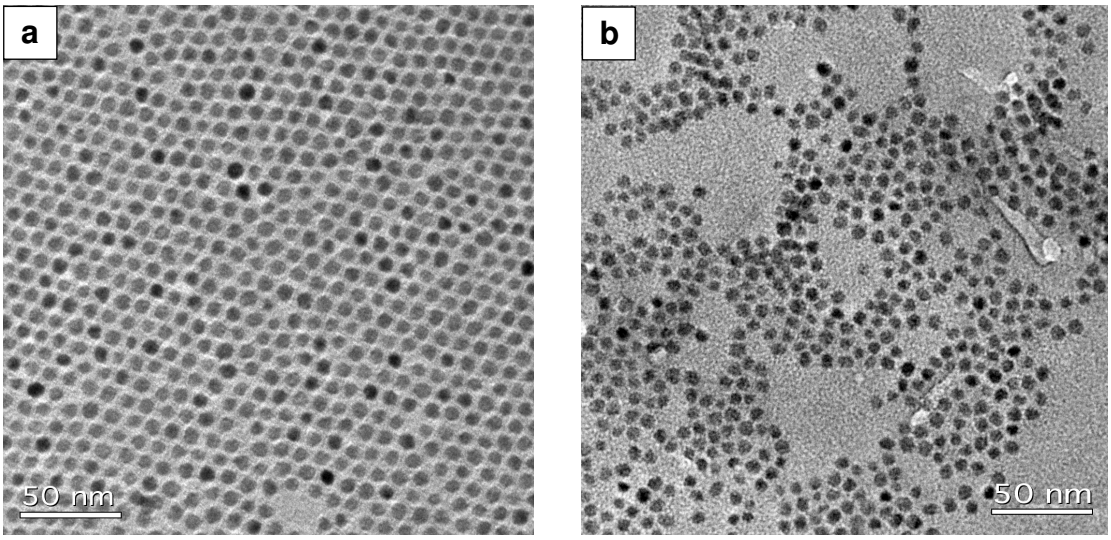

Figure 4.1: TEM images of CdSe/CdS/ZnS QDs (a) before and (b) after PVP coating.

The core-shell QDs used here possess CdSe cores covered with four monolayers of CdS and one monolayer of ZnS. The QDs have a diameter of 6 ~ 7 nm (Figure 4.1 a) and are stabilized by organic ligands that render them hydrophobic. Since silica particles are usually dispersed in polar solvent, QDs have to be functionalized in order to enable their

attachment to a silica surface in an appropriate solvent. The amphiphilic polymer PVP was used for the hydrophilic surface functionalization of QDs. The advantages of using PVP are that it can be simply adsorbed on various colloidal particles due to its amphiphilic character; moreover, a silica shell can be directly grown on PVP-stabilized particles [30]. The solution of the QDs after PVP coating was still clear and no large aggregates were formed. Figure 4.1 b shows the PVP-coated QDs. It has been proven that PVP does not exchange the original organic ligands on the QD surface but is reversibly adsorbed on the QDs [147].

B. Silica cores

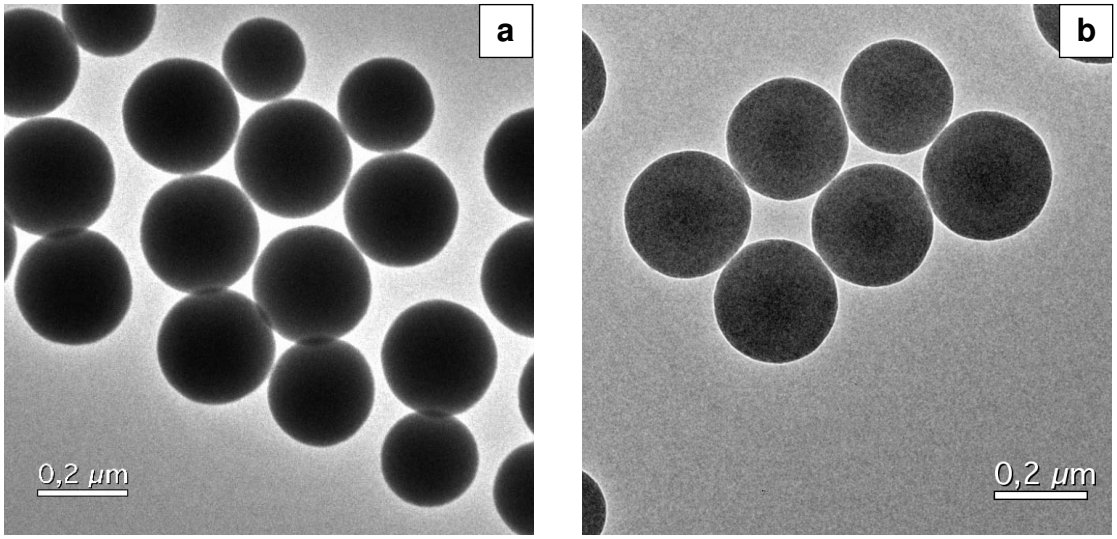

Figure 4.2: TEM images of (a) silica core particles and (b) APS-functionalized silica particles.

As shown in the TEM image (Figure 4.2 a), the silica core particles are monodisperse and have an average diameter of ~ 250 nm. After functionalized with APS, the silica particles are still monodisperse and the APS-functionalized silica particles do not show a change in size (Figure 4.2 b). The functionalization with APS allows the attachment of PVP-coated QDs onto silica cores.

C. Silica-QD-silica hybrid nanoparticles

After mixing APS-functionalized silica particles and PVP-coated QDs, the QDs are evenly distributed on the silica surface to form a QD monolayer (Figure 4.3). Importantly, PVP does not react with the amino groups on APS molecules, but the PVP-functionalized particles are simply adsorbed on the amino-functionalized colloids [147].

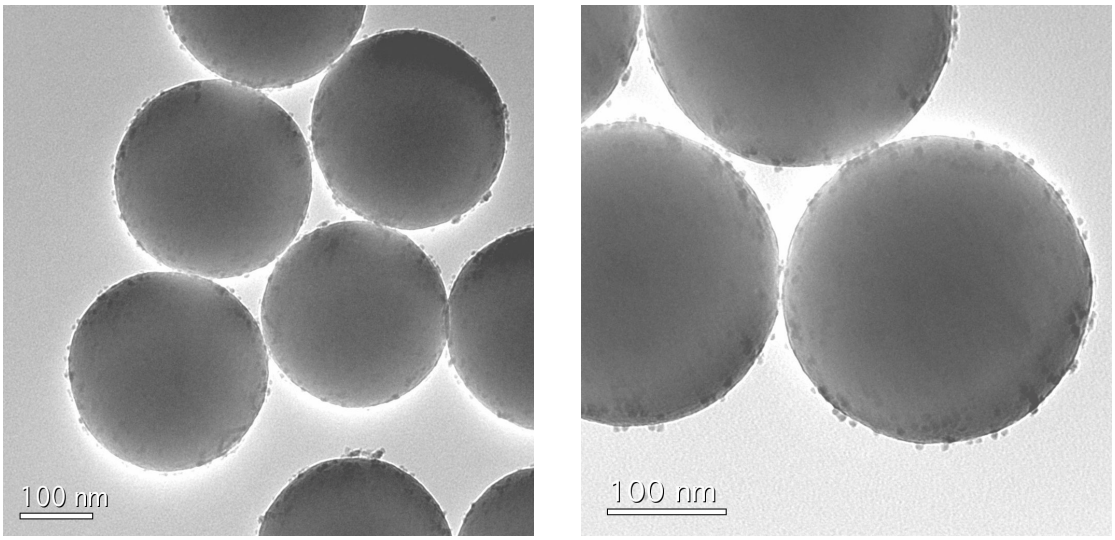

Figure 4.3: TEM images of QD-decorated silica particles.

Further silica shell growth was carried out by a Stöber-like reaction by subsequently introducing a mixture of TEOS and THPMP. The outer silica shell is directly grown onto the adsorbed polymer. As can be seen in Figure 4.4, the QDs are embedded in the silica shell.

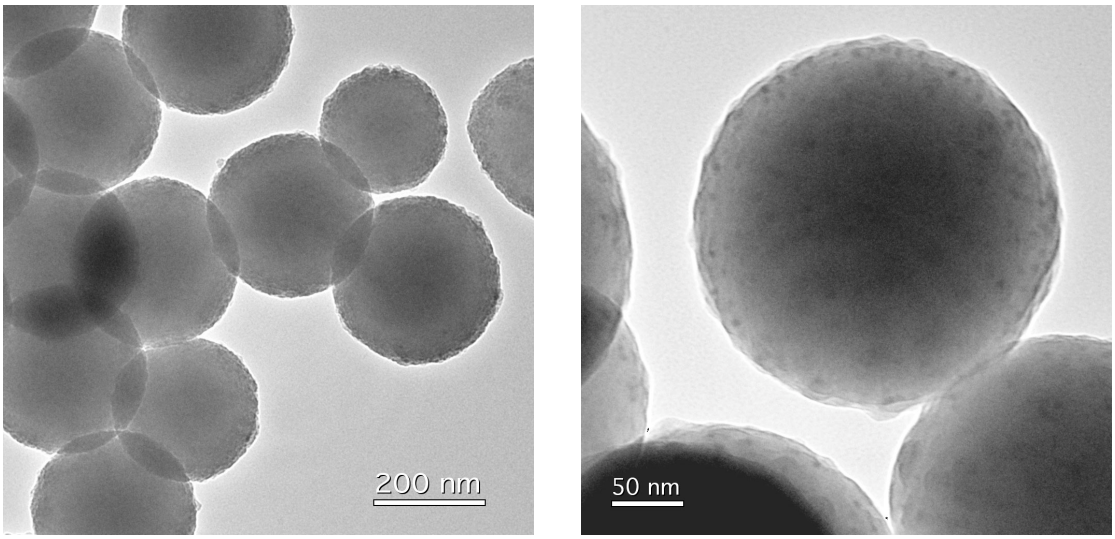

Figure 4.4: TEM images of silica-QD-silica hybrids.

The THPMP was employed to prevent aggregation of the particles in the shell growth step. For the “bare” silica, the OH groups on the surface of the particles introduce negative charges at pH > 7. However, the overall charge on the surface could be still very low and the particles tend to aggregate because the Coulomb interparticle repulsion

is too small to keep them apart. When the THPMP is introduced onto the surface, as shown in Figure 4.5, the overall surface charge becomes more negative, thus increasing the electrostatic repulsion of the particles and reducing the aggregation among the silica nanoparticles [155]. As a result, the final silica-QD-silica particles were highly dispersed and did not form aggregations.

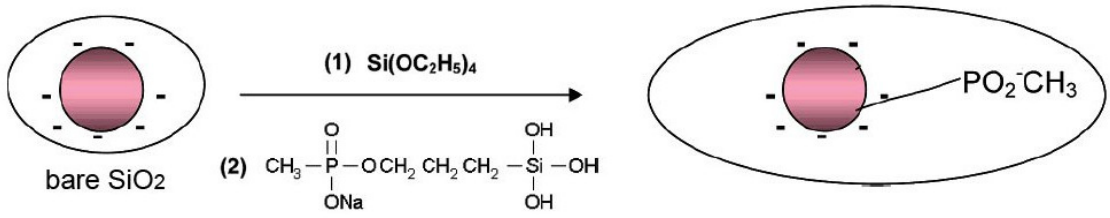

Figure 4.5: Schematic diagram showing the mechanism of the reduced aggregation of silica nanoparticles by the addition of methyl phosphonate groups to the silica nanoparticle surface.

4.2.2.2 Optical properties

The optical properties of the product after each preparation step for constructing the silica-QD-silica hybrid structure were investigated by absorption and fluorescence spectroscopy (Figure 4.6). All spectra were measured in ethanol.

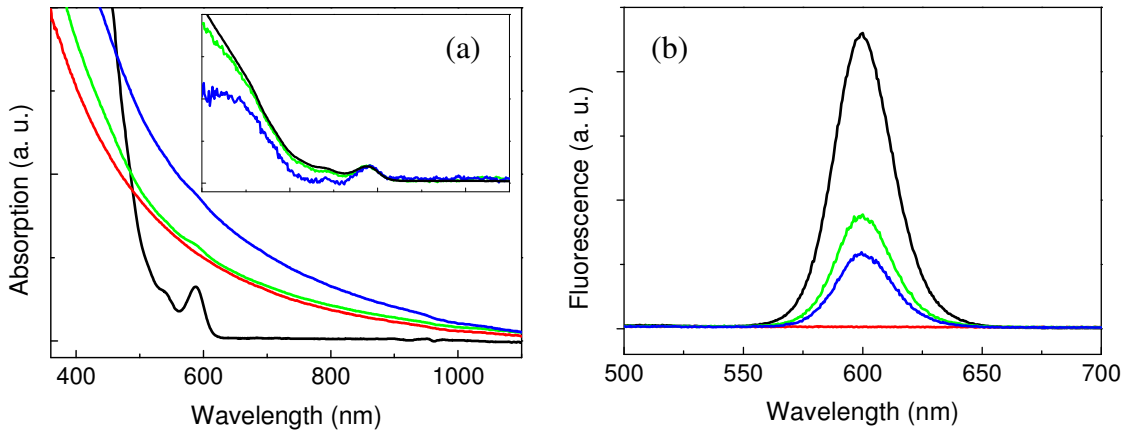

Figure 4.6: (a) Absorption and (b) fluorescence spectra of PVP-coated QDs (black), silica cores (red), QD-decorated silica particles (green) and silica-QD-silica particles (blue). Inset: normalized absorption spectra after subtracting the silica scattering background.

Due to strong scattering by the large silica particles, the absorption peak of QDs at about 580 nm was not clear visible after the QDs were adsorbed on the silica surface (green curve) and further embedded in silica shell (blue curve). After subtracting the

silica scattering background, this peak could be distinguished (see inset of Figure 4.6 a). It seems that the QD absorption peak remains nearly unchanged after the adsorption and embedding steps. The QD emission peaks in the QD-decorated silica particles and the silica-QD-silica particles also did not change compared to that of the PVP-coated QDs.

4.2.2.3 Influence of silica core size

Silica cores with different sizes were employed to study the influence of the core size on constructing the silica-QD-silica hybrid architecture.

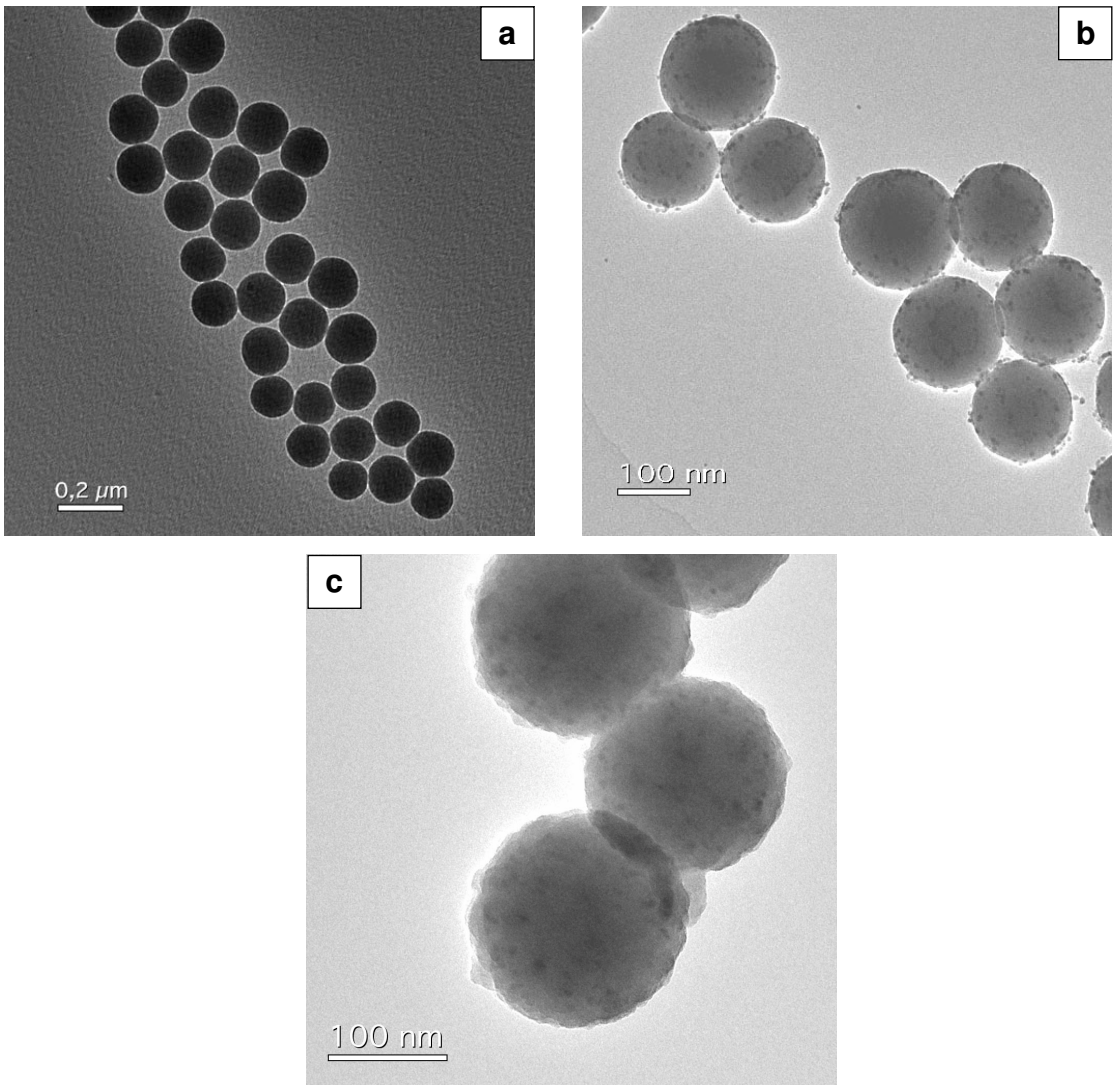

Figure 4.7: TEM images of a) silica core with a diameter of ~ 140 nm, b) QD-decorated silica particles and c) silica-QD-silica hybrid particles.

When the diameter of the used silica core was reduced to ~ 140 nm (Figure 4.7 a), the obtained particle structures in each step were very similar to those prepared using ~ 250 nm silica cores. The QDs were evenly attached to the silica core surface after the QD adsorption step, and these QD-decorated silica particles did not form aggregations, as shown in Figure 4.7 b. After growing the additional silica shell, the QDs were embedded inside a silica matrix (Figure 4.7 c).

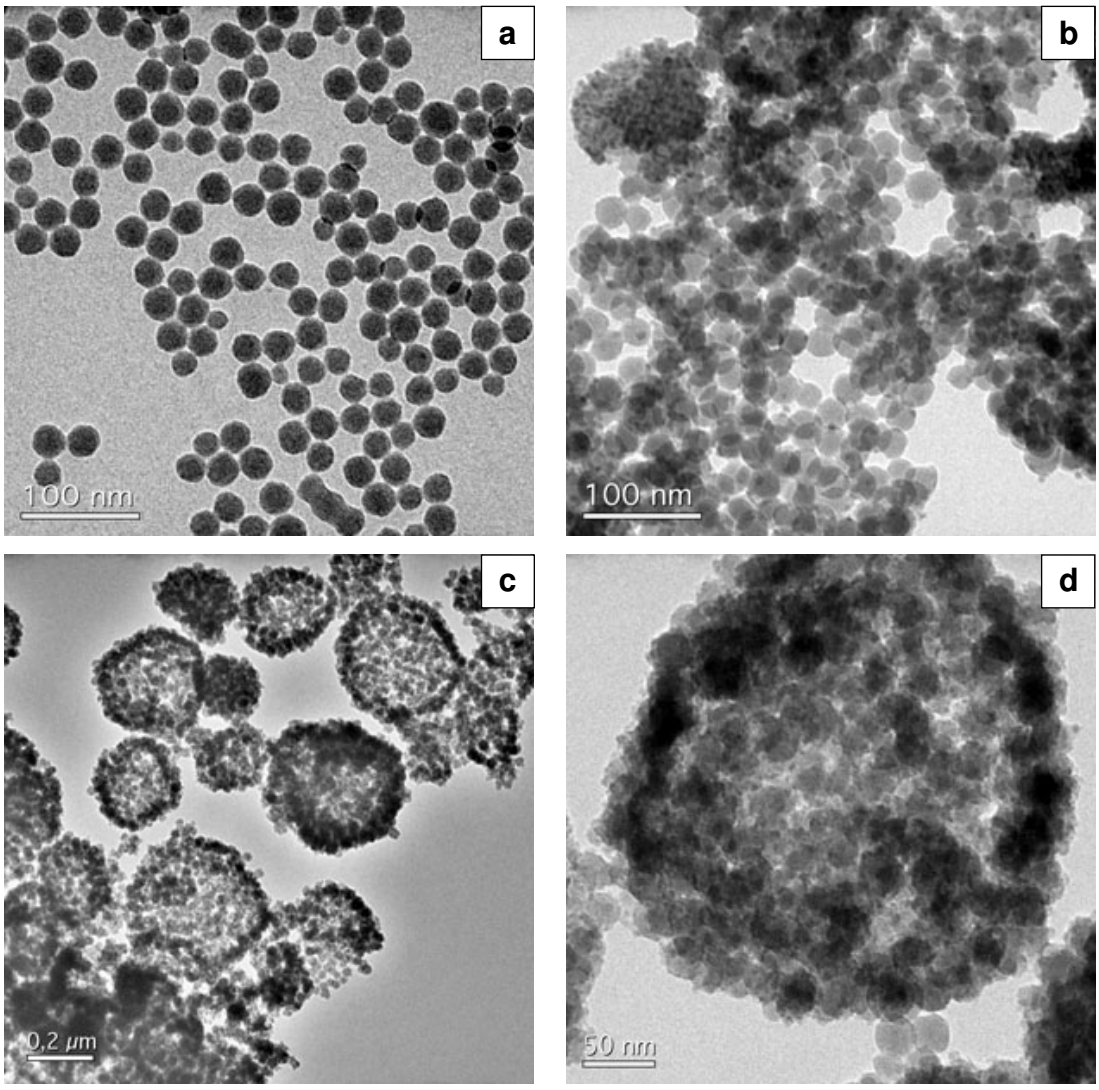

Figure 4.8: TEM images of a) silica cores with diameters of 25 - 30 nm, b) QD-decorated silica particles and c, d) silica-QD-silica hybrid particles.

Totally different architectures were found when even smaller silica cores with a diameter of 25 - 30 nm were used (Figure 4.8 a) to fabricate the silica-QD-silica hybrids. After the QD adsorption step, as shown in Figure 4.8 b, the silica particles were decorated with either only very few QDs (usually 1 - 2 QDs) or no QD at all. Unlike in

the case of larger silica cores, the PVP-coated QDs are hard to cover the surface of small silica cores, on one hand because of the relatively small silica core size compared to 6 - 7 nm of the QD size and on the other hand because the surface coverage density of QDs on silica particles is low (see Figure 4.3 and Figure 4.7 b) which has been observed by Graf et al. that the upper limit of surface coverage is about 30% [147]. Besides, the aggregation of QDs was also observed. This indicates that the free PVP-coated QDs are not stable enough in polar solvent probably due to the detachment of PVP. Therefore, the PVP-coated QDs should not be stored too long and it is suggested that a freshly prepared PVP-coated QD solution has to be used. After further silica growth, the particles surprisingly self-assembled into hollow spheres, as seen in Figure 4.8 c. These big hollow spheres were composed of many small silica particles decorated with QDs (Figure 4.8 d).

Okubo and co-workers [156] have suggested that, while growing a silica shell on pure silica seed particles, small preliminary silica particles are formed first due to the presence of water included in ammonia solution and ethanol, and then the formation of these preliminary particles is followed by their coalescence on the surfaces of the silica seed particles to form the final silica shell coating on the silica seeds. Therefore, the reason for the formation of large hollow spheres in our case might be that small preliminary particles, first formed during shell growth process, act as linkers to connect the silica particles which then self-assemble into the hollow sphere structure.

4.2.2.4 Thickness control

As described above, using small silica cores (less than 50 nm), the desired silica-QD-silica structure was not obtained. On the other hand, using too large silica cores (more than 200 nm), the final particles may be too big for further FRET studies due to the very strong scattering signals, although the silica-QD-silica structure would be well defined. For these reasons, silica cores with a median diameter (~ 140 nm) are at present the best choice. Accordingly, the outer silica shell thickness control was just carried out for silica particles with ~ 140 nm core size.

The thickness of the outer shell could be controlled by the added amount of TEOS. Figure 4.9 shows silica-QD-silica hybrid particles with different outer shell thicknesses, all prepared from identical silica cores with diameter of ~ 140 nm. Obviously, the shell

thickness can be reduced by decreasing the amount of TEOS used in the shell growth step. However, considering the further use, this structure still has some disadvantages. Compared to the more homogenous surface of the thicker shell (Figure 4.9 a, b), the thinner silica shell is not grown evenly on the surface of the QD-decorated silica particles (Figure 4.9 c, d). Therefore, after attaching dye molecules, the distance between QDs and dye molecules will not be well defined.

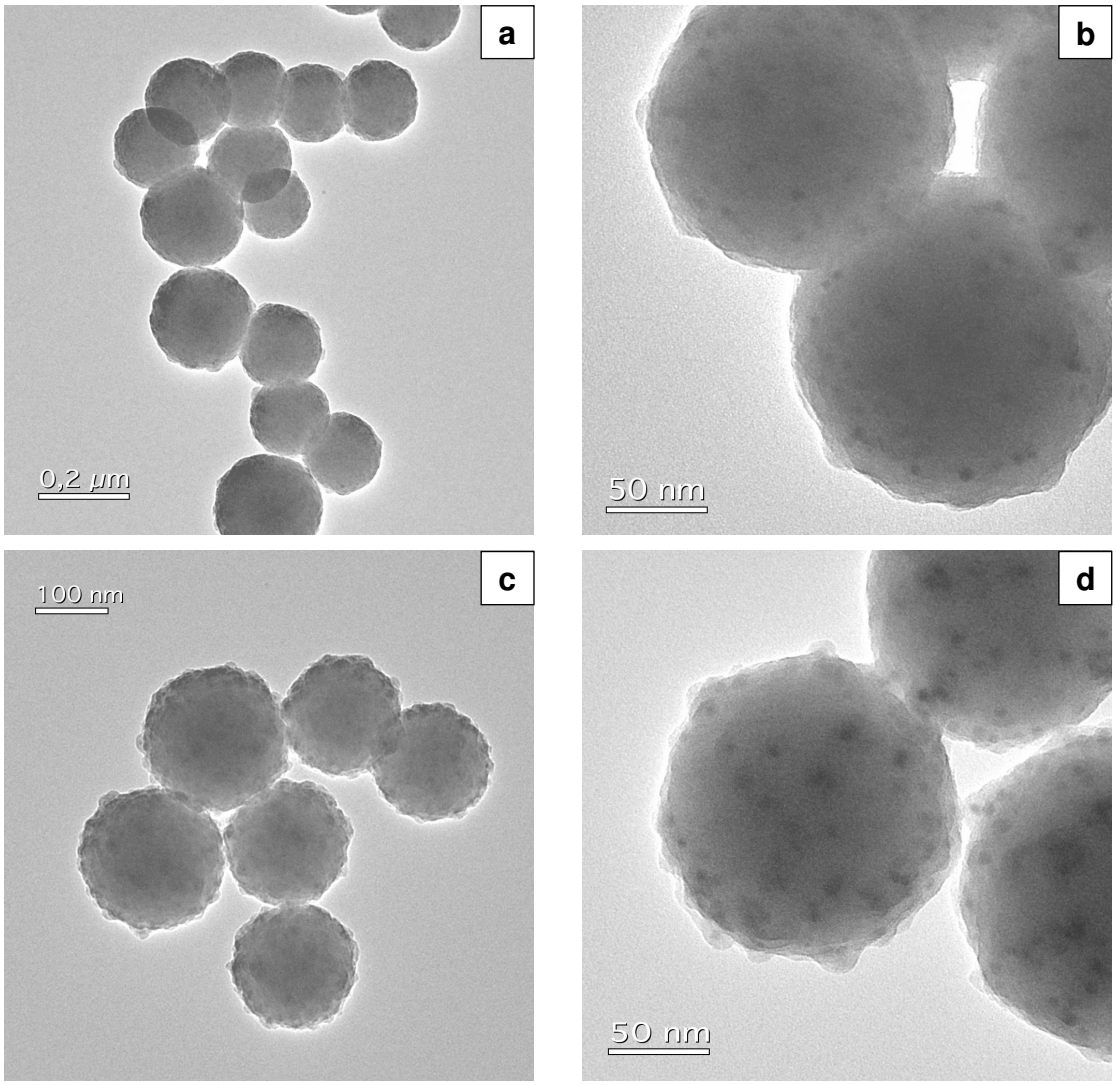

Figure 4.9: TEM images of final products using different TEOS amounts in the shell growth step: a, b) 20 μL and c, d) 10 μL.

4.3 Quantum dot - silica architecture: silica coated quantum dots

4.3.1 Experimental procedure

CdSe/CdS/ZnS QDs were prepared as described in Chapter 3.2.1. A silica shell was applied as follows: In a typical microemulsion using a ternary microemulsion system, 0.1 M surfactant (Igepal CO-520 or Synperonic NP-10) was dissolved in 10 mL of n-hexane (for Igepal CO-520) or cyclohexane (for Synperonic NP-10) containing 100 μL of TEOS and 100 μL QDs (concentration ≈ 20 μM). After stirring for 30 min, 150 μL of 25 wt % ammonia solution was added. For a quaternary microemulsion using Triton X-100 as surfactant, the procedure consisted of mixing 1.77 mL of Triton X-100, 1.8 mL of n-hexanol, 7.5 mL of n-hexane 100 μL of TEOS and 480 μL of H_2O, followed by addition of 100 μL QDs (concentration ≈ 20 μM). The mixture was stirred for 30 min, and then 60 μL of 25 wt % ammonia solution was added. The ternary or quaternary microemulsion solutions were allowed to stir for 24 h followed by addition of ethanol to break the microemulsion and recover the particles. The particles were washed a couple of times with ethanol. The structures of the used surfactants are shown in Figure 4.10.

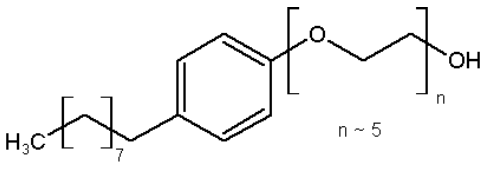

Igepal CO-520

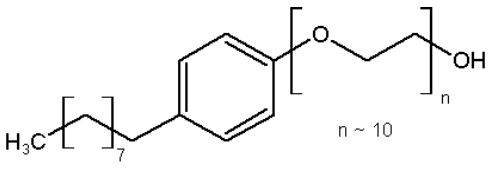

Synperonic NP-10

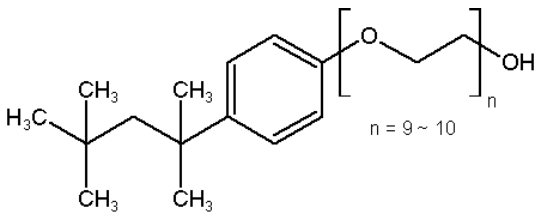

Triton X-100

Figure 4.10: Structures of the surfactants used for QD-silica hybrid system.

4.3.2 Results and discussion

4.3.2.1 TEM characterization

Figure 4.11 shows the TEM images of the QDs and the silica-coated QDs prepared using Igepal CO-520 as the surfactant. The diameter of the QDs is ~ 7 nm. After coating with a silica shell, most of the particles were highly dispersed, and had only one single QD in the center. Particles with no QD inside were also observed. The diameter of the resultant QD-silica particles was 25 - 28 nm and the thickness of the silica shell in the range of 8 - 10 nm.

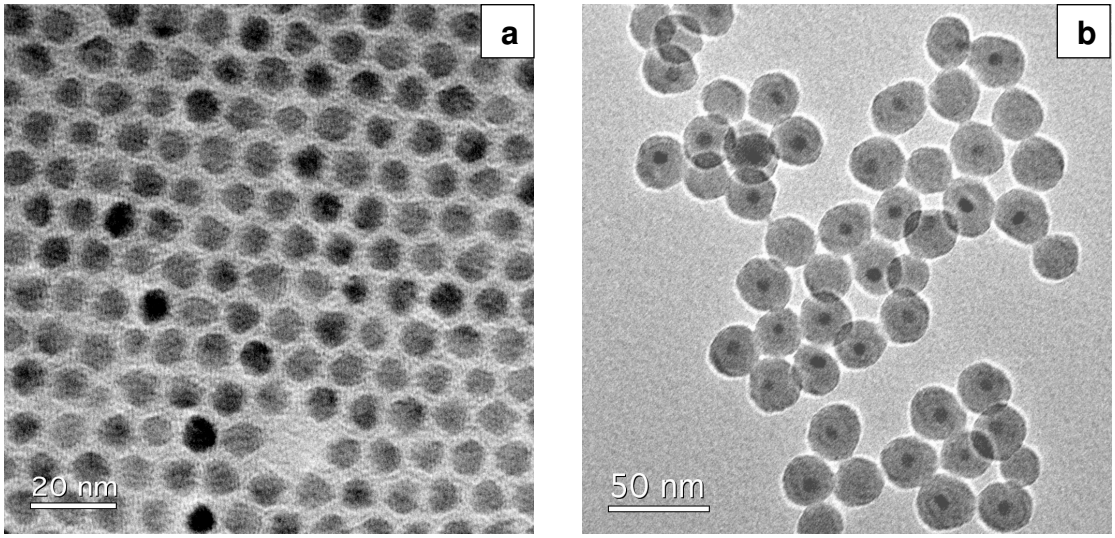

Figure 4.11: TEM images of a) CdSe/CdS/ZnS QDs, and b) QD-silica spheres.

4.3.2.2 Optical properties

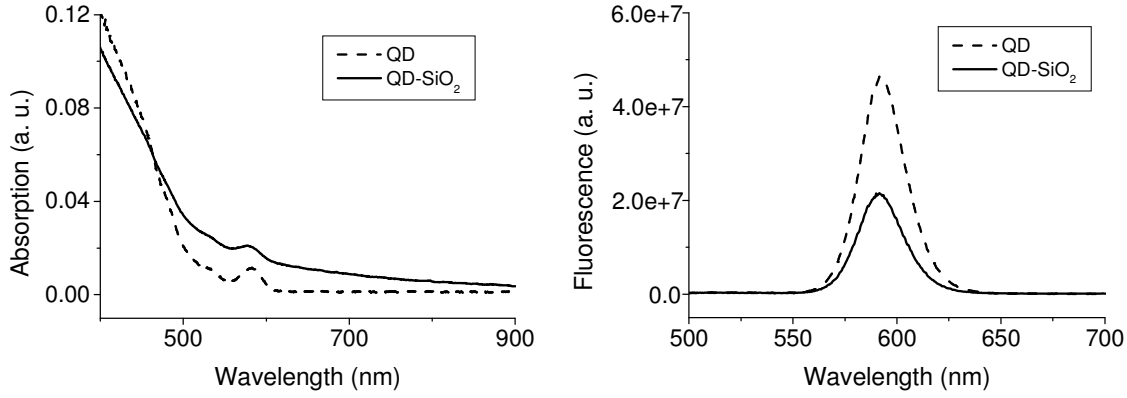

Figure 4.12: Absorption (left) and fluorescence (right) spectra of the QDs and QD-silica spheres.

As seen in Figure 4.12, no significant change in the absorption and fluorescence spectra is observed after encapsulation of the QDs with silica. The baseline of the QD-silica absorption increases compared to the QD absorption due to the scattering of the silica particles. The QY of the QDs before silica coating was 44 %, but was reduced to 20% after coating with the silica shell.

4.3.2.3 Growth process of QD-silica spheres

To study the growth process of QD-silica spheres, samples were taken at different reaction times and characterized by TEM.

Figure 4.13 a shows the TEM image of a sample taken at 30 min. There is so little silica grown around the QDs at 30 min that only QDs can be seen in the image. As the reaction proceeds, more and more silica grows on the QDs (Figure 4.13 b-g). It should be noted that all the samples for the TEM measurement were obtained after breaking the microemulsion. The small particles (Figure 4.13 b-e) were aggregated because the overall negative charge from OH groups on the silica surface was too weak for small particles to keep them apart. When the particles grow bigger (Figure 4.13 f-g), they tended to separate due to the increasing electrostatic repulsion of the particles induced by more negative overall surface charge. However, one could expect that the particles before breaking the microemulsion were separated due to being encapsulated in the micelles. The QY of the QD-silica particles decreased with time, i.e., with increasing silica shell thickness, as shown in Figure 4.14.

In the following an incorporation mechanism (see Figure 4.15) for hydrophobic QDs in silica spheres will be discussed [157]: when TEOS, QDs, surfactant molecules, water and oil (organic solvent) are mixed, the surfactant molecules will rest at the water-oil interface resulting in micelles. Water droplets inside the micelles serve as the nanoreactors for the silica formation. The original organic ligands coated on the QDs are first exchanged with the hydrolyzed TEOS and surfactant molecules in the reverse microemulsion system. This ligand exchange facilitates the transfer of the QDs into the hydrophilic interior of the micelles, where silica growth takes place. Upon the addition of ammonia, TEOS is further hydrolyzed and replaces all the surfactant molecules on the QD surface. The condensation of the hydrolyzed TEOS forms the silica shell around the QDs.

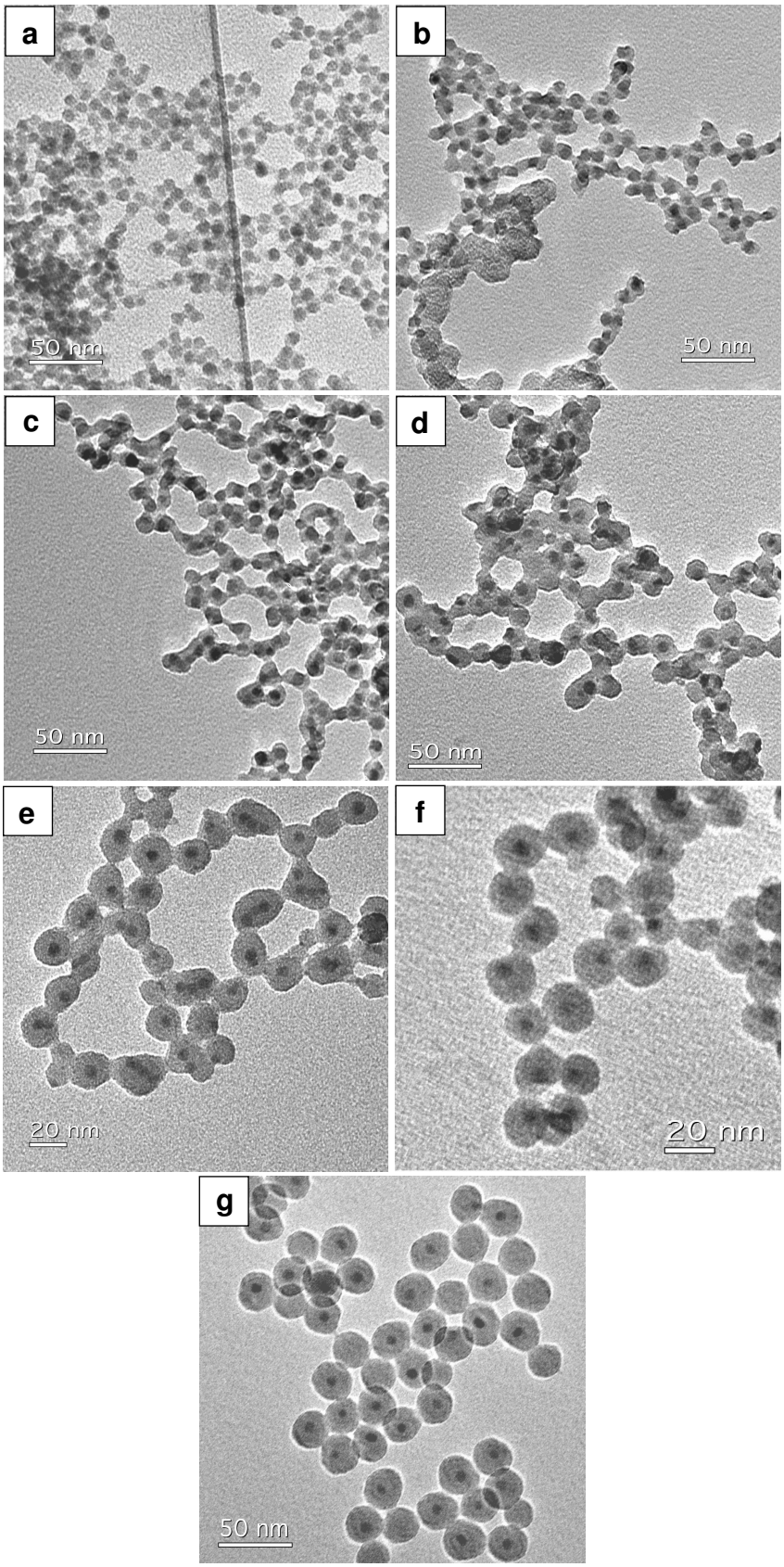

Figure 4.13: TEM images of QD-silica samples taken at different reaction times: a) 30 min, b) 1h, c) 2h, d) 6h, e) 10h, f) 16h and g) 24h.

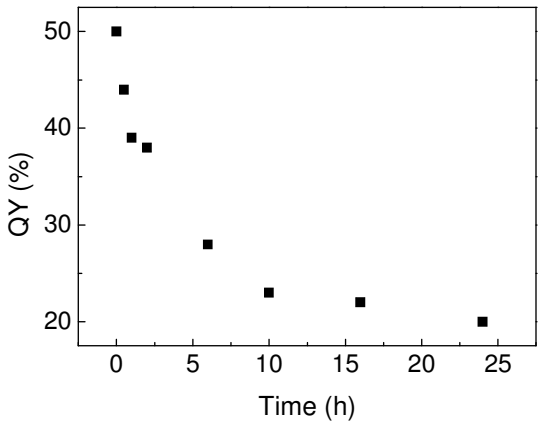

Figure 4.14: Evolution of the quantum yield of QD-silica particles versus reaction time.

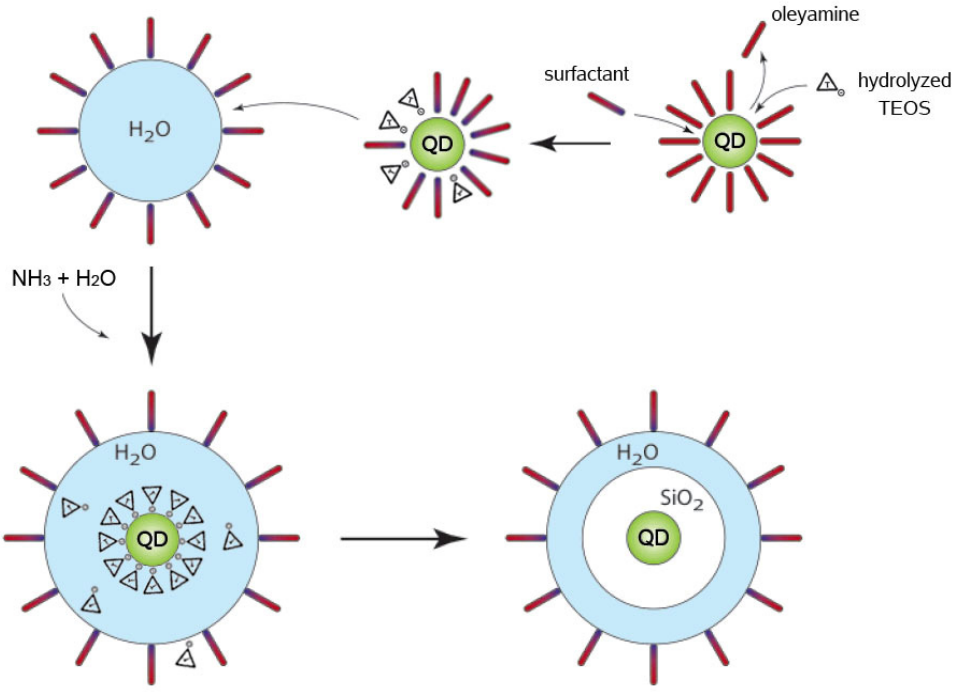

Figure 4.15: Schematic representation of the incorporation mechanism of hydrophobic QDs in silica spheres by the reverse microemulsion method.

The present study on the growth process of the QD-silica particles is not in contradiction with this mechanism. Besides, it also implies that the condensation step that forms the silica shell may occur simultaneously with the replacement process of the surfactant molecules coated on QDs by the further hydrolyzed TEOS in the micelles. The further hydrolyzed TEOS replace the surfactant molecules on the QDs and at the same time condense with the hydrolyzed TEOS on the QDs to form the silica shell. At the beginning of the reaction, only a small fraction of the TEOS molecules is initially

hydrolyzed and these small amounts of the hydrolyzed TEOS are probably not enough to replace all the surfactant molecules, while polymerizing on the QD surfaces. Therefore, part of the QD surface is still coated by the surfactant molecules and the silica shells are not homogeneously grown around the QDs (Figure 4.13 b-d). With increasing reaction time, all the surfactant molecules on the QD surface are gradually replaced by the hydrolyzed TEOS, and the homogeneous silica shell is grown around the entire QD surface (Figure 4.13 e-g). Moreover, the decrease in the QY of the QD-silica particles could be explained using this mechanism. As shown in Figure 4.14, the QY decreases drastically (0.5 - 10 h) and then tends to decrease slowly (10 - 24 h). The drastic QY decrease at the beginning of the reaction could be mainly due to the exchange of the original ligands on the QDs by the hydrolyzed TEOS and surfactant molecules. After that, the further silica shell growth only leads to the minor decrease of the QY.

4.3.2.4 Control of silica shell thickness

According to the original ides, dye molecules should be attached to the QD-silica spheres to study FRET between QD and dye. FRET occurs when the center-to-center distance between QD and dye is comparable to the Föster distance (R_0), at which the FRET efficiency is 50%. R_0 is typically in the range of 2 to 6 nm and it is advantageous if the distance lies in the range of $0.5R_0$ to $2R_0$ [158]. In the case of 7 nm QDs, regardless of the size of the dye, the silica shell thickness should be below 8 nm. To achieve this goal, different reaction conditions were altered based on the typical experimental procedure to reduce the silica shell thickness.

A. Effect of surfactant

To study the effect of the nature of surfactant molecules on the size of the silica particle, QD-silica spheres were prepared in different microemulsions formed using Igepal CO-520, Synperonic NP-10 or TritonX-100 as the surfactant.

Using Igepal CO-520 and Synperonic NP-10, QD-silica spheres with one single QD in one silica particle could be obtained, as shown in Figure 4.16 a and b. The diameter of the QD-silica spheres increased from 25 - 28 nm for Igepal CO-520 to 30 - 35 nm for Synperonic NP-10. Considering the QD size of 7 nm, the thicknesses of the silica shell

are 8 - 10 nm and 11 - 14 nm, respectively. This trend can be explained by the fact that the hydrophilic group of Synperonic NP-10, which consists of 10 oxyethylene groups, is larger than that of Igepal CO-520 with only 5 oxyethylene groups. This leads to an increase in the surfactant's head-to-tail area ratio (head: oxyethylene groups; tail: aliphatic groups) and consequently the formation of larger droplets [159].

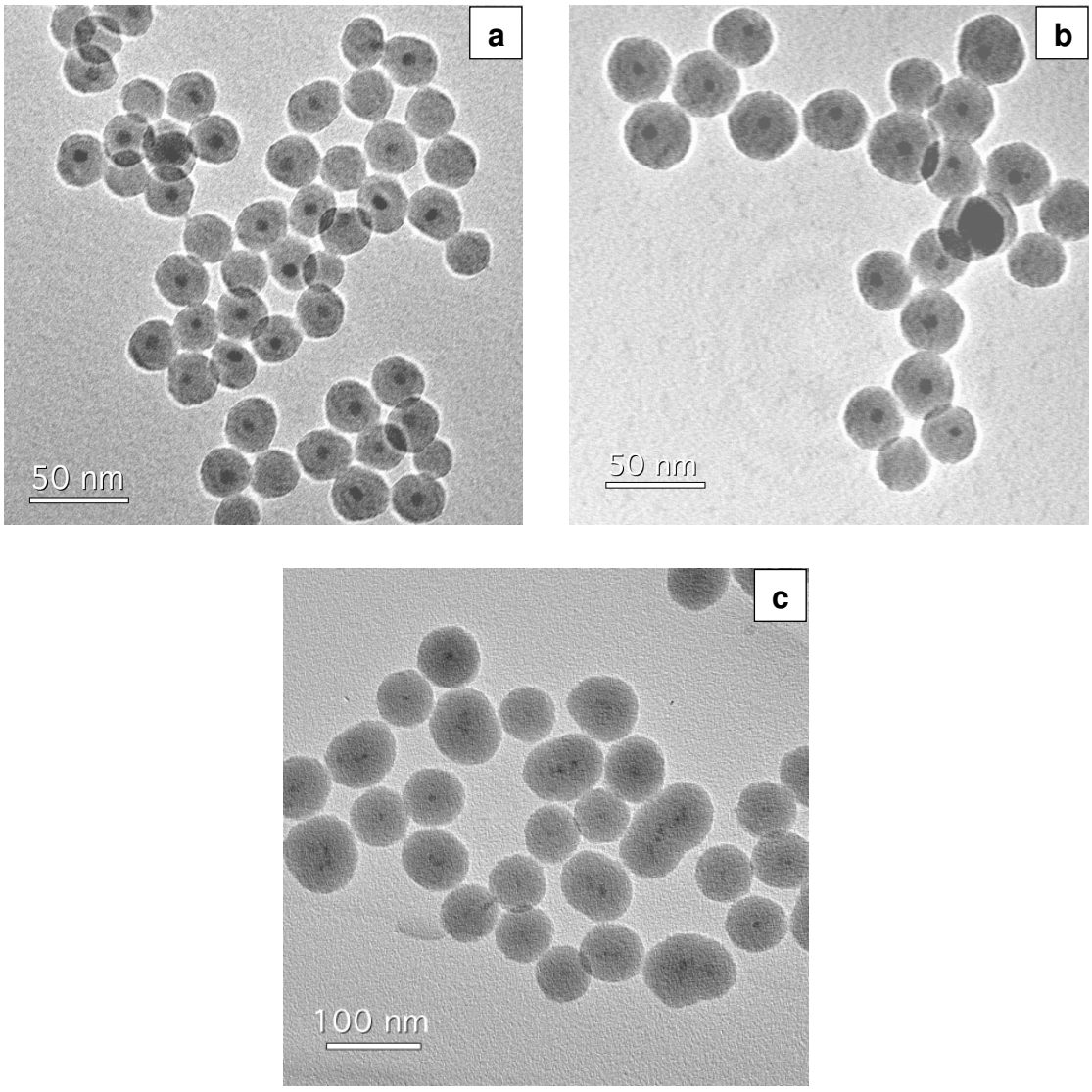

Figure 4.16: TEM images of the QD-silica spheres prepared using different surfactants: a) Igepal CO-520, b) Synperonic NP-10 and c) Triton X-100.

When Triton X-100 was used as the surfactant, the particle diameter was further increased to 60 - 75 nm (Figure 4.16 c), which is consistent with the fact that the size of the silica particles prepared in the quaternary microemulsion is larger than in the ternary microemulsion [160]. QD-silica spheres with not only one single QD but also multiple

QDs inside could be observed. One explanation is that the Triton X-100 droplets are much larger than the others, which makes multiple QDs in one droplet more possible. Another explanation is that Brownian collision [161] of two droplets happens due to the weak attachment of Triton X-100 surfactant films to the droplets. As a consequence, interdroplet open water channels are formed and small silica particles exchange between droplets [162]. The large, lamella-like particles prove the presence of this Brownian collision.

In conclusion, the smallest QD-silica particles could be obtained using Igepal CO-520 as the surfactant. However, even the smallest silica shell thickness is still too large for further FRET investigations.

B. Effect of the amount of ammonium hydroxide

In case of pure silica particles prepared in microemulsion, it is known that [160, 163] the increase in ammonium hydroxide amount, on the one hand, causes more monodisperse and spherical particles, and on the other hand, increases the water concentration, leading to decreasing silica size. Therefore, the amount of ammonia solution was increased from 150 μL to 200 μL to see if the increase in ammonium hydroxide amount can reduce the thickness of the silica shell.

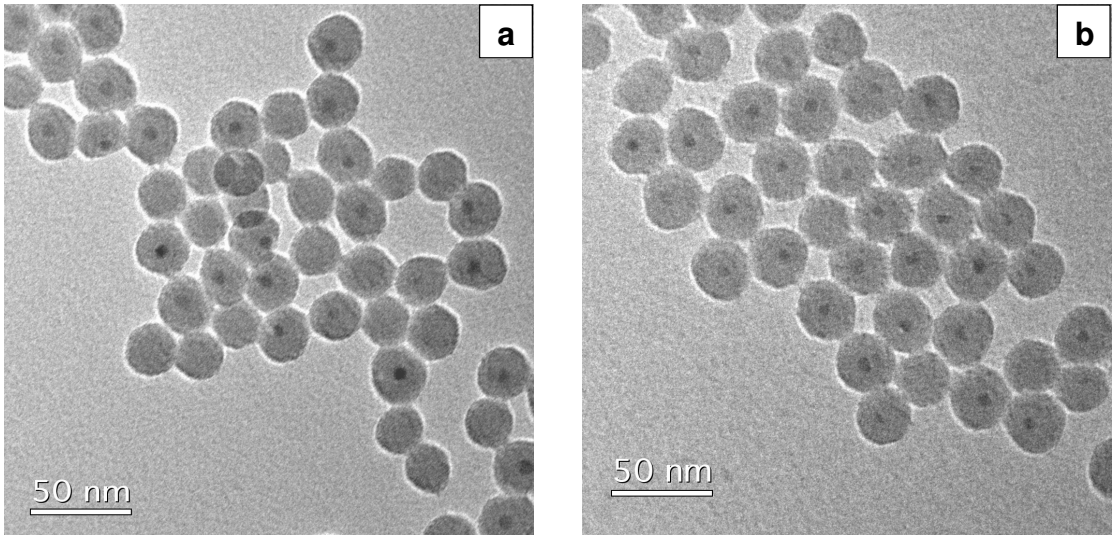

Figure 4.17: TEM images of the QD-silica spheres prepared using different ammonia amounts: (a) 150 μL and (b) 200 μL. Surfactant: Igepal CO-520.

As shown in Figure 4.17, the size of the silica particles appeared to be insensitive to the ammonium hydroxide amount. The particle sizes were 25 - 28 nm using 150 μL of

ammonia and 27 - 30 nm using 200 μL of ammonia. The thickness remained in the range of 8 - 10 nm. For pure silica particles prepared in a microemulsion, with increasing water concentration, more of the TEOS molecules are hydrolyzed in the beginning and thus more silica particles are nucleated, finally leading to smaller silica particles. However, for QD-silica particles, QDs serve as the nuclei for silica shell growth. Therefore, the number of the nuclei for QD-silica particles will not be affected by the water concentration (i.e., ammonia hydroxide amount) in the microemulsion system. This could explain the independence of the QD-silica particle size on the amount of ammonium hydroxide.

C. Effect of TEOS concentration

The amount of added TEOS is expected to directly influence the size of the resulting nanoparticles. Decreasing the amount of the TEOS is the common way to reduce the thickness of the silica shell on seed particles [30, 146]. In contrast, as can be seen in Figure 4.18, when the TEOS amount decreases from 100 μL to 50 μL, the particles aggregate severely and some of the QDs are not completely covered with a silica shell.

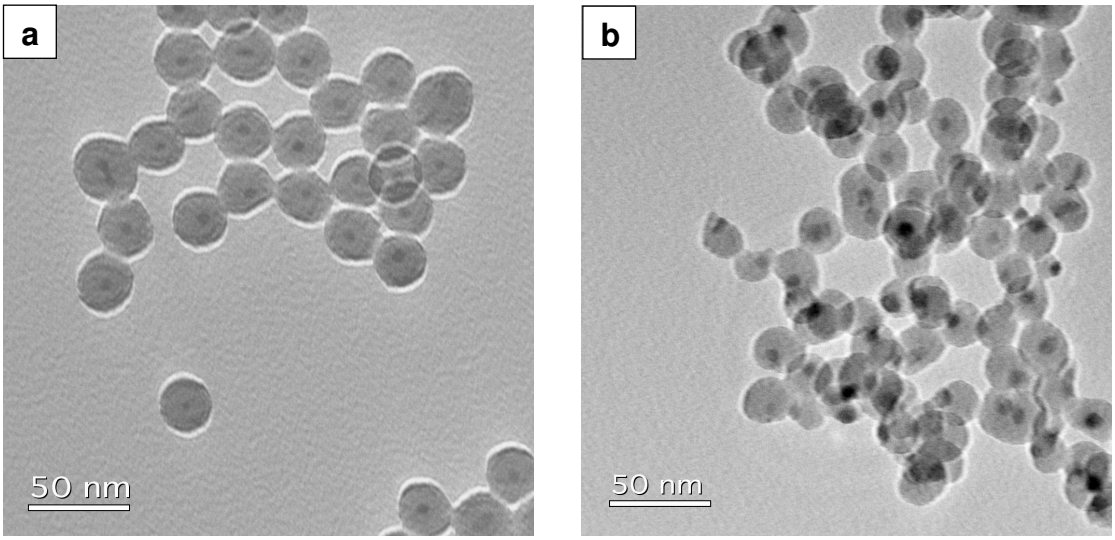

Figure 4.18: TEM images of the QD-silica spheres prepared using different TEOS amounts: (a) 100 μL and (b) 50 μL. Surfactant: Igepal CO-520.

As suggested above, the hydrolyzed TEOS molecules together with the surfactant molecules first exchange the organic ligands on the QDs to transfer the QDs into the micelles. Then the rest of the TEOS is further hydrolyzed to replace the surfactant molecules on the QD surface, and at the same time, the condensation of the hydrolyzed

TEOS occurs to grow a silica shell on the QDs. Those QDs partially coated with a silica shell are probably produced when either the further hydrolyzed TEOS is not enough to replace all the surfactant molecules, or they are enough to replace all the surfactant but not enough to be condensed to form a silica shell.

D. Effect of the size of QD

Figure 4.19 illustrates the effect of QD size on the diameter of the QD-silica spheres prepared in Igepal CO-520 ternary microemulsion. When larger QDs (10 nm) were used, the diameter of the QD-silica spheres increased correspondingly, while the silica shell thickness almost does not change compared with the thickness of 8 - 10 nm when using small QDs of 7 nm in diameter as mentioned before. This can be easily explained by the incorporation mechanism suggesting that TEOS is polymerized on the QD surface. The increase in QD size increases the surface area of the QD. When the same amount of TEOS and the same number of the QDs are used, more TEOS is needed to grow a silica shell around larger QDs. As a result, the number of the "empty" silica particles without QDs inside is reduced, which can also be seen from Figure 4.19.

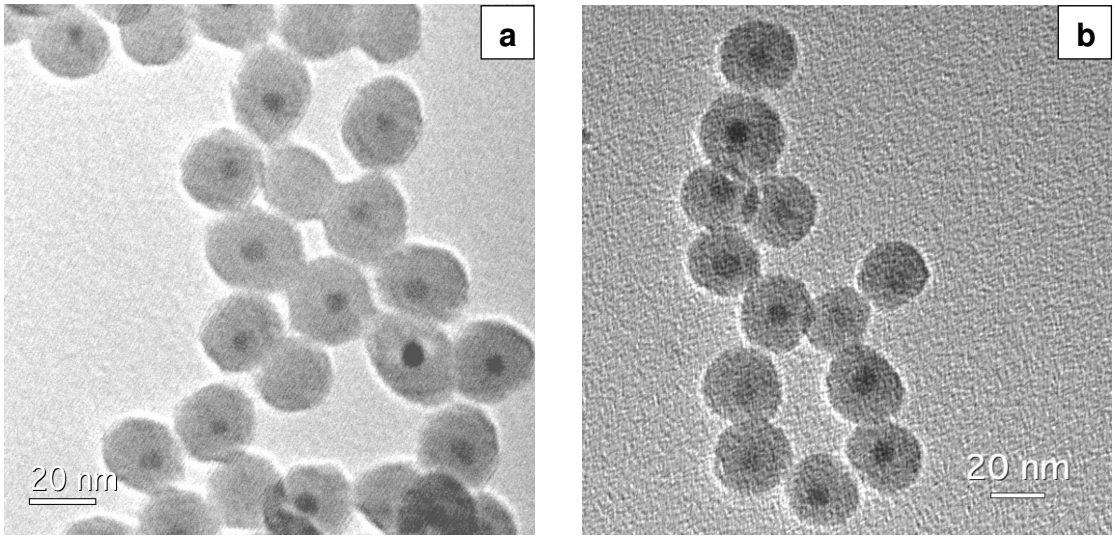

Figure 4.19: TEM images of the QD-silica spheres prepared using QDs with different diameters: (a) 7 nm and (b) 10 nm. Surfactant: Igepal CO-520.

QD size affected the QD-silica spheres prepared in Triton X-100 quaternary microemulsion in a different way. As shown in Figure 4.20, QD-silica particles with multiple QDs inside were observed when small QDs (7 nm) were used. The particles prepared using larger QDs (10 nm) showed mostly one or two QDs in a silica particle.

Moreover, the size of the QD-silica particles decreased using larger QDs. Since QDs act as nuclei for silica growth, when large QDs were used, it was more difficult for the large QDs to undergo interdroplet exchange because it seems to be hard to form sufficiently large interdroplet channels. These nuclei are then covered with silica in their individual droplets to form the silica particles with one single QD inside, and only few of these nuclei exchange between droplets to form silica-covered QD dimers. Furthermore, the decreasing particle exchange between droplets may reduce the coalescence of the particles leading to a smaller size.

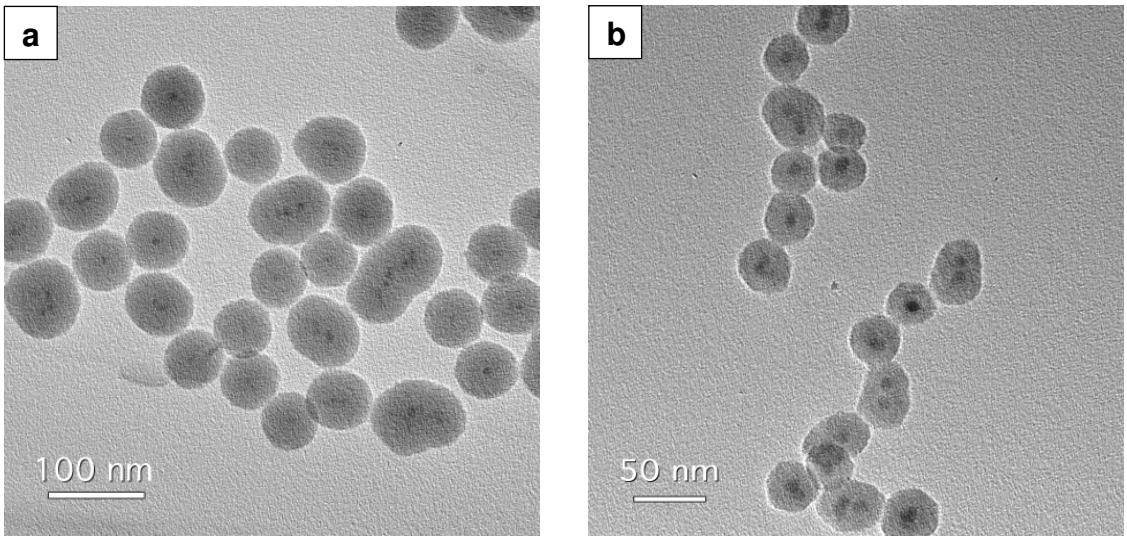

Figure 4.20: TEM images of the QD-silica spheres prepared using QDs with different diameters: (a) 7 nm and (b) 10 nm. Surfactant: Triton X-100.

E. Effect of the concentration of QD

When the other reaction parameters were not unchanged, the amount of added QD only influenced the multiplicity of QDs per silica particle. For the Igepal CO-520 microemulsion system, the amount of the QDs was changed form 100 to 400 μL using a stock solution with a concentration of ~ 20 μM. With a QD amount of 100 μL, most of the particles had one single QD inside and still some silica particles without QDs appeared (Figure 4.21 a). When the QD amount increased to 200 μL, nearly all silica particles had one QD inside and some of them two (Figure 4.21 b). Further increasing the QD amount increased the number of QDs in the silica particles (Figure 4.21 c-d). It was found that with a QD amount of 300 μL, the percentage of silica particles with two QDs inside reached the maximum (30 ~ 40 %).

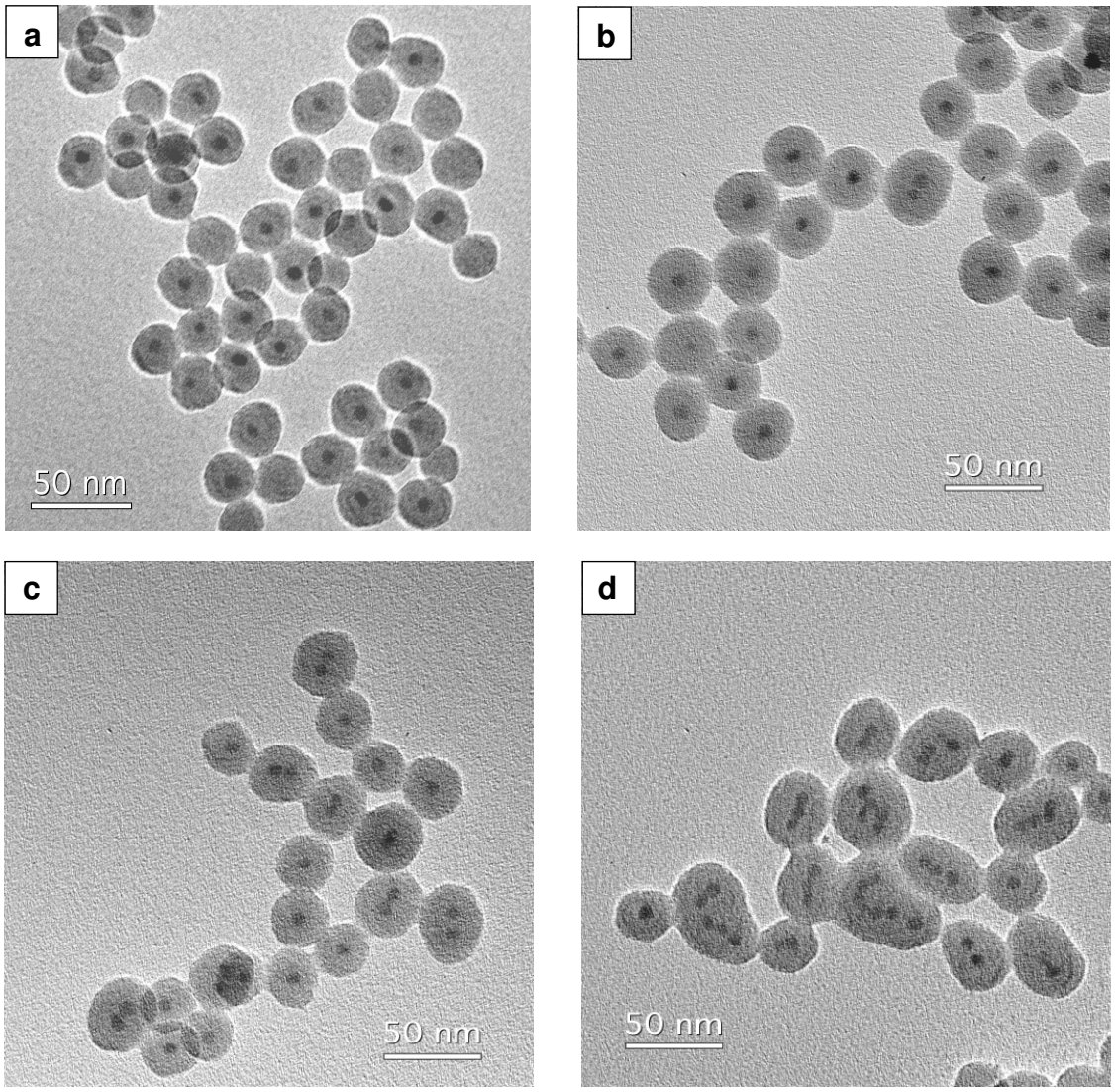

Figure 4.21: TEM images of the QD-silica spheres prepared using different amounts of QDs: (a) 100 μL, (b) 200 μL, (c) 300 μL and (d) 400 μL of QDs. Surfactant: Igepal CO-520.

QD-silica particles prepared in Triton X-100 microemulsion system showed the same trend that the multiplicity of QDs per silica increased with increasing QD amount (Figure 4.22). The percentage of silica particles with two QDs inside reached the maximum (30 ~ 40 %) when 200 μL of QDs with a diameter of 10 nm were used. At higher QD amount the micellar system became unstable, resulting in an aggregation of QD-silica nuclei. Aggregation at an early stage of the silica growth resulted in little or no spacing between the QDs, whereas aggregation at a later stage caused a certain distance between the QDs. Both small and larger interdot distances can be observed in Figure 4.21 and Figure 4.22.

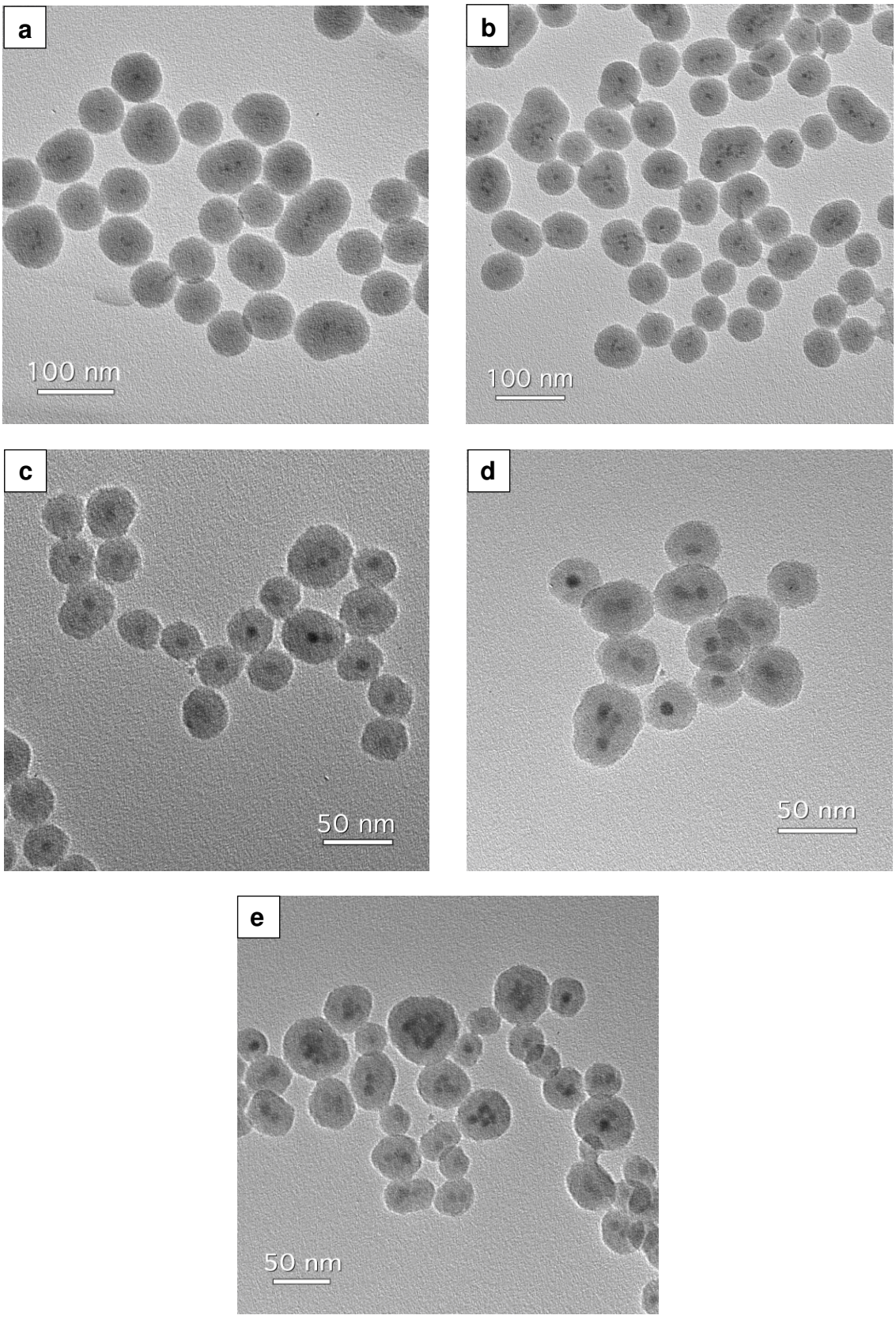

Figure 4.22: TEM images of the QD-silica spheres prepared using different amounts of QDs: QD diameter = 7 nm, (a) 100 μL and (b) 200 μL of QDs; QD diameter = 10 nm, (c) 100 μL, (d) 200 μL and (e) 300 μL of QDs. Surfactant: Triton X-100.

4.4 Conclusion

In order to assemble QD-silica-dye systems for energy transfer studies, QD-silica hybrid particles have been prepared using both "Stöber" and reverse microemulsion methods. Based on the "Stöber" method, QDs could be controllably embedded in silica colloids to form the silica-QD-silica structure. After adsorption of the amphiphilic polymer PVP, the QDs were adsorbed on silica spheres with a diameter larger than 100 nm to form a QD monolayer, and then covered by silica shells with controllable thickness. For the silica-QD-silica structure, although the silica shell thickness could be easily controlled by the TEOS amount, there were disadvantages for further energy transfer studies. The outer thin shell was not grown evenly on the QD covered particle surface so that after attaching dyes the QD-to-dye distance would not be well defined. Using the reverse microemulsion method, one single QD could be encapsulated in one small silica particle to achieve a QD-silica structure. The investigation of the growth process of QD-silica spheres confirmed the suggested incorporation mechanism of QDs in silica spheres in the literature. The influence of the nature of surfactant molecules, the size of QDs, the concentration of ammonium hydroxide, TEOS and QDs on the silica particle size and polydispersity was also studied. For the QD-silica structure, the obtained minimum silica shell thickness was 8 nm after optimizing the reaction parameters. It was not possible to further decrease the thickness to a range where energy transfer between QD and dye would take place. Due to the disadvantages existing for the silica-QD-silica and QD-silica structures, the desired QD-silica-dye system for studying energy transfer between QD and dye separated by a silica shell could not be prepared. Nevertheless, inspired by the investigation of the silica-QD-silica structure, a different QD-silica-dye system was designed, which will be discussed in the next chapter.

5 Quantum dot - silica - dye hybrid system

5.1 Introduction

Inspired by the preparation of the silica-QD-silica structure described in Chapter 4, a new QD-silica-dye hybrid system has been constructed for energy transfer investigations. Instead of attaching dyes on a silica shell that was grown around a silica particle covered with QDs, a "pure" silica core particle was first covered with a silica shell containing organic dye molecules, followed by an adsorption of multishell CdSe/CdS/ZnS QDs onto this silica-dye hybrid particle.

Embedding organic dye molecules into a silica or polysiloxane matrix usually enhances the quantum yield of the organic dye molecules due to immobilization since radiation-less decay mechanisms are suppressed. In addition, the quantum yield of the organic dye molecules stays constant with time due to partially shielding sensitive organic molecules from photobleaching by oxygen. Graf et al. have shown, for example, that the fluorescence of pyrene increases by more than a factor of 6 if the molecules are chemically bound within spherical polyorganosiloxane nanoparticles [164]. Similar results have been found by Imhof et al. [165], who used Stöber particles with embedded fluorescent dye molecules for their optical tracer diffusion studies in colloidal dispersions, an approach which previously was employed by van Blaaderen and co-workers [33, 166]. Besides the enhanced fluorescence intensity, embedding dye molecules into a nanoscopic silica matrix also has other advantageous features such as excellent photostability, easy surface modification and size tunability. In addition, nanoparticles containing several hundred dye molecules serving as carriers allow for unusually high local concentrations of the dye molecules not achievable for dye molecules in solution due to the solubility limit.

Directly adsorbing QDs onto the dye-containing silica shell, which makes it possible to minimize the average distance between QDs and dye molecules, allows for energy transfer between QDs as fluorescence donors and the organic dye molecules as acceptors/emitters. The energy transfer process has been investigated and described in the framework of Förster theory.

5.2 Experimental procedure

A. Silica core particles

Spherical "pure" silica core nanoparticles with diameter of ~ 140 nm and size polydispersity < 5% (according to transmission electron microscopy (TEM)) were prepared by hydrolysis of tetraethyl orthosilicate (TEOS) using the Stöber method: 4.5 mL TEOS, 28.5 mL H_2O and 1.5 mL aqueous ammonia solution (25 wt%) were added to 65.5 mL ethanol. The reaction was allowed to continue for 6 h at room temperature at moderate stirring. For purification, the particles were centrifuged, washed and redispersed in ethanol.

B. APS-dye conjugates

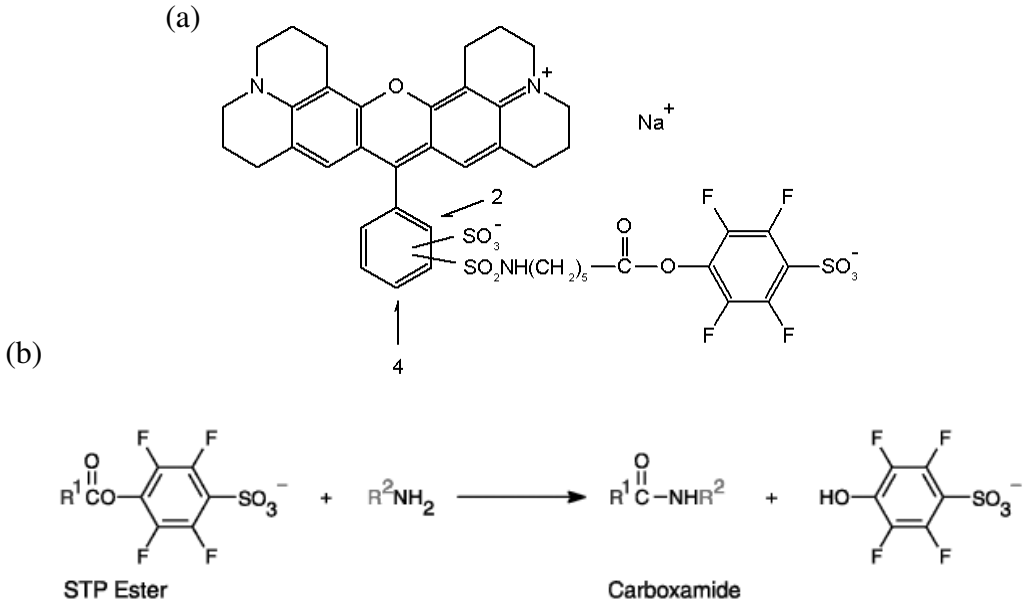

Figure 5.1: (a) Structure of the organic dye Texas Red-X STP ester and (b) the reaction of a primary amine with an STP ester.

The organic dye Texas Red-X STP ester with absorption maximum at wavelength 588 nm was used for the preparation of QD-silica-dye hybrid particles because of its effective spectral overlap with the multishell QDs. This amine reactive dye molecule can be covalently linked to the silane coupling agent (3-aminopropyl)triethoxysilane (APS) and therefore easily chemically incorporated into silica particles, an approach which for the organic dyes fluorescein and rhodamine B has first been published by van Blaaderen et al. [166, 167]: 0.18 mg Texas Red-X STP ester was dissolved in 1.5 mL

DMSO, combined with 2 μL APS, and the mixture was stirred under Ar atmosphere for 24 h in the dark. The structure of Texas Red-X STP ester and the reaction of a primary amine with the STP ester are shown in Figure 5.1.

C. Multishell QDs

CdSe/CdS/ZnS QDs were synthesized using the SILAR method as described in Chapter 3.2.1.

D. QD-silica-dye hybrid nanoparticles

Based on the above-described materials, the QD-silica-dye hybrid nanoparticles were synthesized in four steps as follows:

(i) To prepare silica-dye hybrid nanoparticles, the APS-dye conjugate (see B, total amount 1×10^{17} APS-dye molecules, corresponding to an average of 1×10^4 dye molecules per silica particle if all APS-dye molecules are incorporated in the grown silica-dye shells) was added to a mixture of 1 mL of an ethanol dispersion of silica core particles (c = 13.2 g/L), 45 mL ethanol, different amounts of TEOS (5 - 67 μL) and 3 mL aqueous ammonia solution (25 wt %). These mixtures were then stirred for 48 h to grow a dye-embedded silica shell onto the silica cores. For purification, the samples after centrifugation were washed twice with ethanol to remove the unreacted APS-dye conjugates. The silica-dye nanoparticles were then redispersed in ethanol for further functionalization. 5 ~ 67 μL of TEOS correspond to a theoretical shell thickness of 2.3 - 23.2 nm as calculated from the silica core size and the total amount of added TEOS, assuming a SiO_2 density of 2.6 g/mL. In the calculations of the expected shell thickness, the APS-dye was neglected since it constitutes only a minor fraction of the silica-dye shell.

(ii) The surface of these purified silica-dye hybrid nanoparticles was then functionalized with APS: 10 μL APS were added to the silica-dye nanoparticles, which were redispersed in 47 mL ethanol plus 3 mL ammonia solution (25 wt %). This mixture was stirred for 12 h. The resulting APS-functionalized silica-dye nanoparticles after centrifugation were washed twice with ethanol to remove the unreacted APS and then redispersed in ethanol.

(iii) The CdSe/CdS/ZnS QDs were coated with Poly(vinylpyrrolidone) (PVP) polymer chains prior to mixing with the APS-functionalized silica-dye nanoparticles. For this purpose, a PVP (M = 10,000 g/mol) stock solution was prepared by dissolving 27.1 g PVP/L in butanol and ultrasonification of this solution for 30 min. 7 mL of this PVP solution was then mixed with 500 µL of a QD chloroform dispersion (QD concentration ~ 2×10^{-5} mol/L), and this mixture was stirred for 24 h at room temperature. The amount of PVP had been calculated to yield colloids with about 60 PVP molecules per nm^2 of the QD surface [168]. The dispersion of the PVP-coated QD was not further purified.

(iv) QD-silica-dye hybrid nanoparticles were obtained by mixing 7.5 mL freshly prepared dispersion of PVP-coated QD (see (iii)) and 10 mL of the dispersion of APS-functionalized silica-dye hybrid nanoparticles (see (ii)). This mixture was stirred for 24 h at room temperature. For purification, the reaction mixture was centrifuged, and the precipitate was redispersed in ethanol.

The route from pure silica cores to QD-silica-dye hybrid particles and the corresponding particle topologies are sketched in Figure 5.2.

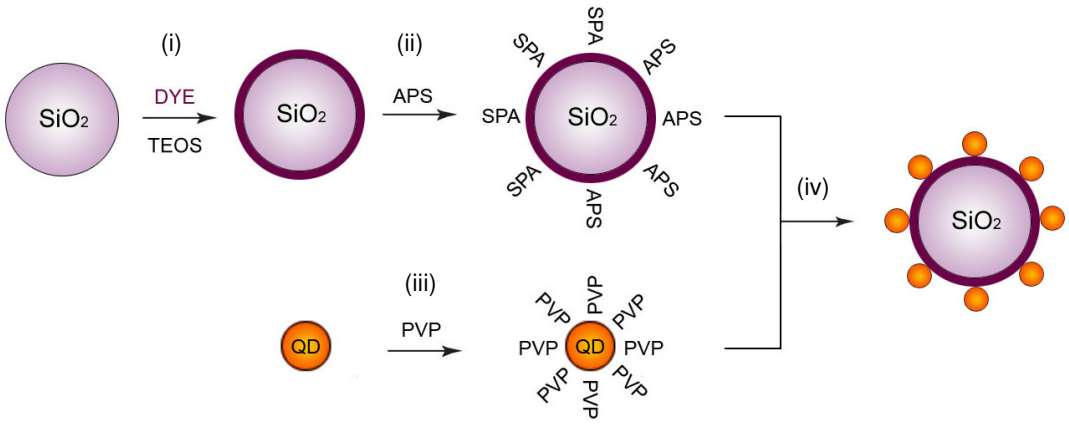

Figure 5.2: Synthesis of QD-silica-dye hybrid nanoparticles, QD not to scale.

5.3 Results and discussion

5.3.1 TEM characterization

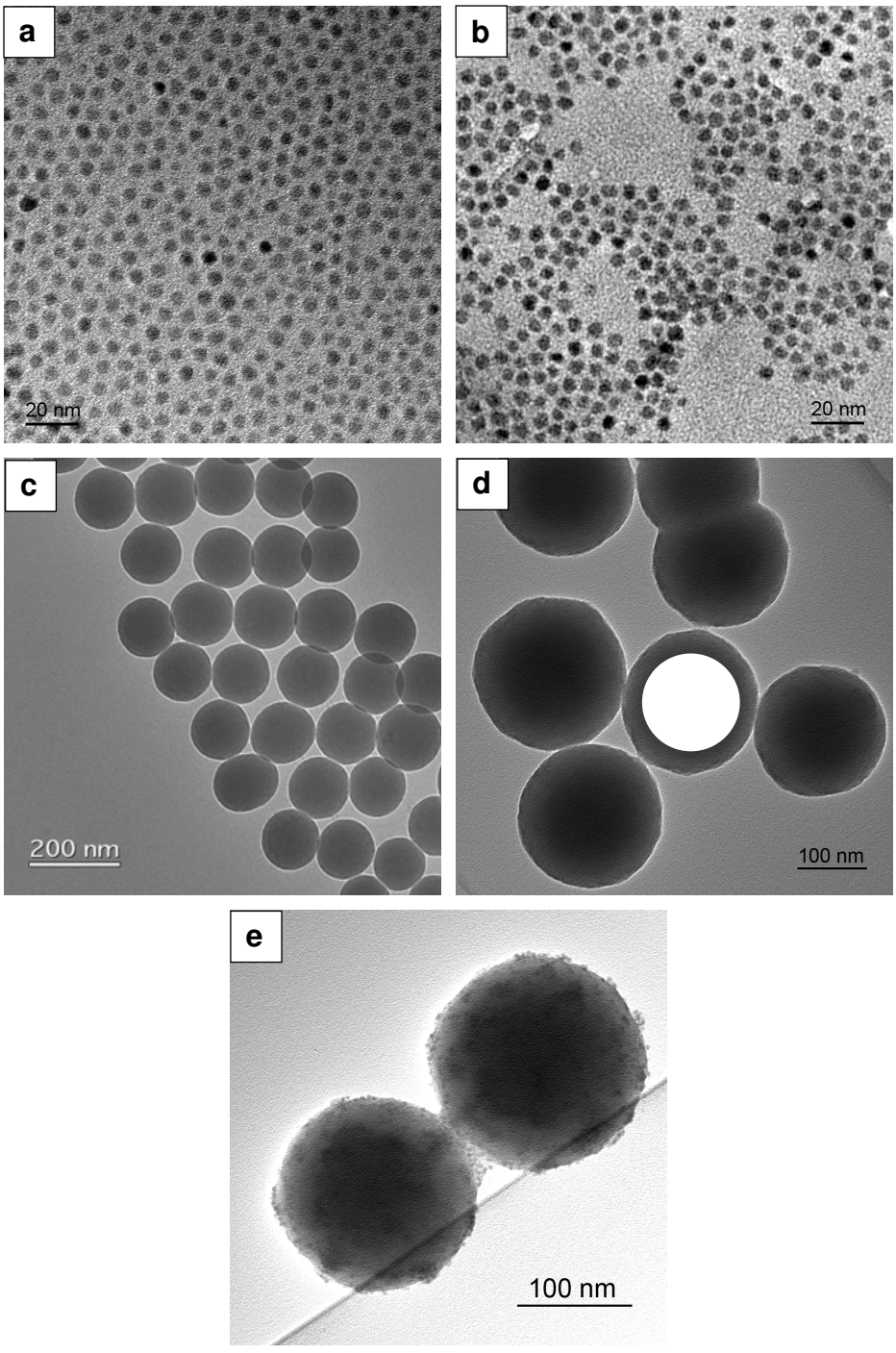

Figure 5.3: TEM images of CdSe/CdS/ZnS QDs (a) before and (b) after PVP-coating, and of (c) silica core particles, (d) silica-core - dye-shell particles with shell thickness 23 nm (the inserted "white sphere" corresponds in size to the silica cores displayed in c (with scale adjusted accordingly)), and (e) Silica-dye-QD hybrid nanoparticles with shell thickness of 23 nm.

5.3.1.1 CdSe/CdS/ZnS QDs

The QDs consist of CdSe cores surrounded by one monolayer of CdS and one monolayer of ZnS. The average particle diameter is 4.5 nm (Figure 5.3 a), with size polydispersity below 15% as determined from particle size statistics, and also indicated by the ordered pattern the sample forms on the TEM grid upon drying. The emission peak of QDs is at 571 nm, and the photoluminescence quantum yield (QY) is 35%. The emission peak and QY remain nearly unchanged before and after absorption of PVP.

5.3.1.2 Silica cores

As also shown by transmission electron microscopy (Figure 5.3 c), the silica core particles are well-defined spheres with low polydispersity < 5%. The average diameter is 140 nm.

5.3.1.3 Silica-dye (silica-core - dye-shell) nanospheres

The growth of the dye-containing silica shell onto the silica cores occurs homogeneously, as shown in Figure 5.3 d. From the chemical composition, the calculated shell thickness of this particular sample should be 23 nm. The average diameter of the core-shell silica spheres according to the TEM measurements is 190 nm, which is in good agreement with the theoretically expected value ($140 + 2 \times 23 = 186$ nm). Here, it should be noted that such silica-dye hybrid nanospheres with various shell thicknesses were prepared, as determined by the amount of added TEOS for the 2^{nd} reaction step, and described in detail above. In all cases, TEM micrographs have proven the homogeneous shell growth as in the case of the example selected here. Further, since a large excess of dye-APS are always used, a constant dye concentration within the growing shell is assumed, an assumption which is consistent with the intensities of the dye emission of the silica-dye hybrid nanospheres (see 5.3.2).

5.3.1.4 QD-silica-dye hybrid nanoparticles

A TEM micrograph of the silica-dye hybrid nanospheres after addition of PVP-coated semiconductor QDs is shown in Figure 5.3 e. The tiny black dots at the particle surface are the QDs. As can be seen, a very large number of QDs (more than several hundred) covers the surface of a single silica particle. Theoretically, according to the total amount

of added QDs, a maximum amount of 1730 QDs per single silica particle independent of shell thickness is expected.

5.3.2 Fluorescence of silica-dye particles

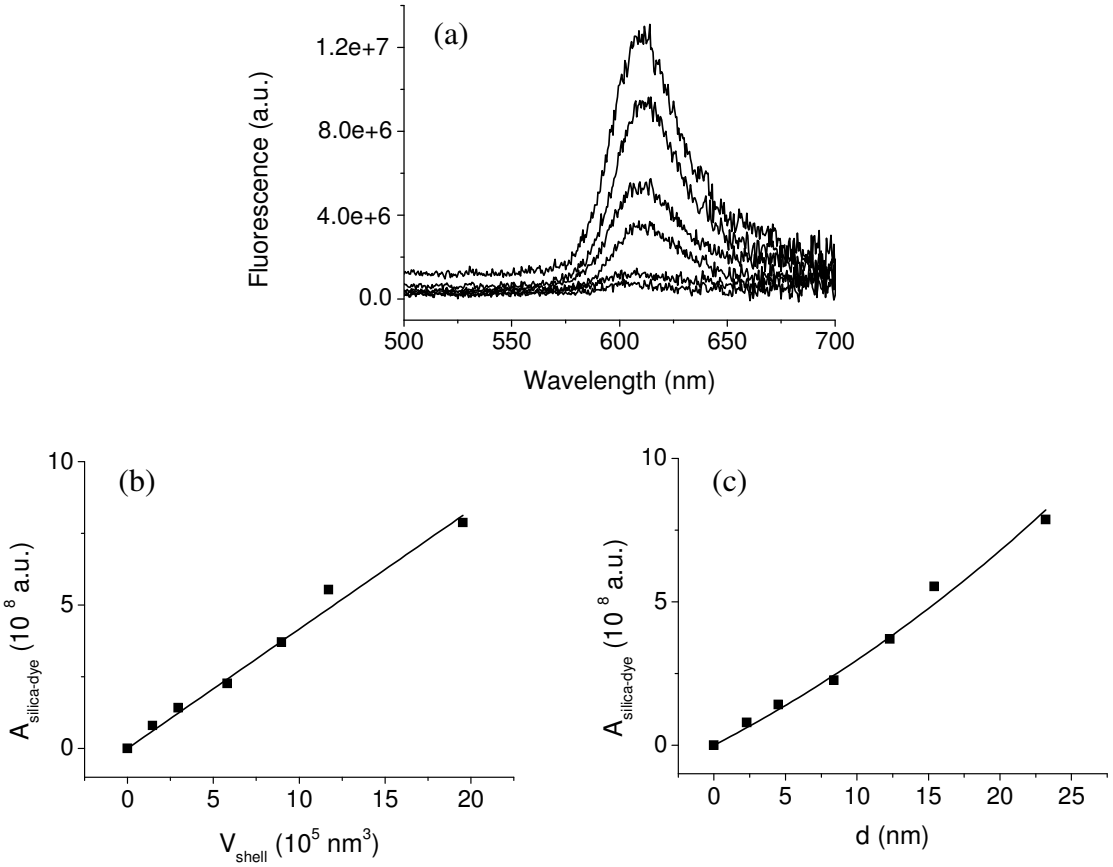

Figure 5.4: (a) Fluorescence spectra of silica-dye particles without adsorbed QDs, for particles with varying silica-dye shell thicknesses (d = 2.3, 4.5, 8.4, 12.3, 15.4 and 23.2 nm from bottom to top), excited at 390 nm far from the dye absorption maximum. Integrated fluorescence intensity ($A_{silica\text{-}dye}$) versus (b) dye-silica shell volume (V_{shell}) and (c) dye-silica shell thickness (d), experimental results (solid symbols) and theoretical fit assuming constant dye concentration within the silica shell.

Figure 5.4 a shows the fluorescence spectra of silica-dye particles without adsorbed QDs, and a numerical calculation of integrated fluorescence intensity versus shell thickness in comparison to the experimental results. These spectra have been measured as a "background" to distinguish dye fluorescence due to FRET from direct dye excitation (see further below). Although excitation takes place at wavelength 390 nm where the dye absorption seems to be negligible, obviously some optical excitation of the dye molecules is found, and the detected fluorescence intensity increases with

increasing amount of dye molecules per silica particle, or increasing dye shell thickness. Note that in the wavelength regime of the emission peak around 600 nm especially for silica particles with shell thicknesses larger than 4.5 nm (and correspondingly higher dye content) the contribution from particle scattering seems to be very small. As mentioned above, a constant dye concentration within the shell is expected, and therefore the total dye amount per silica particle should simply be proportional to the volume of the respective dye-silica shell (Figure 5.4 b and c):

$$A \propto A_{silica\text{-}dye} \propto V_{\text{shell}} = \frac{4}{3}\pi((R+d)^3 - R^3)$$

where A is the number of dye molecules, $A_{silica\text{-}dye}$ is the integrated fluorescence intensity of the silica-dye particles, V_{shell} is the volume of the dye-containing silica shell, R is the radius of the silica core and d is the thickness of the dye-containing silica shell.

The absorption spectra of the silica-dye particles were also recorded (Figure 5.5). With increasing shell thickness, the particle scattering becomes stronger due to the increasing particle size and affects the absorption spectra substantially. After subtracting the scattering background, the dye absorption for different shell thickness could be determined. The result is also consistent with the assumption that the dye concentration in the silica shell is constant.

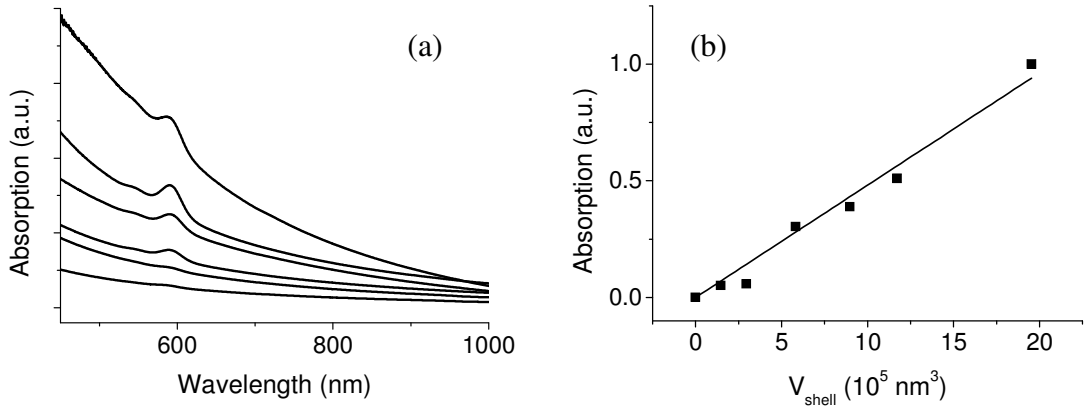

Figure 5.5: (a) Absorption spectra of silica-dye particles without adsorbed QDs, for particles with varying silica-dye shell thicknesses (d = 2.3, 4.5, 8.4, 12.3, 15.4 and 23.2 nm from bottom to top). (b) Dye absorption versus dye-silica shell volume (V_{shell}), experimental results (solid symbols) and theoretical fit assuming constant dye concentration within the silica shell.

5.3.3 Fluorescence of QD-silica-dye particles

5.3.3.1 Optical properties of QD-silica-dye particles

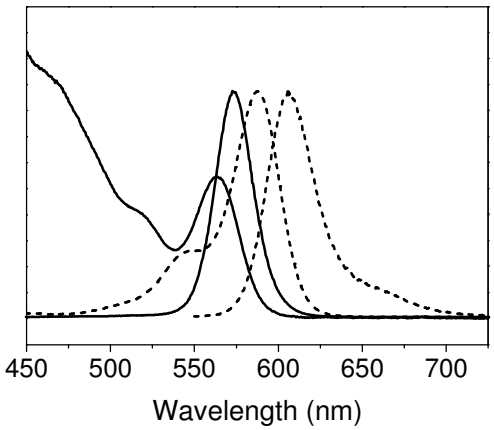

Figure 5.6: Absorption and fluorescence spectra of QDs in chloroform (solid line) and Texas Red in chloroform (dashed line).

Figure 5.6 shows absorption and emission spectra of the QDs (measured in chloroform solution) and Texas Red (measured in ethanol solution), respectively. The absorption and emission spectra of the QD-silica-dye hybrid particles show no shifts in these peaks for the QDs and only slight red shifts for the dye (Table 5.1).

Table 5.1: Absorption and emission peaks of QDs and Texas Red in chloroform and in QD-silica-dye hybrid particles.

	in chloroform	in the hybrid particles
QD absorption (nm)	564	564
QD emission (nm)	573	573
Texas Red absorption (nm)	588	592
Texas Red emission (nm)	606	610

QD emission and Texas Red absorption spectra yield an overlap integral of J = 6.8 $\times 10^{15}$ nm^4 / M cm according to equation 5.1 [169]:

$$J(\lambda) = \frac{\int F_D(\lambda)\varepsilon_A(\lambda)\lambda^4 d\lambda}{\int F_D(\lambda) d\lambda} \tag{5.1}$$

where F_D is the integrated fluorescence intensity of the donor (QD), ε_A is the molar extinction coefficient of the acceptor (dye), and λ is the wavelength. Using equation

(5.2) [169] with a fluorescence quantum yield of the donor (QD) of Φ_0 = 0.35, an orientation factor of κ^2 = 2/3, and the refractive index of silica of n = 1.45 [168] one obtains a Förster radius of R_0 = 5.6 nm.

$$R_0^6 = 8.79\times10^{-11}(nm^2 \cdot M \cdot cm)\times\frac{\kappa^2\Phi_0 J(\lambda)}{n^4} \qquad (5.2)$$

The ensemble average of the orientation factor in the QD-silica-dye hybrid particles was evaluated by Monte-Carlo simulation, giving the same value corresponding to a random dipole orientation.

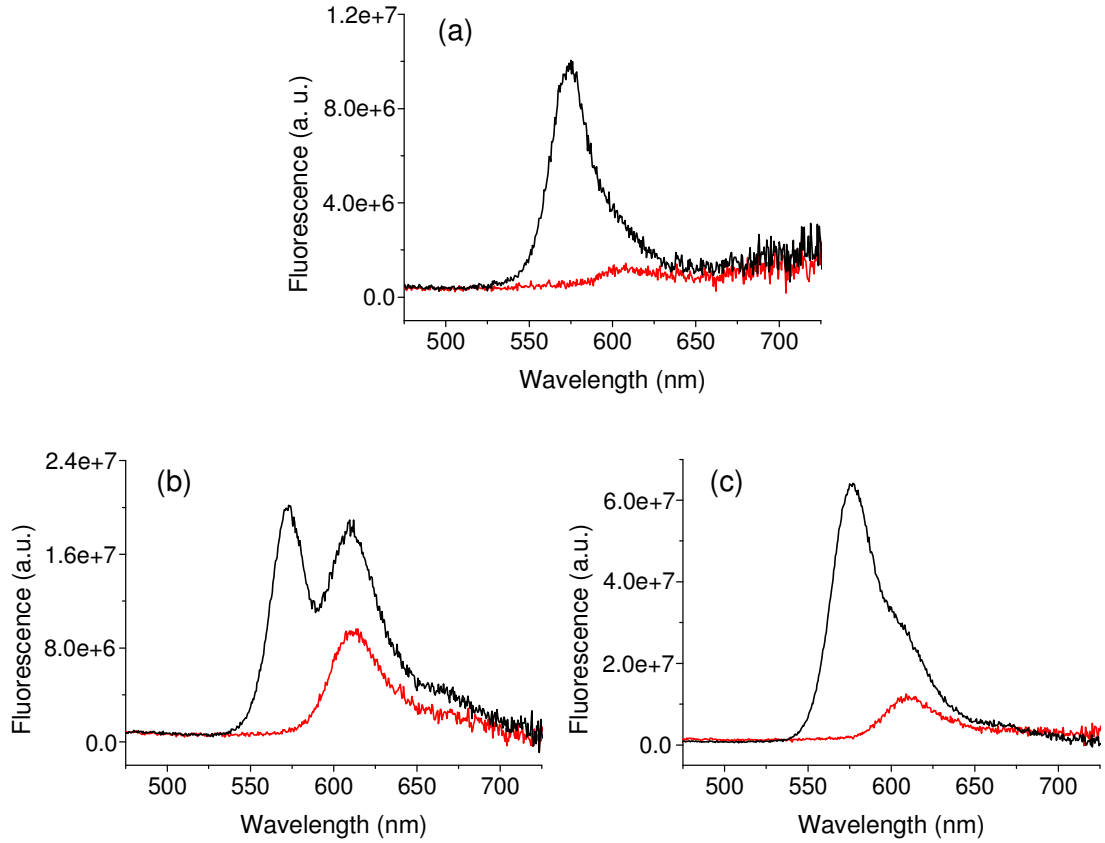

Figure 5.7: Typical fluorescence spectra of silica-dye particles (red), and silica-dye-particles coated with QDs (black), excited at 390 nm. Dye-silica shell thickness as calculated from added TEOS amount: (a) 4.5 nm, (b) 15.4 nm, and (c) 23.2 nm.

Figure 5.7 shows the typical fluorescence spectra of silica-dye particles and QD-silica-dye hybrid nanoparticles, respectively. An excitation wavelength of 390 nm was chosen, where the absorption of the dye should be negligible. Nevertheless, as shown in Figure 5.4 and Figure 5.5 (red curves), the silica-dye particles show some fluorescence if excited at 390 nm. Importantly, this fluorescence peak centred at λ = 615 nm is

increasing in intensity if the QDs are adsorbed at the silica particle surface, as can be seen in Figure 5.7 (black curves). The fluorescence spectra shown in Figure 5.7 therefore indicate energy transfer (FRET) from the QDs (= donors) to the organic dye molecules (= acceptors) within the silica shell. Furthermore, not only the absolute emission intensities of the QDs and the dye molecules increase with increasing silica-dye-shell thickness, but also the ratio of the two emission peaks changes with different silica-dye-shell thicknesses. However, the change in the ratio of the two emission peaks shows no trend since both the QD number and the dye amount increase with increasing shell thickness (detailed discussions about the increase of QD number with increasing shell thickness see sections 5.3.3.2 and 5.3.3.3). This demonstrates the concept for preparing a new dual-colour encoding sensor system with simple, tuneable optical properties: the ratio of the donor and acceptor fluorescence intensity can be tuned by adjusting the shell thickness.

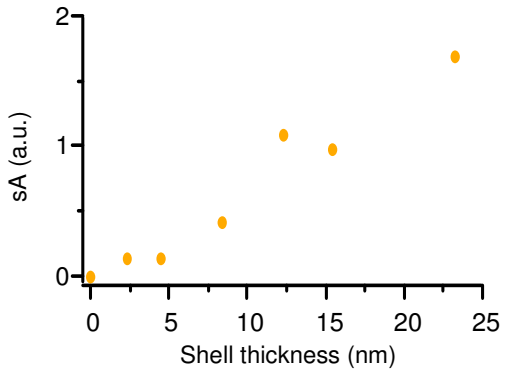

Figure 5.8: Sensitized acceptor fluorescence (*sA*) of QD-silica-dye hybrid particles versus dye-shell thickness. For the calculation, the emission spectra of the hybrid particles were deconvoluted and the contributions of the dyes were integrated and corrected for direct excitation of the dye molecules.

To quantify the enhancement in acceptor emission, the integrated fluorescence of the dye measured with ($A_{QD\text{-}silica\text{-}dye}$) and without ($A_{silica\text{-}dye}$) an adsorbed outer layer of QDs were compared for silica particles with dye-silica shell thickness varying from 2 to 24 nm (see Figure 5.7). The fluorescence of silica-dye particles without adsorbed QD layer, that is, without FRET, is considered as the background. The sensitized acceptor emission (*sA*) then is given by the difference of these two integrated intensities, that is:

$$sA = A_{QD\text{-}silica\text{-}dye} - A_{silica\text{-}dye} \tag{5.3}$$

Figure 5.8 shows the corresponding experimental results. As can be seen in Figure 5.8, the sensitized acceptor emission increases with increasing silica-dye-shell thickness. It remains an open question at this stage how the actual amount of donor particles influences these experimental results.

5.3.3.2 Monte-Carlo Simulations

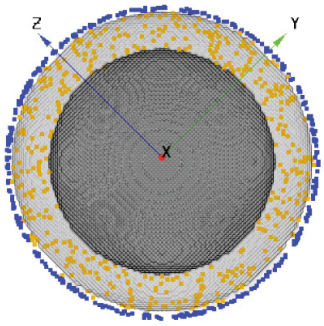

Figure 5.9: Model of the QD-silica-dye hybrid particles used for Monte-Carlo FRET simulations: silica core (dark grey), silica shell (light grey), QD (donor, blue), dye molecules (acceptor, orange).

To get a better understanding of the spectroscopic properties of the QD-silica-dye hybrid particles, Monte-Carlo simulations of the FRET processes were carried out with different models. This analysis was done by Dr. Wolfgang Erker. For simulations of energy transfer in QD-silica-dye hybrid particles, in agreement with the experimental results, the following model was assumed, as illustrated in Figure 5.9: A spherical core with a radius of 70 nm, which does not contain any fluorophores, is surrounded by a shell containing acceptor dye molecules (orange). Location (in the shell) and orientation of the dye molecules are randomly distributed and fixed. On the particle surface, QDs (blue) with a radius of 2.25 nm are attached. Again, location (on top of the shell) and orientation of the QDs are randomly distributed and fixed.

The overall transfer efficiency (E) of such multi-donor multi-acceptor systems can be calculated with equation 5.4 [170]:

$$E = 1 - \frac{1}{D}\sum_{i=1}^{D} \frac{1}{1 + \sum_{j=1}^{A}\left(\frac{R_{0,ij}}{r_{ij}}\right)^6} \tag{5.4}$$

where D is the total number of donors and A is the number of acceptors. Each donor acceptor pair was treated individually, with a specific distance r_{ij} between donor (i) and acceptor (j) and a specific Förster radius $R_{0,\,ij}$. The Förster radius was calculated with equation 5.2, using an individual orientation factor [169]:

$$\kappa_{ij}^2 = (\cos\vartheta_{ij} - 3 \cdot \cos\alpha_{ij} \cdot \cos\delta_{ij})^2 \tag{5.5}$$

where δ is the angle between the transition dipole moment of the donor and the vector joining the donor and the acceptor, α is the corresponding angle for the acceptor, and ϑ is the angle between the transition dipole moments of donor and acceptor. Also, it is taken into account that the QDs possess a two-dimensional degenerated emission transition dipole of the lowest excitonic transition which results in a dark axis and a bright plane [181]. For each donor acceptor pair, five donor emission dipole moments within the bright plane were created randomly and the corresponding orientation factors were calculated and averaged.

The sensitized acceptor emission (sA, see equation 5.3) is proportional to the reduction in the donor emission (ΔF) which is linked to the transfer efficiency (E) by [169] (see Figure 5.7):

$$E = 1 - \frac{F}{F_0} = \frac{\Delta F}{F_0} \tag{5.6}$$

where F and F_0 are the fluorescence integrated intensities of the donor in the presence and absence of the acceptor, respectively. F_0 is proportional to the number of the donor molecules (D). Hence, the sensitized acceptor emission is proportional to both the transfer efficiency and the number of donor molecules.

$$sA \propto \Delta F = E \cdot F_0 \propto E \cdot D \tag{5.7}$$

The models differ with respect to the amount of the surface-adsorbed QDs. In all cases, the dye molecules are homogeneously distributed in the silica-dye shell and therefore their number is proportional to the shell volume. Also, the QDs are only attached to the outer surface of the shell. Model 1 assumes a constant surface density, that is, the number of bound QD is proportional to the surface of the silica particles. Model 5 assumes an increasing surface density, that is, the number of bound QD is proportional to the volume of the shell. Models 2 - 4 are intermediates of the above two models: they

contain two contributions for the amount of adsorbed QDs, scaling with particle surface and silica-dye shell volume, respectively. The fractions of the volume contribution in models 2 - 4 are 25%, 50% and 75%, respectively. The sensitized acceptor emission was simulated for each model and compared to the experimental data.

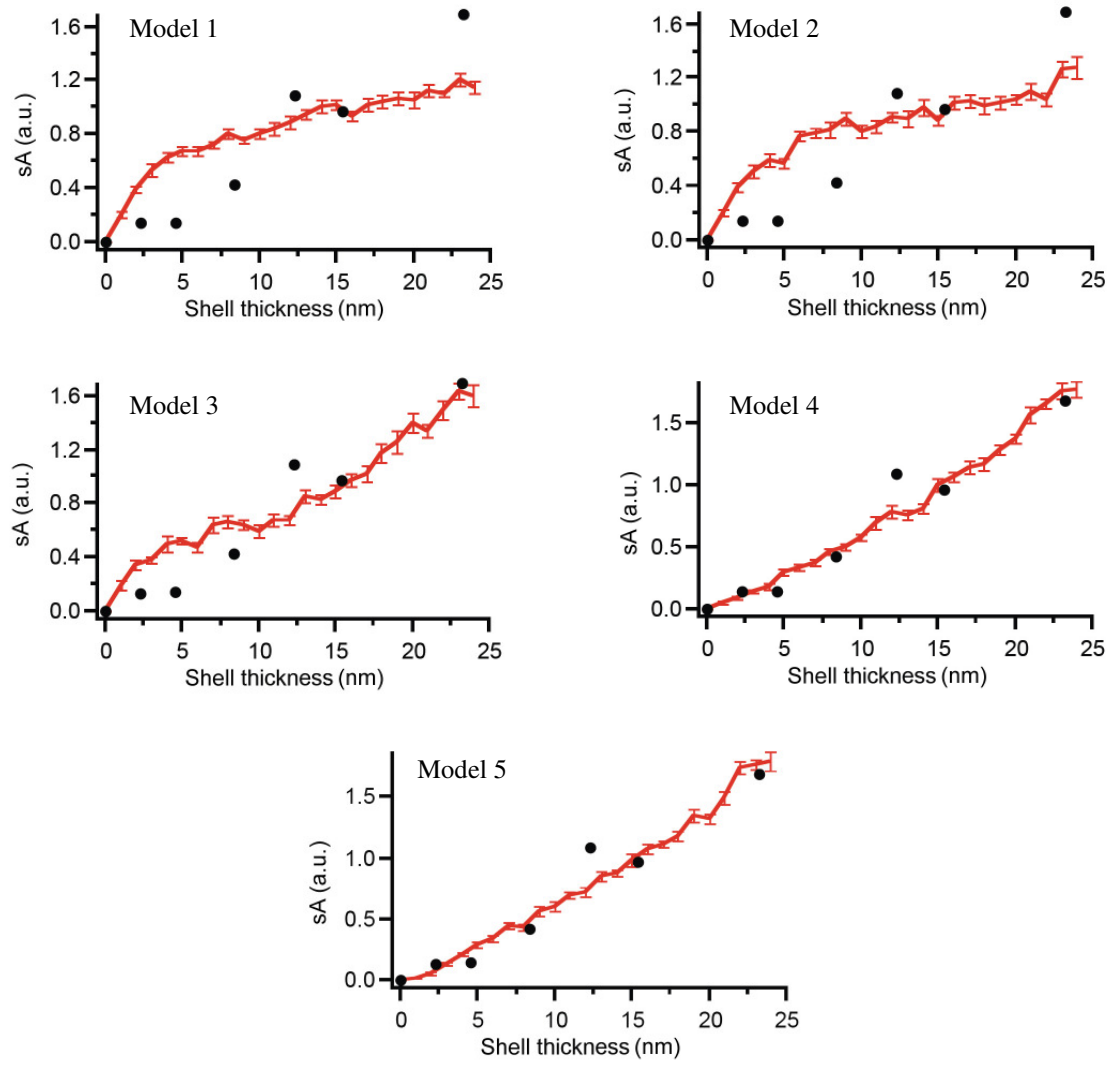

Figure 5.10: Monte-Carlo simulation of the sensitized acceptor emission of QD-silica-dye hybrid particles using models 1 - 5, respectively. In all models, the number of dye molecules per particle is calculated by multiplying the shell volume with 0.0003 / nm^3. The number of QD is the weighted sum of the surface contribution (the shell surface multiplied with 0.003 / nm^2) and volume contribution (the shell volume multiplied with 0.0003 / nm^3). The fractions of the volume contribution in models 1 - 5 are 0%, 25%, 50%, 75% and 100%, respectively. For each thickness, 10 particles were simulated and analyzed (average ± standard deviation of the average). Experimental data (black markers) are the same as shown in Figure 5.8.

As shown in Figure 5.10, models 1 and 2 reveal large deviations with respect to the experimental data. As the volume contribution increases, the models fit better and better. Models 4 and 5 give the best fittings to the experimental data. This suggests that in QD-silica-dye hybrid particles the number of bound QD does not (or only to a minor extent) depend, as expected, on the particle surface but significantly depends on the total amount of organic dye molecules contained within the silica-dye-shell. Based on the Monte-Carlo simulations of sensitized acceptor emission, attractive interactions between QDs and dye molecules are therefore predicted, causing a strong increase in the amount of adsorbed QD donors with increasing thickness of the acceptor dye containing silica shell.

5.3.3.3 Experimental determination of the amount of QDs adsorbed onto pure silica and onto silica-dye particles.

As a reference system, a series of pure silica particles corresponding in total diameter to the various silica-dye hybrid particles were prepared. These pure silica particles have been coated with an outer layer of adsorbed QDs to study both absorption and emission of QD-coated silica spheres in the absence of an acceptor dye.

As experimental crosscheck for the above predictions, the amounts of QDs bound to the pure silica particles and the dye-containing silica particles were determined, based on the absorption spectra. After subtraction of the strong scattering background from the absorption spectra of the QD-silica particles, QD absorption at 564 nm, i.e., the QD amount on pure silica particles could be determined, as shown in Figure 5.11 (hollow circles). Note that for the QD-silica particles "shell thickness" in Figure 5.11 corresponds to a nominal silica shell, the overall silica particle radius given as thickness plus "core" radius 70 nm. The data suggest a slight increase of the total QD amount with increasing particle size. Assuming that the QD amount (D) is proportional to the overall silica particle surface ($S_{QD\text{-}silica}$), the QD amount as a function of shell thickness is given by $D \propto S_{QD\text{-}silica} = 4\pi(R+d)^2$. This fitting (solid line) matches the data within experimental error, indicating a constant QD surface density in the case of the QD-silica particles.

The QD amount adsorbed to the surface of the silica-dye particles in dependence of dye-containing silica shell thickness was estimated as follows: the absorptions of the dye and dye + QD were obtained by subtracting the scattering background from the absorption spectra of the silica-dye particles and the QD-silica-dye particles, respectively. And next, after subtraction of the dye absorption from the dye + QD absorption, QD absorption could be determined (solid circles in Figure 5.11). With increasing shell thickness (or increasing particle size), the QD amount in the QD-silica-dye hybrid particles strongly increases compared to that in the QD-silica particles, suggesting that the presence of the dye in the particle shell has a positive influence on the QD binding affinity. In addition, the QD amount bound to the silica-dye particles is ~ 3 times of that on the QD-silica particles, where the QD amount is proportional to the surface. This is in agreement with the assumption in model 4 that the fraction of the surface contribution is 25%, considering the experimental error caused by the subtraction of the scattering background.

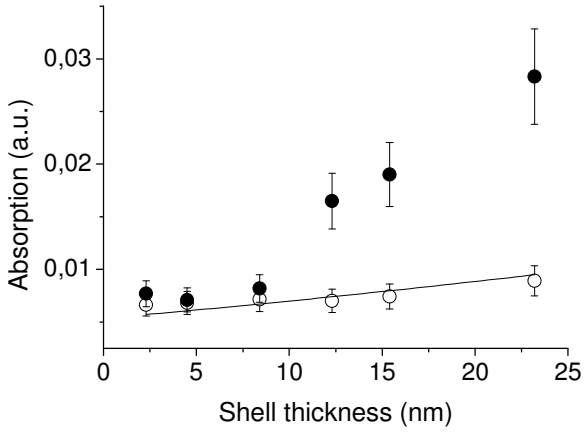

Figure 5.11: Amount of QD bound to dye-containing silica particles (solid circles) and pure silica particles (hollow circles) along with a fit assuming that the QD amount is proportional to the silica surface area.

The preferred attraction of PVP-coated QDs by the dye-containing silica shell is clearly visible also in comparison of TEM micrographs of silica particles and silica-dye particles, both with QDs adsorbed at the particle surface, as shown in Figure 5.12.

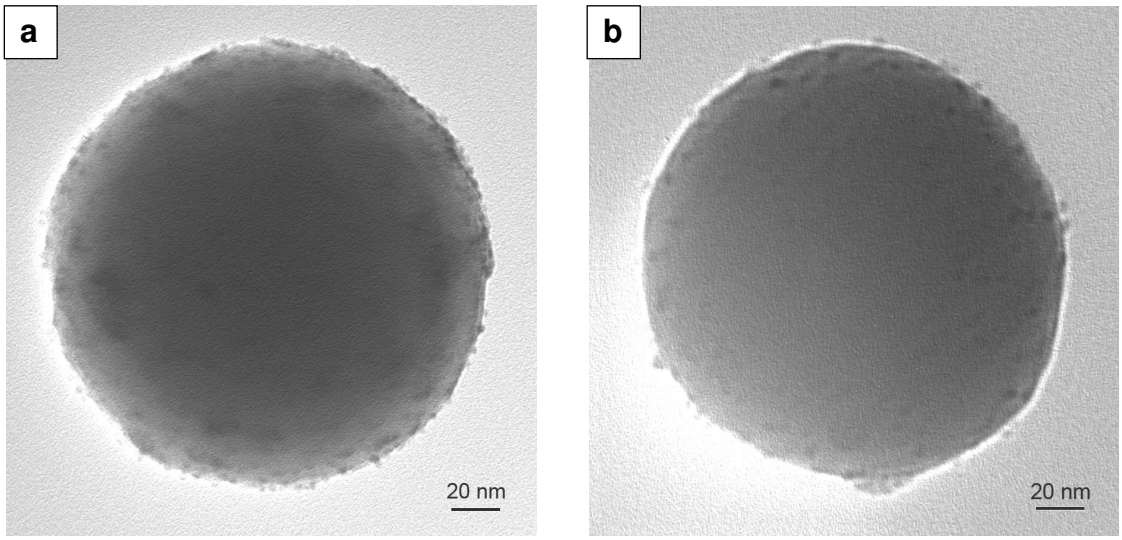

Figure 5.12: TEM micrographs of (a) silica-dye particles with shell thickness of 15.4 nm and (b) silica particles having the same size as the silica-dye particles, both with QDs adsorbed at the particle surface. The amount of the added QDs was ~ 1×10^{-8} mol (1730 QDs per single silica particle).

5.3.3.4 Attraction between QD and Texas Red molecules

To directly confirm the attraction between PVP-coated QDs and Texas Red (TR) dye molecules, further experiments were performed with both components freely dissolved in solution without any silica nanoparticles.

PVP-QD and TR dye at a molar ratio of 1:6 and PVP-QD and APS-TR conjugate at a molar ratio of 1:2 (PVP-QD concentration: 1.19×10^{-7} M), respectively, were mixed in ethanol, and fluorescence spectra were recorded (Figure 5.13). Subsequently, the samples were diluted (1:2) several times by adding ethanol and at each dilution step emission spectra were recorded again. All spectra were normalized and compared to a theoretical spectrum which is expected in the absence of FRET (yellow). The theoretical "no FRET" spectrum is a superposition of the PVP-QD (blue) and the dye spectrum (red), weighted with the corresponding ratio mentioned above (1:6 for the mixture of PVP-QD and TR dye, and 1:2 for the mixture of PVP-QD and APS-TR conjugate). If there is no interaction (no FRET) between PVP-QD and dye, the shape of the emission spectra of the mixtures therefore should match the shape of the yellow curve.

Obviously, all spectra of the QD-dye mixtures (black) clearly reveal a peak or shoulder around 600 nm indicating FRET from PVP-QD to the TR dye or the APS-TR conjugate.

The dilution series spans a QD concentration range from 120 nM down to 15 nM. Because these concentrations are very low and thereby the average inter particle distances are too large for dynamic quenching, FRET is a strong indication for QD-dye complex formation due to mutual attraction. For comparison, a PDI dye (structure see Table 3.2) was also mixed with PVP-QD. The spectra of the QD-PDI mixtures match the theoretical "no FRET" spectrum, implying that there is no attractive interaction between PVP-QD and PDI dye.

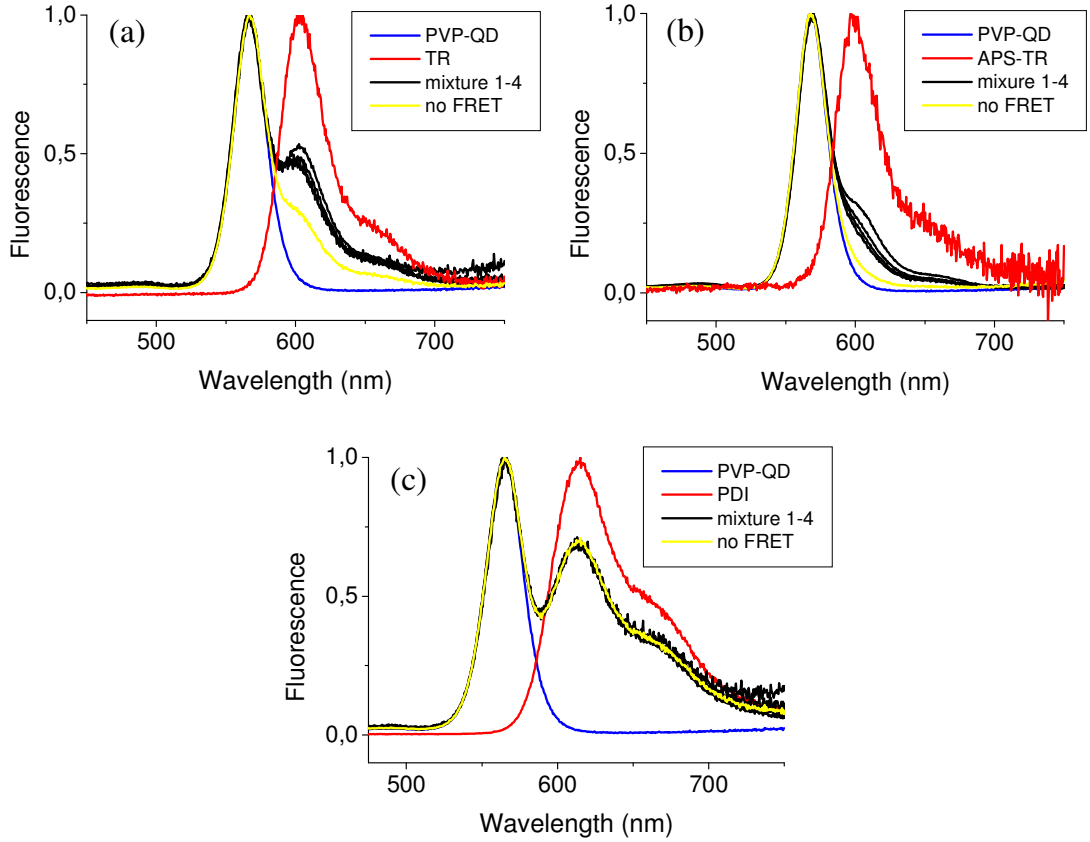

Figure 5.13: (a) Fluorescence spectra of PVP-coated QDs and Texas Red (1:6) in ethanol. Four mixtures were investigated (mixture 1-4) starting with a molar ration PVP-QD: TR of 1:6. Mixtures 2-4 were obtained by subsequent dilution steps (1:2 each). (b) Fluorescence spectra of PVP-coated QDs and APS-Texas Red conjugate (1:2) in ethanol. Four mixtures were investigated (mixture 1-4) starting with a molar ration PVP-QD: APS-TR of 1:2. Mixtures 2-4 were obtained by subsequent dilution steps (1:2 each). (c) Fluorescence spectra of PVP-coated QDs and PDI (1:12) in ethanol. Four mixtures were investigated (mixture 1-4) starting with a molar ration PVP-QD: PDI of 1:12. Mixtures 2-4 were obtained by subsequent dilution steps (1:2 each). All spectra were normalized. The excitation wavelength was 390 nm. Additionally, in each plot there is a theoretical spectrum (yellow) which is a superposition of the blue and red curve, weighted with the corresponding ratio, also normalized. The shape of the yellow curve is expected in the no FRET case.

5.4 Conclusion

The synthesis and characterization of supramolecular nanoparticles potentially useful for multicolour encoding, namely monodisperse Stöber silica particles of radius 70 nm with an outer silica layer of thicknesses 2 - 24 nm containing organic dye molecules Texas Red, and surface-adsorbed multishell CdSe/CdS/ZnS QDs, have been described in this chapter. The QDs serve as donors and transfer excitation energy to the organic dye acceptors, leading to two fluorescence emission peaks of donor and acceptor, respectively, which both are excited at the same wavelength. Modifying the architecture of these particles, by controlling the thickness of the dye-containing silica shell, one can tune the intensity ratio of these two emission peaks and thereby prepare a whole set of different optical codes. The experimentally determined enhanced acceptor emission for particles of varying silica-dye-shell thickness was compared with numerical FRET calculations to extract the surface concentration of QDs, while assuming a constant dye concentration within the shell as deduced from the absorption and emission spectra of silica-dye particles without adsorbed QDs. This comparison resulted in the observation that a strong increase in the number of QDs adsorbed to the particle surface occurs with increasing dye-silica shell thickness. The latter finding was confirmed by control experiments, suggesting the existence of attractive interactions between PVP-coated QDs and Texas Red.

The QD-silica-dye hybrid system could be used as a new type of multiplexing label [171, 172, 173, 174], that is, a sensor particle useful for multicolour detection with one excitation wavelength. Using different organic dyes only, the multiplexing approach is limited to three colors because of spectral overlapping [175]. Due to their broad absorption but narrow emission, and hence reduced spectral overlap, QDs of 5 - 6 different colors all excitable with the same wavelength can be incorporated into one given silica particle to yield a suitable multiplexing label [176]. In the QD-silica-dye hybrid system, combining QDs with suitable dye molecules within one silica nanoparticle, which allows for FRET, and arranging these two species within well-defined distances by varying the thickness of the dye-containing silica shell could further enhance the number of detectable colors and respective intensities. This may lead to a new multiplexing scheme which could “barcode” biomolecules with a very high number of possible spectral signals.

6 Quantum dot - dye hybrid system

6.1 Introduction

In recent years, a number of approaches to prepare QD-dye conjugates in solution have been developed. In early experiments, diazaperylene dye molecules with a bipyridyl group exchanged the organic ligands (TOPO) on the surface of CdSe/ZnS QDs to form the QD-dye complexes [109]. However, the strong QD emission quenching was suggested to be caused by electron transfer. Similarly, nanoassemblies of CdSe/ZnS QD and pyridyl-substituted free-base porphyrin molecules were formed using pyridyl moieties as anchors [177]. Due to the small spectral overlap and the limited number of "vacancies" accessible for dye attachment existing on the QD surface, the energy transfer efficiency was very low. Moreover, the binding of the pyridyl group to the QD surface was not strong and the formed complexes were not very stable. More reliable protocols have been developed in which attachment of dye to QD was mediated by an additional component such as proteins [25, 26], peptides [27, 28], or polymers [18, 24]. Other approaches used interdigitization of alkylamino chains of phthalocyamines (Pc's) into the alkyl-capping layer of QDs to form QD-dye conjugate. A non-Förster-type energy transfer behavior was observed by studying the effect of the donor-acceptor linker chain length on the energy transfer efficiency [41].

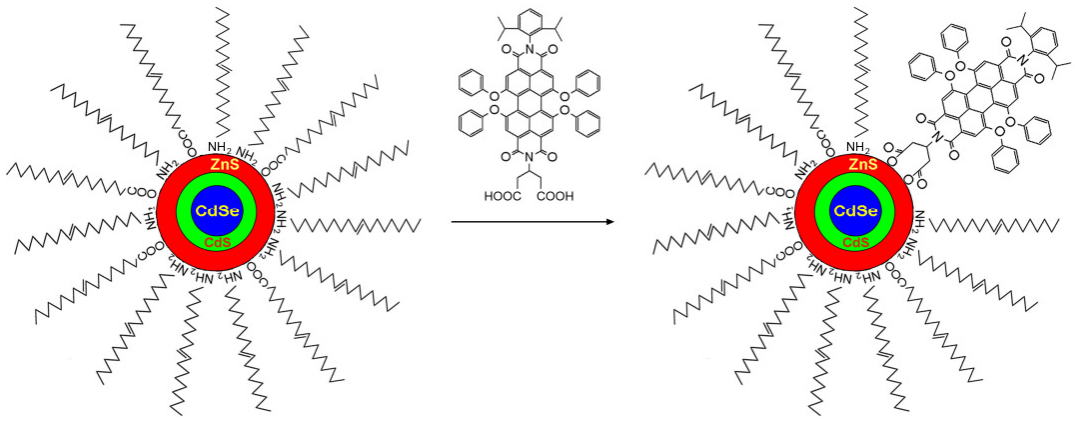

Figure 6.1: Schematic illustration of the formation of the QD-dye complexes.

In this work, a versatile approach to extraordinarily stable QD-dye hybrids has been developed, which uses dicarboxylate anchors to bind ryleneimide dyes to QD. Bidentate

ligands, such as thiol-based [116, 178], phosphine oxide-based [179] and carboxylate-based [180] bidentate ligands, have been reported to be significantly more stable than a single-bonding site. Dicarboxylate groups in ryleneimide dyes were used as the anchoring groups to replace the organic oleyamine and oleic acid ligands on QDs and then form QD-dye complexes, as illustrated in Figure 6.1. This system provides a good basis to study the energy transfer between QD and dye because of its simple and compact design: there is no third kind of molecule linking QD and dye (no spacer), and the affinity of the functional group to the QD surface is strong. Moreover, this system allows control of the donor-acceptor separation distance by varying the QD-dye distance with the number of ZnS monolayers. Due to the high stability, the QD-dye complexes can also be transferred into water. In addition, preliminary experiments were done to link QDs with dye molecules having two dicarboxylate groups at two ends of the dye molecule. The approach that uses the dicarboxylate group as the binding anchor to QDs can not only apply to dye molecules but also other organic molecules. As an example, the QDs have been complexed with calixarene molecules and the QD-calixarene complexes also have potential for QD-based energy transfer study. It should be noted that the molar ratios of dye to QD mentioned in this chapter are all nominal ratios, because the concentration of CdSe cores, accordingly the concentration of core-shell QDs, can not be precisely calculated, as discussed in Chapter 3.2.1.

6.2 Quantum dot - dye hybrids in non-aqueous solution

6.2.1 Experimental procedure

Different kinds of QDs including CdSe QDs, CdSe/CdS QDs, CdSe/ZnS QDs and CdSe/CdS/ZnS QDs were prepared as described in Chapter 3.2.1. Dye molecules used were supplied by the workgroup of Prof. Dr. Klaus Müllen (Max Planck Institute for Polymer Research, Mainz, Germany). The structures of the dyes are shown in Figure 6.2.

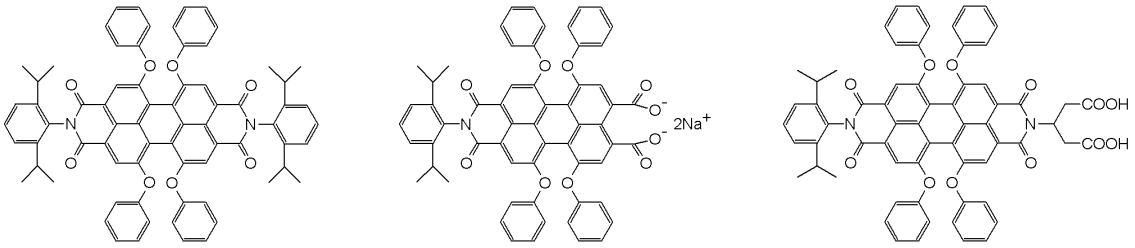

PDI PMIMA PDIDC

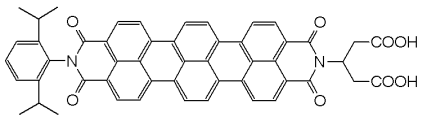

TDIDC

Figure 6.2: Structures of dyes used for preparing QD-dye complexes in organic solution.

Complexes of QDs and dyes were prepared by mixing 2.5 ml of a chloroform solution of QD (concentration ≈ 2 μM) with 2.5 ml of a methanol solution of dye (concentration ≈ 0.5 - 10 μM). Much excess of K_2CO_3 methanol solution (100 μL, 32 mM) was added; the base/dye molar ratio, for instance in the case of using 10 μM dye, was 128. The mixture was then sonicated for 4 h. The resulting solutions were slightly turbid. In order to precipitate the QD-dye complexes, 5 mL of methanol was added and the resulting solution was centrifuged. After decanting the supernatant, the complexes were redispersed in chloroform. Then a purification procedure was carried out: methanol was added to the complex solution until the solution became turbid. The complex particles were precipitated by methanol, while the unattached dye molecules were still dissolved in methanol. After centrifugation, the supernatant containing the unattached dye

molecules was removed. The precipitate was then redispersed in chloroform, leading to a clear solution.

6.2.2 Results and discussion

6.2.2.1 Characterization of QD-dye complexes

A. Absorption and fluorescence measurements

CdSe/CdS/ZnS QDs can be complexed with different kinds of dyes including peryleneimide and terryleneimide derivatives. Table 6.1 lists the properties of the used dyes. CdSe/1ML CdS/3ML ZnS QDs were used to complex with peryleneimide dyes (PMIMA and PDIDC), and CdSe/4ML CdS/1ML ZnS QDs with red-shifted emission were used for QD-terryleneimide dye (TDIDC) complex to get effective spectral overlap. Figure 6.3 shows the normalized absorption and fluorescence spectra of the QDs, different dyes and their complexes. The excitation wavelength of the complex fluorescence spectra was selected at 390 nm, where the absorption is strong for the QDs and weak for all the dyes, in order to reduce the contribution from direct excitation of the dye acceptor.

Table 6.1: Properties of the used peryleneimide and terryleneimide dyes.

	PMIMA	PDIDC	TDIDC
λ_{abs} (nm)	545	577	654
λ_{em} (nm)	593	610	668
Φ_f	0.81[a]	0.96[a]	0.33[b]
ε (cm^{-1} M^{-1})	23500	37000	52500

* λ_{abs} and λ_{em} are the main absorption and emission peak, respectively. All the spectra were measured in chloroform. Φ_f is the quantum yield of the dyes. The reference used to calculate Φ_f was [a] cresyl violet for PMIMA and PDIDC, and [b] ATTO 647N for TDIDC. ε is the extinction coefficient at λ_{abs}.

As shown in Figure 6.3, both absorption and emission spectra of all QD-dye complexes after purification show the peaks corresponding to the absorption and emission from the QD and the dye, respectively. Since the free dyes have been removed by purification, the dye emission must result from the dye molecules attached to the QDs. This clearly

confirms the presence of QD and dye in the final solution and proves the chemical attachment of the dye molecules to the QDs.

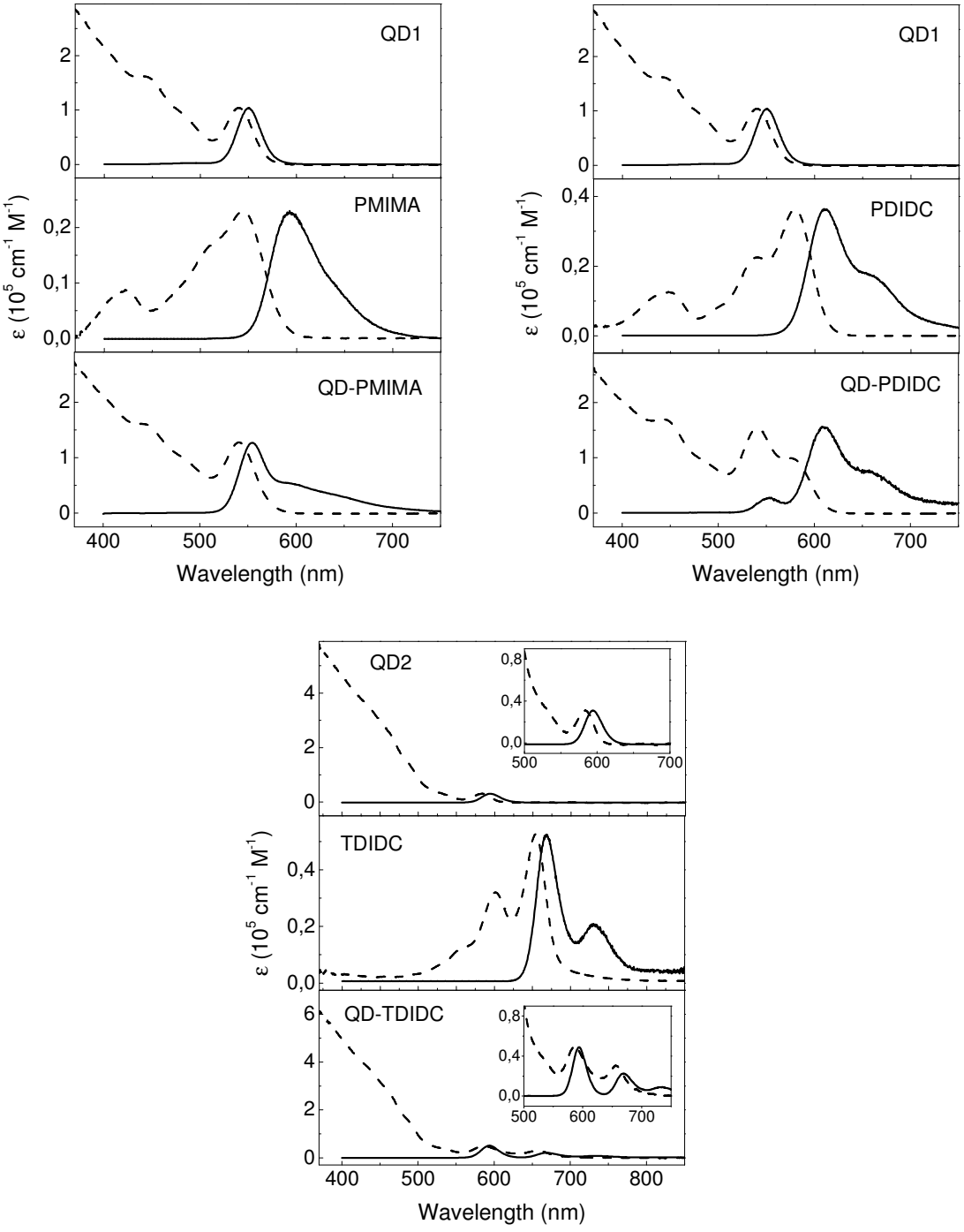

Figure 6.3: Absorption (dash line) and fluorescence (solid line) spectra of QDs, dyes and their corresponding complexes in chloroform. QD1 is CdSe/1ML CdS/3ML ZnS and QD2 is CdSe/4ML CdS/1ML ZnS. For all QD-dye complexes, the nominal molar ratio of dye/QD = 2. In all cases, the excitation wavelength was 390 nm.

Figure 6.3 also illustrates that there is a strong spectral overlap between QD emission and the absorption of each of the dyes. The spectral overlap integral J (nm^4 M^{-1} cm^{-1}) is 1.67×10^{15} for the QD1-PMIMA pair, 2.38×10^{15} for the QD1-PDIDC pair, and 3.37×10^{15} for the QD2-TDIDC pair. Therefore, QDs can act as donor and dyes as acceptor in a fluorescence resonance energy transfer (FRET) process. In the fluorescence spectra of all QD-dye complexes, the contribution due to direct excitation of the dye has been subtracted. Therefore, the emission from the dye in Figure 6.3 is only caused by the energy transfer within the QD-dye complexes. Figure 6.4 shows the fluorescence spectra of the QD-PDIDC complexes (free dye molecules have been removed) before and after subtraction of the contribution due to direct excitation of the PDIDC dye. The control spectrum of the pure PDIDC dye was recorded at the excitation wavelength of 390 nm (red curve). The concentration of the pure PDIDC is the same as the PDIDC concentration in the QD-PDIDC complexes. As can be seen, the pure PDIDC dye only shows very weak emission (red curve) compared to the dye emission in the complexes (blue curve).

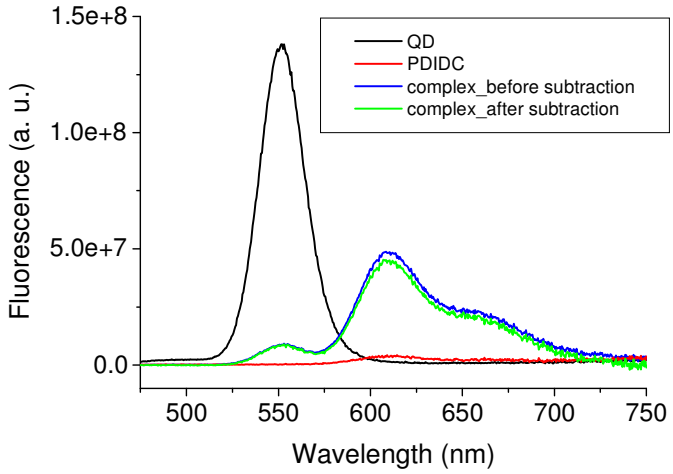

Figure 6.4: Fluorescence spectra of QD (CdSe/1ML CdS/3ML ZnS), PDIDC dye and their complexes before and after subtraction of the contribution due to direct excitation of the PDIDC dye. The nominal molar ratio of PDIDC/QD = 2. The excitation wavelength was 390 nm.

Energy transfer between QDs and different dyes will be discussed in the following section.

B. TEM measurement

Figure 6.5 shows the TEM images of QD-PDIDC and QD-TDIDC complexes. The diameter of the QD particles before complex formation with dyes is 4 - 5 nm for the peryleneimide dyes and 6 - 7 nm for the terryleneimide dye. As can be seen in Figure 6.5, the size of the QD particles does not change before and after complex formation, and more importantly, no aggregates are formed during the preparation of the QD-dye complexes.

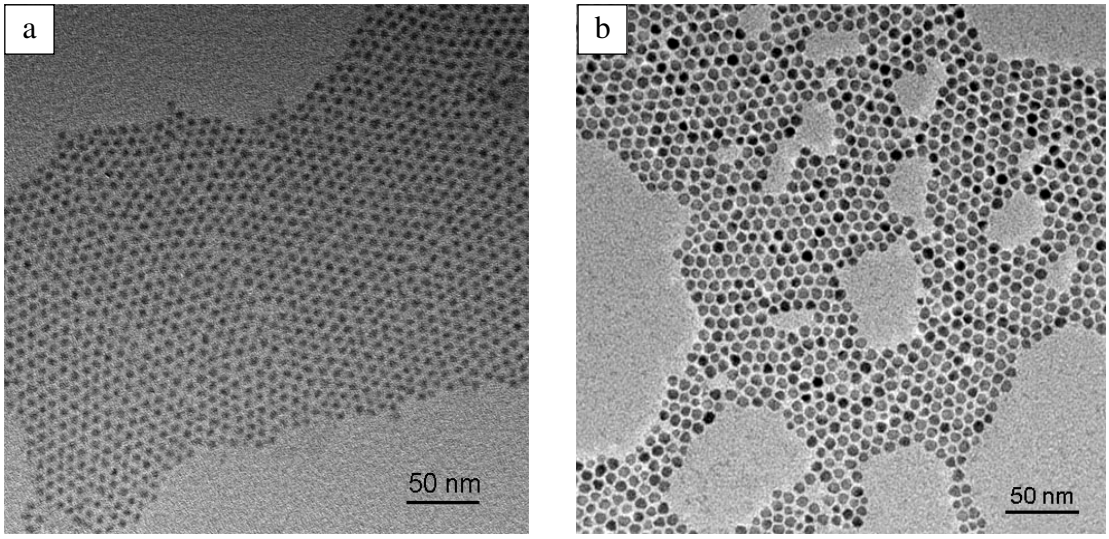

Figure 6.5: TEM images of (a) QD-PDIDC complexes and (b) QD-TDIDC complexes.

6.2.2.2 Study of binding mechanism and reaction conditions

A. Binding anchor

In order to clarify the binding mechanism for the QD-dye complexes, PDI dye was used in comparison. PDI is the starting material for preparing PMIMA and PDIDC, and it has nearly the same absorption and emission spectra as PDIDC (Figure 6.6). The main difference between PDI and PDIDC is that there is no functional group (= dicarboxylate group) in the PDI structure. As can be seen in Figure 6.6, using PDI and going through exactly the same synthesis and purification procedure, the final spectra show neither dye absorption nor emission, which indicates that all added PDI has been removed after the purification steps and no complex is formed with PDI. This result strongly suggests that PMIMA, PDIDC and TDIDC bind specifically via their dicarboxylate groups to QDs, while non-specific binding of PDI does not occur.

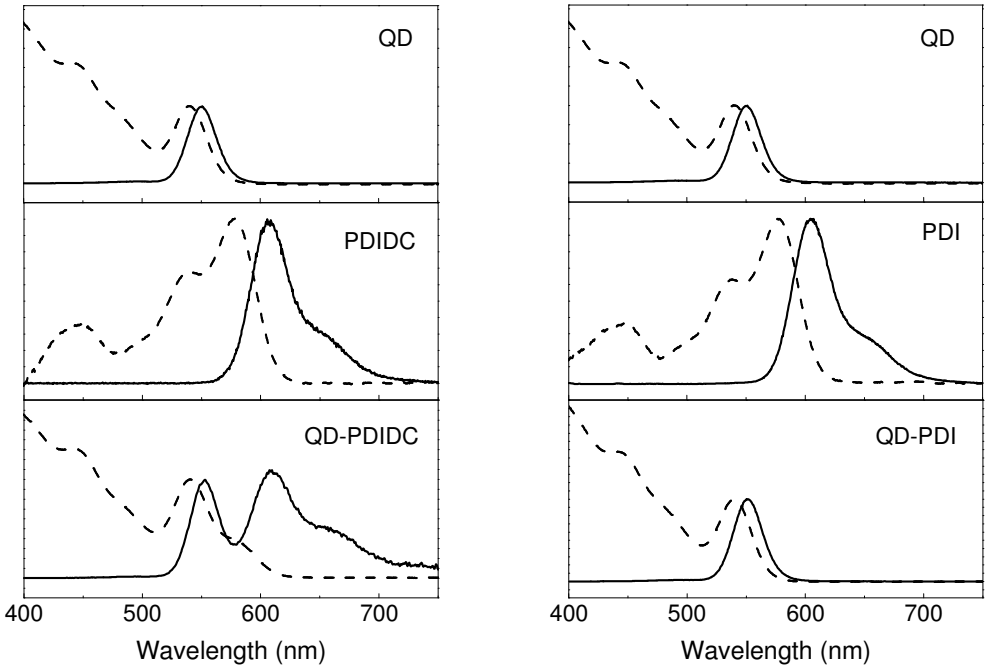

Figure 6.6: Normalized absorption (dash line) and fluorescence (solid line) spectra of QD, PDIDC (left) and PDI (right), and their corresponding complexes. QD is CdSe/1ML CdS/3ML ZnS. The nominal molar ratio of dye/QD = 1. In all cases, the solvent was chloroform. The excitation wavelength was 390 nm.

B. Variation of QD surface

To check if the dicarboxylate group can also bind to other QD surfaces, CdSe and CdSe/2ML CdS QDs were used to prepare complexes with PDIDC dye. In both cases, the nominal dye/QD molar ratio was 1. As shown in Figure 6.7, both absorption and emission spectra confirm the presence of QDs and dye in the final solution after purification. It should be noted that the organic ligands on CdSe QDs are TOPO, for CdSe/CdS and CdSe/CdS/ZnS QDs are oleic acid and oleylamine. The formation of the QD-dye complexes using CdSe, CdSe/CdS and CdSe/CdS/ZnS QDs implies that the dicarboxylate group on the dye molecules is capable of replacing different kinds of organic ligands on QDs. Furthermore, using CdSe/CdS/ZnS QDs capped with only oleic acid ligands rather than QDs capped with both oleylamine and oleic acid ligands, QD-PDIDC complexes were also formed. This indicates that the dicarboxylate groups replace the monocarboxylate groups on the QD surface, and also proves that bidentate ligands have stronger binding strength than a single binding site. Therefore, it is

concluded that the dicarboxylate group is an anchor which binds dyes to QDs with a ZnS (e.g. CdSe/CdS/ZnS and CdSe/ZnS), CdSe or CdS surface (e.g. CdSe/CdS).

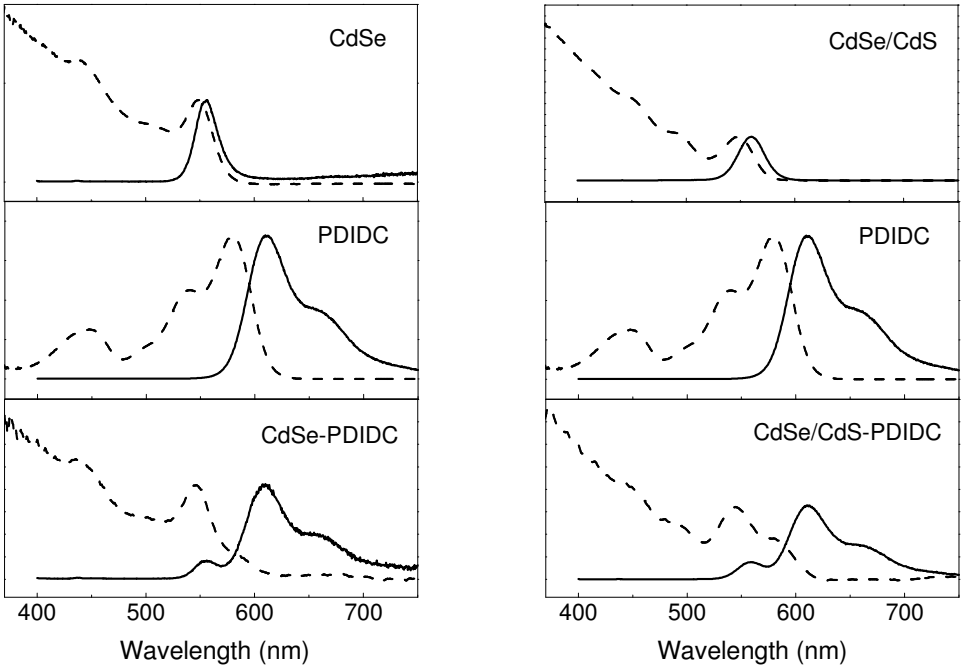

Figure 6.7: Normalized absorption (dash line) and fluorescence (solid line) spectra of CdSe (left) and CdSe/2ML CdS (right), PDIDC and their corresponding complexes. The nominal molar ratio of dye/QD = 1. In all cases, the solvent was chloroform. The excitation wavelength was 390 nm.

To estimate the binding model, the distance between two Zn atoms on the QD surface and the distances between different atoms of the dicarboxylate group on the PDIDC dye were roughly determined. The distance between two Zn atoms was calculated according to the single unit cell of ZnS zinc blende structure (Figure 6.8 a) with the lattice constant of 5.406 Å. The distances between different atoms of the dicarboxylate group (Figure 6.8 b) were obtained based on 3D optimization algorithm using software ACD/ChemSketch 5.11. Two possible binding models are shown in Figure 6.8 c and d. Since the distance between two carboxylate groups (2.4 Å) is smaller than the distance between two Zn atoms (3.8 Å), the model shown in Figure 6.8 c is probably energetically unfavorable. Therefore, a chelate type binding of the bidentate anchors in peryleneimide and terryleneimide dyes to Zn^{2+} or Cd^{2+} ions on the QD surface is proposed (Figure 6.8 d).

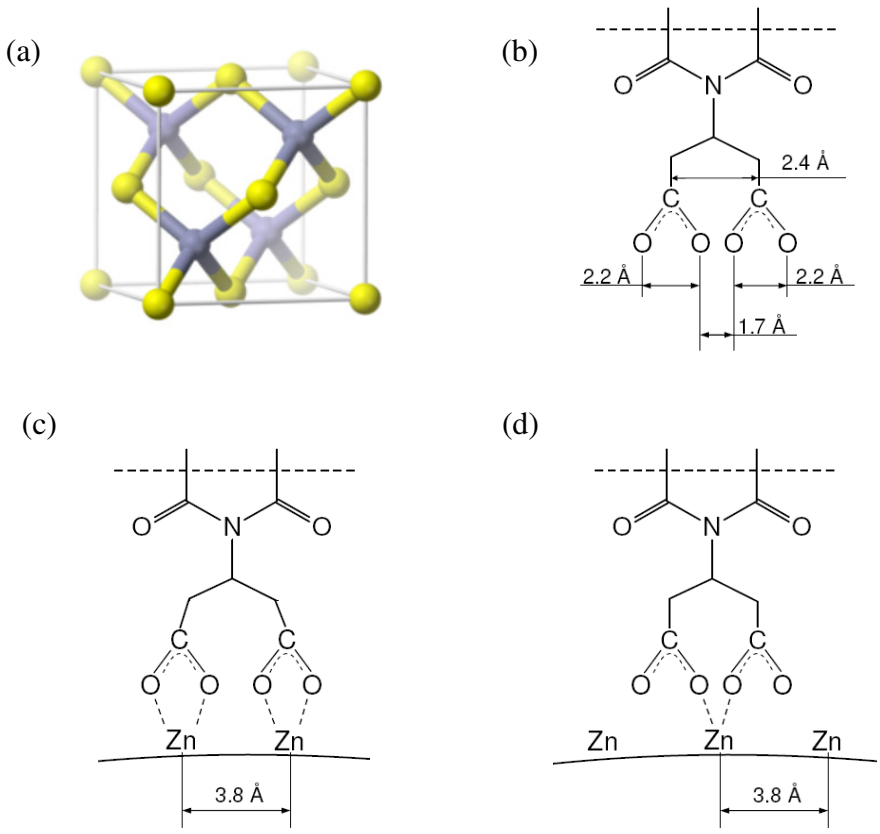

Figure 6.8: (a) A single unit cell of ZnS zinc blende structure (Zn atom: blue, S atom: yellow), and schematic diagrams of (b) distances between different atoms of the dicarboxylate group on PDIDC and (c, d) two possible binding models.

The quenching efficiencies of different QD-PDIDC complexes were preliminarily compared. Figure 6.9 shows the fluorescence spectra of the CdSe, CdSe/2ML CdS and CdSe/1ML CdS/3ML ZnS QDs and their corresponding complexes. The quenching efficiency (Φ_f) is estimated by $1 - F/F_0$, where F is the integrated fluorescence intensity of the QDs in the presence of PDIDC, and F_0 is that of the QDs in the absence of PDIDC. The results are listed in Table 6.2.

The quenching of QD emission in the CdSe/CdS/ZnS-PDIDC complexes had been proven to be caused dominantly by Förster energy transfer (see discussions in section 6.2.2.4 and 6.2.2.5). According to Förster theory, the energy transfer efficiency (E) is strongly dependent on donor-acceptor distance (r) and Förster distance (R_0) [5]

$$E = \frac{1}{1 + (r / R_0)^6} \tag{6.1}$$

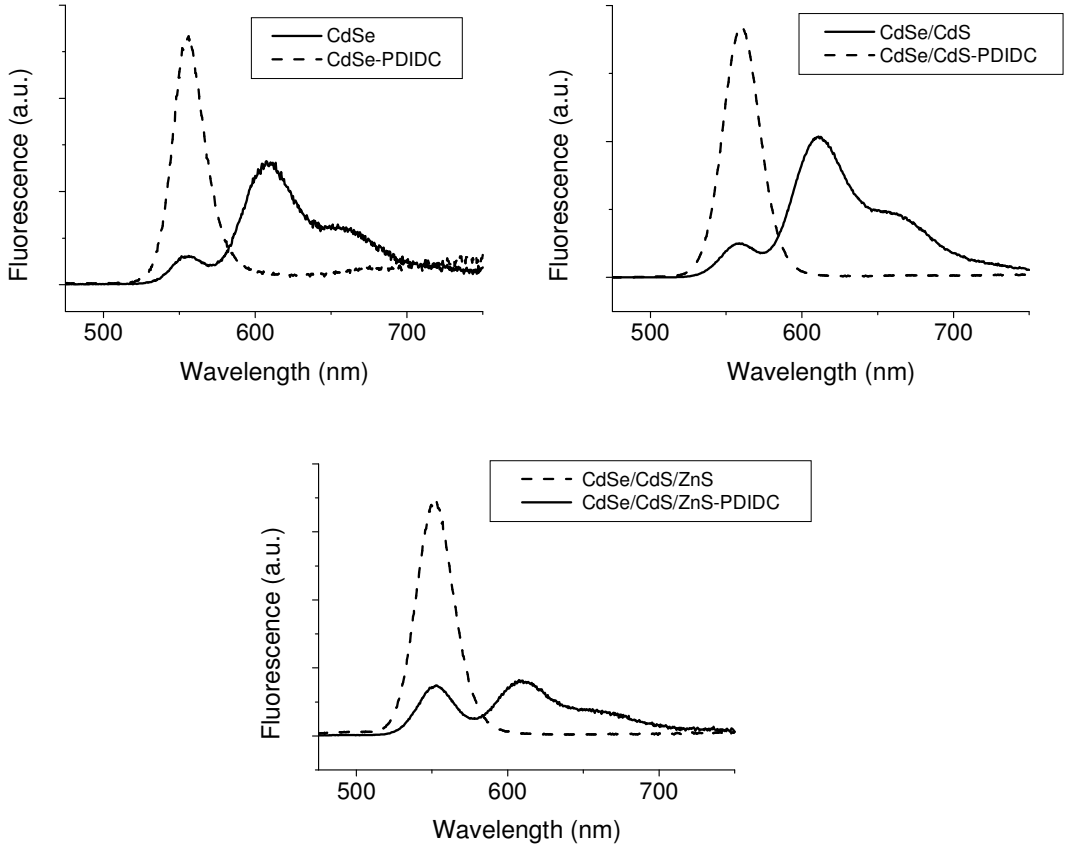

Figure 6.9: Fluorescence spectra of CdSe, CdSe/2ML CdS and CdSe/1ML CdS/3ML ZnS QDs, and their corresponding complexes. The nominal molar ratio of dye/QD = 1. In all cases, the solvent was chloroform. The excitation wavelength was 390 nm.

The center-to-center distance between QD and dye (r) was calculated considering that the size of the PDIDC dye is ~ 2 nm. The Förster radius (R_0) is calculated by

$$R_0 = 0.211(\kappa^2 n^{-4} \Phi_D J(\lambda))^{1/6} \tag{6.2}$$

where the refractive index of the solvent (chloroform) n is 1.445, Φ_D is the quantum yield of the QDs and $J(\lambda)$ is the spectral overlap integral between the donor emission and the acceptor absorption. The orientation factor κ^2 was determined by assuming the binding model given in Figure 6.1. The transition dipole of the S_0-S_1 transition of the dye is parallel to the QD-dye connecting vector and fixed. QD possess a two-dimensional degenerated emission transition dipole of the lowest excitonic transition [181]. Provided the dyes are randomly distributed on the QD surface, the donor (QD) emission transition dipole is randomly orientated with respect to the donor-acceptor connecting vector. The orientation factor was evaluated by a Monte-Carlo simulation and a value of κ^2 = 4/3 was obtained. The calculation of the orientation factor κ^2 was

done by Dr. Wolfgang Erker. Table 6.2 also lists the properties of the different QDs and the calculated r and R_0 values of their corresponding QD-PDIDC pairs.

Table 6.2: Properties of different QDs and their corresponding complexes.

	CdSe	CdSe/2ML CdS	CdSe/1ML CdS/3 ML ZnS
λ_{abs} (nm)	548	545	539
λ_{em} (nm)	556	560	552
Φ_D	0.06	0.36	0.38
d (nm)	3.0	4.4	4.5
	CdSe-PDIDC	CdSe/CdS-PDIDC	CdSe/CdS/ZnS-PDIDC
r (nm)	2.50	3.20	3.25
J ($nm^4\,M^{-1}\,cm^{-1}$)	1.89×10^{15}	2.57×10^{15}	2.38×10^{15}
R_0 (nm)	3.80	5.40	5.39
r / R_0	0.66	0.59	0.60
Φ_f	0.88	0.85	0.77

* λ_{abs} and λ_{em} are the absorption and emission peak, respectively. All the spectra were measured in chloroform. Φ_D is the quantum yield of the QDs. d is the diameter of the QDs. r is the distance between QD and dye. J is the spectral overlap integral. R_0 is the Förster radius. Φ_f is the quenching efficiency. The calculation of the R_0 and Φ_f is described in the text.

As shown in Table 6.2, the CdSe-PDIDC pair has a higher r/R_0 value than the CdSe/CdS/ZnS-PDIDC pair, and the CdSe/CdS-PDIDC pair has a similar r/R_0 value to the CdSe/CdS/ZnS-PDIDC pair. According to equation 6.1, the energy transfer efficiency of the CdSe-PDIDC complexes should be lower than that of the CdSe/CdS/ZnS-PDIDC complexes; the CdSe/CdS-PDIDC and CdSe/CdS/ZnS-PDIDC complexes should have similar energy transfer efficiencies. However, the quenching efficiencies of both the CdSe-PDIDC and CdSe/CdS-PDIDC complexes are higher than the energy transfer efficiency of the CdSe/CdS/ZnS-PDIDC complexes. Therefore, the QD quenching in the CdSe-PDIDC and CdSe/CdS-PDIDC complexes results from not only energy transfer but also other quenching pathways. Boulesbaa et al. demonstrated

ultrafast electron transfer from CdSe and CdS QDs to adsorbed rhodamine B molecules [182, 183]. It is possible that electron transfer is also a quenching pathway in the CdSe-PDIDC and CdSe/CdS-PDIDC complexes. Besides, for CdSe QDs, the increase in quenching efficiency was also observed by Dayal et al. [38], which is explained by the involvement of low-energy surface states involved in the energy transfer from CdSe QDs to the energy acceptor, while these surface states are passivated by the coated inorganic layers in CdS- or ZnS-capped QDs.

C. Optimization of reaction conditions

To optimize the synthetic route, the influence of different reaction conditions on QD-dye complex formation was investigated. CdSe/1ML CdS/3ML ZnS QDs and peryleneimide dyes (both PMIMA and PDIDC) were used under different reaction conditions. In both cases, the nominal ratio of dye/QD was 1. Table 6.3 lists the four different reaction conditions and the results are shown in Figure 6.10. Under all reaction conditions, the precipitation and purification procedures (see section 6.2.1) were carried out to remove dye molecules that were not bound to QDs.

Under condition 1, QDs and dye molecules were simply mixed in chloroform. The particles in the mixture were then precipitated, purified and redispersed in chloroform. As shown in Figure 6.10 - 1, the emission spectra of the samples (red curves) show no change in comparison to the emission spectra of the pure QDs (black curves). This indicates that the dyes are not bound to the QDs, and QD-dye complexes are not formed in the mixtures.

Under condition 2, QDs and dye molecules were mixed in basic condition (pH = 11). After the precipitation and purification steps, the emission spectra of the samples show the dye emission and the quenched QD emission (Figure 6.10 - 2). Since the unattached dye molecules have been removed by the precipitation and purification steps, the dye emission must result form the dye bound to the QDs. Comparing condition 1 with 2, it's concluded that the QD-dye complexes can be formed only under basic condition. The carboxylic acid group in the dyes has to be deprotonated and changed to carboxylate groups for replacing the organic ligand on the QD surface. Otherwise, the dyes can not be attached to the QDs.

Table 6.3: Different reaction conditions for QD-dye complex preparation.

	1	2	3	4
solvent	$CHCl_3$	$CHCl_3$	$CHCl_3$	$CHCl_3$/MeOH
base	–	+	+	+
sonication	–	–	+	+
precipitation and purification	+	+	+	+

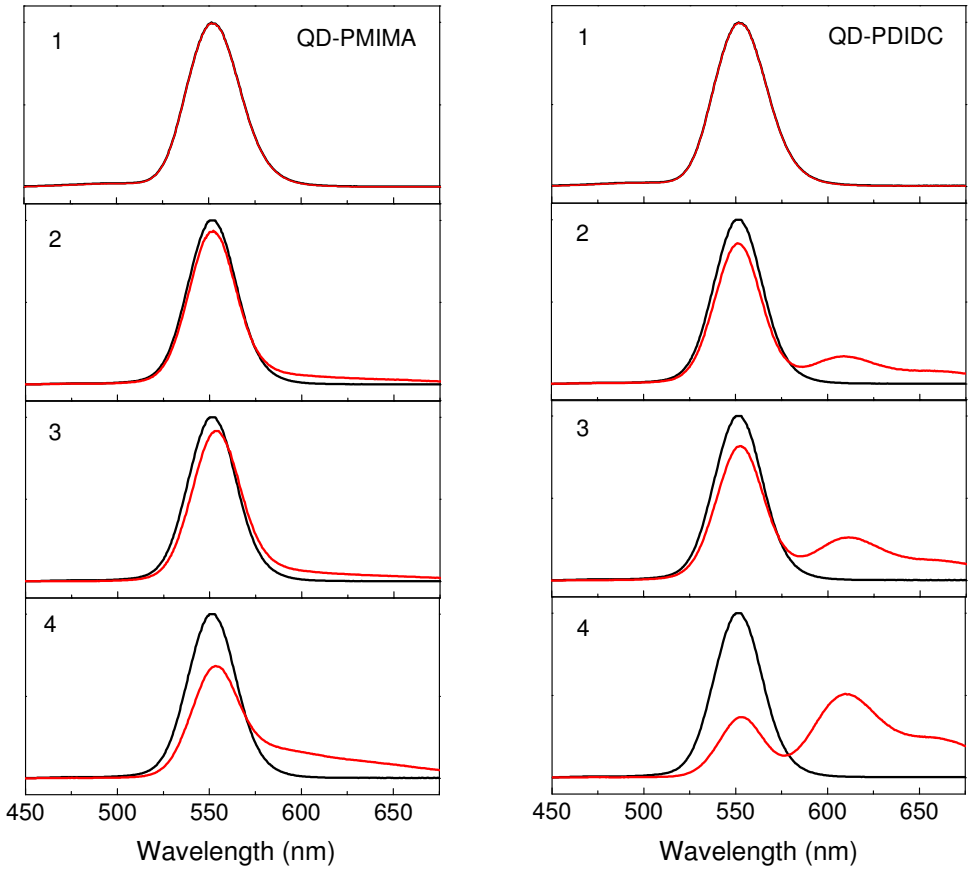

Figure 6.10: Fluorescence spectra of CdSe/CdS/ZnS QDs (black), QD-PMIMA (red, left) and QD-PDIDC (red, right) complexes prepared under different conditions as listed in Table 6.3. The upper left numbers refer to the reaction conditions as specified in Table 6.3. The nominal ratio of dye/QD = 1.

Sonicating the mixture of QDs and dyes under basic conditions (condition 3) followed by the precipitation and purification steps increases the dye emission (Figure 6.10 - 3), suggesting an increased number of dye molecules attached to the QDs. The ultrasonic irradiation can lead to collision between the suspended particles in a liquid [184, 185]. The

increase in the number of attached dye molecules may be attributed to the increase in the probability of collision between two reactants by means of sonication.

In comparison to condition 3, the difference of condition 4 is the addition of methanol during sonication (volume ratio of methanol : chloroform = 1 : 1). The dye emission in the complexes further increases (Figure 6.10 - 4). MeOH is usually used to precipitate QDs. The addition of MeOH could help remove the ligands on QDs, and thus help the attachment of the dye, thereby increasing the number of the attached dye.

Hence, the use of basic condition, sonication and the addition of MeOH favor the formation of the QD-dye complexes.

6.2.2.3 Stability of QD-dye complexes

The QD-dye complexes are very stable. After repeated precipitation-dissolution cycles only minor amounts of dye detached from QD (for example, after two times of precipitation-dissolution operation, only ~ 2% of the dye molecules detached form the QDs), indicating the high stability of the complexes.

Figure 6.11 shows the time dependent absorption and fluorescence spectra of the prepared QD-dye complexes in typical cases. Storage for months even in sunlight produced almost no alteration of the absorption spectra. The decrease in QD emission might be attributed to quenching of the QD itself with time, which affects the energy transfer in the complexes and thereby might change the intensity of dye emission. Although there is no reasonable explanation for the increase of dye emission in the QD-PDIDC complexes after 2 days, it can be concluded that nearly no dye detaches from the QDs with time. Still, there have been also a few exceptional cases where the complex particles precipitate over time, which is probably attributed to poor quality of the QDs used in these studies. Summarizing, the dyes with dicarboxylate functionality revealed a strong and robust attachment to QDs.

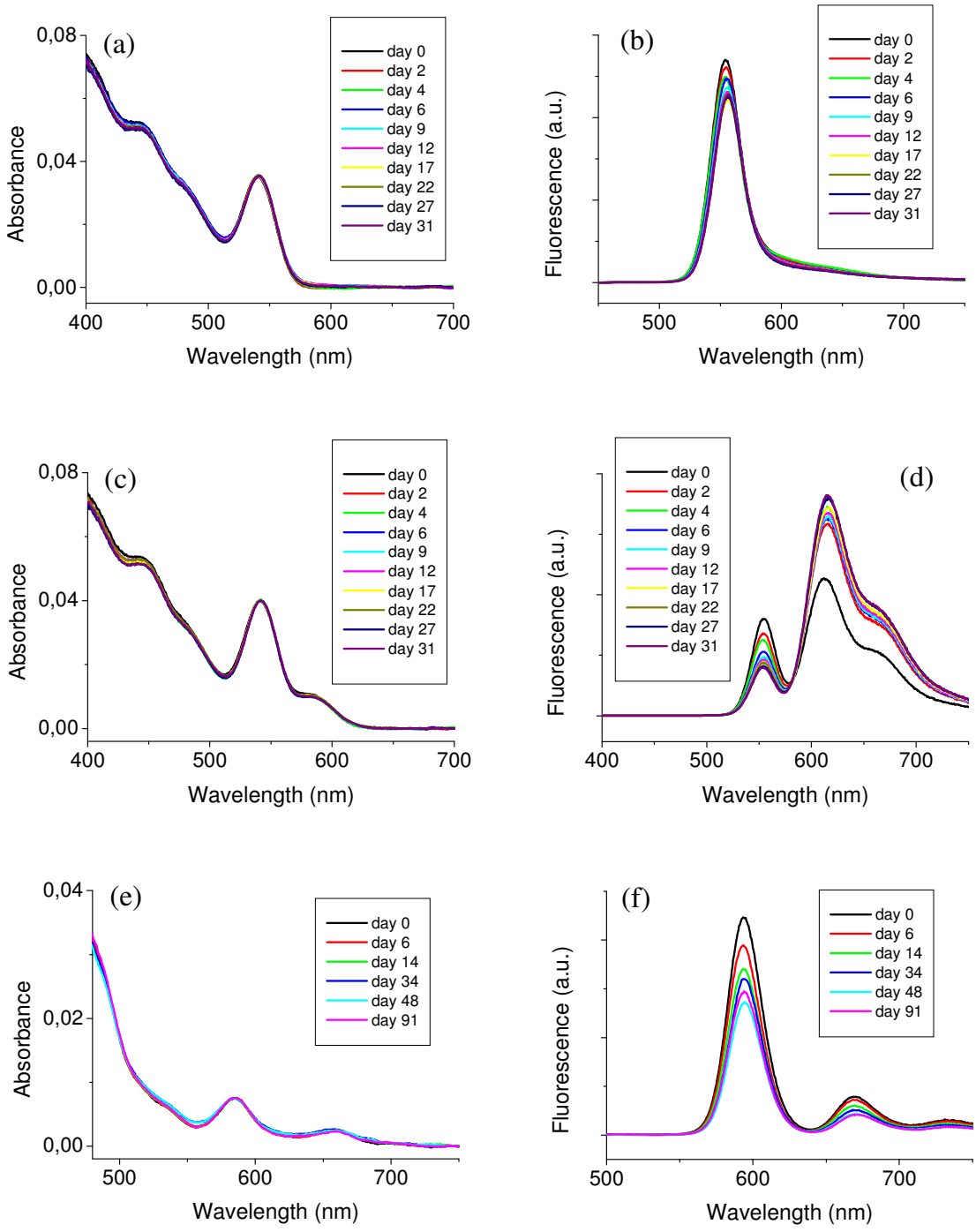

Figure 6.11: Time dependent absorption and fluorescence spectra of (a, b) QD-PMIMA complex, (c, d) QD-PDIDC complex and (e, f) QD-TDIDC complex. The nominal molar ratio of dye/QD = 1. In all cases, the solvent was chloroform. The excitation wavelength was 390 nm.

6.2.2.4 Energy transfer in QD-dye complexes

As described above, there is a strong spectral overlap between QD emission and dye absorption, and energy transfer can occur from QDs to dyes.

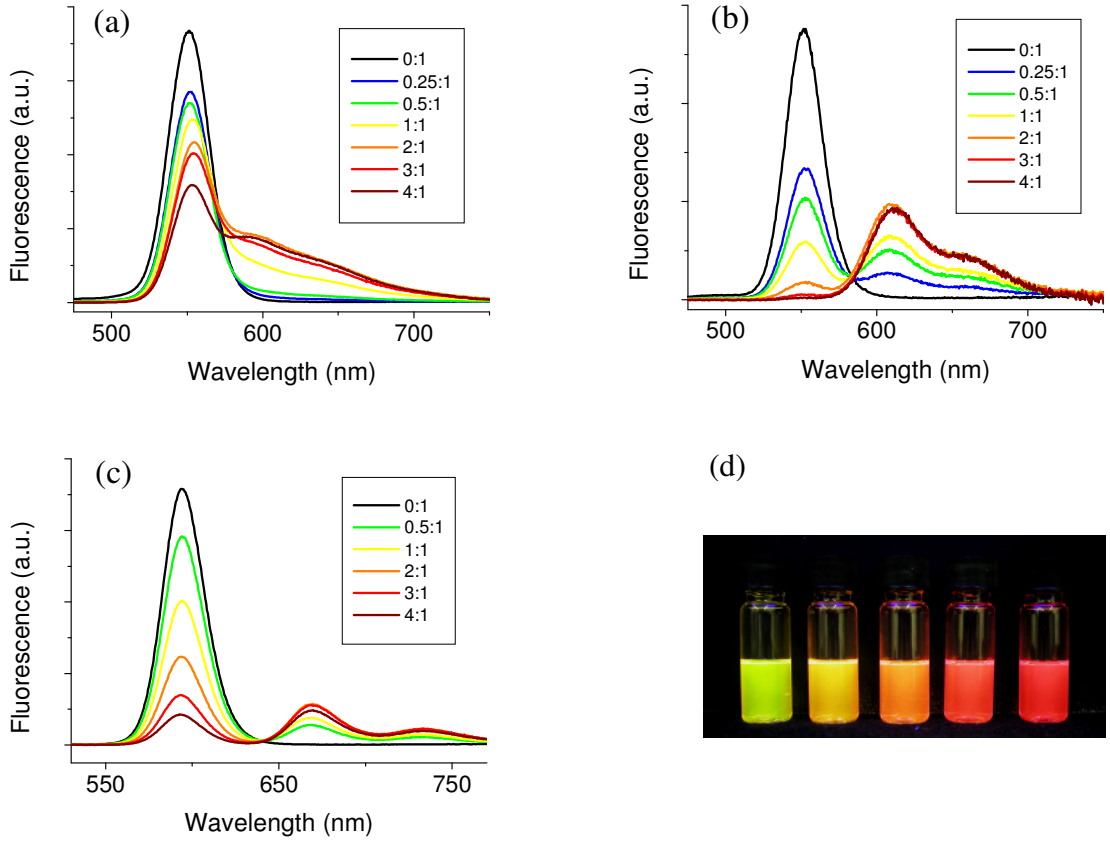

Figure 6.12: Fluorescence spectra of (a) QD-PMIMA complexes, (b) QD-PDIDC complexes and (c) QD-TDIDC complexes in chloroform as a function of the nominal dye/QD ratio. QDs used for QD-PMIMA and QD-PDIDC complexes were CdSe/1ML CdS/3ML ZnS and for QD-TDIDC complexes were CdSe/4ML CdS/1ML ZnS. In all cases, the excitation wavelength was 390 nm. (d) Fluorescence of QD-PDIDC complexes irradiated with UV light. The dye/QD ratios are 0.5, 1, 2, 3 and 4 from left to right.

The quenching of QD emission by peryleneimide and terryleneimide dyes was studied in more detail by increasing the dye/QD molar ratio. Figure 6.12 shows a series of emission spectra obtained from different dye/QD ratios. The given ratios are the nominal values of the starting mixtures, and for each ratio the precipitation and purification steps have been carried out. All complex fluorescence spectra have been corrected for the small contribution from direct excitation of the dye. In all three QD-dye complex cases, with increasing dye amounts the QD emission is successively

quenched and sensitized dye emission increases, indicating efficient energy transfer in the complexes. The decrease in dye emission at high dye/QD ratios might be attributed to the self-quenching of dyes. In the case of the QD-TDIDC complexes, it is noted that there is only slightly increase in TDIDC emission, while the QD quenching is strong.

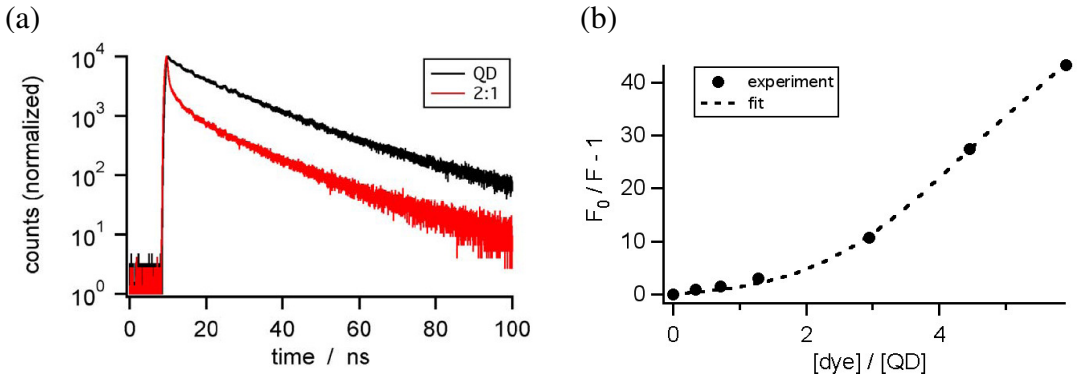

Figure 6.13: (a) Fluorescence decay curves of QDs and QD-PDIDC complexes (nominal dye/QD ratio = 2) in $CHCl_3$. (b) Stern-Volmer plot of QD fluorescence quenching in complex with PDIDC dye. Data were fitted with a model assuming a binomial distribution of the number of dye molecules bound to QD and an FRET process (see text).

Figure 6.13 a shows the fluorescence decay curves of QDs and QD-PDIDC complexes (The time-resolved measurements were done by PD Dr. Gerald Hinze). Both decay curves show strong deviations from a single exponential. An additional fast component is clearly visible in the decay curve of the complex. This also indicates efficient energy transfer in the complex. The energy transfer, however, appears to be faster than the time resolution of the set-up (~ 1 ns).

Figure 6.13 b shows a Stern-Volmer analysis of series of the QD-PDIDC complexes plotted in Figure 6.12 b. This analysis was performed by Dr. Wolfgang Erker. The QD quenching F_0/F - 1 is plotted versus the dye/QD ratio, where F_0 and F are the integrated fluorescence intensity of QDs in the absence and presence of the dye, respectively. As seen in Figure 6.13 b, the quenching is very strong and clearly shows a non-linear behavior.

The quenching of QD emission is described by the following FRET model with transfer efficiency E. Self-assembly of the QD-dye complexes is a process that inherently leads to a heterogeneous distribution in the number of dye molecules per QD. It is assumed

that each QD can bind at most d_{max} dyes but each dye molecule is able to bind only to one QD at the same time. In consequence, the ensemble will consist of different sub-populations where the QD have bound d = 0, 1, 2, …, d_{max} dye molecules. The ensemble transfer efficiency E will be a superposition of the transfer efficiencies of the different sub-populations and the contribution of each sub-population $E(d)$ has to be weighted by its fraction.

$$E = \sum_{d=0}^{d_{max}} a(d) \cdot E(d) \tag{6.3}$$

It is assumed that the distribution of the number of dye molecules attached to one QD nanoparticle follows a binomial distribution, because the number of dye molecules bound to QD is limited.

$$a(d) = \binom{d_{max}}{d} \cdot x^d \cdot (1-x)^{d_{max}-d} \tag{6.4}$$

The quantity x is the ratio [dye] / [binding site], i.e. the dye/QD ratio divided by d_{max}. Since the accurate QD concentration is hard to determine, a correction factor f_c for the dye/QD ratio is introduced to take into account potential deviations of the QD concentrations. Therefore, the quantity x is

$$x = \frac{[dye] \cdot f_c}{[QD] \cdot d_{max}} \tag{6.5}$$

When the bound dye molecules quench QD emission via a FRET process, the transfer efficiency $E(d)$ of each sub-population is given by

$$E(d) = \frac{d}{d + (r/R_0)^6} \tag{6.6}$$

Inserting the relationship between the energy transfer efficiency E and the quenched donor emission

$$E = 1 - \frac{F}{F_0} \tag{6.7}$$

into the Stern-Volmer term, one obtains

$$\frac{F_0}{F} - 1 = \frac{1}{1-E} - 1 = \frac{E}{1-E} \tag{6.8}$$

with $$E = \sum_{d=0}^{d_{\max}} \binom{d_{\max}}{d} \cdot \left(\frac{[dye] \cdot f_c}{[QD] \cdot d_{\max}}\right)^d \cdot \left(1 - \frac{[dye] \cdot f_c}{[QD] \cdot d_{\max}}\right)^{d_{\max} - d} \cdot \frac{d}{d + (r/R_0)^6}$$

The fitting parameters are d_{max}, r/R_0, and f_c.

As shown in Figure 6.13 b, the model describes the experimental data of QD-PDIDC complexes quite well, resulting in $d_{max} = 12$, $r/R_0 = 0.63$ and $f_c = 0.97$.

For the QD-PDIDC complexes, when a κ^2 value of 4/3 evaluated from the Monte-Carlo simulation is used, R_0 is calculated to be 5.39 nm according to equation 6.2, as can also be seen in Table 6.2. Thus, one obtains $r = 0.63 \times 5.39$ nm = 3.4 nm. When κ^2 is chosen as 0.476 [5], which is the value for static random donor-acceptor orientations, R_0 is calculated to be 4.54 nm and $r = 0.63 \times 4.54$ nm = 2.9 nm. From the binding model (see Figure 3.5), a center-to-center distance of 3.3 ± 0.4 nm is estimated considering that the diameter of the QDs is 4.5 ± 0.7 nm and the "length" of the PDIDC dye is 2 nm. The discrepancy between spectroscopic and geometrical data is within the range of error using both κ^2 values, and this indicates that a Förster approach seems to give a reasonable description of energy transfer in the complexes.

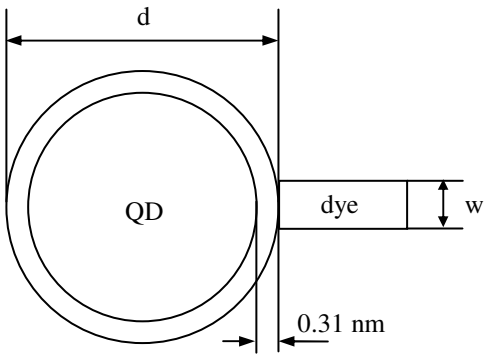

Figure 6.14: Schematic diagram of a QD-dye complex for the calculation of possible maximum number of dye occupation sites.

The possible maximum number of dye occupation sites (N) was also evaluated in terms of binding sites or geometry.

i) Binding sites

The diameter of the QD is 4.5 nm, and the thickness of one ZnS monolayer is 0.31 nm (Figure 6.14). Therefore, the volume of ZnS monolayer ($V_{monolayer}$) is calculated by

$$V_{\text{monolayer}} = \frac{4}{3}\pi(\frac{d}{2})^3 - \frac{4}{3}\pi((\frac{d}{2}) - 0.31)^3)$$

$$= \frac{4}{3}\pi(2.25^3 - 1.99^3)$$

$$= 14.7 \text{ nm}^3$$

The volume of one ZnS unit cell (V_{unitcell}, zinc blende structure) is calculated by

$$V_{\text{unitcell}} = 0.54^3 = 0.157 \text{ nm}^3$$

Taking into account that there are usually 2 Zn atom on one plane of a single unit cell of ZnS zinc blende structure (although there are 4 ZnS molecules per unit cell, see Figure 6.8 a), and supposing 1-PDIDC occupies 2-Zn, the possible maximum number of dye occupation sites (N) is

$$N = 2 \times \frac{1}{2} \times \frac{V_{monolayer}}{V_{unitcell}}$$

$$= 94$$

This value is much larger than $d_{\text{max}} = 12$ obtained from fitting. This is because the size of the dye structure is not considered in this calculation.

ii) Geometry

The width of the PDIDC molecule is 1.5 nm (Figure 6.14). Considering the dye molecule as a cylinder, the possible maximum number of dye occupation sites (N) is the surface area of the QD divided by the area of the circular base of the dye cylinder:

$$N = 4\pi(\frac{d}{2})^2 / \pi(\frac{w}{2})^2 = 4 \times (\frac{d}{2})^2 / (\frac{w}{2})^2$$

$$= 4 \times (\frac{4.5}{2})^2 / (\frac{1.5}{2})^2$$

$$= 36$$

This value is more realistic and closer to $d_{\text{max}} = 12$.

6.2.2.5 Distance dependence of energy transfer in QD-dye complexes

For further experimental clarification of the energy transfer mechanism in the QD-dye hybrid system, the dependence of the energy transfer efficiency on the distance between QD and dye was studied. As discussed above, in the QD-dye complex system, the dye is directly attached to the QD via its dicarboxylate functional group. As illustrated in Figure 6.15, the center-to-center donor-acceptor distance *r* (the radius of the QD plus half of the "length" of the dye molecule) can be tuned by varying the diameter of the QDs. Increasing the number of ZnS monolayers can raise the QD diameter and thereby increase the QD-dye distance, and importantly, will not significantly shift the emission of the QDs.

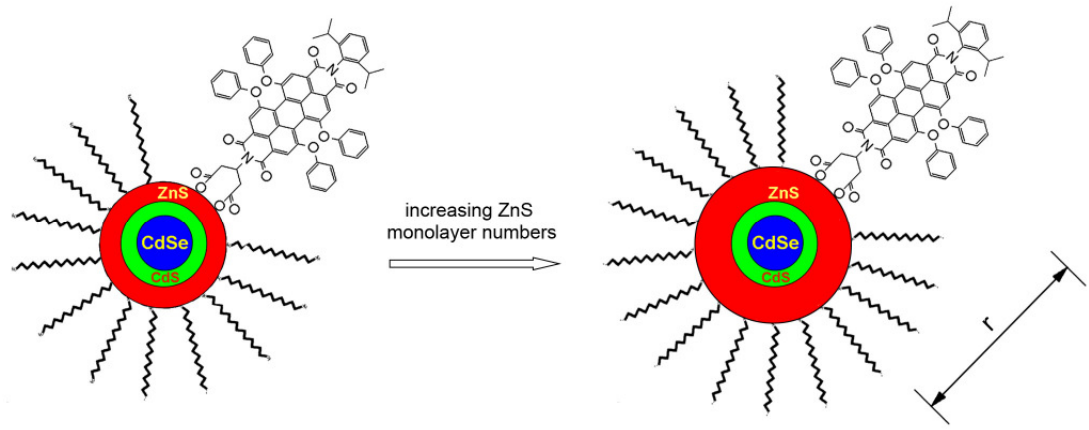

Figure 6.15: Schematic diagram of a dye molecule binding to a CdSe/CdS/ZnS QD. The center-to-center distance between the QD and the dye molecule is controlled by varying the number of the ZnS monolayers.

For the study of distance-dependent energy transfer, several series of QD-dye complexes were prepared, where CdSe/CdS/ZnS or CdSe/ZnS QDs with increasing number of ZnS monolayers were used as the donor and the PDIDC dye was used as the acceptor. The QDs in each series were prepared from the same CdSe core. The nominal molar ratio of dye to QD in all studied complexes was 3:1. The concentration of all the samples for the optical measurements was in nM range, and thus the average distance between two particles was $\langle d \rangle = (N_A \cdot c)^{-1/3} = (6.02 \times 10^{23} \times 40 \times 10^{-9})^{-1/3} = 3.5 \times 10^{-9}$ dm = 350 nm. Therefore, dynamic quenching can be neglected. In the following, the results of two typical series of QD-dye complexes using CdSe/1ML CdS/ZnS and CdSe/ZnS QDs as the donor, respectively, are discussed.

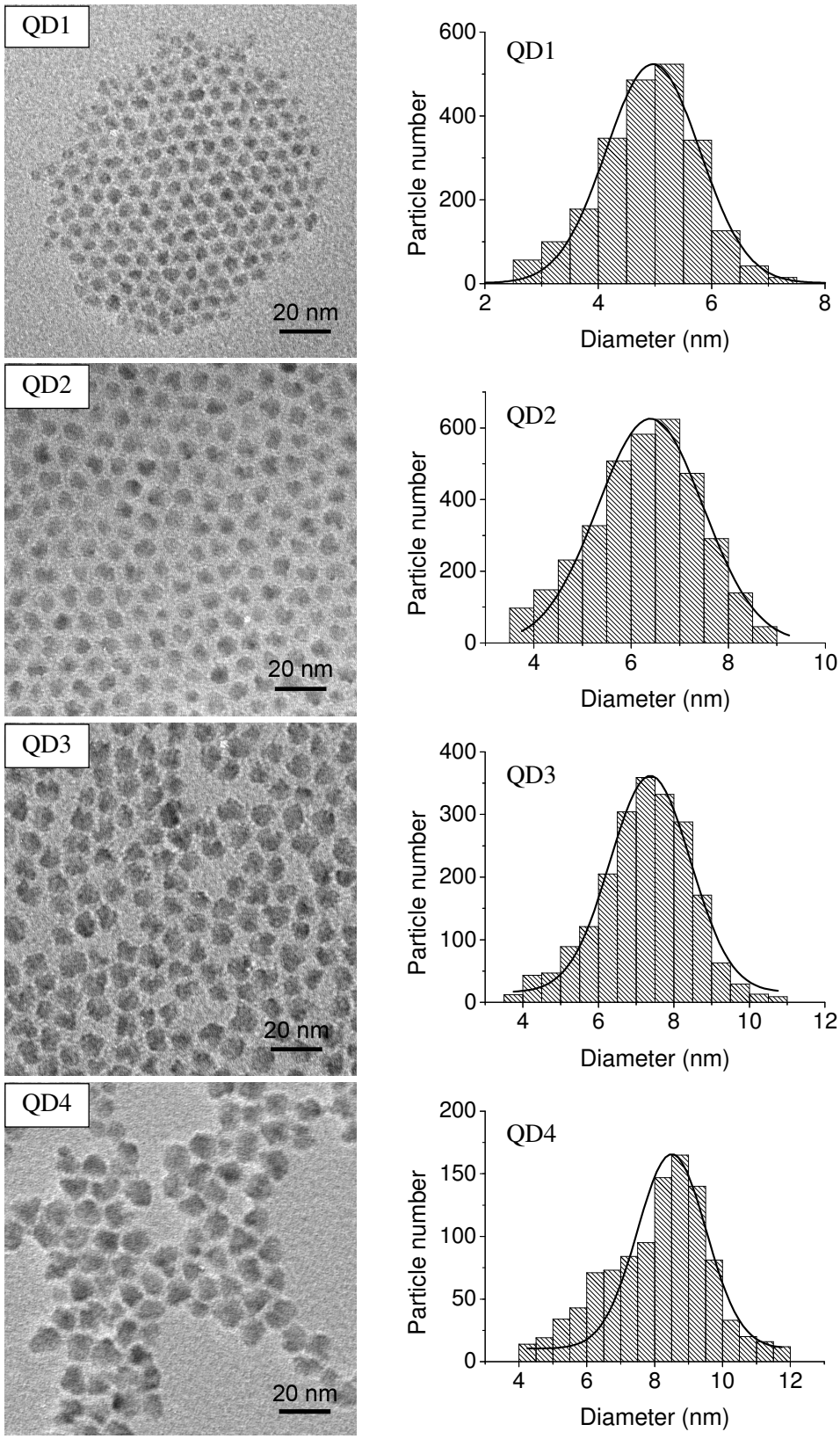

Figure 6.16: TEM images and size distributions of CdSe/CdS/ZnS QDs. QD1 is CdSe/1ML CdS/3ML ZnS, QD2 is CdSe/1ML CdS/5ML ZnS, QD3 is CdSe/1ML CdS/7ML ZnS and QD4 is CdSe/1ML CdS/9ML ZnS.

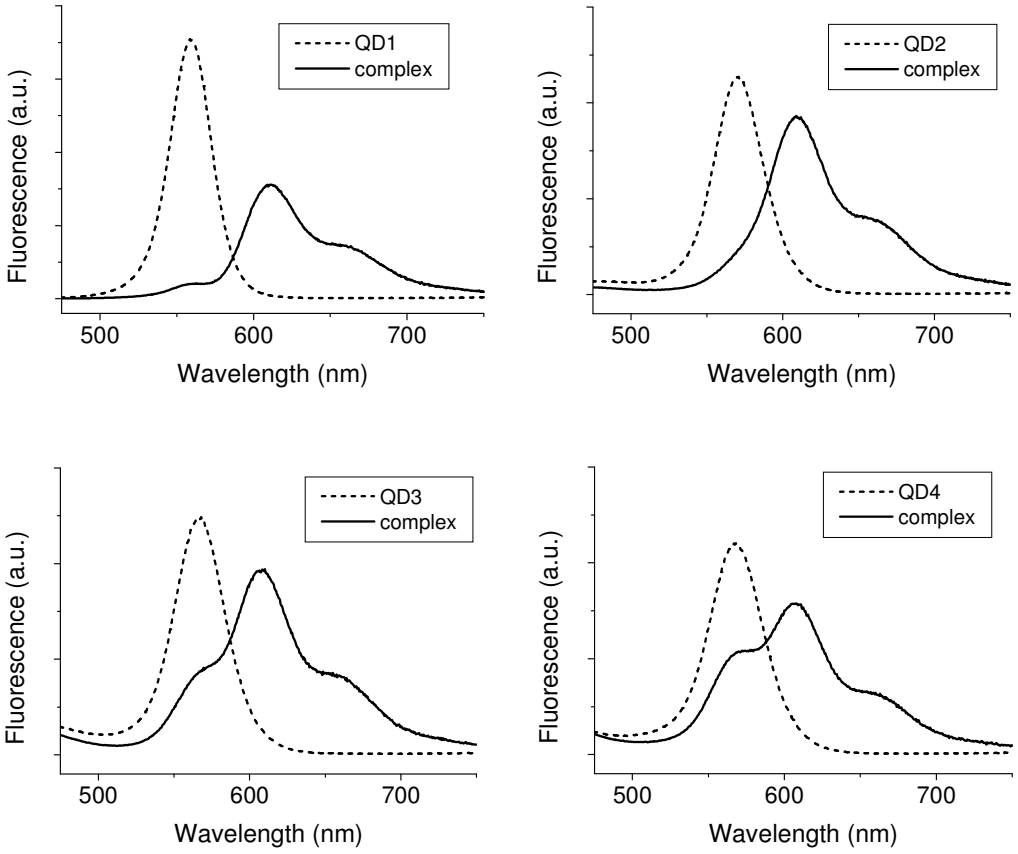

Figure 6.17: Steady-state fluorescence spectra of the CdSe/CdS/ZnS QDs and their corresponding QD-PDIDC complexes. QD1 - QD4 correspond to those shown in Figure 6.16. The nominal molar ratio of PDIDC/QD = 3. In all cases, the solvent was chloroform. The excitation wavelength was 390 nm.

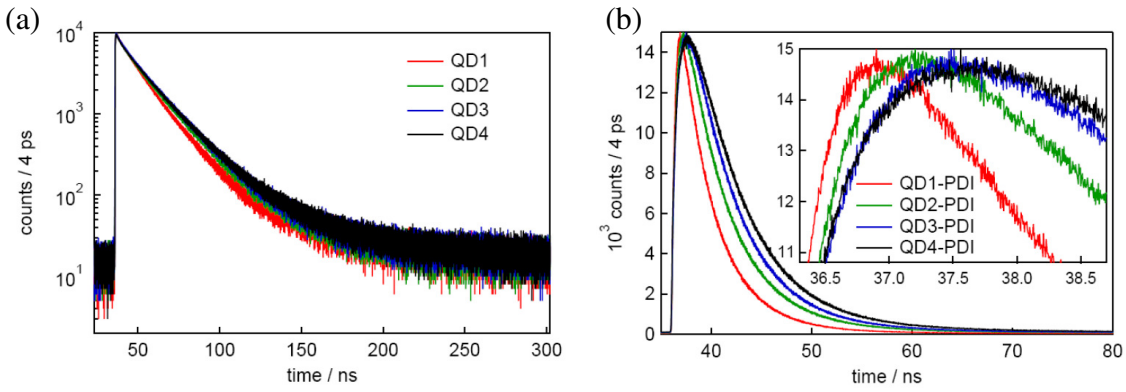

Figure 6.18: Time-resolved fluorescence spectra of (a) the pure CdSe/CdS/ZnS QDs and (b) their corresponding QD-PDIDC complexes. QD1 - QD4 correspond to those shown in Figure 6.16. The nominal molar ratio of PDIDC/QD = 3.

Figure 6.16 shows the TEM images and size distributions of the different sized CdSe/CdS/ZnS QDs. Figure 6.17 and Figure 6.18 show the steady-state and time-resolved fluorescence spectra of these CdSe/CdS/ZnS QDs and their QD-PDIDC

complexes, respectively. The time-resolved fluorescence was measured using the time-correlated single photon counting (TCSPC) technique, and this work was done by Mathias Haase. Table 6.4 summarizes the properties of these different sized CdSe/CdS/ZnS QDs and the results for their corresponding QD-PDIDC complexes.

Table 6.4: Properties of the different sized CdSe/CdS/ZnS QDs and results for their corresponding QD-PDIDC complexes.

	QD1	**QD2**	**QD3**	**QD4**
d (nm)	5.0 ± 0.7	6.4 ± 1.1	7.4 ± 1.0	8.5 ± 1.1
λ_{em} (nm)	558	569	566	568
Φ_D	0.36	0.34	0.37	0.34
τ_{fl}^{QD} (ns)	2.61	2.51	1.88	1.50
	QD1-PDIDC	**QD2-PDIDC**	**QD3-PDIDC**	**QD4-PDIDC**
r (nm)	3.5	4.2	4.7	5.3
J ($nm^4\,M^{-1}\,cm^{-1}$)	2.51×10^{15}	2.64×10^{15}	2.39×10^{15}	2.38×10^{15}
R_0' (nm)	5.132	5.126	5.113	5.039
τ_{EET} (ns)	0.219	0.528	0.924	1.291
E^{SS}	0.945	0.84	0.67	0.54
E^{TCSPC}	0.92	0.82	0.67	0.53

* QD1 - QD4 correspond to those shown in Figure 6.16. d is the diameter of the QDs, λ_{em} is the QD emission, Φ_D is the quantum yield of the QDs, τ_{fl}^{QD} is the fluorescence lifetime of the pure QDs, r is the donor-acceptor distance, J is the spectral overlap, τ_{EET} is the energy transfer time, E^{SS} and E^{TCSPC} is the energy transfer efficiency determined from the steady-state and TCSPC measurements, respectively. The calculation of R_0', E^{SS} and E^{TCSPC} is described in the text.

As shown in Table 6.4, as the diameter of the prepared CdSe/CdS/ZnS QDs increases, the QD-dye center-to-center distance (r) increases. The QDs with different sizes have slightly different emission positions (λ_{em}) and quantum yields (Φ_D) (see Table 6.4). Therefore, according to the expression

$$R_0 = 0.211(\kappa^2 n^{-4} \Phi_D J(\lambda))^{1/6}$$

the Förster radius (R_0) differs for different sized QDs.

Assuming κ^2 is unknown and setting κ^2 as a fitting parameter, we calculated

$$R_0^{'} = R_0 / (\kappa^2)^{1/6} = 0.211 (n^{-4} \Phi_D J(\lambda))^{1/6} \tag{6.9}$$

where n is the refractive index of the solvent chloroform (n = 1.445). The calculated $R_0^{'}$ values are shown in Table 6.4.

From the steady-state measurements (Figure 6.17), the energy transfer efficiency (E^{SS}) was calculated using the relative integrated fluorescence intensity of the QDs, in the absence (F_0) and presence (F) of acceptor:

$$E = 1 - \frac{F}{F_0}$$

As can be seen in Table 6.4, when the diameter of the used QDs increases, that is, when the donor-acceptor distance increases, the energy transfer efficiency decreases.

From the TCSPC measurements (Figure 6.18), the energy transfer efficiency (E^{TCSPC}) was calculated according to

$$E^{TCSPC} = \frac{k_{EET}}{k_{EET} + k_{fl}^{QD}} = \frac{1}{1 + (\tau_{EET} / \tau_{fl}^{QD})} \tag{6.10}$$

where τ_{fl}^{QD} is the fluorescence lifetime of the pure QDs and τ_{EET} is the energy transfer time. The QD decay curves (Figure 6.18 a) were fitted by a four-exponential decay function. The average (amplitude-weighted) QD lifetime τ_{fl}^{QD}, as shown in Table 6.4, was given by the sum of the two short components. τ_{EET} was determined as the rise time form the rise/decay-time profile of the acceptor in the QD-dye complexes (Figure 6.18 b). It can be seen that, as the QD-to-dye distance increases, the rise time/energy transfer time increases. As listed in Table 6.4, the energy transfer efficiencies determined from the TCSPC measurements (E^{TCSPC}) are in good agreement with the efficiencies determined from the steady-state measurements (E^{SS}).

In addition to CdSe/CdS/ZnS QDs, CdSe/ZnS QDs with shorter emission wavelengths were also used for preparing QD-PDIDC complexes to study the distance dependent energy transfer efficiency. Figure 6.19 shows the TEM images and size distributions of the different sized CdSe/ZnS QDs. Figure 6.20 shows the steady-state fluorescence spectra of these CdSe/ZnS QDs and their QD-PDIDC complexes.

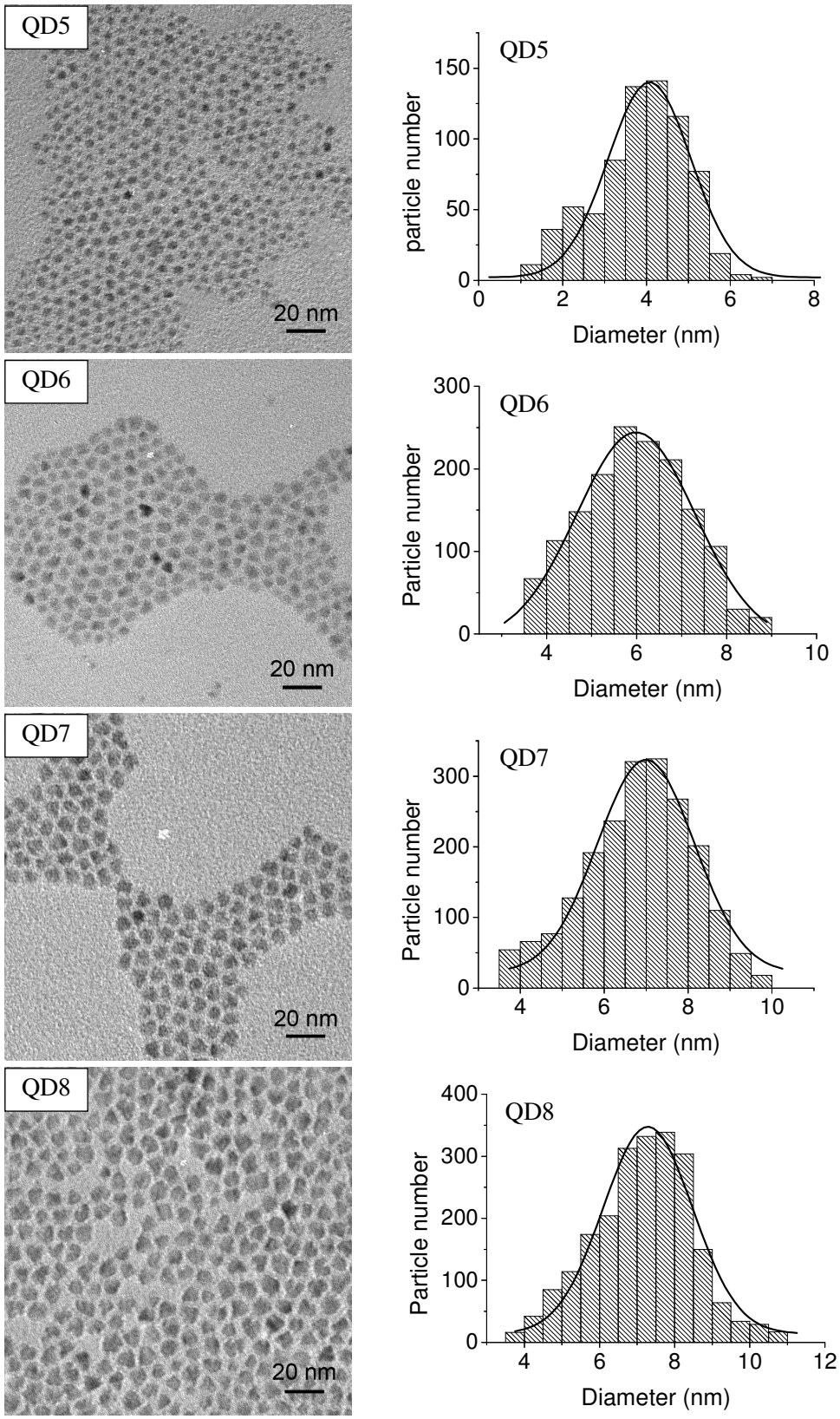

Figure 6.19: TEM images and size distributions of CdSe/ZnS QDs. QD5 is CdSe/2ML ZnS, QD6 is CdSe/6ML ZnS, QD7 is CdSe/8ML ZnS and QD8 is CdSe/10ML ZnS.

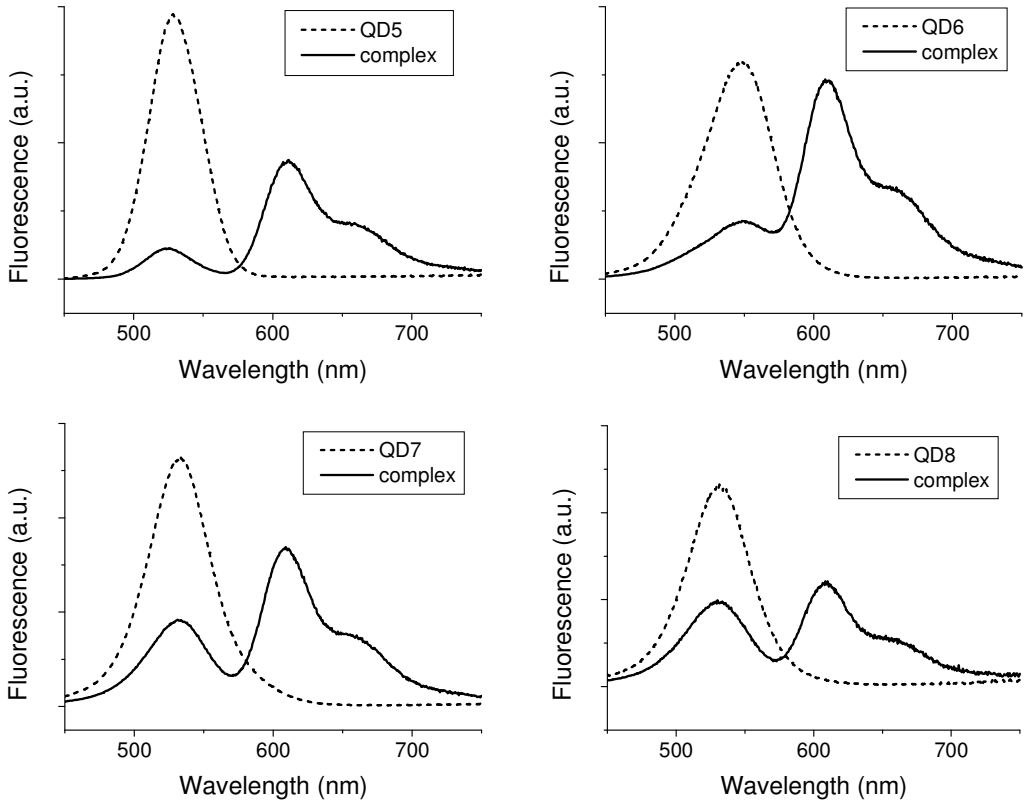

Figure 6.20: Fluorescence spectra of the CdSe/ZnS QDs and their corresponding QD-PDIDC complexes. QD5 - QD8 correspond to those shown in Figure 6.19. The nominal molar ratio of PDIDC/QD = 3. In all cases, the solvent was chloroform. The excitation wavelength was 390 nm.

Table 6.5: Properties of the different sized CdSe/ZnS QDs and the parameters and results of their corresponding QD-PDIDC complexes.

	QD5	**QD6**	**QD7**	**QD8**
d (nm)	4.2 ± 0.9	6.0 ± 1.2	7.0 ± 1.2	7.3 ± 1.1
λ_{em} (nm)	526	547	531	531
Φ_D	0.16	0.22	0.33	0.36
	QD1-PDIDC	**QD2-PDIDC**	**QD3-PDIDC**	**QD4-PDIDC**
r (nm)	3.1	3.93	4.49	4.58
J ($\mathrm{nm^4\,M^{-1}\,cm^{-1}}$)	1.45×10^{15}	1.93×10^{15}	1.59×10^{15}	1.48×10^{15}
$R_0^{'}$ (nm)	4.093	4.527	4.687	4.701
E^{SS}	0.89	0.74	0.65	0.60

* QD5 - QD8 correspond to those shown in Figure 6.19.

Table 6.5 gives a summary of the properties of these different sized CdSe/ZnS QDs and results for their corresponding QD-PDIDC complexes. The energy transfer efficiency also decreases with increasing center-to-center distance between CdSe/ZnS QD and PDIDC dye.

Besides the two series discussed before, two other series of QD-PDIDC complexes using CdSe/CdS/ZnS or CdSe/ZnS QDs as the donor were prepared. The QD-dye distances and the energy transfer efficiencies of all the prepared complexes are listed in Table 6.6. As shown in Table 6.6, the energy transfer efficiencies calculated from the steady-state measurements (E^{SS}) and the TCSPC measurements (E^{TCSPC}) are in good agreement.

Table 6.6: Energy transfer parameters for all series of QD-dye complexes.

	r	R_0'	E^{SS}	E^{TCSPC}
CdSe/CdS/ZnS-PDIDC				
Series 1	3.35	5.010	0.915	0.93
	4.97	5.397	0.68	0.68
Series 2	3.5	5.132	0.945	0.92
	4.2	5.126	0.84	0.82
	4.7	5.113	0.67	0.67
	5.3	5.039	0.54	0.53
CdSe/ZnS-PDIDC				
Series 3	2.97	4.397	0.92	
	4.17	5.071	0.72	
	4.39	4.943	0.67	
Series 4	3.1	4.093	0.89	
	3.93	4.527	0.74	
	4.49	4.687	0.65	
	4.58	4.701	0.6	

The efficiency of energy transfer as a function of distance is given by [186]

$$E = \frac{1}{1 + (r / R_0)^j} \tag{6.11}$$

where j is the exponent of the distance dependence. For Förster energy transfer, $j = 6$. Taking equation 6.9 and 6.11 together, the transfer efficiency can be described as

$$E = \frac{1}{1 + \left(\frac{r}{R_0^{'}}\right)^j \frac{1}{\kappa^2}} \tag{6.12}$$

It has been discussed above that taking into account a distribution for the number of dye molecules bound to one QD, the efficiency of energy transfer can be expressed as

$$E = \sum_{d=0}^{d_{\max}} a(d) \cdot E(d)$$

Since the maximum numbers of dye molecules bound to QD ($d_{\max}$) are different for QDs with different diameters, the Poisson distribution is used to describe the number of dye molecules bound to QD, instead of the binomial distribution

$$a(d) = \frac{N^d \cdot e^{-N}}{d!} \tag{6.13}$$

where N is the average number of dye molecules bound to QD. Since the nominal dye/QD ratio is 3, introducing the correction factor f_c for the dye/QD ratio due to the uncertainty of the QD concentration,

$$N = f_c \cdot \frac{[dye]}{[QD]} = 3 f_c \tag{6.14}$$

Therefore, the energy transfer efficiency as a function of distance is given by

$$E = \sum_d a(d) \cdot E(d) = \sum_{d=0}^{\infty} \frac{3 f_c{}^d \cdot e^{-3 f_c}}{d!} \frac{d}{d + \left(\frac{r}{R_0^{'}}\right)^j \frac{1}{\kappa^2}} \tag{6.15}$$

The fitting parameters are j, f_c and κ^2.

The energy transfer efficiency E, including E^{SS} and E^{TCSPC} listed in Table 6.6, as a function of distance plotted versus r/R_0' is given in Figure 6.21. The solid line corresponds to an r^{-6} distance dependence, i.e., j is fixed to be 6 in equation 6.15. The Förster model fits well with the experimental data, resulting in $f_c = 1.55 \pm 0.60$ and $\kappa^2 = 0.34 \pm 0.16$. This κ^2 value is close to the value of 0.476 for static random donor-acceptor orientations.

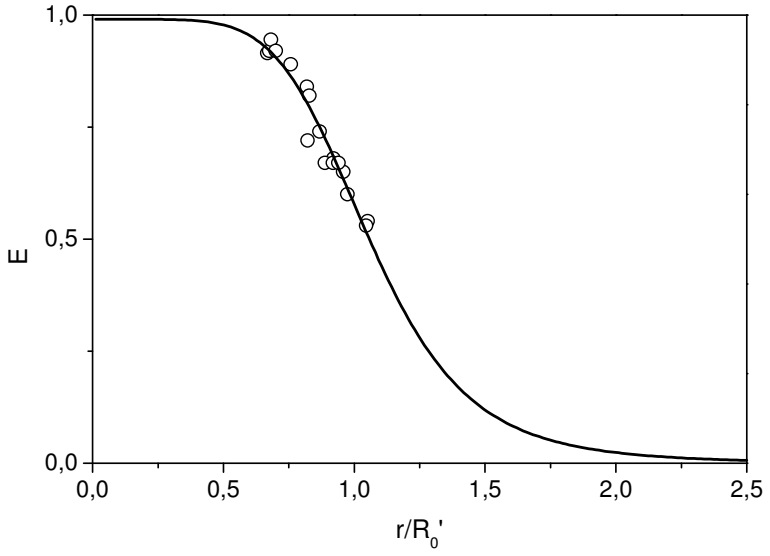

Figure 6.21: Energy transfer efficiency as a function of distance in the QD-PDIDC complexes. The solid line corresponds to an r^{-6} distance dependence.

In conclusion, the Förster dipole-dipole formalism provides a reasonable fit to the energy transfer efficiencies measured in the QD-PDIDC hybrid system. The data confirms that Förster energy transfer dominates electronic coupling between luminescent QDs and proximal dye molecules, with a resulting r^{-6} dependence of the FRET efficiency.

6.3 Quantum dot - dye hybrids in aqueous solution

6.3.1 Experimental procedure

QD-dye complexes were transferred from organic solvent to water via two methods: phase transfer and "refluxing". QD-PDIDC complexes were used and the QDs used were CdSe/1ML CdS/3ML ZnS. The original organic ligands on the QD-PDIDC complexes were oleic acid and oleylamine.

Phase transfer method A mixture of 2 mL of QD-PDIDC complex chloroform solution (concentration ≈ 3 μM) with different PDIDC/QD ratios, 3 mL of water containing 100 μL mercaptopropionic acid (MPA, the molar ratio of MPA molecules to the ligands on the complexes was ~ 200) and 100 μL tetramethylammonium hydroxide ($(CH_3)_4NOH$) was vigorously stirred for 6 h. The aqueous solution was then centrifuged and the precipitate was redispersed in water. The pH of the final solution was adjusted to ~ 10 with $(CH_3)_4NOH$. In phase transfer method, only MPA was used as the exchange ligands.

"Refluxing" method Different exchange ligands, including MPA, 11-mercaptoundecanoic acid (MUA) and dihydrolipoic acid (DHLA), were used to transfer complexes into water via the "refluxing" method. The solvents used in the synthesis were different for different exchange ligands (Table 6.7). Typically, 2 μL MPA or 7.5 μL DHLA was added to 5 mL *isopropanol* and the pH of this solution was adjusted to ~ 13 with $(CH_3)_4NOH$. In the case of MUA, 5 mL of *a mixture of methanol and dioxane* (1:1 vol. ratio) was used to dissolve 5 mg MUA, and the pH of this solution was adjusted to ~ 13 with $(CH_3)_4NOH$. 1 mL of QD-PDIDC complex solution in chloroform (concentration ≈ 4 μM) was then added, and the mixture was heated upon stirring under Ar. The particles were precipitated with ethyl acetate and, after centrifugation, redispersed in water.

Table 6.7: Solvents used for different exchange ligands.

	MPA	MUA	DHLA
solvent	isopropanol	methanol + diaxane (1:1 vol.)	isopropanol

6.3.2 Results and discussion

Since the prepared QD-dye complexes are stable and the dicarboxylate functional group has a strong affinity to QDs, this feature offers a good possibility to transfer the complexes into water via ligand exchange. Thiols are common ligands used to exchange the organic ligands on a QD surface and render QDs water soluble due to their high binding strength, although ligand exchange by thiols generally quenches QD fluorescence (it is found that the quantum yield of the CdSe/1ML CdS/3ML ZnS QDs was reduced on average by ~ 40% after ligand exchange by thiols). If the affinity of dicarboxylate groups is stronger than that of thiol groups, dye molecules will not be exchanged by thiol ligands and will not detach from QDs. In this case, thiol groups only exchange the organic ligands on QDs rather than dye molecules. Consequently, the QDs are transferred into water with dye molecules attached to the QD surface, and the QD-dye complexes survive in water after ligand exchange. There are usually two methods to carry out ligand exchange: phase transfer method and "refluxing" method.

6.3.2.1 Phase transfer method

Before phase transfer, the aqueous phase was colorless and the organic phase (chloroform), where the QD-dye complexes were dispersed, was dark orange. After phase transfer, the color of the aqueous phase turned to orange, indicating the successful transfer of the QDs from the organic phase to the aqueous phase. However, the organic phase after phase transfer was purple, which corresponds to the color of the dye in chloroform solution. This finding implies that many dye molecules detach from QDs during transfer process and remain in the organic phase. The detachment of the dye molecules from QDs can be further proved by the absorption spectra. As shown in Figure 6.22 a, the absorption of the organic phase after phase transfer (red curve) is mainly due to the dye absorption (pure dye absorption see Figure 6.3).

Although many dye molecules (~ 80%) detached from QDs during phase transfer, there were still some dye molecules attached to QDs and the complexes still existed in aqueous solution. This can be proved by both QD and dye peaks in the emission spectra of the final product in aqueous solution after phase transfer (green curve in Figure 6.22 b). The loss of part of dye molecules after phase transfer implies that dicarboxylate groups may have a similar affinity to thiol groups.

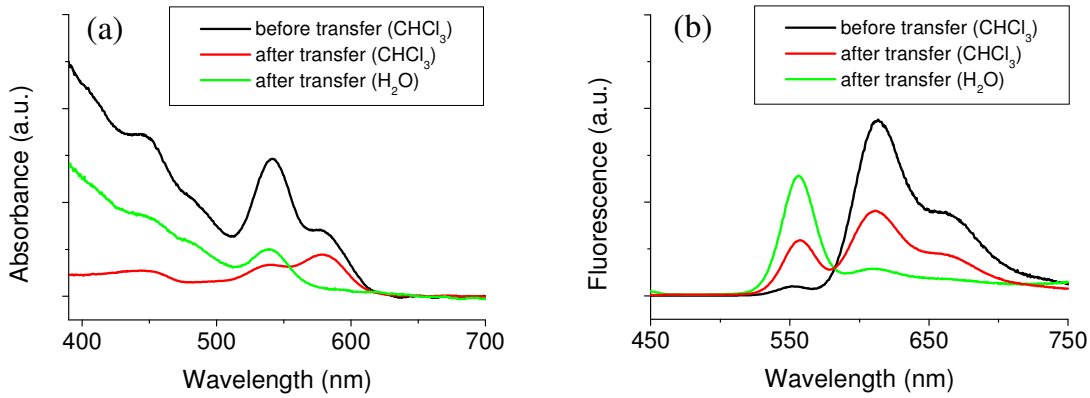

Figure 6.22: (a) Absorption and (b) fluorescence spectra of the organic phase before (black curves) and after phase transfer (red curves), and the QD-PDIDC complexes in aqueous phase after phase transfer (green curves). The nominal PDIDC/QD ratio of the complexes before phase transfer is 2.

Furthermore, it was checked how the transfer into water did depend on the dye/QD ratio of complexes in the organic phase. Figure 6.23 shows the emission spectra of QD-PDIDC complexes after phase transfer. The dye/QD ratio of the complexes before phase transfer was 2 and 3, respectively. As can be seen, using complexes with higher dye/QD ratio does not increase the number of the attached dye after phase transfer. There is no explanation for this observation so far, and experiments using complexes with more different ratios have to be done.

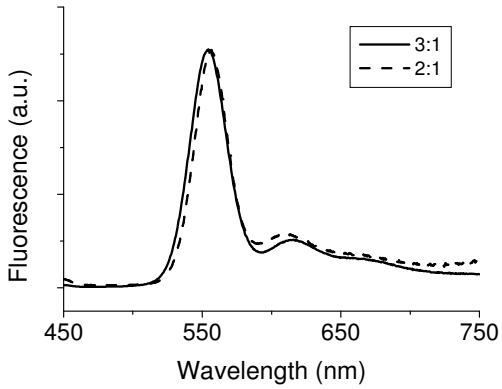

Figure 6.23: Fluorescence spectra of QD-PDIDC complexes in aqueous solution. The nominal dye/QD ratios of the complexes before phase transfer are 3 (solid line) and 2 (dash line).

Although the complexes can be transferred into water via phase transfer, the transfer process was very hard to control. Large numbers of dye molecules were lost during phase transfer. Moreover, not all of the particles were transferred into water; there are still some of QDs in the organic phase, as shown in the fluorescence spectrum of the

organic phase after phase transfer (red curve in Figure 6.22 b). Besides, a lot of particles existed at the interface between organic and aqueous phase and these particles could not be redispersed in water. Therefore, the yield of final products was very low.

6.3.2.2 "Refluxing" method

The "Refluxing" method is a more successful method than phase transfer method for transferring QDs into water. Besides different exchange ligands, different reaction conditions, such as exchange ligand amount, reaction time and reaction temperature, were studied to minimize dye detachment during complex transfer. For the water-soluble complexes prepared at different reaction conditions, it can be assumed that the QD-dye distance, the spectral overlap and the orientation factor κ^2 are not altered. In addition, the change in quantum yield of QDs after transfer into water due to different reaction conditions is not significant. Hence, the number of attached dye molecules per QD after the transfer dominates the energy transfer efficiency of the water-soluble complexes. Therefore, the extent of dye detachment after transferring complexes into water can be judged by the relative change in QD and dye emission. The stability of the water-soluble complexes was also studied. Moreover, the pH value of the obtained complex aqueous solution was found to have an interesting influence on energy transfer.

A. Comparison of different exchange ligands

The emission spectra of complexes after ligand exchange, using MPA, MUA and DHLA respectively, is shown in Figure 6.24. The black curve is the emission of the QD-PDIDC complexes before the transfer with the nominal dye/QD ratio of 3. After transfer into water, the dye emission decreases and the QD emission increases drastically.

The complexes after being transferred by using MPA and MUA, respectively, show nearly the same emission profile. This indicates that the MPA and MUA seem to have the same influence on the dye detachment during refluxing. However, since the pKa value of MUA (pKa = 4.8 [187, 188]) is larger than that of MPA (pKa = 4.3 [188, 189]) due to its longer chain length, MUA is harder to be deprotonated than MPA. Therefore, in order to prevent aggregation and get clear complex aqueous solution, higher pH value of the final solution was needed when MUA was used. The pH value of the final solution

was ~ 10 when using MPA, and ~ 12 or even higher when using MUA. Moreover, the yield of products using MUA as the exchange ligand was also low. Therefore, in the following reaction condition optimization section, MUA-complexes were not studied.

In the case of using DHLA as the exchange ligand, the water-soluble DHLA-complexes (blue curve) show a higher QD emission and a lower dye emission than the MPA- and MUA-complexes. This indicates that DLHA molecules replace more dye molecules than MPA and MUA molecules during ligand exchange due to the stronger affinity of the dithiol group in DLHA to QDs than that of the mono-thiol in MPA and MUA.

From above comparison and discussion, it appears that MPA should be the best exchange ligand for direct transfer of complexes into water with respect to reducing the dye detachment.

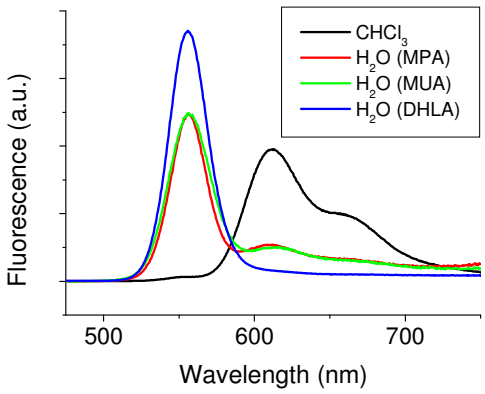

Figure 6.24: Fluorescence spectra of QD-PDIDC complexes (nominal PDIDC/QD = 3) in chloroform (black) and after the transfer into water using MPA (red), MUA (green) and DHLA (blue) as exchange ligands, respectively. Reaction time: 10 min. Reaction temperature: 65 °C.

However, the dye emission in the DHLA-complexes (blue curve in Figure 6.24) can hardly be seen. Does it mean the affinity of the dithiol group in DLHA is strong enough to be able to replace all dye molecules attached to QDs? Figure 6.25 shows the emission spectra of the complexes transferred into water using MPA and DLHA as exchange ligands, respectively, at shorter reaction time. The presence of the dye emission of the DHLA-complexes (green curve) proves that there are still dye molecules attached to the QDs after the transfer using DHLA. The trend of the change in emission intensity after the transfer is the same: the water-soluble DHLA-complexes have a higher QD emission and a lower dye emission than the MPA-complexes. Moreover, the dye emission of the MPA- and DHLA-complexes increases when decreasing the reaction

time, which indicates that the dye detachment from QDs during refluxing can be controlled by adjusting reaction conditions. The influence of reaction conditions will be discussed below.

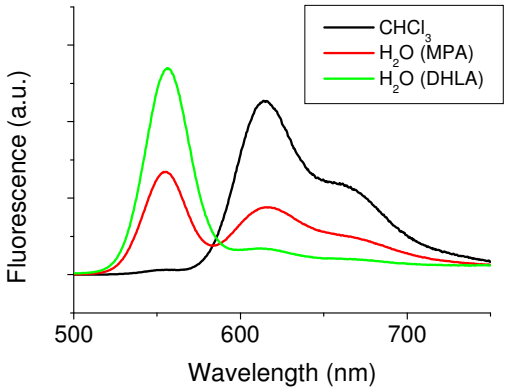

Figure 6.25: Fluorescence spectra of QD-PDIDC complexes (nominal PDIDC/QD = 3) in chloroform (black) and after transfer into water using MPA (red) and DHLA (green) as exchange ligands, respectively. Reaction time: 5 min. Reaction temperature: 65 °C.

B. Influence of reaction conditions

Amount of exchange ligands

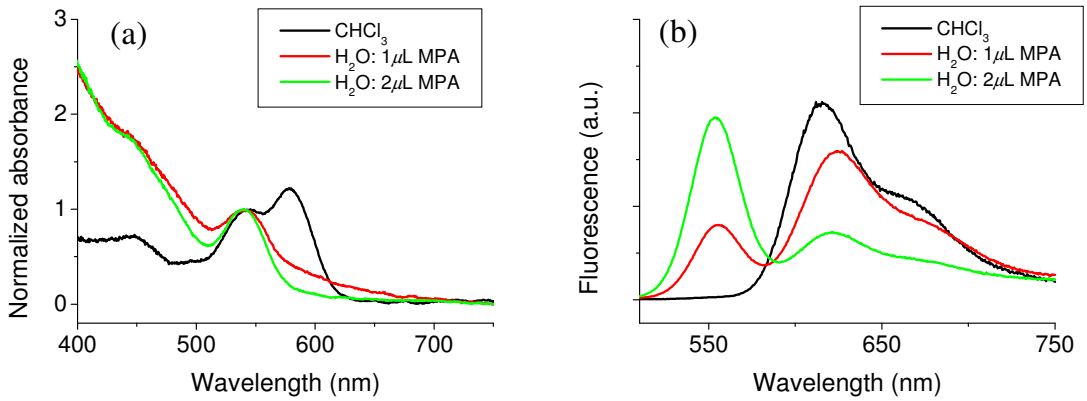

Figure 6.26: (a) Absorption and (b) fluorescence spectra of the QD-PDIDC complexes (nominal PDIDC/QD = 5) in chloroform and after transfer into water using different amount of MPA. Reaction time: 5 min. Reaction temperature: 65 °C.

Figure 6.26 and Figure 6.27 show the absorption and emission spectra of QD-PDIDC complexes after the transfer using different amounts of MPA and DHLA. In the case of DHLA, shorter reaction time was used, because the dye emission after the transfer was very low at longer reaction time and thereby the trend of the change in dye emission

intensity was not easy to be observed. The black curves in Figure 6.26 and Figure 6.27 are the absorption and emission of the complexes (PDIDC/QD = 5) in organic solvent before the transfer. As shown in Figure 6.26 b and Figure 6.27 b, decreasing the amount of the exchange ligands increases the dye emission and decreases the QD emission. Hence, decreasing the amount of the exchange ligands can reduce the detachment of dye molecules from QDs. However, a decrease in the amount of the exchange ligand also induces aggregation of the particles, which is indicated by the scattering contribution in the absorption spectra (Figure 6.26 a and Figure 6.27 a). When the amount of the exchange ligands is not enough to replace a sufficient amount of the original organic ligands (oleic acid and oleylamine) on QDs, the complex particles tend to aggregate after being transferred into water due to the unexchanged organic ligands.

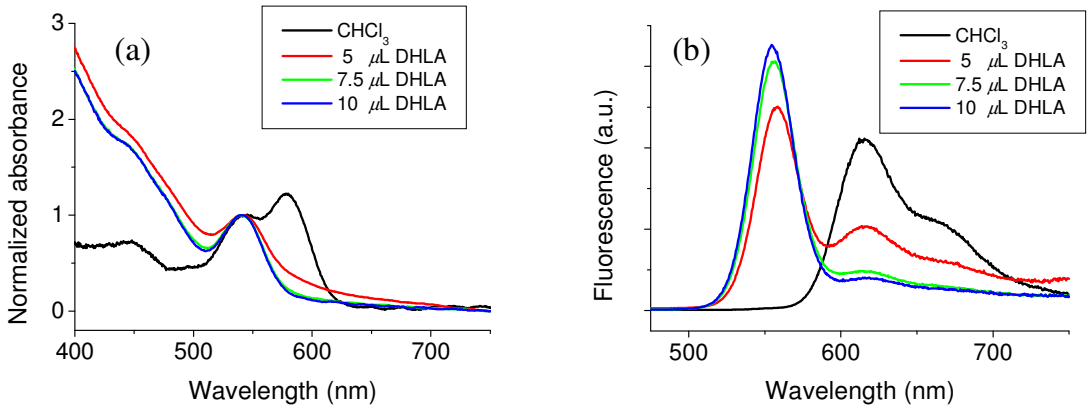

Figure 6.27: (a) Absorption and (b) fluorescence spectra of the QD-PDIDC complexes (nominal PDIDC/QD = 5) after the transfer into water using different amount of DHLA. Reaction time: 2 min. Reaction temperature: 65 °C.

Reaction time

For both MPA and DHLA, as the reaction time decreases, the QD emission decreases and the dye emission increases gradually (Figure 6.28 b and Figure 6.29 b), which indicates that the decrease in reaction time can reduce the detachment of dye molecules from QDs. However, the decrease in reaction time also induces aggregation of the particles due to the insufficient ligand exchange, as indicated by the scattering in the absorption spectra in Figure 6.28 a and Figure 6.29 a.

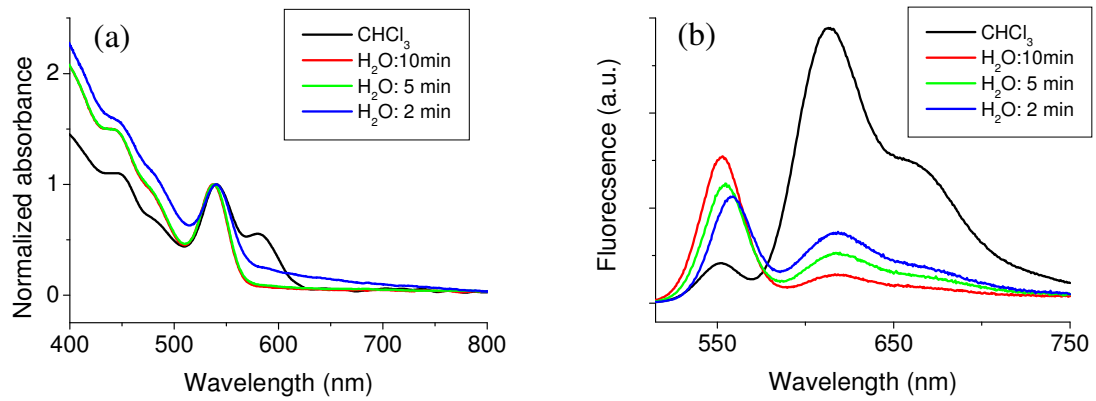

Figure 6.28: (a) Absorption and (b) fluorescence spectra of the QD-PDIDC complexes (nominal PDIDC/QD = 3) in chloroform and after the transfer into water using MPA at different reaction times. Reaction temperature: 65 °C.

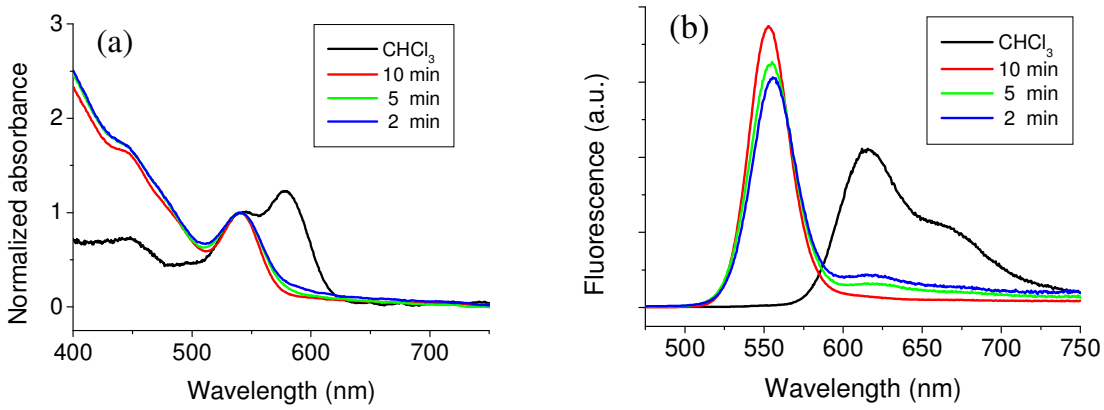

Figure 6.29: (a) Absorption and (b) fluorescence spectra of the QD-PDIDC complexes (nominal PDIDC/QD = 5) in chloroform and after the transfer into water using DHLA at different reaction times. Reaction temperature: 45 °C.

Reaction temperature

Using MPA as the exchange ligand, the decrease in reaction temperature reduces the detachment of dye molecules from QDs (Figure 6.30 b). As can also be seen from the absorption spectra (Figure 6.30 a), a lower reaction temperature increases the number of attached dye molecules attached to QD after transfer, and does not lead to particle aggregation. Comparing MPA-complex and DHLA-complex, the reaction temperature does not seem to have a significant influence on the DHLA-complexes. The emission from dye does not increase too much with decreasing reaction temperature (Figure 6.31).

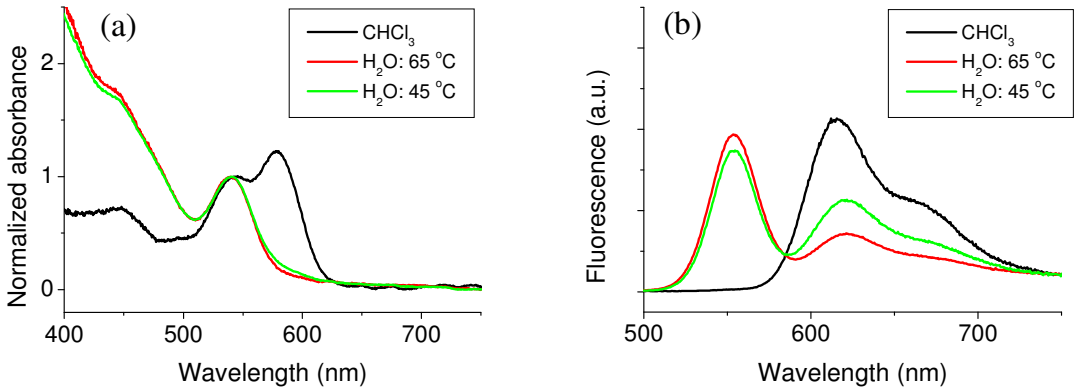

Figure 6.30: (a) Absorption and (b) fluorescence spectra of the QD-PDIDC complexes (nominal PDIDC/QD = 5) in chloroform and after the transfer into water using MPA at different reaction temperatures. Reaction time: 5 min.

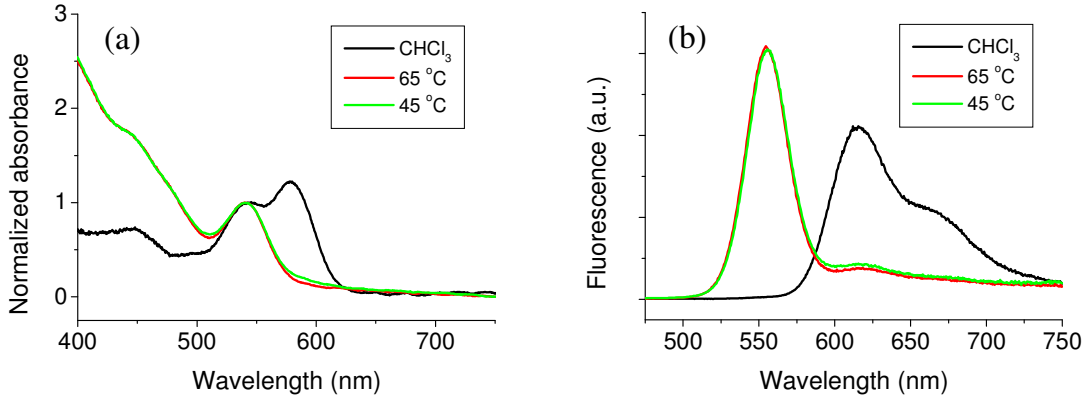

Figure 6.31: (a) Absorption and (b) fluorescence spectra of the QD-PDIDC complexes (nominal PDIDC/QD = 5) in chloroform and after the transfer into water using DHLA at different reaction temperatures. Reaction time: 2 min.

Table 6.8: Optimal conditions for the transfer using different exchange ligands.

	MPA	DHLA
Ligand amount	2 μL	7.5 μL
Reaction time	5 min	2 min
Reaction temperature	45 °C	45 °C

As a conclusion, Table 6.8 lists the optimal conditions for the transfer using the refluxing method.

C. Stability

Figure 6.32 shows time dependent absorption and emission spectra of QD-PDIDC complexes after transfer in water using MPA under the optimal reaction conditions (see Table 6.8). The pH of the sample solution is ~ 10. The emission from QDs decreased with time, and the emission from dyes increased in the first day and then decreased with time. The tendency is similar to that of complexes in organic solvent. After 25 days, the particles started to precipitate, and all the particles precipitated after one month. The precipitation of the complexes is due to the limited temporal colloidal stability of the MPA-capped QDs (between 3 days and 1 month) [190].

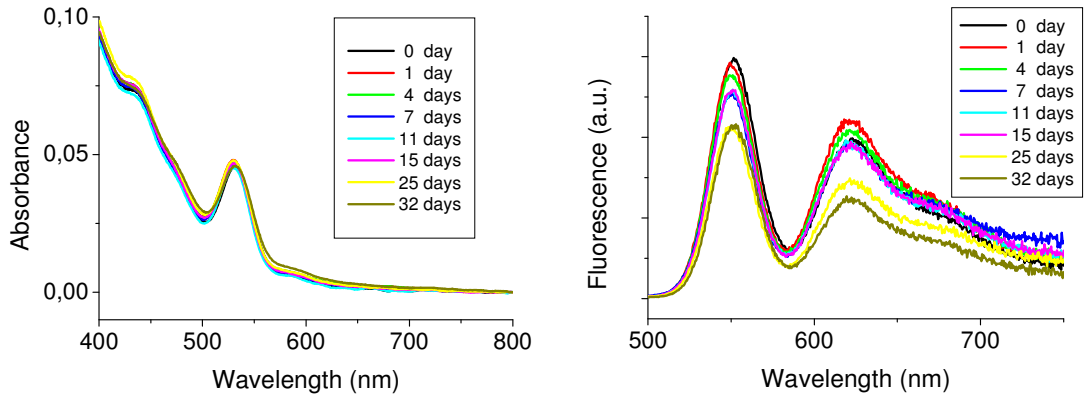

Figure 6.32: Time dependent absorption and fluorescence spectra of QD-PDIDC complexes (nominal PDIDC/QD = 8) after transfer into water using MPA.

D. Influence of pH value

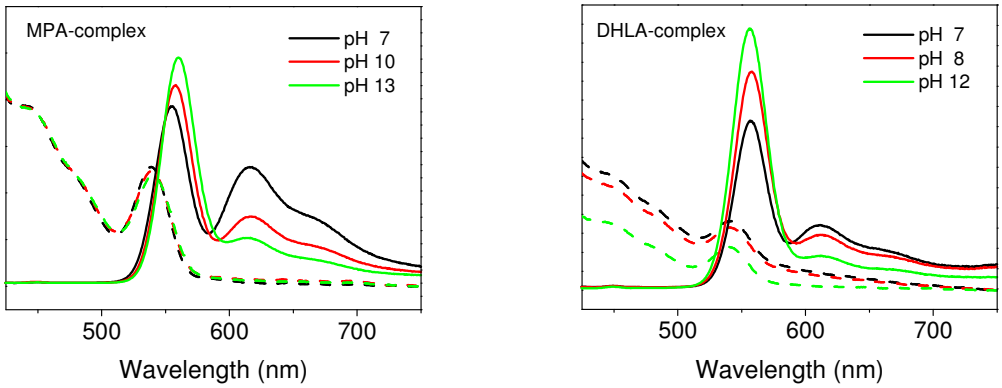

Figure 6.33: Absorption (dash line) and fluorescence (solid line) spectra of the QD-PDIDC complexes after transfer in water using MPA (left) and DHLC (right) at different pH values adjusted by $(CH_3)_4NOH$.

Both for MPA-complexes and DHLA-complexes, when the pH of their aqueous solutions was increased by adding $(CH_3)_4NOH$, the emission from QDs increased while the emission from dyes decreased, as shown in Figure 6.33.

One explanation for such a phenomenon is that the complex particles tend to aggregate at low pH value and this affects the energy transfer between QDs and dye molecules. The aggregation at low pH is more apparent in the case of DHLA-complexes. The pKa value of DHLA (pKa = 4.73 [188]) is larger than that of MPA (pKa = 4.3) and thus a higher pH is needed for deprotonation of DHLA. Therefore, the solution was a little turbid when the pH was 7, corresponding to the strong scattering in the absorption spectra. The solution turned clear when the pH reached ~ 12. Although the MPA-complex aqueous solution was clear at neutral pH and there was no strong scattering in the absorption spectra, it is believed that small clusters or aggregates were still present. The aggregation is thought to be driven by the reduction of the net surface charges induced by lowering the pH value [191]. When the complex particles are aggregated, energy from one QD can not only be transferred to the dye molecules attached to this QD but also to adjacent QDs. As a result, the QD emission is quenched and the sensitized dye emission is enhanced.

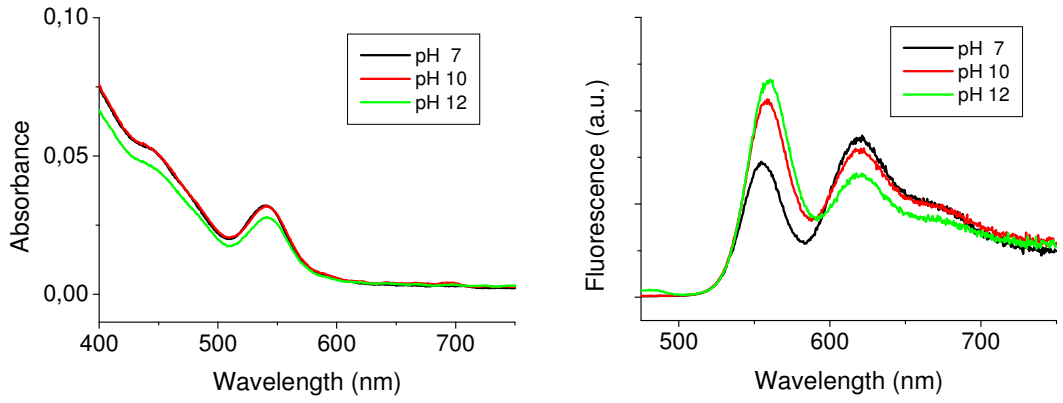

Figure 6.34: Absorption (left) and fluorescence (right) spectra of the QD-PDIDC complexes after transfer in water using MPA at different pH values adjusted by NaOH.

The amine group has been proven to enhance the fluorescence intensity of QDs [192], and from my previous experience on water-soluble QDs, the addition of $(CH_3)_4NOH$ can also increase the QD fluorescence intensity. The increasing $(CH_3)_4NOH$ amount might be another explanation for the increasing QD emission intensity with increasing pH

value. To investigate the influence of organic base $(CH_3)_4NOH$ on the QD emission in water-soluble complexes, the inorganic base NaOH was also used to adjust the pH of the aqueous solution. Figure 6.34 shows the absorption and emission spectra of MPA-complexes at different pH values adjusted by using NaOH. As can be seen, the QD emission in the complexes still increased with increasing pH adjusted with NaOH. Therefore, it can be concluded that no matter which base is used, the QD emission increases and the dye emission decreases with increasing pH. The degree of aggregation is probably the main reason for the above observations.

Due to the dependence of the relative emission intensities of QD and dye on pH, the water-soluble QD-dye complexes might have potential to be a pH sensor, and more importantly, this pH sensor is ratiometric. Compared to typical chemo- and biosensors that display a single intensity-based response to analytes, the ratiometric sensor is more powerful because it is not sensitive to fluctuations of light excitation or collection efficiency as sensing is self-referencing [193]. However, so far, the problem is that this pH dependence is not reversible, and more experiments need to be done to further understand the influence of pH value on the water-soluble QD-dye complexes.

6.4 Quantum dot assemblies

The ideal aim of the work presented in this section was to prepare QD dimers using dyes with bifunctional groups (two dicarboxylate groups at two ends of the molecule) as binding anchors. Metal nanoparticle dimers, such as gold and silver nanoparticle dimers, have been successfully prepared using different approaches [194, 195, 196, 197]. However, there are, so far, very few reports on the assembly of semiconductor nanoparticle dimers [198, 199]. In these works, CdSe [198] or CdTe [199] QDs were linked by bifunctional molecules. Due to the non-specific binding of bifunctional molecules to QDs, the final products were composed of monomers, dimers and oligomers. Similar to the work reported in the literature, since here bifunctional dye molecules are used to link QDs, the formation of a mixture of QD monomers, dimers, oligomers and small aggregates (in this section called QD assemblies) can not be avoided.

6.4.1 Experimental procedure

QD assemblies were prepared in organic solution using a similar procedure as described in section 6.2.1. The structures of the dyes are shown in Figure 6.35. The dye molecules were supplied by the workgroup of Prof. Dr. Klaus Müllen (Max Planck Institute for Polymer Research, Mainz, Germany).

TA-PDI stock solution (0.1 mM) was prepared by dissolving 1.02 mg of TA-PDI in 10 ml of THF. TDA stock solution (0.1 mM) was prepared by dissolving 1.44 mg of TDA in 10 ml of chloroform.

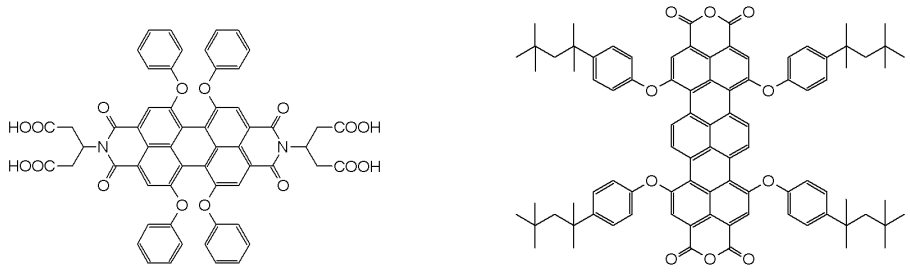

TA-PDI TDA

Figure 6.35: Structures of dyes used to link QDs in organic solution.

QD assemblies using CdSe/4ML CdS/1ML ZnS QDs Typically, the TA-PDI THF solution or TDA chloroform solution, the volume of which was calculated according to the QD/dye ratio, was first mixed with 2.5 ml of methanol. Then, 100 μL of K_2CO_3 methanol solution (32 mM) and 2.5 ml of a toluene solution of QD (concentration ≈ 3 μM) were added. The mixture was sonicated for 4 h. Then 5 mL of methanol was added and the resulting turbid solution was centrifuged. After decanting the supernatant, the precipitate was redispersed in chloroform or toluene to obtain a clear solution.

QD assemblies using CdSe/1ML CdS/3ML ZnS or CdSe/4ML ZnS QDs Typically, the TA-PDI THF solution or TDA chloroform solution, the volume of which was calculated according to the QD/dye ratio, was first mixed with 2.5 ml of methanol. Then, 100 μL of K_2CO_3 methanol solution (32 mM) and 2.5 ml of a toluene solution of QD (concentration ≈ 3 μM) were added. The mixture was shaken for 1 min. Then 5 mL of methanol was added and the resulting turbid solution was centrifuged. After decanting the supernatant, the precipitate was redispersed in chloroform or toluene. This turbid solution was then directly centrifuged at 4,000 rpm for 10 min, and the supernatant was taken as the final product.

6.4.2 Results and discussion

6.4.2.1 Optical properties of dye molecules

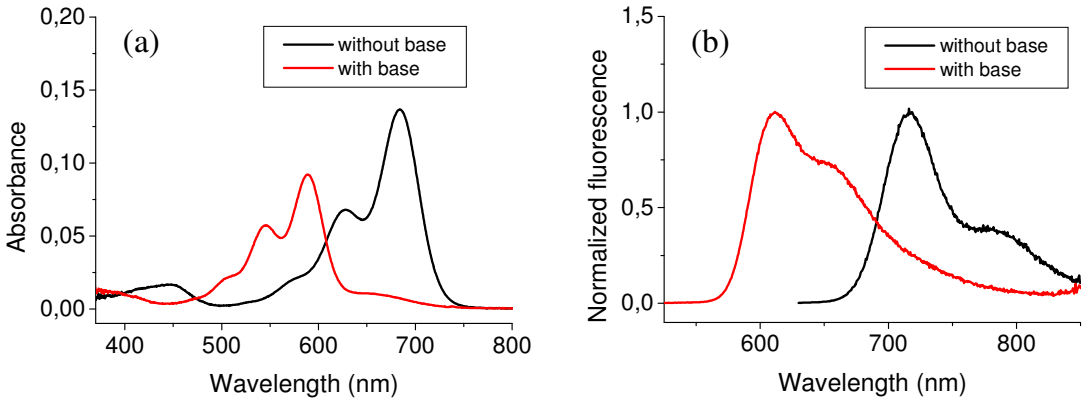

Figure 6.36: (a) Normalized absorption spectra and (b) fluorescence spectra of TDA dye in chloroform (concentration: 2.20×10^{-6} M) before and after adding K_2CO_3 base.

When the K_2CO_3/methanol solution was added into the TDA chloroform solution, the color of the TDA solution immediately turned from blue-green to purple. A blue shift of

~ 100 nm was observed in the absorption and fluorescence spectra of the TDA dye in chloroform, as shown in Figure 6.36. This shift is caused by the dianhydride ring opening of the TDA molecule. The absorbance of the TDA dye decreases after the addition of the K_2CO_3 base. In the case of TA-PDI, the addition of the K_2CO_3 base did not change the absorbance and the positions of the absorption and fluorescence peaks, as can be seen in Figure 6.37.

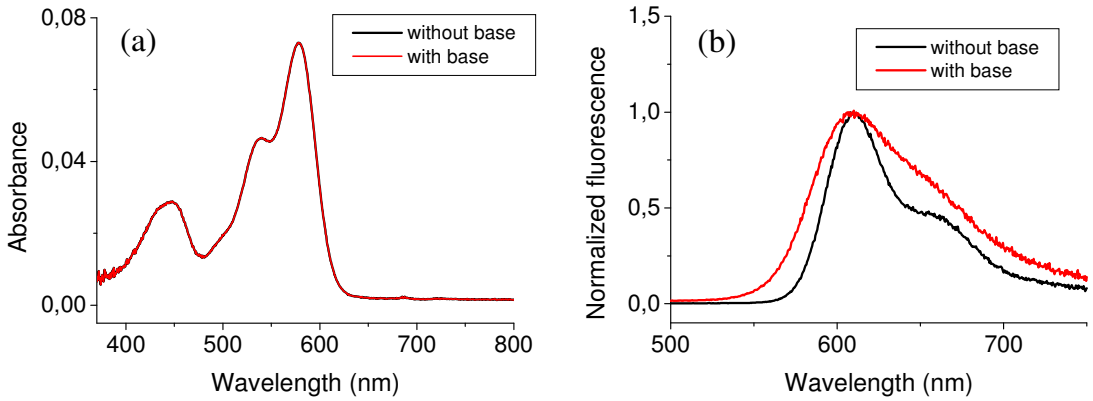

Figure 6.37: (a) Normalized absorption spectra and (b) fluorescence spectra of TA-PDI dye in chloroform (concentration: 2.46×10^{-6} M) before and after adding K_2CO_3 base.

6.4.2.2 QD assemblies using CdSe/4ML CdS/1ML ZnS QDs

CdSe/4ML CdS/1ML ZnS QDs had an emission peak at 602 nm and an average diameter of 7.1 nm (the CdSe core had an absorption peak of at 545 nm).

When CdSe/4ML CdS/1ML ZnS QDs were mixed with TA-PDI molecules at a QD/TA-PDI ratio of 1, the particles after centrifugation stuck to the wall of the centrifuge tube and could not be dispersed in chloroform or toluene. This is attributed to the formation of large QD aggregates or even a network of particles. As the amount of the TA-PDI molecules decreased, i.e. the QD/TA-PDI ratio increased to 3, a mixture of monomers, dimers and oligomers were formed (Figure 6.38 a). The percentage of dimers determined from the TEM measurements is ~ 17 % (27 out of 156 "particles"). It should be noted that monomers, dimers, oligomers and small aggregates are all counted as one "particle" when determining the percentage of dimers. When the QD/TA-PDI ratio was further increased to 5, most of the QDs remained monomers, as seen in Figure

6.38 b. The inset shows one of the few cases of QD dimers in this mixture. This indicates that the amount of the TA-PDI molecules was not sufficient to link QDs.

When CdSe/4ML CdS/1ML ZnS QDs were mixed with TDA molecules at the QD/TDA ratios of 1 and 2, a mixture of monomers, dimers and oligomers were formed, as shown in Figure 6.39. According to the TEM measurements, the percentage of the dimers at ratio 1 (~ 33 %, 71 out of 213 "particles") is larger than that of the dimers at ratio 2 (~ 21 %, 28 out of 132 "particles").

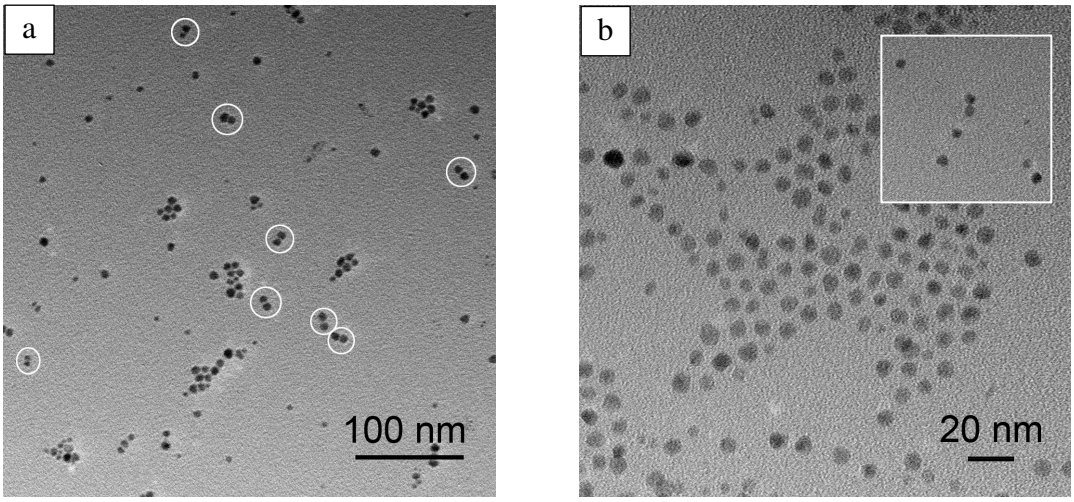

Figure 6.38: TEM images of CdSe/4ML CdS/1ML ZnS QD assemblies linked by TA-PDI at different QD/ TA-PDI ratios: (a) QD/ TA-PDI = 3 and (b) QD/ TA-PDI = 5.

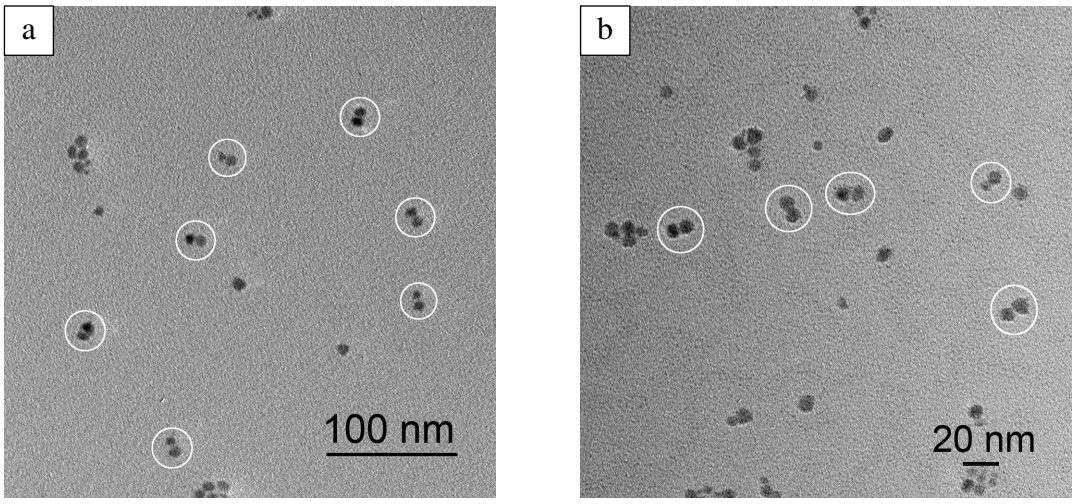

Figure 6.39: TEM images of CdSe/4ML CdS/1ML ZnS QD assemblies linked by TDA at different QD/ TDA ratios: (a) QD/ TDA = 1 and (b) QD/ TDA = 2.

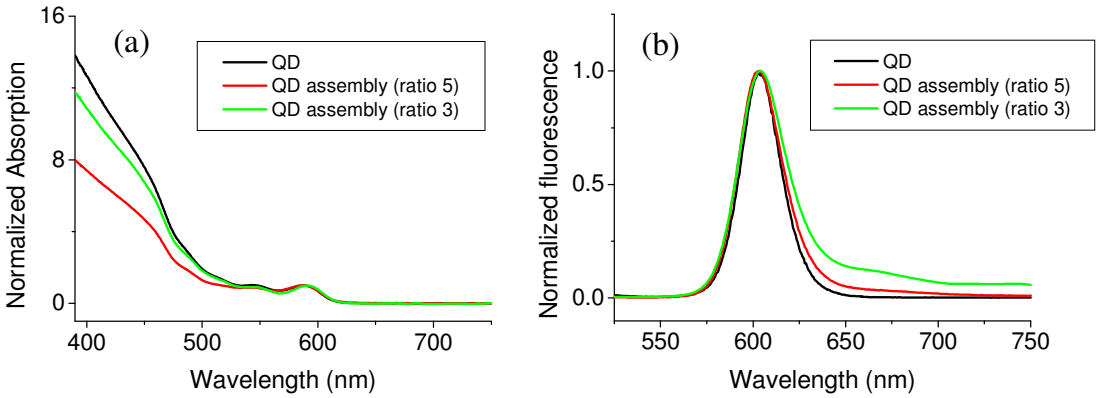

Figure 6.40: (a) Normalized absorption spectra and (b) fluorescence spectra of CdSe/4ML CdS/1ML ZnS QDs and their corresponding assemblies linked by TA-PDI in toluene at different QD/ TA-PDI ratios (λ_{ex} = 390 nm).

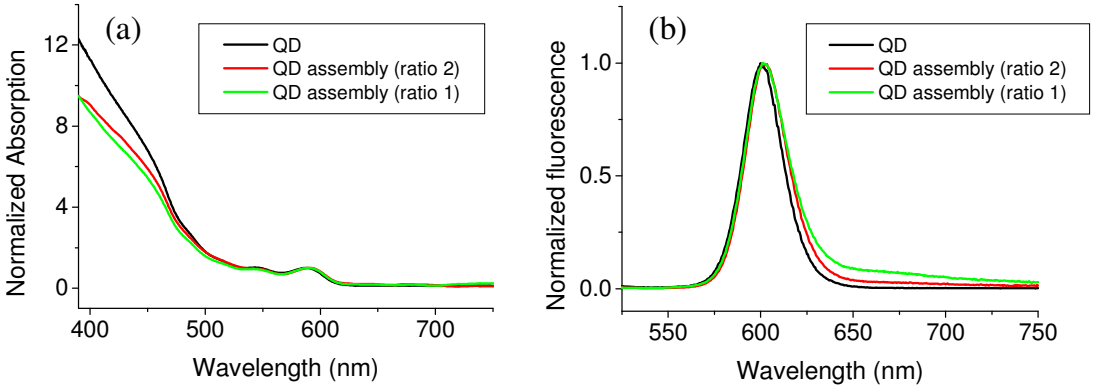

Figure 6.41: (a) Normalized absorption spectra and (b) fluorescence spectra of CdSe/4ML CdS/1ML ZnS QDs and their corresponding assemblies linked by TDA in toluene at different QD/TDA ratios (λ_{ex} = 390 nm).

The linkage of QDs by dye molecules can be provn by the presence of dye emission in the emission spectra of the QD assemblies (Figure 6.40 b and Figure 6.41 b). Since the contribution due to direct excitation of the dye has been subtracted and dynamic quenching can be neglected (the concentration of the solution for the optical measurements is in nM range), the emission from the dye in Figure 6.40 b and Figure 6.41 b is only caused by the energy transfer from the QDs to the dye molecules that link the QDs. The dye emission at smaller ratio (ratio 3 for TA-PDI, and ratio 1 for TDA) is stronger than at higher ratio (ratio 5 for TA-PDI, and ratio 2 for TDA), which is consistent with the fact that the dye amount in the solution at smaller ratio is larger than that at higher ratio. The absorption spectra of the QD assemblies do not show significant

dye absorption (Figure 6.40 a and Figure 6.41 a). This can be attributed to the low concentration of the dye molecules relative to the QD concentration in the solution.

6.4.2.3 QD assemblies using CdSe/1ML CdS/3ML ZnS or CdSe/4ML ZnS QDs

CdSe/1ML CdS/3ML ZnS QDs had an emission peak at 574 nm and an average diameter of 6.0 nm (the CdSe core had an absorption peak of at 547 nm). CdSe/4ML ZnS QDs had an emission peak at 541 nm and an average diameter of 4.9 nm (the CdSe core had an absorption peak of at 525 nm).

In the presence of K_2CO_3 base, when the mixture of CdSe/1ML CdS/3ML ZnS QDs and dye linker (TA-PDI or TDA) at the QD/dye ratio of 1 was sonicated for 4 h, the final products after centrifugation could not be dispersed in chloroform or toluene. After decreasing the dye amount, i.e., increasing the QD/TA-PDI ratio from 1 to 3, 5 and 8 or increasing the QD/TDA ratio from 1 to 2 and 4, the obtained products still could not be dispersed in chloroform or toluene. The same phenomenon was observed when reducing the sonication time from 4h to 2h, 1h and 30 min, using high QD/dye ratio (QD/TA-PDI = 8, QD/TDA = 4). These indicate that, under all the conditions mentioned above, the QDs formed big aggregates or networks.

In order to decrease the number of collisions between QDs and dye molecules and accordingly decrease the possibility of the formation of aggregates, mixtures of CdSe/1ML CdS/3ML ZnS QDs in chloroform and dye in methanol (QD/dye ratio: QD/TA-PDI = 8, QD/TDA = 4), in the presence of K_2CO_3, were only shaken for 1 min and then centrifuged. After decanting the supernatant, the precipitate was redispersed in chloroform or toluene. These solutions were a little turbid. This indicates that QDs are still linked by the dye molecules and some big QD aggregates are formed, although the mixture of QD and dye is shaken for a very short time. As discussed in section 6.2.2.2 C, the addition of methanol to the mixtures could help to remove the ligands from QDs, and thus help the attachment of the dye molecules even without sonication. To separate out the big aggregates, the turbid solution was then directly centrifuged at 4,000 rpm for 10 min. The precipitate was composed of large aggregates and the clear supernatant was taken as the final product. The mixtures with CdSe/4ML ZnS QDs were treated in the same fashion.

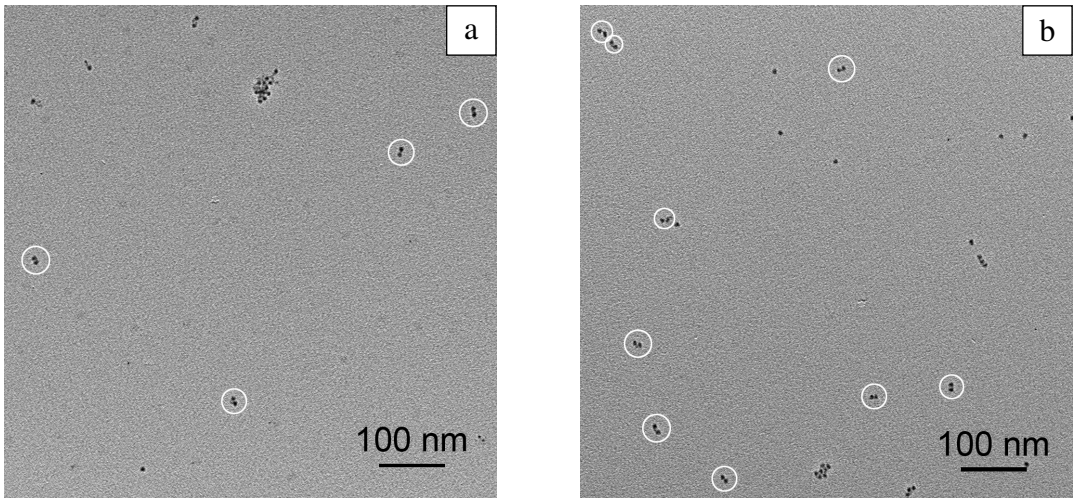

Figure 6.42: TEM images of CdSe/1ML CdS/3ML ZnS QD assemblies linked by (a) TA-PDI: QD/TA-PDI = 8, and (b) TDA: QD/TDA = 4.

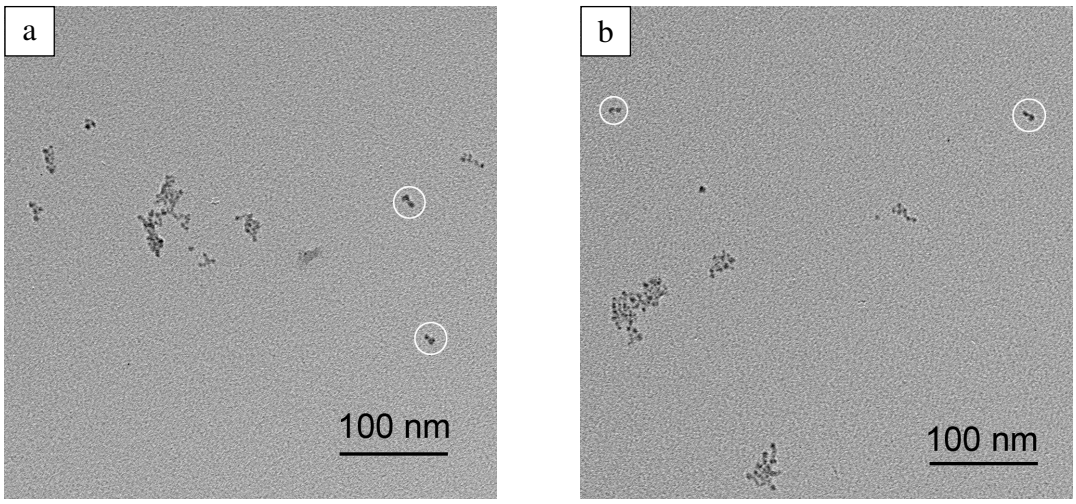

Figure 6.43: TEM images of CdSe/4ML ZnS QD assemblies linked by (a) TA-PDI: QD/TA-PDI = 8, and (b) TDA: QD/TDA = 4.

Figure 6.42 and Figure 6.43 show the TEM images of the CdSe/1ML CdS/3ML ZnS QD assemblies and the CdSe/4ML ZnS QD assemblies linked by TA-PDI or TDA dye molecules. The percentages of CdSe/1ML CdS/3ML ZnS QD dimers using TA-PDI and TDA linkers were ~ 24 % (32 out of 136 "particles") and ~ 39 % (73 out of 187 "particles"), respectively. The percentages of CdSe/4ML ZnS QD dimers using TA-PDI and TDA linkers were ~ 15 % (18 out of 113 "particles") and ~ 19 % (30 out of 155 "particles"), respectively. Using CdSe/1ML CdS/3ML ZnS QDs can produce more dimers than using CdSe/4ML ZnS QDs, and the latter tend to form more oligomers or small aggregates than dimers. The reason might be that CdSe/4ML ZnS QDs with

smaller sizes than CdSe/1ML CdS/3ML ZnS QDs have a higher surface energy and are more reactive, which facilitates the binding of the dye linkers to the QDs.

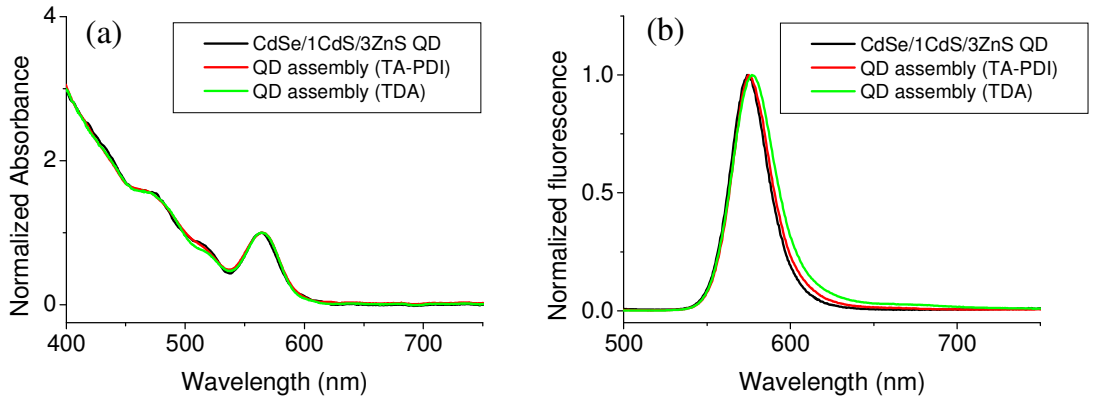

Figure 6.44: (a) Normalized absorption spectra and (b) fluorescence spectra of CdSe/1ML CdS/3ML ZnS QDs and their corresponding assemblies linked by TA-PDI and TDA in toluene, respectively (λ_{ex} = 390 nm). QD/TA-PDI = 8, and QD/TDA = 4.

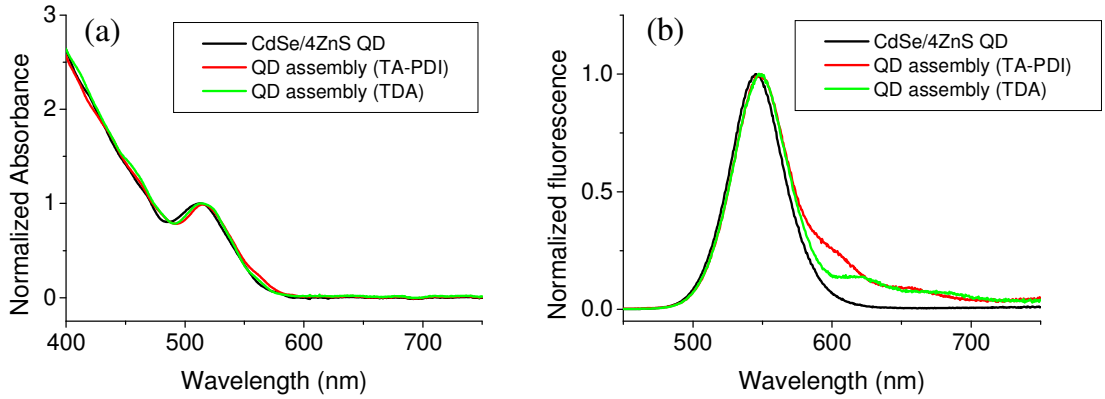

Figure 6.45: (a) Normalized absorption spectra and (b) fluorescence spectra of CdSe/4ML ZnS QDs and their corresponding assemblies linked by TA-PDI and TDA in toluene, respectively (λ_{ex} = 390 nm). QD/TA-PDI = 8, and QD/TDA = 4.

Figure 6.44 and Figure 6.45 show the optical properties of the CdSe/1ML CdS/3ML ZnS QD and CdSe/4ML ZnS QD assemblies, respectively. The absorption of both QD assemblies shows no significant change compared with that of the corresponding QDs. The dye emission in the emission spectra of the QD assemblies indicates the presence of the dye in the final solution. Figure 6.46 shows the emission spectra of the CdSe/4ML ZnS QD assemblies excited at different wavelengths. The dye absorption at 390 nm is much lower than that at 550 nm (see Figure 6.36 a and Figure 6.37 a). If the dye

emission comes from the free dye, the intensity of the dye emission in the emission spectra of the assemblies excited at 390 nm will be lower than that excited at 550 nm. However, as shown in Figure 6.46, in both cases of TA-PDI and TDA, the dye emission excited at 390 nm is stronger than that excited at 550 nm, which indicates that the dye emission in the QD assemblies is mainly caused by the energy transfer from the QDs to the dye molecules that link the QDs, because the QD emission excited at 390 nm is stronger than that excited at 550 nm due to the higher absorption of QDs at 390 nm than at 550 nm (see Figure 6.44 a and Figure 6.45 a). This also proves at least partial linkage of the QDs by the dye molecules.

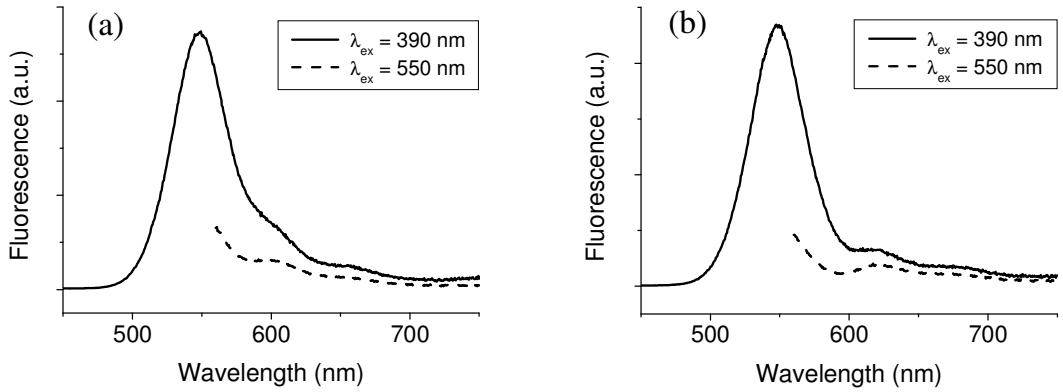

Figure 6.46: Fluorescence spectra of CdSe/4ML ZnS QD assemblies linked by (a) TA-PDI and (b) TDA in toluene at different excitation wavelengths.

Table 6.9: Summary of preliminary results of QD assemblies using different QDs and dyes.

QDs	Dyes	QD/dye ratio	Preparation	Dimer percentage
CdSe/4ML CdS/1ML ZnS (diameter: 7.1 nm)	TA-PDI	3:1	sonicating	0.17
	TDA	1:1		0.33
CdSe/1ML CdS/3ML ZnS (diameter: 6.0 nm)	TA-PDI	8:1	shaking	0.24
	TDA	4:1		0.39
CdSe/4ML ZnS (diameter: 4.9 nm)	TA-PDI	8:1	shaking	0.15
	TDA	4:1		0.19

Table 6.9 summarizes the preliminary results for QD assemblies using different QDs and dyes. It can be seen that, using bigger QDs seems to be more favorable with respect to forming QD dimers and preventing the aggregation of QDs than using smaller ones, and the percentage of QD dimers using TDA linker appears to be larger than that using TA-PDI linker.

The experiments described above are preliminary and further experiments and measurements need to be done to improve the preparation and separation of QD dimers and oligomers. For instance, the density gradient rate separation method [200, 201] could be tried to separate dimers from monomers, oligomers and small aggregates. Combined AFM and confocal fluorescence microscopy could be used to further characterize dimers or higher oligomers.

6.5 Quantum dot - calixarene complexes

6.5.1 Experimental procedure

The preparation of QD-calixarene complexes is similar to that of QD-dye complexes in organic solvent described in the previous section. CdSe/4ML CdS/1ML ZnS QDs were used. Calix[4]arenes with dicarboxylic acid groups were supplied by the workgroup of Prof. Dr. Böhmer (Abteilung für Lehramtskandidaten der Chemie der Johannes-Gutenberg-Universität Mainz). The structure of the used calix[4]arene is shown in Figure 6.47.

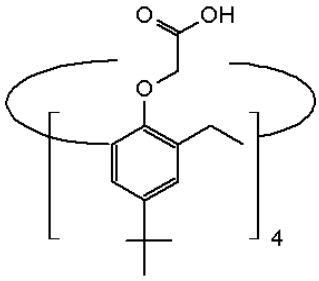

Figure 6.47: Structure of the used calixa[4]rene.

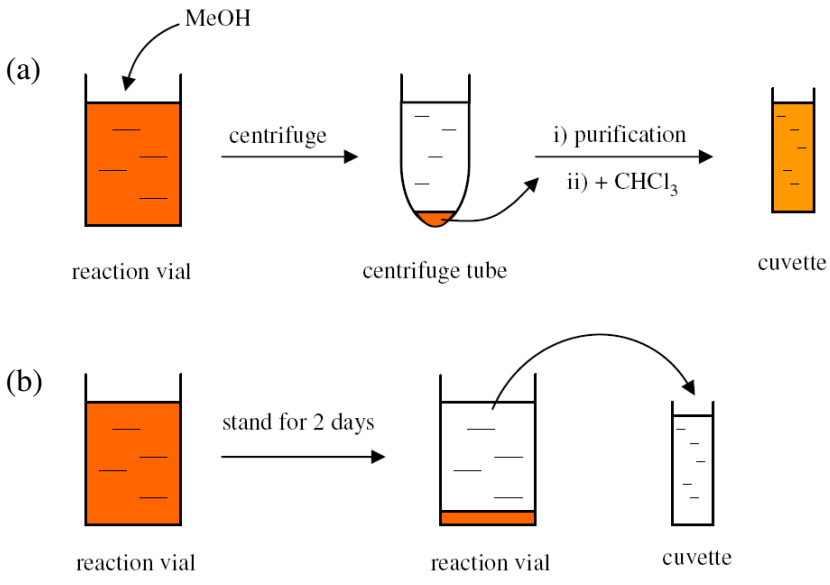

Figure 6.48: Schematic diagram of two different treatment methods for absorption measurements.

Typically, 2.5 ml of a chloroform solution of QD (concentration ≈ 2 μM) were mixed with 2.5 ml of a methanol solution of calix[4]arene (concentration ≈ 4 - 20 μM). After

adding 100 μL of K_2CO_3 methanol solution (32 mM), the mixture was sonicated for 4 h to obtain the raw QD-calixarene complex solution. The as-prepared solution was then treated in two different ways for absorption measurements.

One was to add 5 mL of methanol to the raw QD-calixarene complex solution, centrifuge the solution and then redisperse the precipitate in chloroform. The purification procedure was then performed by adding methanol, centrifuging, and re-dissolving the precipitate in chloroform to obtain the final QD-calixarene complex solution. The precipitation and purification procedure helps remove the calixarene molecules that are not attached to the QDs. The absorption of the final QD-calixarene complex solution was then measured. The whole process is illustrated in Figure 6.48 a. The results and discussion are shown in section 6.5.2.1.

The other was to leave the raw QD-calixarene complex solution stand for two days to let the particles precipitate out and directly measure the absorption of the supernatant, as illustrated in Figure 6.48 b. In the supernatant were the organic ligands (oleic acid and oleylamine) detached from the QDs during sonication and the unattached calixarene molecules. For comparison, the QDs were also sonicated under the same conditions but without adding calixarene molecules, and the absorption of the supernatant of the pure QDs was measured. In this supernatant were only the organic ligands detached from the QDs. The results and discussion are shown in section 6.5.2.2.

6.5.2 Results and discussion

6.5.2.1 Spectral characterization

Since calixarene has a pronounced absorption peak at ~ 280 nm (see green curve in Figure 6.49 a), absorption spectra were used to characterize the formation of QD-calixarene complexes. If QD-calixarene complexes show the absorption peak of calixarene, it proves the attachment of calixarene molecules to QD. However, as shown in Figure 6.49 a, the absorption of the final QD-calixarene complexes (nominal calixarene/QD ratio = 10) after removing the unattached calixarene by precipitation and purification procedure (red curve) shows no difference compared to pure QD absorption (black curve). Does this mean that the calixarenes can not be attached to QDs?

To find out the answer, QDs were simply mixes with calixarene molecules in chloroform at different calixarene/QD ratios, and absorption spectra of the mixtures were recorded. As can be seen in Figure 6.49 b, the calixarene absorption in the mixture can be distinguished only when the calixarene/QD ratio is at least 100:1. If the calixarene/QD ratio in the case of QD-calixarene complexes is smaller than 100, the difference between QD and complex absorptions will not be observed. Therefore, it is hard to prove the formation of QD-calixarene complex by analyzing the complex absorption spectra.

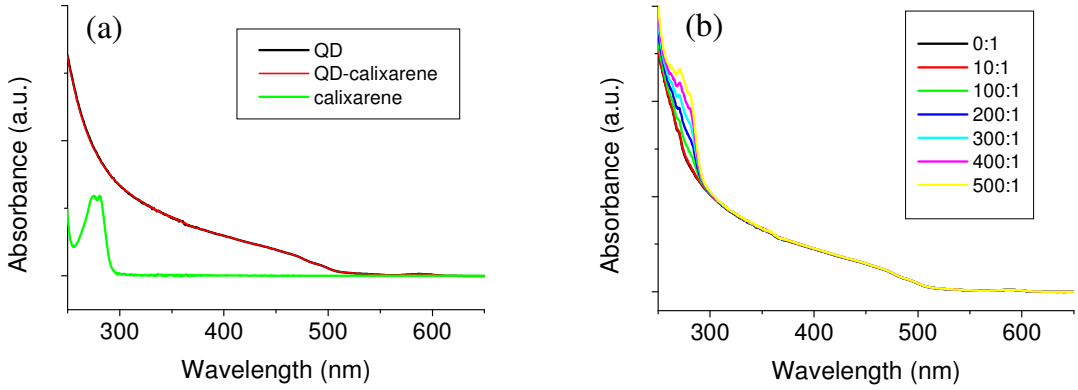

Figure 6.49: (a) Absorption spectra of pure QD (black), QD-calixarene complex (red) and pure calixarene (green) in chloroform. The concentration of the pure QDs is 1.7×10^{-7} M. The concentration of the pure calixarene is 5.9×10^{-5} M. (b) Absorption spectra of mixtures of QD and calixarene at different calixarene/QD ratios in chloroform.

6.5.2.2 Determination of the number of the attached calixarene

The strategy for investigating the attachment of calixarene to QD was therefore changed. As illustrated in Figure 6.48 b, the raw complex solution or pure QD solution after sonication was left for 2 days to let the particles precipitate, and then the absorption of the supernatant of the raw QD-calixarene complex solution and the pure QD solution were directly measured.

As shown in Figure 6.50, the absorption of the supernatant of the pure QD solution (black curves) has a broad peak at around 270 nm. This peak could be from the absorption of the organic ligands (oleic acid and oleylamine) detached from QD surface upon sonication. The red curves are the absorption spectra of the pure calixarene used for complex preparation at different initial calixarene/QD ratios. The absorption of the

supernatant of the raw complex solution (green curves) consist of the absorption of both the organic ligands detached from QD surface and the unattached calixarene. Therefore, subtracting the contribution of the organic ligand absorption (the absorption of the QD supernatant, red curves) from the absorption of the complex supernatant (green curves), the absorption of the unattached calixarene can be obtained (blue curves).

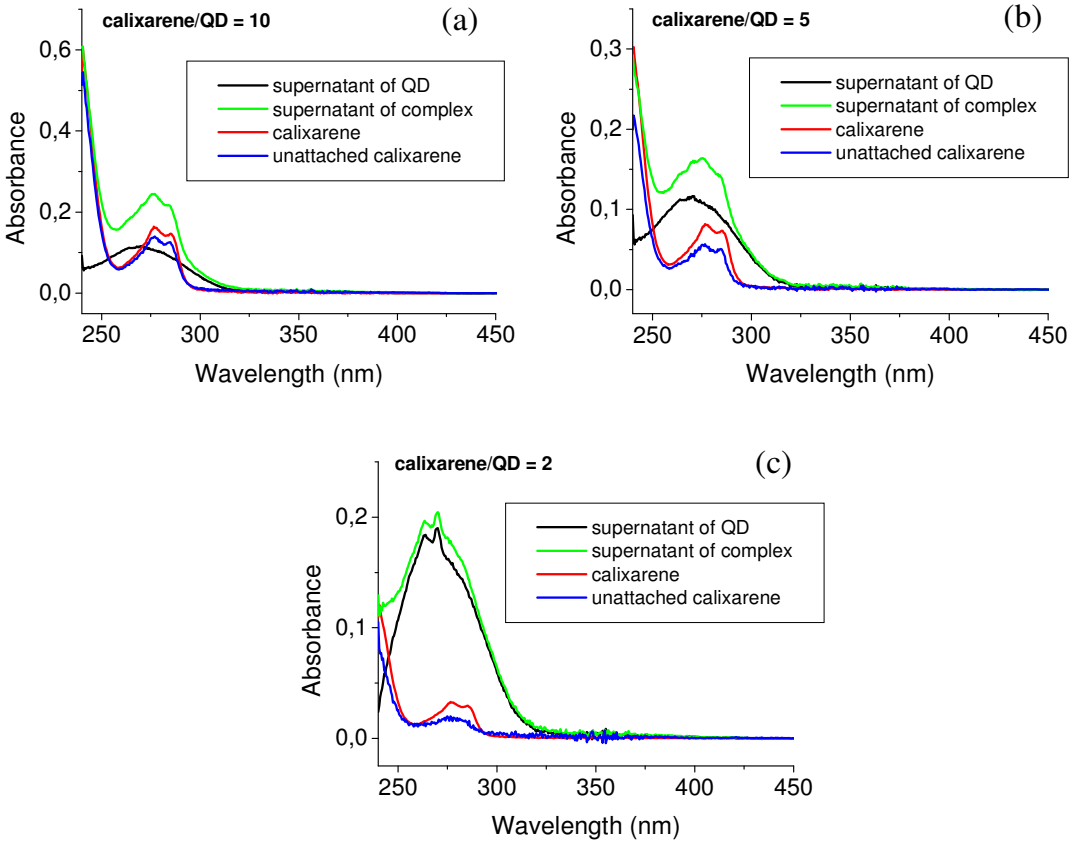

Figure 6.50: Absorption spectra of the supernatant of the pure QD solution (black), the supernatant of the row complex solution (green), the calixarene (red) and the unattached calixarene (blue) at different initial calixarene/QD ratios: (a) 10:1, (b) 5:1 and (c) 2:1.

Obviously, in all cases, the unattached calixarene absorption decreases (blue curves) relative to the absorption of the initially added calixarene (red curves). This proves the attachment of the calixarene to the QDs and indicates that only few calixarene molecules can be attached. By comparing the absorbance of the calixarene and unattached calixarene, the number of the attached calixarene for each calixarene/QD ratio can be determined. It is calculated that there are 1.6 calixarenes per QD in the cases of ratio 10 and 5, and 0.8 calixarenes per QD in the case of ratio 2. Therefore, it

can be concluded that only 1 ~ 2 calixarenes can be attached to QDs no matter how many calixarenes were added in the beginning.

6.5.2.3 Potential application

The above conclusion is interesting. Although there will always have a mixture of QDs with 0, 1, 2 … calixarene molecules in the solution, the percentage of QDs with 1 or 2 calixarene molecules should be still high due to the large size of the calixarene molecule. Therefore, there could be two potential applications of such QD-calixarene hybrid system due to the fact that only 1 ~ 2 calixarene per QD can be achieved. Since dyes can be connected to the calixarene molecule and the number of the dye can be well controlled as well. If only one calixarene can be attached, then the number of the dye molecules per QD can be exactly controlled (Figure 6.51 a). Moreover, two calixarenes can also be connected to form a dimer. The attachment of only one QD to calixarene allows forming a QD-QD dimer controllably (Figure 6.51 b).

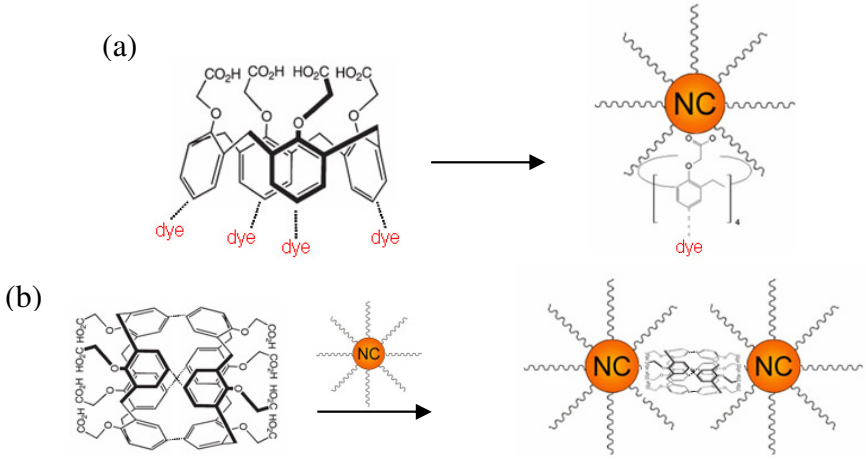

Figure 6.51: Two potential applications of the QD-calixarene hybrid system.

6.6 Conclusion

A versatile route for the preparation of extraordinarily stable QD-dye complexes by furnishing ryleneimide dyes with dicarboxylate anchors has been established. By proper choice of dye and QD components, a broad spectral range from the visible up to the NIR can be covered and additionally the efficiency of energy transfer can be easily tuned. A progressive and substantial enhancement in the energy transfer efficiency with increasing number of dye molecules attached to a single QD was observed. Through Stern-Volmer analysis, FRET was suggested as the mechanism of the energy transfer. The systematic study of the dependence of PL dynamics on the QD-dye distance, which was varied by controlling number of ZnS layers while preserving the binding geometry, provided additional proof confirming that FRET was the dominant mechanism. The stable QD-dye complexes can be easily transferred into the aqueous phase, although part of the dye molecules detached during transfer. The water-soluble QD-dye complexes showed a pH-dependent emission between QD and dye, and this allows for speculation about potential applications as ratiometric pH sensors. Using the same approach, QD dimers linked by dye molecules with two dicarboxylate groups at two ends of the molecule can also be prepared. A mixture of QD monomers, dimers, oligomers and small aggregates was obtained. The optical properties of the mixtures have proven the linkage of the QDs by the dye molecules. Further separation procedures need to be done to separate out the dimers in the mixture. Using the same route, QD-calixarene complexes have been prepared using calix[4]arene with dicarboxylic acid groups as the anchor. It was found that only 1 ~ 2 calixarenes can be attached to the QDs no matter how many calixarenes were offered in the beginning. This feature promises to assemble QD-calixarene-dye hybrids with controllable dye number per QD or QD-QD dimers for deeper insight into the energy transfer in these two systems.

7 Summary

Energy transfer based QD hybrid systems have been successfully self-assembled: QD-silica-dye hybrid system and QD-dye hybrid system. The energy transfer from QDs to dyes in both hybrid systems has been investigated.

First, two kinds of QD-silica hybrid systems, i.e. silica-QD-silica and QD-silica structures, were constructed in order to assemble QD-silica-dye hybrids where QDs were covered by a silica shell which then was labeled by dyes. In these structures energy transfer from QDs to dyes by an approach could be studied. Based on the "Stöber" method, QDs could be controllably embedded in silica colloids to form the silica-QD-silica structure. After adsorption of the amphiphilic polymer PVP, the QDs were adsorbed on APS-functionalized silica spheres with a diameter larger than 100 nm to form a QD monolayer, and then covered by silica shells. The thickness of the outer silica shell could be simply controlled by varying the TEOS amount. It was found that the silica-QD-silica structure was not formed when smaller silica core particles were used. Using the reverse microemulsion method, one single QD could be encapsulated in one small silica particle with a diameter smaller than 50 nm to achieve the QD-silica structure. The growth process was investigated and the incorporation mechanism of QDs into silica spheres was clarified. Different reaction parameters, such as the nature of surfactant molecules, the size of QDs, and the concentration of ammonium hydroxide, TEOS and QDs, were varied to achieve thin silica shell thickness. Unfortunately, both of these two structures were found to be not suitable for further FRET studies. For the QD-silica structure, the obtained minimum silica shell thickness of 8 nm is still large with respect to donor-to-acceptor distances at which FRET occurs. QD-dimers encapsulated in one silica particle, however, could be prepared which promises to study energy transfer between two single QDs. For the silica-QD-silica structure, the uneven surface after growing a thin silica shell does not favor a precise definition of the donor-to-acceptor distance.

Inspired by the silica-QD-silica structure, a QD-silica-dye hybrid system was prepared successfully: the "pure" silica cores with a diameter of 140 nm were prepared using the "Stöber" method. The organic dye molecules Texas Red were conjugated with APS molecules and incorporated into the silica shell during the next shell growth step to

form the dye-containing silica shell. The dye concentration within the shell was shown to be constant by absorption and fluorescence spectra of the silica-dye (silica-core – dye-shell) particles. The silica-dye particles were then functionalized with APS molecules and mixed with the QDs coated with PVP molecules, forming the final QD-silica-dye hybrid system. Directly adsorption of QDs onto the dye-containing silica shell and the strong spectral overlap between QD emission and dye absorption allowed for energy transfer from QD donors to dye acceptors, leading to enhanced acceptor emission. The sensitized acceptor emission strongly increased as the thickness of the dye-containing silica shell increased. To get a better understanding of the spectroscopic properties of the QD-silica-dye hybrid particles, Monte-Carlo FRET simulations were carried out with different models differing with respect to the amount of the surface-adsorbed QDs, suggesting that in QD-silica-dye hybrid particles the number of the bound QDs does not (or only to a minor extent) depend, as expected, on the particle surface, but significantly depends on the total amount of organic dye molecules within the dye-containing silica shell. The Monte-Carlo simulations gave an indication of an increase in the QD concentration adsorbed onto the particle surface with increasing dye-containing silica shell thickness, which was further confirmed by comparison of the amounts of QDs bound to silica-dye particles with different dye-containing silica shell thicknesses and pure silica particles corresponding in total diameter to the various silica-dye particles based on the absorption spectra, showing that with increasing shell thickness, the QD amount on the silica-dye particles strongly increased compared to that on the pure silica particles. This was also clearly visible in comparison of TEM images of silica-dye particles and pure silica particles, both with QDs adsorbed at the particle surface. The finding of the increase in QD amount with increasing dye-containing silica shell thickness suggested the existence of attractive interactions between PVP-coated QDs and Texas Red, which was supported by the observation of FRET from PVP-coated QDs to Texas Red in their mixtures. Moreover, the intensity ratio of QD and dye emission peaks, both of which are excited at the same wavelength, can be tuned by varying the thickness of the dye-containing silica shell and thereby give a set of different optical codes. Therefore, the QD-silica-dye hybrid system may lead to a new multiplexing scheme which could “barcode” biomolecules with a very high number of possible spectral signals.

A versatile approach to prepare QD-dye hybrids without a third material mediating the coupling has also been developed. Ryleneimide dyes were directly bound to the QD surface using dicarboxylate functional groups as anchors, which bind dyes to QDs with a CdSe, CdS (e.g. CdSe/CdS) or ZnS (e.g. CdSe/CdS/ZnS and CdSe/ZnS) surface. Dye molecules with dicarboxylate functionality revealed a strong and robust attachment to QDs and the prepared QD-dye hybrids were stable against repeated precipitation-dissolution cycles and long-term storage. After optimizing reaction conditions, it was found that the use of basic condition, sonication and the addition of methanol favored the formation of the QD-dye hybrids. By proper choice of dye and QD components, a broad spectral range from the visible up to the NIR can be covered and additionally the efficiency of energy transfer can be easily tuned. With increasing dye amounts, the QD emission was successively quenched and sensitized dye emission increased, indicating efficient energy transfer in the QD-dye hybrid system. Through Stern-Volmer analysis, FRET was suggested as the mechanism of the energy transfer. The systematic study of the dependence of PL dynamics on the QD-dye distance, which was varied by controlling number of ZnS layers while preserving the binding geometry, provided additional proof confirming that FRET was the dominant mechanism. Due to the high stability of the QD-dye hybrids, they could be easily transferred into the aqueous phase via the "refluxing" method. MPA and DHLA ligands were used to exchange the original organic ligands on the surface of the QD-dye hybrids and render the QD-dye hybrids water-soluble. The QD-dye hybrids were found to survive in water after the transfer, although a part of dye molecules detached from the QD-dye hybrids during the transfer. Reaction conditions, such as the amount of exchange ligands, reaction time and reaction temperature, were optimized in order to reduce the dye detachment. The water-soluble QD-dye hybrids showed a pH-dependent emission between QD and dye that as the pH value of their aqueous solutions increased, the emission from QDs increased while the emission form dye molecules decreased. In addition, preliminary experiments were done to link QDs with dye molecules carrying two dicarboxylate groups at the two ends of the dye molecule. QD dimers were formed, although further separation procedures need to be developed to separate dimers from monomers, oligomers and small aggregates. After removal of free dye molecules by purification procedures, the linkage of QDs by dye molecules was proven by the presence of dye emission. The approach of preparing QD-dye hybrids was also applied to prepare QD-calixarene

complexes using calix[4]arene with dicarboxylic acid groups as anchors. It was found that only 1 ~ 2 calixarenes could be attached to the QDs regardless of the amount of calixarene molecules added in the beginning. This feature promises to assemble QD-calixarene-dye hybrids with controllable dye number per QD or QD-QD dimers for deeper insight into the energy transfer in these two systems.

References

[1] Murray, C. B.; Norris, D. J.; Bawendi, M. G. *J. Am. Chem. Soc.* **1993**, 115, 8706.

[2] Mattoussi, H.; Radzilowski, L. H.; Dabbousi, B. O.; Thomas, E. L.; Bawendi, M. G.; Rubner, M. F. *J. Appl. Phys.* **1998**, 83, 7965.

[3] Rodriquez-Viejo, J.; Mattoussi, H.; Heine, J. R.; Kuno, M. K.; Michel, J.; Bawendi, M. G.; Jensen, K. F. *J. Appl. Phys.* **2000**, 87, 8526.

[4] Förster, T. *Discuss. Faraday Soc.* **1959**, 27, 7.

[5] Lakowicz, J. R. *Principles of Fluorescence Spectroscopy. 3rd.* New York, Plenum Press, **2006**.

[6] Hines, M. A.; Guyot-Sionnest, P. *J. Phys. Chem. B* **1996**, 100, 468.

[7] Dabbousi, B. O.; Rodriguez Viejo, J.; Mikulec, F. V.; Heine, J. R.; Mattoussi, H.; Ober, R.; Jensen, K. F.; Bawendi, M. G. *J. Phys. Chem. B* **1997**, 101, 9463.

[8] Leatherdale, C. A.; Woo, W. K.; Mikulec, F. V.; Bawendi, M. G. *J. Phys. Chem. B* **2002**, 106, 7619.

[9] Jaiswal, J. K.; Mattoussi, H.; Mauro, J. M.; Simon, S. M. *Nat. Biotechnol.* **2003**, 21, 47.

[10] Medintz, I. L.; Clapp, A. R.; Mattoussi, H.; Goldman, E. R.; Fisher, B.; Mauro, J. M. *Nat. Mater.* **2003**, 2, 630.

[11] Rurack, K.; Martínez-Máñez, R. *The Supramolecular Chemistry of Organic-Inorganic Hybrid Materials.* New Jersy, John Wiley & Sons, Inc., **2010**.

[12] Lidke, D. S.; Wilson, B. S. *Trends Cell Biol.* **2009**, 19, 566.

[13] Medintz, I. L.; Uyeda, H. T.; Goldman, E. R.; Mattoussi, H. *Nat. Mater.* **2005**, 4, 635.

[14] Clapp, A. R.; Medintz, I. L.; Mattoussi, H. *ChemPhysChem* **2006**, 7, 47.

[15] Dubertret, B. *Nat. Mater.* **2005**, 4, 797.

[16] Medintz, I. L.; Deschamps, J. R. *Curr. Opin. Biotechnol.* **2006**, 17 (1), 17.

[17] Lin, C.-A. J.; Liedl, T.; Sperling, R. A.; Fernández-Argüelles, M. T.; Costa-Fernández, J. M.; Pereiro, R.; Sanz-Medel, A.; Chang, W. H.; Parak, W. J. *J. Mater. Chem.* **2007**, 17 (14), 1343.

[18] Potapova, I.; Mruk, R.; Hübner, C.; Zentel, R.; Basché, T.; Mews, A. *Angew. Chem. Int. Ed.* **2005**, 44, 2437.

[19] Ebenstein, Y.; Mokari, T.; Banin, U. *J. Phys. Chem. B* **2004**, 108, 93.

[20] Müller, F.; Gotzinger, S.; Gaponik, N.; Weller, H.; Mlynek, J.; Benson, O. *J. Phys. Chem. B* **2004**, 108, 14527.

[21] Ebenstein, Y.; Yoskovitz, E.; Costi, R.; Aharoni A.; Banin, U. *J. Phys. Chem. A* **2006**, 110, 8297.

[22] Chang, E.; Miller, J. S.; Sun, J.; Yu, W. W.; Colvin, V. L.; Drezek, R.; West, J. L. *Biochem. Biophys. Res. Commun.* **2005**, 334, 1317.

[23] Xu, C.; Xing, B.; Rao, J. Biochem. *Biophys. Res. Commun.* **2006**, 344, 931.

[24] Fernandez-Arguelles, M. T.; Yakovlev, A.; Sperling, R. A.; Luccardini, C.; Gaillard, S.; Medel, A. S.; Mallet, J. M.; Brochon, J. C.; Feltz, A.; Oheim, M.; Parak, W. J. *Nano Lett.* **2007**, 7, 2613.

[25] Clapp, A. R.; Medintz, I. L.; Mauro, J. M.; Fisher, B. R.; Bawendi, M. G.; Mattoussi, H. *J. Am. Chem. Soc.* **2004**, 126, 301.

[26] Willard, D. M.; Carillo, L. L.; Jung, J.; Van Orden, A. *Nano Lett.* **2001**, 1, 469.

[27] Shi, L.; De Paoli, V.; Rosenzweig, N.; Rosenzweig, Z. *J. Am. Chem. Soc.* **2006**, 128, 10378.

[28] Medintz, I. L.; Sapsford, K. E.; Clapp, A. R.; Pons, T.; Higashiya, S.; Welch, J. T.; Mattoussi, H. *J. Phys. Chem. B* **2006**, 110, 10683.

[29] Ow, H. D.; Larson, R.; Srivastava, M.; Baird, B. A.; Webb, W. W.; Wiesner, U. *Nano Lett.* **2005**, 5, 113.

[30] Graf, C.; Vossen, D. L. J.; Imhof, A.; Van Blaaderen, A. *Langmuir* **2003**, 19, 6693.

[31] Mornet, S.; Elissalde, C.; Hornebecq, V.; Bidault, O.; Duguet, E.; Brisson, A.; Maglione, M. *Chem. Mater.* **2005**, 17, 4530.

[32] Kobayashi, Y.; Katakami, H.; Mine, E.; Nagao, D.; Konno, M.; Liz-Marzán, L. M. *J. Colloid Interface Sci.* **2005**, 283, 392.

[33] van Blaaderen, A.; Vrij, A. *Langmuir* **1992**, 8, 2921.

[34] Rogach, A. L.; Klar, T. A.; Lupton, J. M.; Meijerink, A.; Feldmann, J. *J. Mater. Chem.* **2009**, 19, 1208.

[35] Medintz, I. L.; Mattoussi, H. *Phys. Chem. Chem. Phys.* **2009**, 11, 17.

[36] Pons, T.; Medintz, I. L.; Sykora, M.; Mattoussi, H. *Phys. Rev. B* **2006**, 73, 245302.

[37] Clapp, A. R.; Medintz, I. L.; Fisher, B. R.; Anderson, G. P.; Mattoussi, H. *J. Am. Chem. Soc.* **2005**, 127, 1242.

[38] Dayal, S.; Burda, C. *J. Am. Chem. Soc.* **2007**, 129, 7977.

[39] Blaudeck, T.; Zenkevich, E. I.; Cichos, F.; von Borczyskowski, C. *J. Phys. Chem. B* **2008**, 112, 20251.

[40] Kowerko, D.; Schuster, J.; Amecke, N.; Abdel-Mottaleb, M.; Dobrawa, R.; Würthner, F.; von Borczyskowski, C. *Phys. Chem. Chem. Phys.* **2010**, 12, 4112.

[41] Dayal, S.; Lou, Y.; Samia, A. C. S.; Berlin, J. C.; Kenney, M. E.; Burda, C. *J. Am. Chem. Soc.* **2006**, *128*, 13974.

[42] Reiss, P.; Protière, M.; Li, L. *Small* **2009**, 5, 154.

[43] Pankove, J. I. *Optical processes in semiconductors.* New York, Dover Publications Inc., **1970**.

[44] Trindade, T. *Chem. Mater.* **2001**, 13, 3843.

[45] Gaponenko, S. V. *Optical Properties of Semiconductor Nanocrystals*. Cambridge U.K., Cambridge University, **1998**.

[46] Alivisatos, A. P. *J. Phys. Chem.* **1996**, 100, 13226.

[47] Brus, L.E. *Appl. Phys. A* **1991**, 53, 465.

[48] Alivisatos, A. P. *Science* **1996**, 271, 933.

[49] Haug, H.; Koch, S. W. *Quantum theory of the optical and electronic properties of semiconductors*. London, World Scientific Publishing Co. Pte. Ltd., **1990**.

[50] Brus, L. E. *J. Chem. Phys.* **1983**, 79, 5566.

[51] Brus, L. E. *J. Chem. Phys.* **1984**, 80, 4403.

[52] Steigerwald, M. L.; Brus, L. E. *Acc. Chem. Res.* **1990**, 23, 183.

[53] Murray, C. B.; Kagan, C. R.; Bawendi, M. G. *Annu. Rev. Mater. Sci.* **2000**, 30, 545.

[54] Norris, D. J.; Sacra, A.; Murray, C. B.; Bawendi, M. G. *Phys. Rev. Lett.* **1994**, 72, 2612.

[55] Norris, D. J.; Bawendi, M. G. *J. Chem. Phys.* **1995**, 103, 5260.

[56] Nirmal, M.; Brus, L. *Acc. Chem. Res.* **1999**, 32, 407.

[57] Yoffe, A. D. *Adv. Phys.* **2001**, 50, 1.

[58] Norris, D. J.; Bawendi, M. G. *Phys. Rev. B* **1996**, 53, 16338.

[59] Houtenpen, A. J.; Vanmaekelbergh, D. *J. Phys. Chem. B* **2005**, 109, 19634.

[60] Xie, R. G. *Synthesis and surface modification of semiconductor nanocrystals* (PhD). University of Mainz, **2005**, 7.

[61] Soloviev, V. N.; Eichhöfer, A.; Fenske, D.; Banin, U. *J. Am. Chem. Soc.* **2000**, 122, 2673.

[62] Rogach, A. L.; Koronowski, A.; Gao, M.; Eychmu¨ler, A.; Weller H. J. *Phys. Chem. B* **1999**, 103, 3065.

[63] Yu, W. W.; Qu, L.; Guo, W.; Peng, X. *Chem. Mater.* **2003**, 15, 2854.

[64] Bawendi, M. G.; Wilson, W. L.; Rothberg, L.; Carroll, P. J.; Jedju, T. M.; Steigerwald, M. L.; Brus, L. E. *Phys. Rev. Lett.* **1990**, 65, 1623.

[65] Bawendi, M. G.; Carroll, P. J.; Wilson, W. L.; Brus, L. E. *J. Chem. Phys.* **1992**, 96, 946.

[66] Spanhel, L.; Haase, M.; Weller, H.; Henglein, A. *J. Am. Chem. Soc.* **1987**, 109, 5649.

[67] Danek, M.; Jensen, K. F.; Murray, C. B.; Bawendi, M. G. *Chem. Mater.* **1996**, 8, 173.

[68] Hoener, C. F.; Allan, K. A.; Bard, A. J.; Campion, A.; Fox, M. A.; Mallouk, T. E.; Webber, S. E.; White, J. M. *J. Phys. Chem.* **1992**, 96, 3812.

[69] Kortan, A. R.; Hull, R.; Opila, R. L.; Bawendi, M. G.; Steigerwald, M. L.; Carroll, P. J.; Brus, L. E. *J. Am. Chem. Soc.* **1990**, 112, 1327.

[70] Mews, A.; Eychmuller, A.; Giersig, M.; Schooss, D.; Weller, H. *J. Phys. Chem.* **1994**, 98, 934.

[71] Mews, A.; Kadavanich, A. V.; Banin, U.; Alivisatos, A. P. *Phys. Rev. B.* **1996**, 53, 13242.

[72] Tian, Y.; Newton, T.; Kotov, N. A.; Guldi, D. M.; Fendler, J. H. *J. Phys. Chem.* **1996**, 100, 8927.

[73] Xie, R. G.; Battaglia, D.; Peng, X. *J. Am. Chem. Soc.* **2007**, 129, 15432.

[74] Li, L.; Reiss, P. *J. Am. Chem. Soc.* **2008**, 130, 11588.

[75] Xu, J.; Cui, D. H.; Zhu, T.; Paradee, G.; Liang, Z. Q.; Wang, Q.; Xu, S. Y.; Wang, A. Y. *Nanotechnology* **2006**, 17, 5428.

[76] Talapin, D. V.; Yu, H.; Shevchenko, E. V.; Lobo, A.; Murray, C. B. *J. Phys. Chem. C* **2007**, 111, 14049.

[77] Wilson, W. L.; Szajowski, P. F.; Brus, L. E. *Science* **1993**, 262, 1242.

[78] Xie, R. G.; Kolb, U.; Li, J. X.; Basché, T.; Mews, A. *J. Am. Chem. Soc.* **2005**, 127, 7480.

[79] Hines, M. A.; Guyot-Sionnest, P. *J. Phys. Chem.* **1996**, 100, 468.

[80] Mekis, I.; Talapin, D. V.; Kornowski, A.; Haase, M.; Weller, H. *J. Phys. Chem. B* **2003**, 107, 7454.

[81] Peng, X.; Schlamp, M. C.; Kadavanich, A.; Alivisatos, A. P. *J. Am. Chem. Soc.* **1997**, 119, 7019.

[82] Li, J. J.; Wang, Y. A.; Guo, W.; Keay, J. C.; Mishima, T. D.; Johnson, M. B.; Peng, X. *J. Am. Chem. Soc.* **2003**, 125, 12567.

[83] Talapin, D. V.; Koeppe, R.; Götzinger, S.; Kornowski, A.; Lupton, J. M.; Rogach, A. L.; Benson, O.; Feldmann, J.; Weller, H. *Nano Lett.* **2003**, 3, 1677.

[84] Reiss, P.; Carayon, S.; Bleuse, J.; Pron, A. *Synth. Met.* **2003**, 139, 649.

[85] Baranov, A. V.; Rakovich, Y. P.; Donegan, J. F.; Perova, T. S.; Moore, R. A.; Talapin, D. V.; Rogach, A. L.; Masumoto, Y.; Nabiev, I. *Phys. Rev. B* **2003**, 68, 165306.

[86] Reiss, P.; Bleuse, J.; Pron, A. *Nano Lett.* **2002**, 2, 781.

[87] Talapin, D. V.; Mekis, I.; Götzinger, S.; Kornowski, A.; Benson, O.; Weller, H. *J Phys. Chem. B* **2004**, 108, 18826.

[88] Schooss, D.; Mews, A.; Eychmuller, A.; Weller, H. *Phys. Rev. B* **1994**, 49, 17072.

[89] Henderson, B.; Imbusch, G. F. *Optical Spectroscopy of Inorganic Solids.* Oxford University Press, **1989**.

[90] Scholes, G. D. *Annu. Rev. Phys. Chem.* **2003**, 54, 57.

[91] Förster, T. *Ann. Phys.* **1948**, 2, 55.

[92] Förster, T. *Zeitschrift für Naturforschung*, **1949**, 4a, 321.

[93] Clegg, R. M. *Fluorescence resonance energy transfer.* New York, John Wiley & Sons, **1996**.

[94] Medintz, I. L.; Clapp, A. R.; Mattoussi, H.; Goldman, E. R.; Mauro, J. M. *Nat. Mater.* **2003**, 2, 630.

[95] Cheung, H. C. *Resonance energy transfer. In Topics in fluorescence spectroscopy*. New York, Plenum Press, **1991**.

[96] Kagan, C. R.; Murray, C. B.; Nirmal, M.; Bawendi, M. G. *Phys. Rev. Lett.* **1996**, 76, 1517.

[97] Kagan, C. R.; Murray, C. B.; Nirmal, M.; Bawendi, M. G. *Phys. Rev. B* **1996**, 54, 8633.

[98] Crooker, S. A.; Hollingsworth, J. A.; Tretiak, S.; Klimov, V. I. *Phys Rev. Lett.* **2002**, 89, 186802.

[99] Achermann, M.; Petruska, M. A.; Crooker, S. A.; Klimov, V. I. *J Phys. Chem. B* **2003**, 107, 13782.

[100] Kim, D. G.; Okahara, S.; Nalayama, M. *Phys. Rev. B* **2008**, 78, 153301.

[101] Koole, R.; Liljeroth, P.; Donega, C. D.; Vanmaekelbergh, D.; Meijerink, A. *J. Am. Chem. Soc.* **2006**, 128, 10436.

[102] Wargnier, R.; Baranov, A. V.; Maslov, V. G.; Stsiapura, V.; Artemyev, M.; Pluot, M.; Sukhanova, A.; Nabiev, I. *Nano Lett.* **2004**, 4, 451.

[103] Oh, M. H. J.; Gentleman, D. J.; Scholes, G. D. *Phys. Chem. Chem. Phys.* **2006**, 8, 5079.

[104] Wang, M. F.; Oh, J. K.; Dykstra, T. E.; Lou, X. D.; Scholes, G. D.; Winnik, M. A. *Macromolecules* **2006**, 39, 3664.

[105] Mayilo, S.; Hilhorst, J.; Susha, A. S.; Höhl, C.; Franzl, T.; Klar, T. A.; Rogach, A. L.; Feldmann, J. *J Phys. Chem. C* **2008**, 112, 14589.

[106] Sadhu, S.; Patra, A. *ChemPhysChem* **2008**, 9, 2052.

[107] Sadhu, S.; Tachiya, M.; Patra, A. *J. Phys. Chem. C* **2009**, 113, 19488.

[108] Sadhu, S.; Haldar, K. K.; Patra, A. *J. Phys. Chem. C* **2010**, 114, 3891.

[109] Schmelz, O.; Mews, A.; Basché, T.; Herrmann, A.; Müllen, K. *Langmuir* **2001**, 17, 2861.

[110] Funston, A. M.; Jasieniak, J. J.; Mulvaney, P. *Adv. Mater.* **2008**, 20, 4274.

[111] Boulesbaa, A.; Huang, Z.; Wu, D.; Lian T. *J. Phys. Chem. C* **2010**, 114, 962.

[112] Blaudeck, T.; Zenkevich, E. I.; Cichos, F.; von Borczyskowski, C. *J. Phys. Chem. C* **2008**, 112, 20251.

[113] Boldt, K.; Bruns, O. T.; Gaponik, N.; Eychmüller, A. *J. Phys. Chem. B* **2006**, 110, 1959.

[114] Bruchez, M.; Moronne, M., Gin, P.; Weiss, S.; Alivisatos A. P. *Science* **1998**, 281, 2013.

[115] Chan, W. C. W.; Nie, S. *Science* **1998**, 281, 2016.

[116] Mattoussi, H.; Mauro, J. M.; Goldman, E. R.; Anderson, G. P.; Sundar, V. C.; Mikulec, F. V.; Bawendi, M. G. *J. Am. Chem. Soc.* **2000**, 122, 12142.

[117] Mamedova, N. N.; Kotov, N. A.; Rogach, A. L.; Studer, J. *Nano Lett.* **2001**, 1, 281.

[118] Wang, S. P.; Mamedova, N.; Kotov, N. A.; Chen W.; Studer, J. *Nano Lett.* **2002**, 2, 817.

[119] Clapp, A. R.; Goldman E. R.; Mattoussi, H. *Nat. Protocols* **2006**, 1, 1258.

[120] Clapp, A. R.; Medintz, I. L.; Mattoussi, H. *ChemPhysChem* **2006**, 7, 47.

[121] Clapp, A. R.; Medintz, I. L.; Uyeda, H. T.; Fisher, B. R.; Goldman, E. R.; Bawendi, M. G.; Mattoussi, H. *J. Am. Chem. Soc.* **2005**, 127, 18212.

[122] Clapp, A. R.; Pons, T.; Medintz, I. L.; Delehanty, J. B.; Melinger, J. S.; Tiefenbrunn, T.; Dawson, P. E.; Fisher, B. R.; O'Rourke, B.; Mattoussi, H. *Adv. Mater.* **2007**, 19, 1921.

[123] Pons, T.; Medintz, I. L.; Wang, X.; English, D. S.; Mattoussi, H. *J. Am. Chem. Soc.* **2006**, 128, 15324.

[124] Zhang, J.; Badugu, R.; Lakowicz, J. R. *Plasmonics* **2008**, 3, 3.

[125] Pons, T.; Medintz, I. L.; Sapsford, K. E.; Higashiya, S.; Grimes, A. F.; English, D. S.; Mattoussi, H. *Nano Lett.* **2007**, *7*, 3157.

[126] Shevchenko, E. V.; Ringler, M.; Schwemer, A.; Talapin, D. V.; Klar, T. A.; Rogach, A. L.; Feldmann, J.; Alivisatos, A. P. *J. Am. Chem. Soc.* **2008**, 130, 3274.

[127] Gueroui, Z.; Libchaber, A. *Phys. Rev. Lett.* **2004**, 93, 166108.

[128] *Tetradecylphosphonic acid (TDPA) was prepared by Michaela Wagner. Dihydrolipoic acid (DHLA) was prepared as follows: 3.0 g of lipoic acid, 1.5 g of $NaHCO_3$ and 60 mL of H_2O were mixed in a three-necked flask. The mixture was cooled to 5 °C with ice under Ar, and then 0.6 g of $NaBH_4$ was added slowly. After the addition of $NaBH_4$ was finished, the reaction mixture was stirred for 30 min at room temperature. After that, 60 mL of benzene was added and the pH of the solution was adjusted to 1 with ice-cold HCl (5 M). After separating the organic phase from the aqueous phase, the organic phase (benzene) was*

distilled at 80 °C under normal pressure. The final products were stored under Ar and in the dark.

[129] Peng, Z. A.; Peng, X. *J. Am. Chem. Soc.* **2001**, 123, 183.

[130] Striolo, A.; Ward, J.; Prausnitz, J. M.; Parak, W. J.; Zanchet, D.; Gerion, D.; Milliron, D.; Alivisatos, A. P. *J. Phys. Chem. B* **2002**, 106, 5500.

[131] Leatherdale, C. A.; Woo, W. K.; Mikulec, F. V.; Bawendi, M. G. *J. Phys. Chem. B* **2002**, 106, 7619.

[132] Kuçur, E.; Boldt, F. M.; Cavaliere-Jaricot, S.; Ziegler, J.; Nann, T. *Anal. Chem.* **2007**, 79, 8987.

[133] Baeyens, W. R. G.; Keukeleire, D. De; Korkidis K. *Luminescence Techniques in Chemical and Biochemical Analysis. Practical Spectroscopy Series, Vol. 12* New York, Marcel Dekker, **1991**.

[134] Berne, B. J.; Pecora, R. *Dynamic Light Scattering:With Applications to Chemistry, Biology, and Physics.* New York, Dover, **2000**.

[135] Zhang, T. T.; Stilwell, J. L.; Gerion, D.; Ding, L. H.; Elboudwarej, O.; Cooke, P. A.; Gray, J. W.; Alivisatos, A. P.; Chen, F. F. *Nano Lett.* **2006**, 6, 800.

[136] Stöber, W.; Fink, A.; Bohn, E. J. *Colloid Interface Sci.* **1968**, 26, 62.

[137] Philipse, A. P. *Colloid Polym. Sci.* **1988**, 266, 1174.

[138] Bogush, G. H.; Zukosi, C. F. *J. Colloid Interface Sci.* **1991**, 142, 19.

[139] van Blaaderen, A.; van Geest, J.; Vrij, A. *J. Colloid Interface Sci.* **1992**, 154, 481.

[140] Ohmori, M.; Matijevic, E. *J. Colloid Interface Sci.* **1992**, 150, 594.

[141] Ryan, J. N.; Elimelech, M.; Baeseman, J. L.; Magelky, R. D. *Environ. Sci. Technol.* **2000**, 34, 2000.

[142] Liz-Marzán, L. M.; Giersig, M.; Mulvaney, P. *Langmuir* **1996**, 12, 4329.

[143] Kobayashi, Y.; Correa-Duarte, M. A.; Liz-Marzán, L. M. *Langmuir* **2001**, 17, 6375.

[144] Rogach, A. L.; Nagesha, D.; Ostrander, J. W.; Giersig, M.; Kotov, N. A. *Chem. Mater.* **2000**, 12, 2676.

[145] Gerion, D.; Pinaud, F.; Williams, S. C.; Parak, W. J.; Zanchet, D.; Weiss, S.; Alivisatos, A. P. *J. Phys. Chem. B* **2001**, 105, 8861.

[146] Nann, T.; Mulvaney, P. *Angew. Chem. Int. Ed.* **2004**, 43, 5393.

[147] Graf, C.; Dembski, S.; Hofmann, A.; Ruhl, E. *Langmuir* **2006**, 22, 5604.

[148] Osseo-Asare, K.; Arriagada, F. *J. Colloids Surf.* **1990**, 50, 321.

[149] Li, T.; Moon, J.; Morrone, A. A.; Mecholsky, J. J.; Talham, D. R.; Adair, J. H. *Langmuir* **1999**, 15, 4328.

[150] Yu, K.; Thompsett, D.; Tsang, S. *Chem. Commun.* **2003**, 1522.

[151] Santra, S.; Tapec, R.; Theodoropoulou, N.; Dobson, J.; Hebard, A.; Tan, W. *Langmuir* **2001**, 17, 2900.

[152] Yi, D. K.; Selvan, S. T.; Lee, S. S.; Papaefthymiou, G. C.; Kundaliya, D.; Ying, J. Y. *J. Am. Chem. Soc.* **2005**, 127, 4990.

[153] Selvan, T. S.; Tan, T. T.; Ying J. Y. *Adv. Mater.* **2005**, 17, 1620.

[154] Darbandi, M.; Thomann, R.; Nann, T. *Chem. Mater.* **2005**, 17, 5720.

[155] Bagwe, R. P.; Hilliard, L. R.; Tan, W. H. *Langmuir* **2006,** 22*,* 4357.

[156] Okubo, T.; Miyamoto, T.; Umemura, K.; Kobayashi, K. *Colloid Polym. Sci.* **2001**, 279, 1236.

[157] Koole, R.; van Schooneveld, M. M.; Hilhorst, J.; Donegá, C. D.;'t Hart, D. C.; van Blaaderen, A.; Vanmaekelbergh, D.; Meijerink, A. *Chem. Mater.* **2008**, 20, 2503.

[158] Lakowicz, J. R. *Principles of Fluorescence Spectroscopy.* 3rd. New York, Plenum Press, **2006**.

[159] Chang, C. L.; Fogler, H. S.; *Langmuir* **1997**, 13, 3295.

[160] Bagwe, R. P.; Yang, C. Y.; Hilliard, L. R.; Tan, W. *Langmuir* **2004**, 20, 8336.

[161] Bommarius, A. S.; Holzwarth, J. F.; Wang, D. I. C.; Hatton, T. A. *J. Phys. Chem.* **1900**, 94, 7232.

[162] Jin, Y. H.; Lohstreter, S.; Pierce, D. T.; Parisien, J.; Wu, M.; Hall III, C.; Zhao, J. X. *Chem. Mater.* **2008**, 20, 4411.

[163] Arriagada, F. J.; Osseo-Asare. K. *J. Colloid Interface Sci.* **1999**, 211, 210.

[164] Graf, C.; Schärtl, W.; Fischer, K.; Hugenberg, N.; Schmidt, M. *Langmuir* **1999**, *15*, 6170.

[165] Imhof, A.; Dhont, J. K. G. *Colloids and Surfaces A: Physicochem. Eng. Aspects* **1997**, *122*, 53.

[166] van Blaaderen, A.; Vrij, A. *J. Colloid Interface Sci.* **1993**, 56, 1.

[167] van Blaaderen A, Vrij A, *J.Colloid Interface Sci.* **1993**, 56, 1.

[168] Graf, C.; Dembski, S.; Hofmann, A.; Ruhl, E. *Langmuir* **2006**, 22, 5604.

[169] Lakowicz, J. R. *Principles of fluorescence spectroscopy*. New York, Springer, **2006**.

[170] Erker, W.; Hübler, R.; Decker, H. *European Biophys.J.* **2004**, 33, 386.

[171] Quarta, A.; Di Corato, R.; Manna, L.; Argentiere, S.; Cingolani, R.; Barbarella, G.; Pellegrino, T. *J. Am. Chem. Soc.* **2008**, *130*, 10545.

[172] Sathe, T. R.; Agrawal, A.; Nie, S. M. *Anal. Chem.* **2006**, *78*, 5627.

[173] Krutzik, P. O.; Nolan, G. P. *Nat. Meth.* **2006**, *3*, 361.

[174] Chuanliu Wu, J. Z., Chaobiao Huang, Jinping Lai, Shuyan Li, Chen Chen, Yibing Zhao, *Ang. Chem. Int. Ed.* **2007**, *46*, 5393.

[175] Wang, L.; Tan, W. H. *Nano Lett.* **2006**, *6*, 84.

[176] Fournier-Bidoz, S.; Jennings, T. L.; Klostranec, J. M.; Fung, W.; Rhee, A.; Li, D.; Chan, W. C. W. *Ang. Chem. Int. Ed.* **2008**, *47*, 5577.

[177] Zenkevich, E.; Cichos, F.; Shulga, A.; Petrov, E. P.; Blaudeck, T.; von Borczyskowski, C. *J. Phys. Chem. B* **2005**, 109, 8679.

[178] Pinaud, F.; King, D.; Moore, H.; Weiss, S. *J. Am. Chem. Soc.* **2004**, 126, 6115.

[179] Kim, S.; Bawendi, M. G. *J. Am. Chem. Soc.* **2003**, 125, 14652.

[180] Liu, Y.; Kim, M.; Wang, Y.; Wang, Y. A.; Peng, X. *Langmuir* **2006**, 22, 6341.

[181] Empedocles, S. A.; Neuhauser, R.; Bawendi, M. G. *Nature* **1999**, 399, 126.

[182] Boulesbaa, A.; Issac, A.; Stockwell, D.; Huang, Z.; Huang, J.; Guo, J.; Lian, T. *J. Am. Chem, Soc.* **2007**, 129, 15132.

[183] Boulesbaa, A.; Huang, Z.; Wu, D.; Lian, T. *J. Phys. Chem.C* **2010**, 114, 962.

[184] Doktycz, S. J.; Suslick, K. *Science* **1990**, 247, 1067.

[185] Fridman, V. M. *Ultrasonics* **1972**, 10, 162.

[186] Stryer, L.; Haugland, R. P. *Biochemistry* **1967**, 58, 719.

[187] Sugihara, K.; Teranishi, T.; Shimazu, K.; Uosaki, K. *Electrochemistry* **1999**, 67, 1172.

[188] Algar, W. R.; Krull, U. J. *ChemPhysChem* **2007**, 8, 561.

[189] Zhao, J.; Luo, L.; Yang, X.; Wang, E.; Dong, S. *Electroanalysis* **1999**, 11, 1108.

[190] Pong, B. K.; Trout, B. L.; Lee, J. Y. *Langmuir* **2008**, 24, 5270.

[191] Schärtl, W. ; Xie, R. G. ; Ren, T.; Sejfic, M.; Wenz, G.; Heisel, R.; Scherer, C.; Maskos, M.; Fischer, K.; Basché, T. *J. Lumin.* **2009**, 129, 1428.

[192] Talapin, D. V.; Rogach, A. L.; Kornowski, A.; Haase, M.; Weller, H. *Nano Lett.* **2001**, 1, 207.

[193] Snee, P. T.; Somers, R. C.; Nair, G.; Zimmer, J. P.; Bawendi, M. G.; Nocera, D. G. *J. Am. Chem. Soc.* **2006**, 128, 13320.

[194] Sardar, R.; Heap, T. B; Shumaker-Parry, J. S. *J. Am. Chem. Soc.* **2007**, 129, 5356.

[195] Wang, X.; Li, G.; Chen, T, Yang, M.; Zhang, Z.; Wu, T.; Chen, H. *Nano Lett.* **2008**, 8, 2643.

[196] Claridge, S.A.; Mastroianni, A. J.; Au, Y. B.; Liang, H. W.; Micheel, C. M.; Fréchet, J. M. J.; Alivisatos A. P. *J. Am. Chem. Soc.* **2008**, 130, 9598.

[197] Zhang, J.; Fu, Y.; Chowdhury, M. H.; Lakowicz, J. R. *Nano Lett.* **2007**, 7, 2101

[198] Peng, X. G.; Wilson, T. E.; Alivisatos A. P.; Schultz, P. G. *Angew. Chem. Int. Ed. Engl.* **1997**, 36, 145.

[199] Koole R.; Liljeroth, P.; Donegá, C. M.; Vanmaekelbergh, D.; Meijerink, M. *J. Am. Chem. Soc.* **2006**, 128, 10436

[200] Bai, L.; Ma, X. J.; Liu, J. F.; Sun, X. M.; Zhao, D. Y.; Evans, D. G. *J. Am. Chem. Soc.* **2010**, 132, 2333.

[201] Chen, G.; Wang, Y.; Yang, M. X.; Xu, J.; Goh, S. J.; Pan, M.; Chen, H. Y. *J. Am. Chem. Soc.* **2010**, 132, 3644.